UNIVERSITY OF CRETE

SCHOOL OF SCIENCES AND ENGINEERING

DEPARTMENT OF MATERIALS SCIENCE & ENGINEERING

Porous Mesoscopic Assemblies of Spinel Chalcogenide and Transition Metal Phosphide Nanoparticles for Photocatalytic Energy Conversion Applications

Ph.D. Thesis

Evangelos K. Andreou

Supervisor: **Gerasimos S. Armatas**

Heraklion 2024

ΠΑΝΕΠΙΣΤΗΜΙΟ ΚΡΗΤΗΣ

ΣΧΟΛΗ ΘΕΤΙΚΩΝ ΚΑΙ ΤΕΧΝΟΛΟΓΙΚΩΝ ΕΠΙΣΤΗΜΩΝ

ΤΜΗΜΑ ΕΠΙΣΤΗΜΗΣ ΚΑΙ ΜΗΧΑΝΙΚΗΣ ΥΛΙΚΩΝ

Πορώδη Μεσοσκοπικά Δίκτυα Νανοσωματιδίων Χαλκογονιδίου Σπινελίου και Φωσφιδίου Μετάλλου Μετάπτωσης για Εφαρμογές Φωτοκαταλυτικής Μετατροπής Ενέργειας

Διδακτορική Διατριβή

Ευάγγελος Ανδρέου

Επιβλέπων καθηγητής: **Γεράσιμος Αρματάς**

Ηράκλειο 2024

ΠΑΝΕΠΙΣΤΗΜΙΟ ΚΡΗΤΗΣ
ΣΧΟΛΗ ΘΕΤΙΚΩΝ ΚΑΙ ΤΕΧΝΟΛΟΓΙΚΩΝ ΕΠΙΣΤΗΜΩΝ
ΤΜΗΜΑ ΕΠΙΣΤΗΜΗΣ ΚΑΙ ΜΗΧΑΝΙΚΗΣ ΥΛΙΚΩΝ

ΠΡΑΚΤΙΚΟ ΔΗΜΟΣΙΑΣ ΠΑΡΟΥΣΙΑΣΗΣ ΚΑΙ ΕΞΕΤΑΣΗΣ
ΤΗΣ ΔΙΔΑΚΤΟΡΙΚΗΣ ΔΙΑΤΡΙΒΗΣ ΤΟΥ
κ. ΕΥΑΓΓΕΛΟΥ ΑΝΔΡΕΟΥ
ΥΠΟΨΗΦΙΟΥ ΔΙΔΑΚΤΟΡΟΣ ΤΟΥ ΤΜΗΜΑΤΟΣ
ΕΠΙΣΤΗΜΗΣ ΚΑΙ ΜΗΧΑΝΙΚΗΣ ΥΛΙΚΩΝ

Η Επταμελής Επιτροπή της Διδακτορικής Διατριβής του κ. Ευάγγελου Ανδρέου η οποία ορίσθηκε στην 161η Σ.Τ./5.4.2024, εκλήθη την Πέμπτη 13 Ιουνίου 2024 να εξετάσει την σύμφωνα με το Νόμο υποστήριξη της διατριβής του υποψήφιου με τίτλο:

«Porous Mesoscopic Assemblies of Spinel Chalcogenide and Transition Metal Phosphide Nanoparticles for Photocatalytic Energy Conversion Applications»
«Πορώδη Μεσοσκοπικά Πλέγματα Νανοσωματιδίων Χαλκογονιδίου Σπινελίου και Φωσφιδίου Μετάλλου Μετάπτωσης για Εφαρμογές στη Μετατροπή Ενέργειας»

Τα παρόντα μέλη της επταμελούς Επιτροπής εκφράζουν ομόφωνα την πλήρη ικανοποίησή τους για την υψηλή ποιότητα του περιεχομένου και της υποστήριξης της διατριβής.
Τα ερευνητικά αποτελέσματα της εργασίας του κ. Ευάγγελου Ανδρέου είναι σημαντικά, πρωτότυπα και διευρύνουν το πεδίο της έρευνας στην Επιστήμη και Μηχανική Υλικών.
Ως εκ τούτου, η Εξεταστική Επιτροπή προτείνει ομόφωνα την απονομή του Διδακτορικού Διπλώματος στον κ. Ευάγγελο Ανδρέου

Η Επταμελής Επιτροπή:

Γεράσιμος Αρματάς (Επιβλέπων),
Καθηγητής, Τμήματος Επιστήμης και Μηχανικής Υλικών, Πανεπιστημίου Κρήτης
Gerasimos Armatas
Digitally signed by Gerasimos Armatas
Date: 2024.06.14 08:37:55 +03'00'

Γεώργιος Κιοσέογλου,
Καθηγητής, Τμήματος Επιστήμης και Μηχανικής Υλικών, Πανεπιστημίου Κρήτης
GEORGIOS KOSEOGLOU
14/06/2024 09:33

Κωνσταντίνος Στούμπος,
Αν. Καθηγητής, Τμήματος Επιστήμης και Μηχανικής Υλικών, Πανεπιστημίου Κρήτης
KONSTANTINOS STOUMPOS
14/06/2024 10:56

Γεώργιος Κοπιδάκης,
Αν. Καθηγητής, Τμήματος Επιστήμης και Μηχανικής Υλικών, Πανεπιστημίου Κρήτης
GEORGIOS KOPIDAKIS
14/06/2024 11:42

Παντελής Τρικαλίτης,
Καθηγητής, Τμήματος Χημείας, Πανεπιστημίου Κρήτης
Digitally signed by Panteleimon Trikalitis
Date: 2024.06.14 12:05:21 +03'00'

Κωνσταντίνος Μήλιος,
Καθηγητής, Τμήματος Χημείας, Πανεπιστημίου Κρήτης
Konstantinos Milios
Digitally signed by Konstantinos Milios
Date: 2024.06.14 12:08:28 +03'00'

Ιωάννης Δεληγιαννάκης,
Καθηγητής, Τμήματος Φυσικής, Πανεπιστημίου Ιωαννίνων
IOANNIS DELIGIANNAKIS
IOANNIS DELIGIANNAKIS
14.06.2024 14:02

Abstract

The persistent rise in fossil fuel consumption, driven by the need to satisfy current energy demands, poses a significant environmental hazard, primarily due to the substantial emissions of hazardous gases into the atmosphere. While it is evident that renewable energy sources must replace a significant portion of fossil fuels, existing renewable energy production methods often lack efficiency and still present environmental challenges. Photocatalytic water splitting for hydrogen production stands out as a low-cost technique, offering a high solar to chemical conversion efficiency while emitting zero hazardous gases. Over the last few decades, the research community has explored various photocatalysts, including metal oxides, chalcogenides, nitrides, and more. Despite considerable progress in the development of photocatalytic materials, current synthetic methods often fail to provide precise control over electrochemical properties, morphology, and size of particles, leading to subpar photocatalytic performance.

In this dissertation, we introduce a new, cost-effective and environmentally friendly synthetic protocol for fabricating mesoporous networks of interconnected thiospinel (MIn_2S_4, M = Zn, Cd) nanocrystals, serving as versatile building blocks. This synthetic approach provides the advantage of adjusting the size of the constituent inorganic nanocrystals, offering significant benefits for photocatalytic energy conversion applications. Such a controllable synthesis enables precise engineering of the optical and electronic properties of the resulting photocatalysts. Namely, employing a straightforward polymer-templated self-assembly process, the thiospinel nanocrystals are organized into three-dimensional (3D) mesoporous networks with large internal surface area and we-defined pores. This structural arrangement leads to improved charge transfer kinetics and better intraparticle diffusion of the electrolyte. Given their advantageous characteristics, the mesoporous ensembles were investigated as potential photocatalysts for the water splitting reaction towards hydrogen evolution. Furthermore, by carefully selecting suitable co-catalysts such as Ni_2P, Co_2P, and β-$Ni(OH)_2$, we uncovered their significant impact on the photochemical properties of the resulting composite structures. Utilizing a combination of spectroscopic and (photo)electrochemical techniques, we identified that the formation of the thiospinel/metal phosphide/hydroxide nano-heterojunctions significantly enhances the separation and transfer ability of the photogenerated charge carriers, leading to high photocatalytic stability and activities. Notably, these improvements exceed those reported for previously studied high-performance multicomponent thiospinel-based photocatalytic systems. Overall, this research presents a novel synthetic

perspective for the rational design of photocatalysts and advances our understanding of next generation photocatalysts for clean energy conversion applications. By shedding light on key aspects of inorganic synthetic chemistry, interface engineering and photochemical reactions, the findings of this work make a significant contribution to the broader research endeavor focused on the development of sustainable energy technologies.

Περίληψη

Η συνεχής αύξηση της κατανάλωσης ορυκτών καυσίμων για την κάλυψη των αυξανόμενων ενεργειακών αναγκών αποτελεί μια σημαντική περιβαλλοντική απειλή λόγω του μεγάλου όγκου εκπομπών ρυπογόνων αερίων στην ατμόσφαιρα. Ενώ είναι σαφές ότι οι ανανεώσιμες πηγές ενέργειας πρέπει να αντικαταστήσουν ένα μεγάλο μέρος των ορυκτών καυσίμων, οι υπάρχουσες μέθοδοι παραγωγής ενεργείας από ανανεώσιμες πηγές στερούνται υψηλή απόδοσης και εξακολουθούν να μολύνουν το περιβάλλον. Η φωτοκαταλυτική διάσπαση του νερού προς παραγωγή υδρογόνου είναι μια χαμηλού κόστους τεχνική, η οποία παρέχει υψηλή απόδοση μετατροπής της ηλιακής σε χημική ενεργεία με μηδενική εκπομπή αερίων ρύπων. Τις τελευταίες δεκαετίες, οι ερευνητικές προσπάθειες έχουν οδηγήσει στην ανάπτυξη ενός μεγάλου αριθμού φωτοκαταλυτικών υλικών, συμπεριλαμβανομένων οξειδίων μετάλλων, χαλκογονιδίων, νιτριδίων και πολλά άλλα. Παρά τη σημαντική πρόοδο στη σύνθεση φωτοκαταλυτών, οι τρέχουσες συνθετικές μέθοδοι συχνά αποτυγχάνουν να παρέχουν ακριβή έλεγχο των ηλεκτροχημικών ιδιοτήτων, της μορφολογίας και του μεγέθους των σωματιδίων Αυτό έχει ως αποτέλεσμα τη δημιουργία υλικών με χαμηλή φωτοκαταλυτική απόδοση.

Στην παρούσα διατριβή, παρουσιάζουμε ένα νέο, οικονομικά αποδοτικό και φιλικό προς το περιβάλλον συνθετικό πρωτόκολλο για την ανάπτυξη μεσοπορωδών πλεγμάτων από συνδεδεμένους νανοκρυστάλλους θειοσπινελίου (MIn_2S_4, M = Zn, Cd), τα οποία χρησιμεύουν ως ευέλικτα δομικά στοιχεία. Η συγκεκριμένη συνθετική μέθοδος παρέχει ακριβή ελέγχο του μεγέθους των ανόργανων δομικών μονάδων, κάτι που είναι ιδιαίτερα επωφελές για εφαρμογές φωτοκαταλυτικής μετατροπής ενεργείας. Αυτός ο έλεγχος επιτρέπει τον βέλτιστο σχεδιασμό των οπτικών και ηλεκτροχημικών ιδιοτήτων των φωτοκαταλυτών. Συγκεκριμένα, χρησιμοποιώντας μια απλή διαδικασία αυτο-συναρμολόγησης με πρότυπο πολυμερές, οι νανοκρύσταλλοι θειοσπινελίου οργανώνονται σε τρισδιάστατα (3D) μεσοπορώδη πλέγματα με μεγάλη εσωτερική επιφάνεια και ομοιόμορφους μεσοπόρους. Αυτή η μοναδική δομική διάταξη οδηγεί σε βελτιωμένες ιδιότητες μεταφοράς φορτίου και καλύτερη διάχυση του ηλεκτρολύτη μεταξύ των νανοσωματιδίων. Λόγω αυτών των εξαιρετικών χαρακτηριστικών, αυτά τα μεσοπορώδη υλικά μελετήθηκαν ως δυνητικοί φωτοκαταλύτες για τη διάσπαση του νερού προς παραγωγή καθαρού υδρογόνου. Επιπρόσθετα, με την κατάλληλη επιλογή συγκαταλυτών όπως Ni_2P, Co_2P και β-$Ni(OH)_2$, εξετάστηκε η επίδραση τους στις διαδικασίες μεταφοράς φορτίου και την κινητική των ηλεκτροχημικών αντιδράσεων στα σύνθετα υλικά. Χρησιμοποιώντας έναν συνδυασμό φασματοσκοπικών και (φωτο)ηλεκτροχημικών τεχνικών, διαπιστώσαμε ότι ο σχηματισμός νανο-ετεροδομών θειοσπινελίου/φωσφιδίου

μετάλλου/υδροξειδίου ενισχύει σημαντικά την ικανότητα διαχωρισμού και μεταφοράς των φωτοπαραγόμενων φορέων, οδηγώντας σε υψηλή φωτοκαταλυτική σταθερότητα και αποτελεσματικότητα. Αξιοσημείωτο είναι ότι παρούσες αποδόσεις υπερβαίνουν αυτές που αναφέρθηκαν στο παρελθόν για παρόμοια φωτοκαταλυτικά συστήματα πολλαπλών συστατικών υψηλής απόδοσης. Αυτή η ερευνητική εργασία προτείνει μια καινοτόμο συνθετική προσέγγιση για τον ορθολογικό σχεδιασμό φωτοκαταλυτών και συνεισφέρει στην κατανόηση της λειτουργίας προηγμένων φωτοκαταλυτικών συστημάτων επόμενης γενιάς για εφαρμογές μετατροπής ενέργειας. Ρίχνοντας φως σε βασικές πτυχές της ανόργανης συνθετικής χημείας, της μηχανικής διεπιφανειών και των φωτοχημικών αντιδράσεων, τα ευρήματα αυτής της εργασίας συνεισφέρουν σημαντικά στην ευρύτερη ερευνητική προσπάθεια για την ανάπτυξη τεχνολογιών βιώσιμης ενέργειας.

Acknowledgements

First, I would like to thank the Department of Materials Science and Engineering of the University of Crete for providing the opportunity and infrastructure to pursue my Ph.D. diploma in this prestigious institution.

In order for me to carry out this academic research journey, I would like to express my sincere appreciation to several people that played a key role in my pursuit of this Ph.D. journey.

First of all, I would like to thank my supervisor Prof. Gerasimos Armatas for his continuous guidance, support, and encouragement. It is fair to say that without his remarkable supervision and support, I would not be able to complete my doctoral research studies.

Also, I would like to express my gratitude to my previous supervisor Prof. Constantinos Milios. During his previous supervision at my BSc. and MSc. studies, he provided me with strong foundations and guidance that was and still is necessary for me to succeed in this and future endeavors.

I would also like to thank Prof. Constantinos Stoumpos, Prof. Pantelis Trikalitis, Prof. George Kopidakis, Prof. Ioannis Deligiannakis and Prof. George Kioseoglou, for accepting to be members of my doctoral committee.

Furthermore, I would like to express my deepest gratitude to all former and present members of the ChemMater Lab that supported me and helped in every conceivable way they could. In particular, I would like to thank Dr. Ioannis Vamvasakis for his continuous and on-going help and friendship during my PhD research. Also, I would like to thank Dr. Thomai Tziotzi for the beautiful friendship and guidance from my early academic steps.

Moreover, I would like to thank Dr. Panagioti Siozo and Ms. Evangelia Giannaki from the Foundation for Research and Technology Hellas (FORTH) for the Raman and DSC measurements, and Dr. Benoit Loppinet and Dr. Lampro Papoutsakis (FORTH) for help with the handling of the SAXS data.

Lastly, I would like to thank my family, who are always supporting me in everything I want to achieve.

This work was supported by the Hellenic Foundation for Research and Innovation (H.F.R.I.) under the “1st Call for H.F.R.I. Research Projects to support Faculty Members & Researchers and the Procurement of High-cost research equipment grant” (Project Number: 400). Also, I gratefully acknowledge financial support from Special Account for Research Funds of University of Crete (SARF UOC) (KA 11203).

Contents

Chapter 1: Introduction **1**

1.1 Hydrogen the future energy source: Photocatalytic water splitting towards hydrogen production 1

1.2 Semiconductor-based photocatalytic hydrogen production 2

1.3 Metal-chalcogenides: Thiospinels a rising family of materials for photocatalytic energy conversion applications 12

1.4 Transition metal phosphides and Ni-based co-catalysts 19

1.5 Thesis statement and objectives 27

Chapter 2: Experimental Section **29**

2.1 Synthesis of $ZnIn_2S_4$ and $CdIn_2S_4$ colloidal nanocrystals 29

2.2 Synthesis of mesoporous $ZnIn_2S_4$ and $CdIn_2S_4$ frameworks 29

2.3 Synthesis of transition metal phosphides 30

2.3.1 Synthesis of Ni_2P nanosheets 30

2.3.2 Synthesis of Co_2P nanoparticles 30

2.4 Preparation of $CdIn_2S_4$-based heterostructures 31

2.4.1 Preparation of Ni_2P-modified $CdIn_2S_4$ heterostructures 31

2.4.2 Preparation of Co_2P-modified $CdIn_2S_4$ heterojunctions 31

2.4.3 Preparation of Ni-modified $CdIn_2S_4$ heterostructures 32

2.5 Physical characterization 32

2.6 (Photo)electrochemical measurements 34

2.7 Photochemical water splitting study 35

Chapter 3: Results and Discussion **37**

3.1 Size Dependent Photocatalytic Activity of Mesoporous $ZnIn_2S_4$ Nanocrystal Networks 37

3.1.1 Synthesis, structural investigation, and morphology 37

3.1.2 Photocatalytic hydrogen evolution activity 50

3.1.3 Size-dependent electronic properties of mesoporous $ZnIn_2S_4$ structures 55

3.1.4 Conclusions 64

3.2 Mesoporous Catalysts of Hexagonal $CdIn_2S_4$ Nanocrystals Decorated with Ni_2P Nanosheets 65

3.2.1 Synthesis, phase structure and morphology 65

3.2.2 Photocatalytic study 86
3.2.3 Effect of Ni_2P on the photocatalytic activity 92
3.2.4 Conclusions 101
3.3 Mesoporous Mott-Schottky heterojunctions of Co_2P-modified $CdIn_2S_4$ nanocrystals 102
3.3.1 Synthesis and structural characterization 102
3.3.2 Photocatalytic study 111
3.3.3 Charge transfer and reaction mechanism 118
3.3.4 Conclusions 128
3.4 Mesoporous networks of p-n β-$Ni(OH)_2$-$CdIn_2S_4$ nano-heterojunctions 130
3.4.1 Synthesis, structural characterization, and morphology 130
3.4.2 Photocatalytic hydrogen evolution study 141
3.4.3 Energy band structure and charge transfer kinetics 147
3.4.4 Conclusions 156
Chapter 4: Concluding Remarks **157**
Annex I: Photocatalytic comparison with other reported materials 159
References 161

Chapter 1: Introduction

1.1 Hydrogen the future energy source: Photocatalytic water splitting towards hydrogen production

The last few decades, the rapid industrialization along with the continuous growth of the life-expectancy and life-quality has resulted to a growing energy consumption need. Until now, a major fraction of the energy produced to cover the ongoing demands derives from combustion of fossil fuels [1–4]. This fossil fuel energy dependence has become an economic and environmental burden [5,6]. The fact that the current fossil fuel reserves will be diminished from the increased consumption rate provides an economic uncertainty, which may lead to a global energy crisis with skyrocketed fossil fuel prices [7]. Also, due to the emissions of greenhouse gases from the utilization of fossil fuels, it poses a major threat to the environment, contributing to the global warming effect [8–10]. Hydrogen (H_2) is considered as well-qualified candidate to meet our energy demands due to high gravimetric energy density (120 MJ kg^{-1}) and zero-carbon emission when converted into electricity or heat, yielding only water as byproduct according to the following equation:

$$2H_2(g) + O_2 \rightarrow 2H_2O(g) + \text{energy} \quad (1)$$

Hydrogen, as the most abundant element in the universe and non-toxic in its natural form, represents a promising and sustainable solution to meet our current energy requirements [11]. Furthermore, hydrogen can be utilized as a fuel in power generation systems and internal combustion engines, enabling its storage and usage in transportation systems [12,13]. However, despite the extraordinary properties of hydrogen, over 90% of it is currently produced from fossil fuels using inefficient production techniques (e.g. steam methane reforming), resulting in the emission of various hazardous gases into the environment (mainly CO and CO_2) [14,15]. Hence, it is imperative to explore alternative methods of hydrogen production that combine high efficiency, low cost, and environmental sustainability.

Photocatalytic water splitting has gained tremendous attention over the recent years [16–18]. The rationale behind this approach lies in (a) its classification as a low-cost production technique, leveraging sunlight irradiation, which stands as the cheapest and cleanest energy source for chemical conversion applications. Moreover, it can exhibit (b) exceptional high solar-to-hydrogen efficiency and (b) the capability of simultaneously producing H_2 and O_2 gases in separation processes. During photocatalytic water splitting, (d) there is no production of hazardous gases in the atmosphere, and (e) the tunable size of the photocatalytic reactors

offers significant flexibility to the industrial sector. Given the aforementioned advantages, the significant interest of the research community in photocatalytic hydrogen production is well-justified. For sustainable photocatalytic water splitting, the manufactured photocatalysts (which utilize solar light for redox processes) must combine (a) high activity towards the hydrogen reduction reaction, (b) exceptional photochemical stability, (c) high solar-to-chemical conversion efficiency, (d) low-cost and (e) non-toxicity [19,20]. To this end, over the last few decades, the research community has extensively investigated numerous materials, focusing primarily on semiconductor materials to identify the optimal photocatalyst for large-scale hydrogen [21,22].

1.2 Semiconductor-based photocatalytic hydrogen production

Mechanism and thermodynamics of the photocatalytic water splitting

The groundbreaking work of Fujishima and Honda in 1972 set the grounds for photocatalytic water splitting in semiconductor materials [23]. Briefly, when a photocatalyst absorbs light irradiation, the electrons (e^-) in the valence band (VB) of the photocatalyst get excited to the conduction band (CB), leaving photogenerated holes (h^+) in the valence band. After this process, the population of electrons and holes separates and emigrates to the photocatalyst surface, where the photoexcited electrons act as reducing agents, producing H_2, while the photogenerated holes act as oxidizing agents, producing O_2 [24,25]. The water splitting reaction requires a standard Gibbs free energy change of ΔG^o = +237 kJ mol^{-1} or 1.23 eV as can be seen in following equation (**eq. 2**).

$$H_2O \rightarrow \frac{1}{2} O_2 + H_2,\ \Delta G = +237\ \text{kJ mol}^{-1} \quad (2)$$

For this reason, the energy difference between the valence band and the conduction band of the semiconductor (band gap energy, E_g), should be larger than 1.23 eV (or >1000 nm) in order for the overall photocatalytic water splitting reaction to take place. A schematic of semiconductor-based photocatalytic water splitting is depicted in **Figure 1-1**.

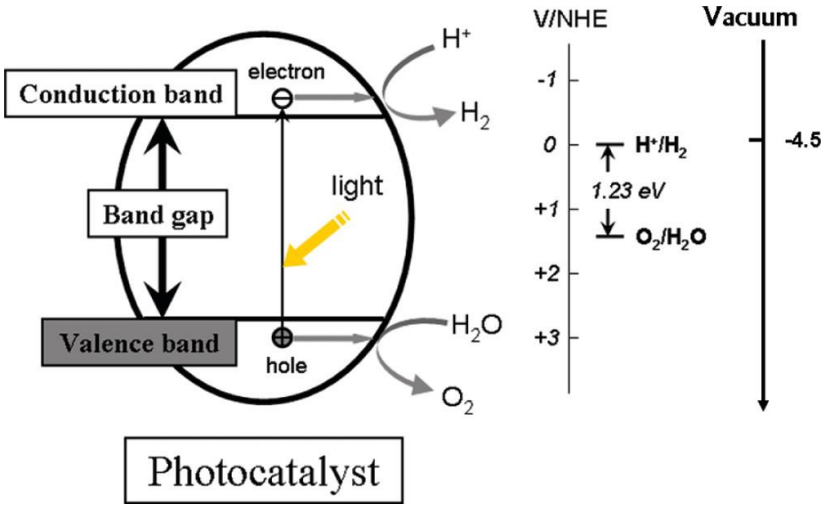

Figure 1-1. Schematic illustration of semiconductor-based photocatalytic water splitting toward hydrogen evolution. Reprinted with permission from ref. [24]. Copyright 2010 American Chemical Society.

The overall photocatalytic water splitting consists of two half reactions: (a) the hydrogen evolution reaction (HER) or water reduction and (b) the oxygen evolution reaction (OER) or water oxidation. The redox potentials (E^0) of those half-reactions (V vs NHE) are pH dependent and can be written as follows in acidic and alkaline solution conditions (eq. 3-7).

pH =0

(HER) $2H^+ + 2e^- \rightarrow H_{2(g)}$	E_{red} = 0.0 V	(3)
(OER) $2H_2O_{(l)} + 4h^+ \rightarrow O_{2(g)} + 4H^+$	E_{ox} = 1.23 V	(4)

pH =14

(HER) $2H_2O_{(l)} + 2e^- \rightarrow H_{2(g)} + 2OH^-$	E_{red} = –0.826 V	(5)
(OER) $4\ OH^- + 4h^+ \rightarrow O_{2(g)} + 2H_2O$	E_{ox} = 0.404 V	(6)

Overall water splitting reaction

$2H_2O_{(l)} \rightarrow 2H_{2(g)} + O_{2(g)}$	ΔE = 1.23 V	(7)

The redox potentials are pH dependent, and they follow the Nernst equation as follows (eq. 8-9):

E_{red} = –0.059 V × pH (vs NHE) (8)

E_{ox}= 1.23 V – 0.059 V × pH (vs NHE) (9)

Considering the above, a photocatalyst must fulfill certain requirements for the photocatalytic water splitting reaction to occur. Specifically, the conduction band (CB) must be located at a more negative position than the reduction potential of the H^+/H_2 couple, while the valence band (VB) must be positioned at a more positive potential than the oxidation potential of the H_2O/O_2 couple. For instance, in a pH 7 environment (vs normal hydrogen electrode, NHE), the CB of the photocatalyst must be positioned at potentials above –0.41 V (vs NHE), while the valence band (VB) should be located at potentials below 0.82 V (vs NHE). **Figure 1-2** depicts the thermodynamic requirements for semiconductor photocatalytic overall water splitting.

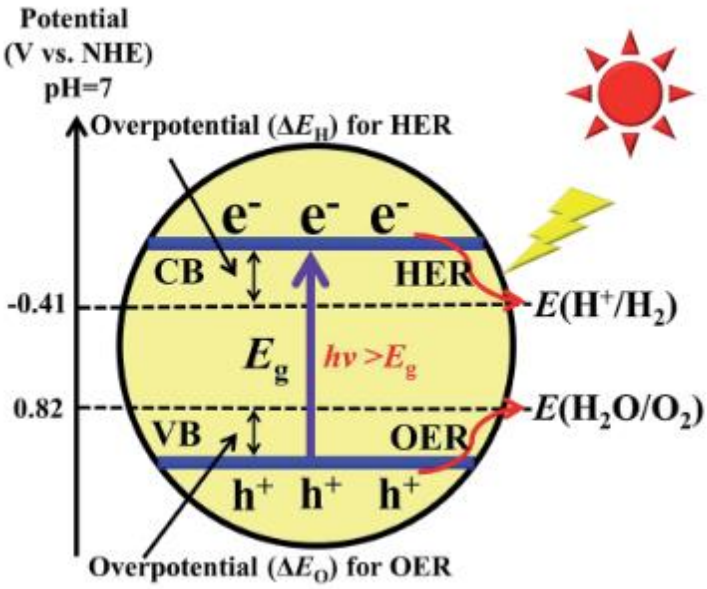

Figure 1-2. Overall water splitting thermodynamic requirements. The dashed lines represent the water redox potentials in V (vs NHE), at pH 7. Reproduced from ref. [25] with the permission of Royal Society of Chemistry.

When photocatalytic water splitting occurs on the surface of the semiconductor, multiple processes take place simultaneously [26]. A more detailed photocatalytic water splitting mechanism is depicted in **Figure 1-3**. As can be seen in Figure 1-3, the photocatalytic water splitting reaction is consisted of five main processes (I-V): (I) photon absorption, (II) separation of charge carriers, (III) migration of charges to the semiconductor/electrolyte interface, (IV) charge carrier recombination and (V) redox reaction. Specifically, when photons with energy greater than band gap energy of the semiconductor (E_g) are absorbed, electrons (e^-) are excited to the CB, while holes (h^+) are generated in the VB of the photocatalyst. Subsequently, the separated electron/hole pairs migrate from the semiconductor to the semiconductor/electrolyte

interface, where the water oxidation and reduction reactions occur. Unfortunately, not all the photoexcited charge carriers contribute to the redox reactions, as a significant fraction undergoes recombination phenomena in the bulk region and at the surface of the photocatalyst, generating thermally induced phonons. It is widely believed that charge recombination phenomena play a significant role in the loss of photoexcited charge carriers, thereby limiting the efficiency of solar-to-hydrogen conversion.

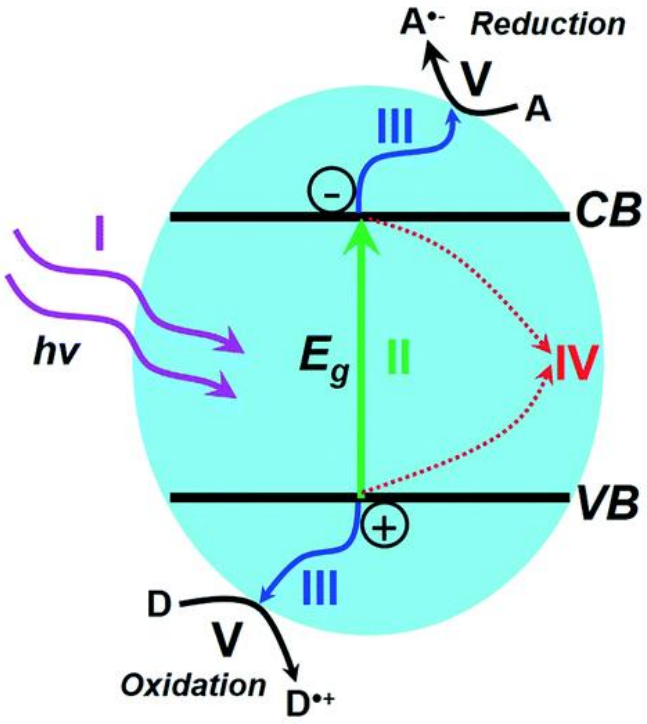

Figure 1-3. Photocatalytic water splitting of a particulate photocatalyst. Five main processes occur: (I) light absorption, (II) charge separation, (III) charge migration, (IV) charge recombination and (V) redox reactions. Reproduced from ref. [26] with the permission of Royal Society of Chemistry.

Designing photocatalysts at the nanoscale

Many semiconductor materials (especially metal oxides) suffer from sluggish redox kinetics, low density of catalytic active sites and rapid recombination of the photoexcited electron/hole pairs, resulting to poor photocatalytic performance. The rational synthetic design of photocatalysts in the nanoscale has been proven quite effective, boosting the photocatalytic activity. The radical size reduction to the nanometer scale results in an abundance of atoms or ions on the surface of the photocatalyst, leading to an increased number of catalytic sites. The plethora of surface-active sites results in a higher catalytic activity of the semiconductor compared to larger bulk particles of the same material [27]. Also, the electronic and optical

properties are altered as a result of the size reduction [28–30]. Specifically, when the size of a semiconductor is smaller than its Bohr radius, the movement of charge carriers is confined to a very small physical space due to the quantum confinement effect. This leads to size-dependent electronic and optical characteristics (**Figure 1-4**).

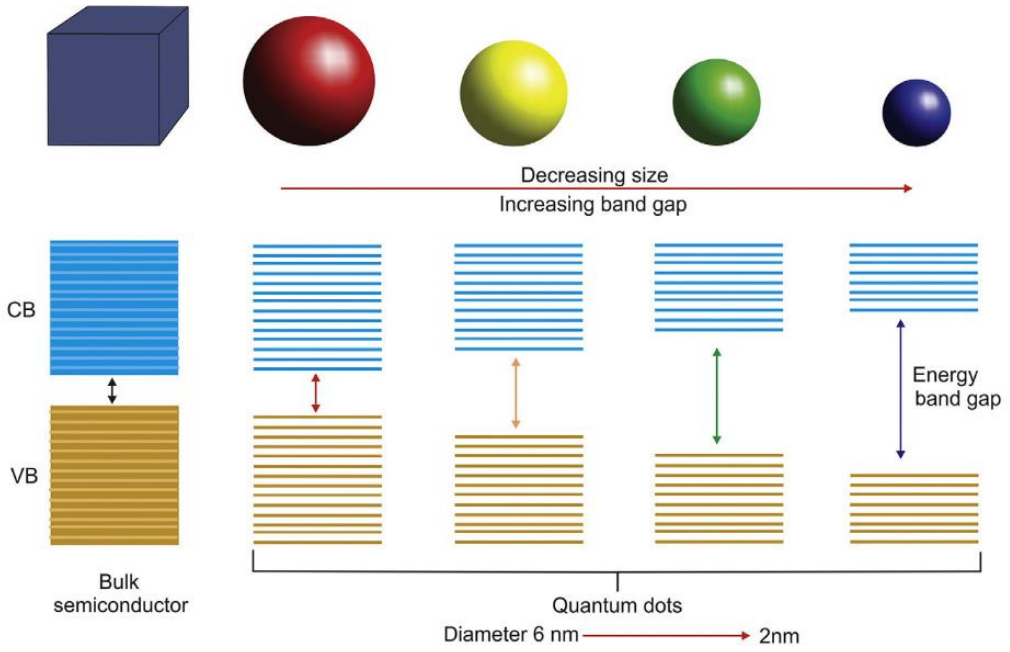

Figure 1-4. Schematic illustration of the electronic and optical properties alteration due to the quantum confinement effect. Reproduced from ref. [30] with the permission of Elsevier.

Moreover, the size of the photocatalyst plays a crucial role in efficient light absorption. Semiconductor light absorption also follows the Beer-Lambert law (eq. 10).

$$I_d = I_0 \cdot e^{-\alpha d} \quad (10)$$

The optical penetration depth (δ_p) is dependent on the wavelength-dependent absorption coefficient (α) (eq. 11), thus the semiconductor ability to effectively absorb the incident light is size-dependent and the existence of nanoparticles enhances the absorption ability of the semiconductor.

$$\delta_p = \frac{1}{a} \quad (11)$$

The charge recombination during the photoexcitation of electron/hole pairs is one of the leading causes of the poor photocatalytic performance in many photocatalysts. The very small size of nanostructured catalysts allows photogenerated charge carriers to migrate efficiently to the surface of the catalyst, reducing recombination rates within the material. However, while the

charge recombination rate inside the material is delayed due to the migration of charge carriers to the surface, there is a possibility of a considerable increase in the charge recombination rate on the surface [31]. To address the increase in surface charge recombination, the assembly of nanoporous semiconductors, particularly mesoporous ones comprising closely packed nanoparticles, can mitigate this effect.

The synthesis of mesoporous architectures (pore size ranging from 2 to 50 nm) has been at the forefront of research. Recently, they have demonstrated significant catalytic potential in environmental and energy conversion applications [32–34]. Especially, self-assembled materials comprising semiconductor nanoparticles as building blocks, which create a three-dimensional (3D) mesoporous network, combine the merits of mesoporous structures with desirable electronic and optical properties from the nanoscale. Additionally, they offer a plethora of catalytic active sites [35]. Although numerous synthetic methods have emerged for constructing mesoporous materials in recent years, template-assisted methods are predominantly utilized. The template-assisted strategies can be divided into two main methods: (a) the soft-template and (b) the hard-template method [36]. Briefly, in the soft-template method the mesopore architecture is constructed using soft-matter supramolecular aggregates, such as block copolymers, which are co-assembled with the inorganic components [37]. **Figure 1-5** illustrates the general soft-template strategies consisting of three main pathways for devising mesoporous materials: (a) cooperative self-assembly (CSA), (b) true liquid-crystal templating (TLCT), (c) evaporation-induced self-assembly (EISA) and (d) hard-template strategy [38–42]. In the hard-template method, the synthetic route mainly involves using mesoporous silica as a template to construct the mesoporous skeleton. In a typical procedure, the desired precursors are deposited into the pores of the hard template and through thermal or chemical treatment, along with the selective removal of the template (using HF or NaOH), the desired mesoporous structure is obtained. In general, mesoporous architectures offer large accessible surfaces, facilitating improved mass and charge carrier diffusion along the mesoporous skeleton. Additionally, the porous nature of these materials enhances electrolyte diffusion. When combined with unique electronic and optical properties derived from semiconductor nanoparticles due to the quantum confinement effect, along with the abundance of catalytic sites, the resultant photocatalyst may exhibit superior performance in the water splitting reaction.

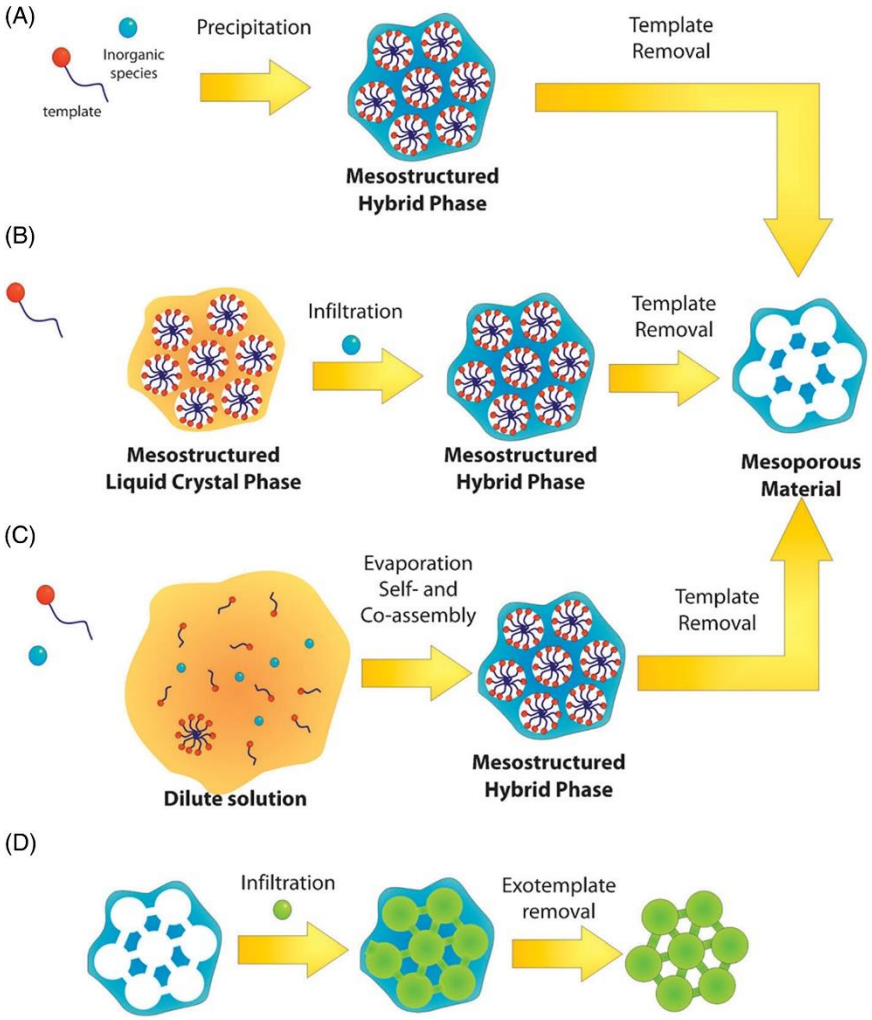

Figure 1-5. Schematic representation of the main synthetic routes for obtaining mesoporous materials. (A-C) Soft-template methods: (A) Cooperative self-assembly (CSA), (B) true liquid-crystal templating (TLCT), and (C) evaporation-induced self-assembly (EISA). (D) Hard-template method. Reproduced from ref. [42] with the permission of Royal Society of Chemistry.

Interface engineering strategies for improving photocatalytic activity

In addition to synthetic engineering pathways, enhancing the photocatalytic performance of semiconductors can be achieved through (a) the deposition of noble metals, (b) doping with metals (such as Ag, Ni, Fe) or non-metals (such as N, S, F) into the crystal structure, and (c) the construction of heterojunctions with co-catalysts. Among the above methods, constructing heterojunctions between the semiconductor and another material (co-catalyst), is one of the most effective ways of boosting photocatalytic activity. Given that rapid charge recombination phenomena significantly reduce photocatalytic efficiency, the creation of heterojunctions is an effective way to enhance the spatial separation of photogenerated electron/hole pairs. A

heterojunction can be formed by combining a metal and a semiconductor material, resulting in a Schottky type junction. When the metal's work function (φ_M) is higher than the electrochemical potential of the semiconductor, the metal-semiconductor contact gives rise to a Schottky barrier [43]. The work function of a metal is the energy required to transfer an electron from the Fermi level (E_F) of the metal to vacuum. In general, metals exhibit lower Fermi level energy and are more conductive compared to semiconductor materials [44]. In most n-type semiconductors, the Fermi level energy is located very close to the CB and is almost equal to the electron affinity (η_{SM}) of the semiconductor, which represents the energy required for a CB electron to move to the vacuum [45] (**Figure 1-6a**). When a semiconductor and metal come into contact during the formation of a Schottky junction, electrons migrate from the semiconductor Fermi level (E_F) to the Fermi level of the metal until a state of equilibrium of both E_F is reached [46] (**Figure 1-6b**). Such electron transfer results in an electron deficiency in the semiconductor side and an accumulation of positive holes (h^+) near the semiconductor/metal interface. Simultaneously, a large number of electrons are accumulated in the metal near the interface to maintain electrical neutrality. This process leads to the formation of a depletion layer at the junction, creating an energy barrier for the charge carriers known as the Schottky barrier (**Figure 1-6c**). In order for the charge carriers to migrate from the semiconductor to the metal, they must overcome this energy barrier. The Schottky energy barrier provides an electron trapping state, forcing electrons to return to the semiconductor. This reduces charge recombination of photoexcited carriers, leading to enhanced photocatalytic activity [47,48].

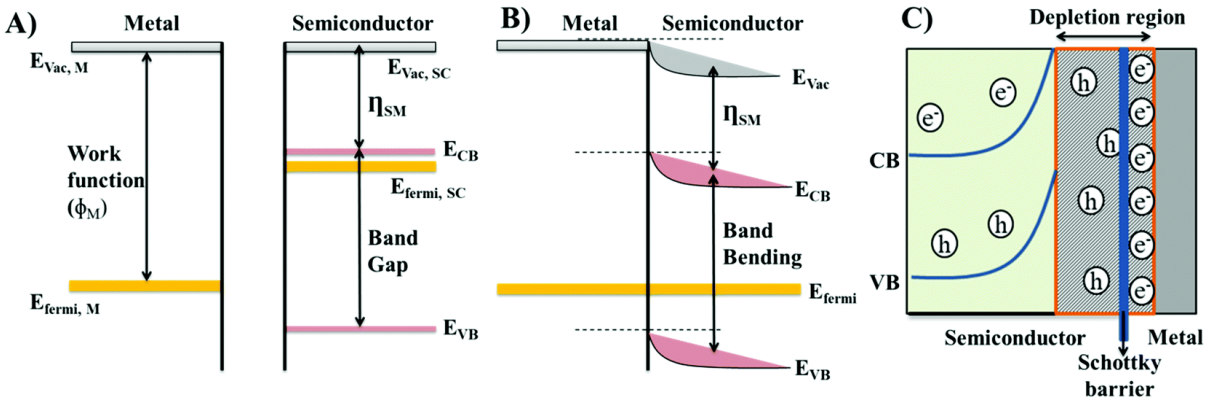

Figure 1-6. (a) Metal and n-type semiconductor band structures before contact. (b) Band structures after contact of the metal and the n-type semiconductor. (c) Schematic representation of the charge carriers flows and the formation of the Schottky-like energy barrier. Reproduced from ref. [47] with the permission of Royal Society of Chemistry.

Except for metal/semiconductor contacts, semiconductor/semiconductor heterojunctions can be formed to enhance the photocatalytic activity. Regarding the conductivity type of semiconductor, whether it's p-type (where holes are the majority charge carriers) or n-type (where electrons are the majority charge carriers), heterojunctions can be characterized as p-p, n-n, and p-n. From two n-type (p-type) semiconductors, an n-n (p-p) heterojunction is formed, while a p-n heterojunction derives from the contact of one p-type and one n-type semiconductor material. Also, the semiconductor heterojunctions can further be categorized as Type I, II and III based on the band alignment of the two semiconductors (SC-1 and SC-1). In the Type I band alignment scheme, the CB of semiconductor SC-1 is more negatively positioned than that of SC-2, and the VB is more positively positioned than that of SC-2. In Type II, the CB of SC-1 is located in more negative values than that of SC-2, while the VB of SC-1 is in less positive values than that of SC-2. In Type III, the CB and VB edges of SC-2 are located lower those of SC-1 [49]. **Figure 1-7** depicts the possible band alignments for a semiconductor/semiconductor heterojunction.

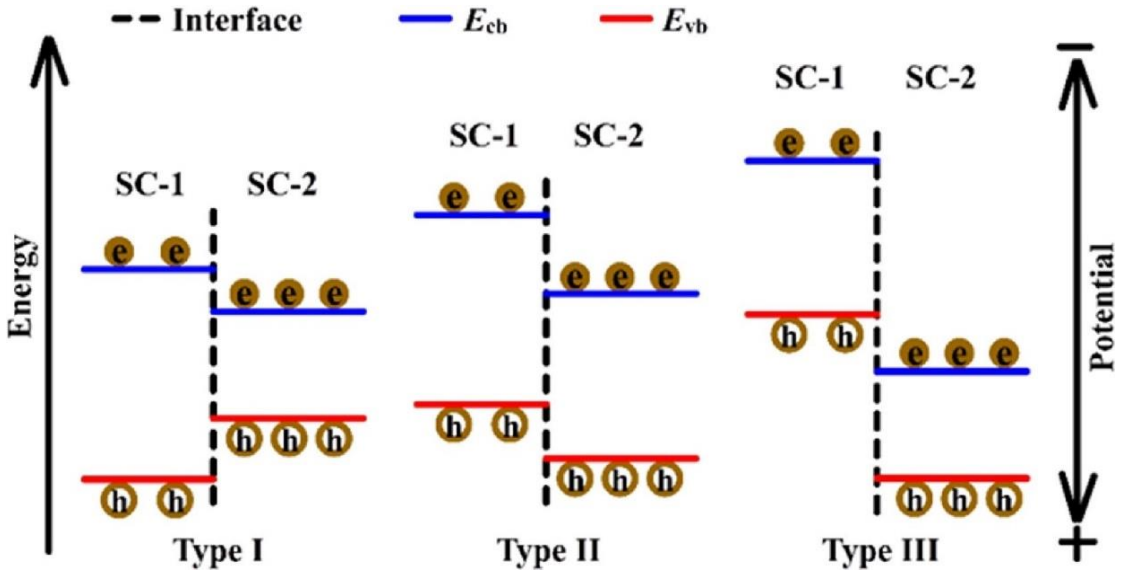

Figure 1-7. Possible band alignments of two semiconductors in heterojunctions. Reproduced from ref. [49] with the permission of Elsevier.

In particular,

- *In Type I band alignment*, when SC-1 exhibits a higher E_F than SC-2, electrons from the SC-1 will migrate to SC-2, until equilibrium of the Fermi levels of two semiconductors is achieved. Due to the transfer of electrons from SC-1 to SC-2, the surface of SC-2 will display a negative charge, while SC-1, having lost electrons, will exhibit a positive charge,

creating an internal electric field directed from SC-1 to SC-2. During light irradiation, the photogenerated holes (h^+) will transfer from SC-1 to SC-2, facilitated by the internal electrical field [46]. On the other hand, the migration of photoexcited electrons from SC-1 to SC-2 is obstructed, causing electrons from SC-2 to accumulate at the interface and preventing their migration to SC-1 due to the more negative CB of SC-1 (Type I-1) [50]. Such an electron accumulation in the interface can be averted in the case of p-n type heterojunction, in which SC-1 is p-type and SC-2 is n-type. In this scheme, the migration of electrons from SC-2 to SC-1 is favored, while the photogenerated holes accumulate at the interface (Type I-2). It should be noted that in both cases, there is enhanced charge separation of electron/hole pairs.

- *In Type II band alignment*, when the E_F of SC-1 is higher than that of SC-2, an internal electric field is generated from SC-1 to SC-2 (Type II-1). During light irradiation, photoexcited electrons from the space charge region of SC-1 will transfer to the interior, while the holes will migrate to the interface. Simultaneously, the photogenerated electrons of SC-2 will transfer to the interface, while the holes will migrate to the interior, in contrast to SC-1. This results in the interception of electrons from SC-2 and holes from SC-1, leading to reduced charged carrier recombination [51]. Thus, the remaining population of electrons from SC-1 and holes from SC-2 are free to take part in redox reactions. This type of heterojunction is called the Z-scheme system because the processes of photoexcitation and recombination display a Z-shaped route [52–54]. In the case where the E_F of p-type SC-2 is located higher than that of n-type SC-1, the internal electric field direction is from SC-2 to SC-1 (Type II-2).
- *In Type III band alignment*, electrons and holes cannot transfer to the band of the other semiconductor and accumulate at the interface (Type III-1). To facilitate the transfer of electrons and holes from the interface in Type III heterojunctions, the introduction of a suitable charge mediator is necessary. This mediator can connect the two semiconductors via a Z-scheme [55].

A schematic representation of the different heterojunctions taking into account the internal electric field is depicted in **Figure 1-8**.

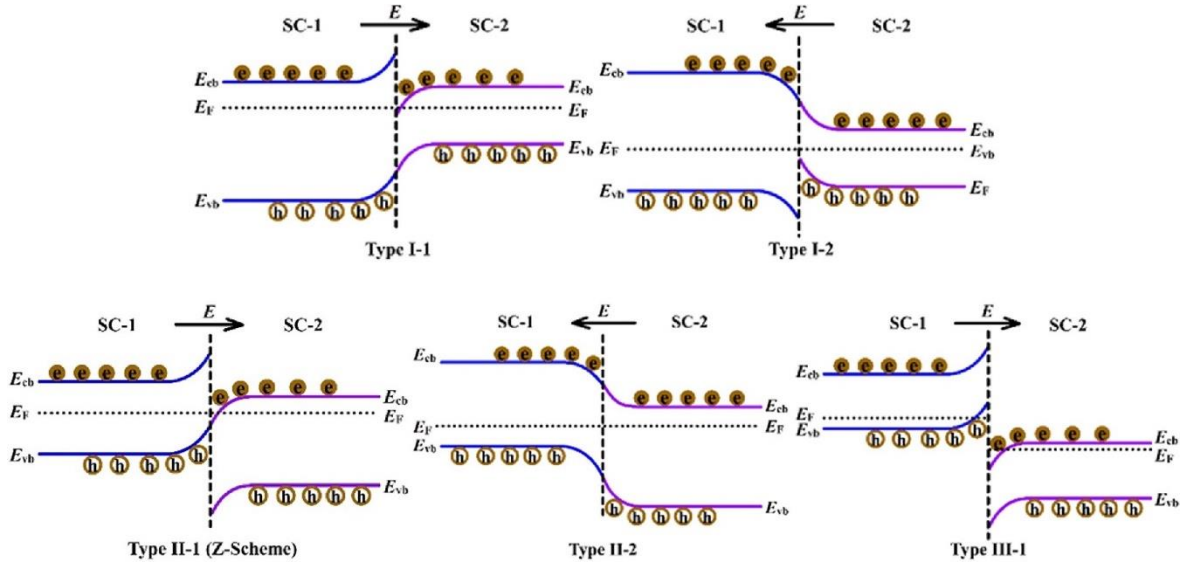

Figure 1-8. Different heterojunction types and proposed charge transfer characteristics, taking into consideration the resulting internal electric field. Reproduced from ref. [49] with the permission of Elsevier.

1.3 Metal-chalcogenides: Thiospinels a rising family of materials for photocatalytic energy conversion applications

Metal chalcogenides are chemical compounds composed of at least one chalcogen anion (such as S^{2-}, Se^{2-} or Te^{2-}) and at least one metal cation (such as Cd^{2+}, Zn^{2+} etc.). The last decades, metal chalcogenides have attracted significant attention due to their unique physical and chemical properties. The narrow band gap energy, high electrical conductivity, high redox activity and low cost of metal chalcogenides make them ideal candidates for photocatalytic energy conversion applications [56,57]. In recent years, thiospinel compounds and especially ternary thiospinel materials $A^{II}B^{III}_2S_4$, where A and B are nominally divalent (Cd^{2+}, Zn^{2+}, etc.) and trivalent (In^{3+}, Co^{3+} etc.) metal ions, respectively, have emerged as promising candidates for electro- and photo-chemical applications [58]. The strong absorption ability of thiospinel compounds in the visible light region (they have an energy gap of ~2.1-2.8 eV), along with their multiple redox behavior and exceptional photochemical stability (especially in harsh alkaline conditions), provides them with great potential for photocatalytic redox reactions. Also, these materials are of low cost and non-toxicity. So far, several thiospinels compounds, such as $CdIn_2S_4$, $ZnIn_2S_4$ and $CuCo_2S_4$, have been investigated as photocatalysts for a range of energy and environmental-related applications, including photocatalytic reduction of Cr(VI),

CO_2 and N_2, as well as photocatalytic water splitting [59–63]. Among others, $CdIn_2S_4$ and $ZnIn_2S_4$ have shown the greatest catalytic potential for the water reduction reaction and will be the main focus of this dissertation [64,65].

$ZnIn_2S_4$ thiospinel compound

Zinc indium sulfide ($ZnIn_2S_4$ or ZIS) exists in three different crystal structures: (a) hexagonal ($P6_3mc$), (b) cubic (Fd-3m) and (c) trigonal (R-3m), as illustrated in **Figure 1-9** [66]. In hexagonal ZIS, Zn atoms exhibit a tetrahedral coordination geometry with S atoms, while half of the In atoms display tetrahedral geometry and the other half display octahedral geometry. In cubic ZIS, Zn atoms are tetrahedrally coordinated with S atoms, while In atoms are octahedrally coordinated with S atoms. In the trigonal crystal structure, Zn and In atoms share a mixed occupancy of the tetrahedral coordination sites. Several reports have demonstrated that both hexagonal and cubic ZIS exhibit remarkable photocatalytic activity under visible light irradiation thanks to their excellent photoconductivity and photoluminescence properties [67,68].

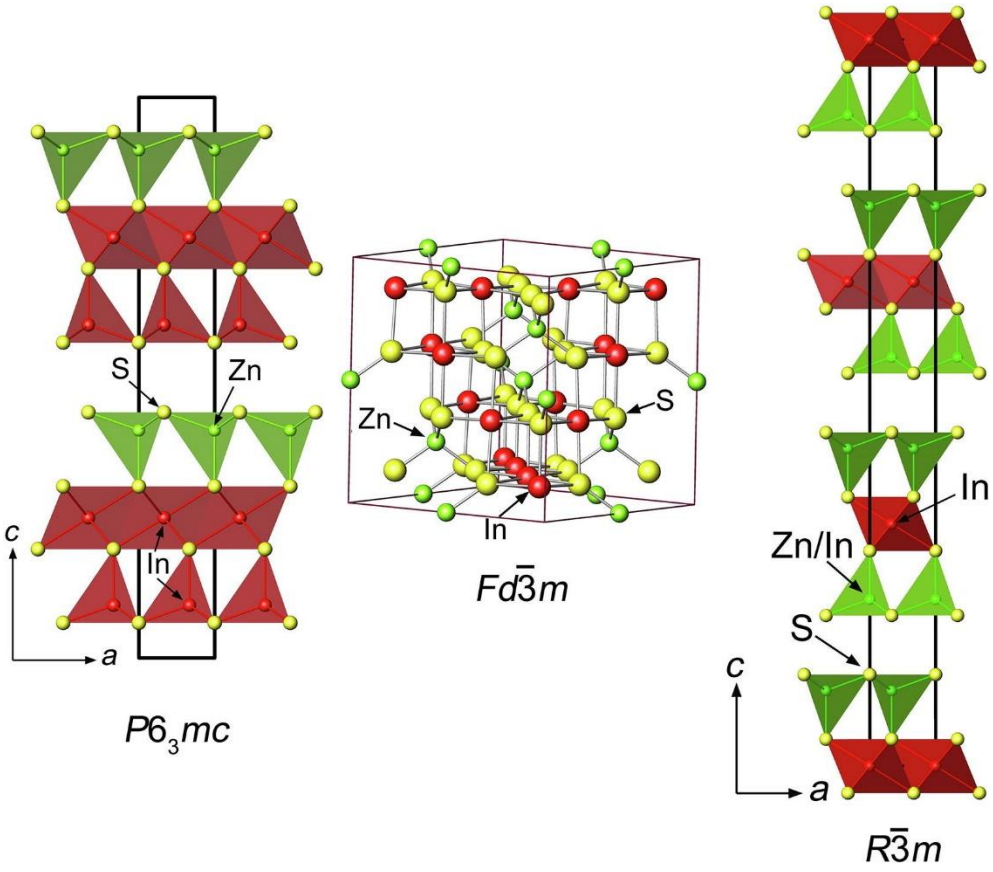

Figure 1-9. Different crystal structures of $ZnIn_2S_4$: (left) hexagonal ($P6_3mc$) $ZnIn_2S_4$, (center) cubic $ZnIn_2S_4$ (Fd-3m) and (right) trigonal $ZnIn_2S_4$ (R-3m). Reproduced from ref. [66] with the permission of Wiley.

To date, a variety of morphologies have been reported for $ZnIn_2S_4$ [66]. The morphologies can be categorized into (a) zero-dimensional (0D), (b) one-dimensional (1D), (c) two-dimensional (2D) and (d) three-dimensional (3D) structures (**Figure 1-10**). 0D ZIS compounds mainly consist of nanoparticles and quantum dots, with a particle size typically ranging from 1–100 nm. The physical properties of these nanoparticles are significantly affected by quantum confinement effects, leading to an increase in the energy gap compared to bulkier ZIS compounds. As a result of the quantum confinement, 0D ZIS compounds exhibit greater redox ability, improved light absorption efficiency and an abundance of catalytic surface-active sites. Also, 1D structures of ZIS, such as nanowires and nanotubes, demonstrate superior photocatalytic performance owing to their high aspect ratio and expansive specific surface area. Due to the layered crystal structure, ZIS tends to grow into 2D shapes, such as nanosheets. The 2D morphology provides a large specific surface area, numerous surface-active sites and short charge-carrier diffusion distance, thus limiting charge recombination. 3D morphologies of ZIS, including hollow microspheres, microspheres and flower-like assemblies of nanosheets, have garnered attention in recent years. These structures enhance light harvesting ability, provide an abundance of surface-active sites, and suppress charge recombination due to the short charge transfer distance along the structure.

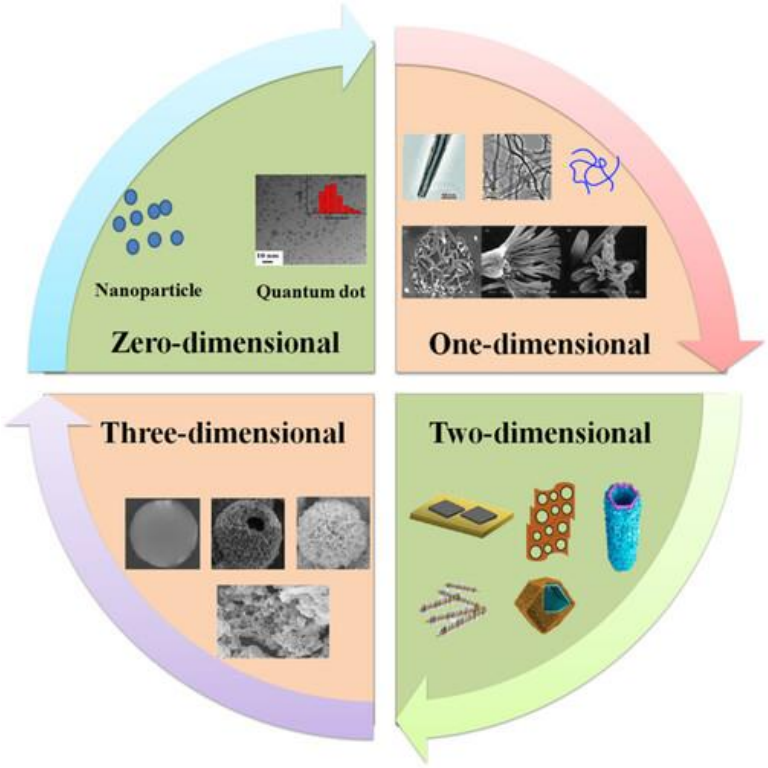

Figure 1-10. Schematic representation of the typical morphologies of $ZnIn_2S_4$ catalysts. Reproduced from ref. [66] with the permission of Wiley.

The electronic and optical properties of ZIS vary with the different crystal structures. The energy gap for the crystal polymorphs of ZIS ranges from 2.06 to 2.85 eV, rendering appropriate for photocatalytic applications due to its strong visible light-harvesting capability. Also, the CB position of ZIS in each crystal structure is more negative than the reduction potential of the H^+/H_2 couple (approximately –1.0 to –0.8 V vs –0.4 V (NHE), at pH 7), making it suitable for the hydrogen reduction reaction [69,70]. Over the years, the research community has developed several synthetic strategies to obtain $ZnIn_2S_4$ with the desired morphological, textural, and optoelectronic characteristics. The most commonly used methods include (a) hydrothermal, (b) solvothermal (c) microwave-assisted and (d) template methods (**Figure 1-11**).

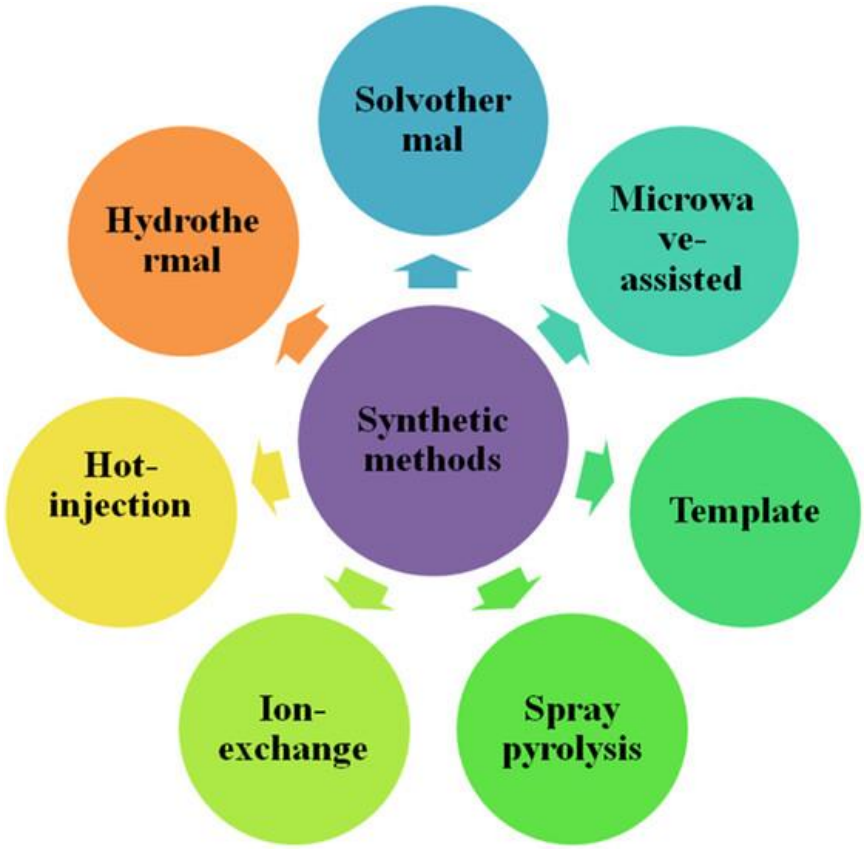

Figure 1-11. Schematic representation of several synthetic strategies of obtaining $ZnIn_2S_4$ catalysts. Reproduced from ref. [66] with the permission of Wiley.

The hydrothermal reaction is the most ordinary method for the synthesis of ZIS due to its high yield, speed, and cost-effectiveness. Also, this synthetic strategy offers the advantage of controlling crystal size, resulting in ZIS photocatalysts with enhanced crystallinity and phase purity. In the hydrothermal method, metal precursors (Zn and In) along with a sulfur source

are introduced into a sealed autoclave, where they undergo a reaction under high temperatures and pressures to yield the $ZnIn_2S_4$ catalyst. Compared to the hydrothermal reaction, the organic solvents used in the solvothermal synthesis have a more significant impact on morphology, structure, and photocatalytic activity of the ZIS. For instance, in the study by Shen et al., ZIS synthesized in water exhibited a flower-like morphology similar to when methanol was used as a solvent [71]. However, when ethylene was used, the morphology of ZIS changed, resulting in a micro-cluster morphology. Additionally, the results of this study indicated that the ZIS catalyst synthesized in water solvent displayed the highest crystallinity and photocatalytic activity among the others. The microwave-assisted strategy is characterized by its low-temperature and rapid nature. The uniform heating of the sample facilitates the creation of homogeneous nucleation centers, while its low energy consumption makes it highly environmentally friendly, even for large-scale synthesis. The template method is a dominant approach for constructing nanocomposites with adjustable shapes and sizes. It can be categorized into soft-template and hard-template methods, as mentioned earlier. One of its main advantages is the ability to achieve high specific surface areas and an abundance of adsorption sites, which can enhance photocatalytic performance [72,73]. Besides the chemical synthetic methods mentioned above, there are also physical methods for preparing ZIS, such as spray pyrolysis and chemical vapor deposition. However, these methods are not commonly used [74–76].

Although ZIS is a semiconductor material with photocatalytic potential, in many cases, it exhibits a poor photon to hydrogen conversion efficiency. This is due to the poor utilization of the photogenerated electrons for the hydrogen evolution reaction. For this reason, several methods have been developed to modulate the charge carrier's dynamics, such as metal deposition, element doping, vacancy engineering and semiconductor combination (formation of heterojunctions). As mentioned before, the deposition of metals onto semiconductor photocatalysts represents an effective strategy for enhancing their photocatalytic behavior. In the case of ZIS with Pt co-catalyst, Pt nanoparticles can serve as electron acceptors, enhancing charge separation and migration efficiency. This results in improved photocatalytic performance compared to pristine ZIS [77]. Element doping has also proven to be highly effective for ZIS semiconductors. For instance, when molybdenum (Mo) was deposited onto the surface of ZIS, the photocatalytic hydrogen evolution performance was enhanced by a factor of 10 [78]. This improvement was attributed to enhanced light absorption and separation of the photoexcited charge carriers. Vacancy engineering can also enhance the light absorption capability of ZIS. The defective ZIS structure, with sulfur or metal defects, exhibits altered

electronic and optical behavior. If ZIS contains sulfur vacancies (V_s), these vacancies can act as electron traps for the photogenerated electrons, thereby reducing the electron-hole recombination effect [79]. When metal defects are introduced into the ZIS structure (such as Zn vacancies), they increase the carrier density. Overall, vacancy engineering in ZIS can enhance photocatalytic activity by modulating the dynamics of charge carriers [80]. Lastly, the formation of heterojunctions between ZIS and another semiconductor is one of most commonly used techniques to enhance photocatalytic activity [81]. The strong electronic interactions between ZIS and the co-catalyst can indeed facilitate efficient interracial charge transfer and separation, thereby enhancing the overall photocatalytic activity [69].

$CdIn_2S_4$ thiospinel compound

$CdIn_2S_4$ (CIS) thiospinel has received less attention in research compared to ZIS, primarily due to its poorer catalytic performance. CIS, unlike ZIS, exhibits only one crystal polymorph, the cubic (Fd-3m) structure, where the Cd atoms are tetrahedrally coordinated with the sulfur atoms, while the In atoms are octahedrally coordinated [64]. The morphology of this thiospinel also varies, displaying 1D structures such as nanoribbons, nanotubes and nanowires, as well as 2D structures like nanosheets, and 3D structures such as sphere-like particles. The 1D structure of CIS exhibits enhanced photocatalytic activity due to the high crystallinity of the obtained particles. For example, in the study by Wang et al., where In_2S_3 nanosheets were combined with CIS nanotubes, the resulting composites displayed enhanced catalytic activity towards CO_2 photoreductions [82]. The morphology of CIS nanotubes plays a crucial role in enhancing the photoreduction activity. By facilitating more efficient charge carrier migration and separation, the nanotube structure enables effective utilization of photogenerated charge carriers, leading to improved photocatalytic performance. In addition, the nanotube morphology provides an abundance of active sites for the adsorption of CO_2 molecules. The nanosheet structure of CIS has gained a tremendous popularity due to its ability to facilitate fast charge carrier migration, and its large specific surface area [83]. The fabrication of CIS nanosheets is relatively straightforward, as they can be synthesized through a simple solvothermal reaction. Similarly to ZIS, 3D CIS structures can be obtained via straightforward synthetic routes, with hydrothermal and solvothermal methods being the most commonly used. These 3D CIS materials exhibit enhanced photocatalytic activity attributed to delayed charge carrier recombination, improved interfacial charge transfer, and the high crystallinity of the thiospinel structure [84].

CIS possesses an energy gap between 2.0 and 2.6 eV, which is ideal for photocatalytic applications under visible-light irradiation [85–87]. Also, the band structure of CIS is suitable for the water reduction reaction, showing strong reduction and oxidation abilities [88,89]. The main synthetic procedures used to obtain CIS thiospinel are similar to those used for ZIS and will not be discussed further [64]. Similar to ZIS, several techniques have been developed to improve the charge transfer efficiency and thus the photocatalytic activity of CIS. The most popular method is through the deposition of co-catalysts to form heterojunctions. These modulation strategies have also been proved quite effective, especially when constructing p-n junctions, which can effectively increase the stability of the thiospinel. For example, upon light irradiation of the p-n junction between p-type Co_3O_4 and n-type CIS, the electrons in both semiconductors are excited from the valence band to the conduction band. Due to the band alignment of the semiconductors, photoexcited electrons transfer from Co_3O_4 to the CIS semiconductor, while photogenerated holes migrate from CIS to Co_3O_4. This prevents the self-oxidation of CIS and improves photochemical stability and activity (**Figure 1-12**) [90]. Also, element doping (both metal and non-metal) and surface modification are crucial for enhancing the photocatalytic properties of CIS, although they are generally less effective than the construction of heterojunctions in CIS [91–94]. Briefly, doping with elements can enhance the light absorption of CIS and promote the charge carrier separation and migration, while surface modification can significantly improve the redox capabilities of CIS, leading to higher photocatalytic efficiency.

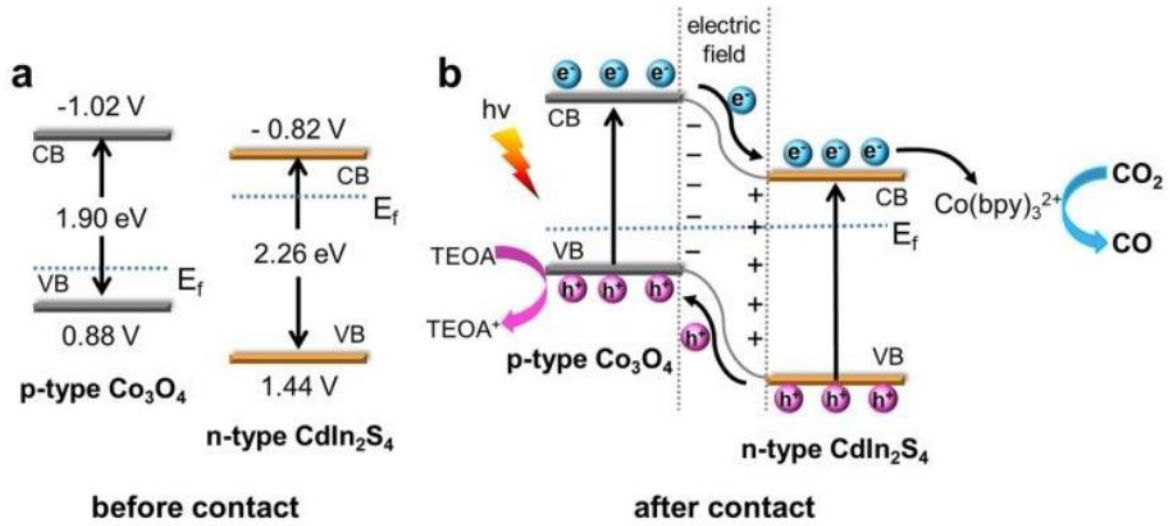

Figure 1-12. (a) Band structures of CIS (n-type) and Co_3O_4 (p-type) semiconductors. (b) Schematic representation of a possible p-n junction mechanism during light irradiation. Reproduced from ref. [90] with the permission of Royal Society of Chemistry.

Overall, ternary thiospinels ($A^{II}B_2^{III}S_4$) have attracted significant attention from the research community in recent years owing to their desirable electronic and optical properties, particularly for applications in energy conversion and environmental remediation. $ZnIn_2S_4$ and $CdIn_2S_4$ indeed show great potential for photocatalytic reactions. Both thiospinels offer versatility in synthesis methods and morphological structures, allowing for a wide range of approaches to tailor their physical and chemical properties for specific applications. However, the rapid charge recombination is a significant challenge for these materials, limiting their photocatalytic efficiency. Efforts to mitigate this issue through various strategies, such as heterojunction formation, element doping and surface modification, are crucial for enhancing their photocatalytic performance.

1.4 Transition metal phosphides and Ni-based co-catalysts

Transition metal phosphides (TMPs) are typically represented by the general chemical formula M_xP_y, where M denotes a metal cation [95,96]. The nature of the M-P bond can vary, being either ionic or covalent, contingent upon the electronegativity difference between the metal and phosphorus atoms. When the electronegativity difference is significant, the M-P bond tends to exhibit predominantly ionic characteristics, whereas when the electronegativity difference is minimal, the M-P bond tends to display more covalent properties [97]. In most TMPs, the M-P bond exhibits a mixture of both ionic and covalent characteristics [98]. Moreover, TMPs can categorized into two main categories: (a) metal-rich phosphides, when the x/y ratio is greater or equal to 1, and (b) phosphorus-rich phosphides, when the x/y ratio is smaller than 1 [96,99]. In metal-rich phosphides, the electrons are not confined around individual atoms, leading to stronger M-M interatomic interactions. This phenomenon contributes to the metallic nature of the TMP [100]. On the other hand, in phosphorus-rich phosphides, the lack of metal atoms leads to poorer electrical conductivity but higher reactivity [101]. An illustration of different stoichiometries of TMPs is provided in **Figure 1-13**, showcasing the diverse chemical compositions of nickel phosphides, ranging from metal-rich to phosphorus-rich structures.

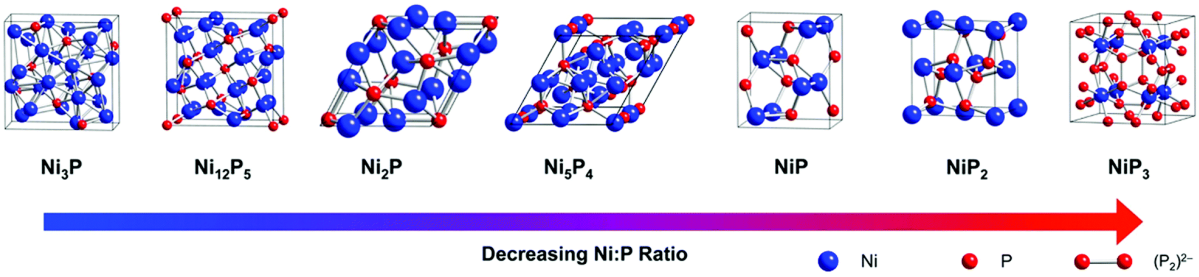

Figure 1-13. Nickel phosphide various crystal structures. Reproduced from ref. [99] with the permission of American Chemical Society.

TMPs exhibit remarkable electrochemical activity, a characteristic that can be attributed, in part, to their chemical structure and electronic composition. If we consider TMPs as P-doped metal alloys, then the introduction of P atoms plays a crucial role in catalytic activity [102,103]. Specifically, the P atoms, which are negatively charged can function as electron acceptors from the metal atoms. Also, owing to their negative charge, P atoms can act as trap sites for positively charged cations like protons (H^+), thereby further improving catalytic activity (e.g., hydrogen evolution reaction). Although the presence of phosphorus is advantageous in the structure of TMPs, it can also lead to a reduction in electrical conductivity, potentially limiting the catalytic activity. The Sabatier principle states that to achieve optical catalytic performance in the hydrogen evolution reaction (HER), the material should possess moderate binding energies for the reactive intermediates [104]. When the Gibbs free energy of hydrogen adsorption (ΔG_{H^*}) on the catalyst's surface approaches 0 eV, the catalyst has the potential to attain high activity in the hydrogen evolution reaction. A smaller ΔG_{H^*} tends to delay the release of adsorbed hydrogen (H*) because of the strong interaction between the material and H*, while a larger ΔG_{H^*} necessitates energy input (endothermal step) for proton-electron transfer to occur. Jaramillo's research group provided the initial evidence that TMPs exhibit favorable ΔG_{H^*} values and demonstrate promising activity in the hydrogen evolution reaction (**Figure 1-14**) [105]. This thesis dissertation will primarily focus on rich-metal phosphides due to their high electrical conductivity and redox ability. Specifically, nickel and cobalt phosphides will be investigated as possible co-catalysts for the photocatalytic water reduction reaction.

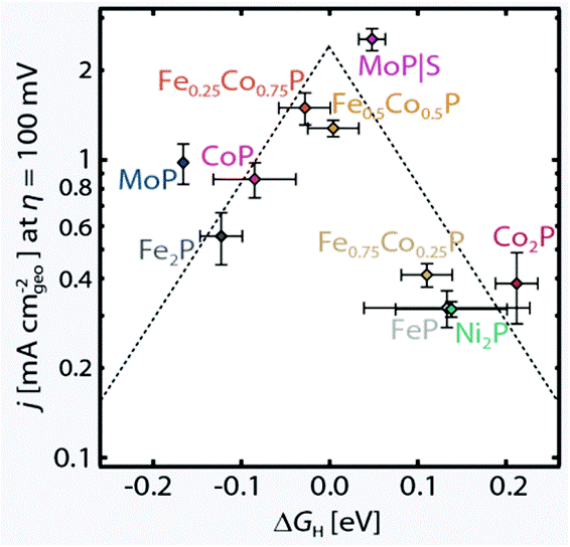

Figure 1-14. Activity volcano for the HER showing the geometric current density from (A) at an overpotential of η = 100 mV as a function of hydrogen adsorption free energy (ΔG_H). Reproduced from ref. [105] with the permission of the Royal Society of Chemistry.

Nickel phosphides

Nickel phosphides (Ni_xP_y) are one of most investigated materials among the TMPs [106]. Ni_xP_y exhibits a range of crystal structures, including metal-rich compositions like Ni_2P, $Ni_{12}P_5$, and Ni_3P, as well as phosphorus-rich forms such as NiP_2 and NiP_3, as illustrated in **Figure 1-13**. Nickel phosphides with high P/Ni ratios, such as Ni_5P_4, demonstrate superior catalytic activity for the hydrogen evolution reaction (HER) and photocatalytic water splitting, while in lower P/Ni ratios, they exhibit an enhanced catalytic activity towards the oxygen evolution reaction (OER) [107,108]. Among them, Ni_2P stands out for its remarkable catalytic activity in both the HER and OER, despite its metal-rich nature. In terms of chemical stability, metal-rich nickel phosphides generally maintain their stability, while it tends to decrease with the inclusion of more P atoms in phosphorus-rich compounds [109]. The rationale behind this lies in the composition of metal-rich nickel phosphides, which feature metallic bonds (Ni-Ni) alongside ionic bonds (Ni-P). With the introduction of phosphorus atoms, the metallic and ionic bonds are replaced by P-P bonds, which are inherently less stable. Consequently, this renders the phosphorus-rich variants more susceptible to corrosion phenomena.

Recently, it was found that Ni_2P displays catalytic properties comparable to those of [NiFe] hydrogenase. Notably, the (001) plane of Ni_2P demonstrated higher thermostability and HER activity similar to that of the [110] crystal plane of hydrogenase. Also, investigations revealed a surplus of non-stoichiometric phosphorus atoms occupying the Ni_3 hollow sites within the

Ni_3P_2 layers of Ni_2P, contributing to increased stability. Moreover, Ni_2P demonstrates notable catalytic activity for OER [111]. Indeed, the higher concentration of metal atoms in the structure of Ni_2P promotes the formation of Ni-O and Ni-O-O bonds, which enhance the efficiency of oxygen evolution. Considering these characteristics, Ni_2P shows remarkable reduction and oxidative capabilities. Moreover, its semiconductor form exhibits a small energy gap of approximately 1 eV, rendering it highly promising as a catalyst for the electro- and photo-catalytic hydrogen evolution reaction.

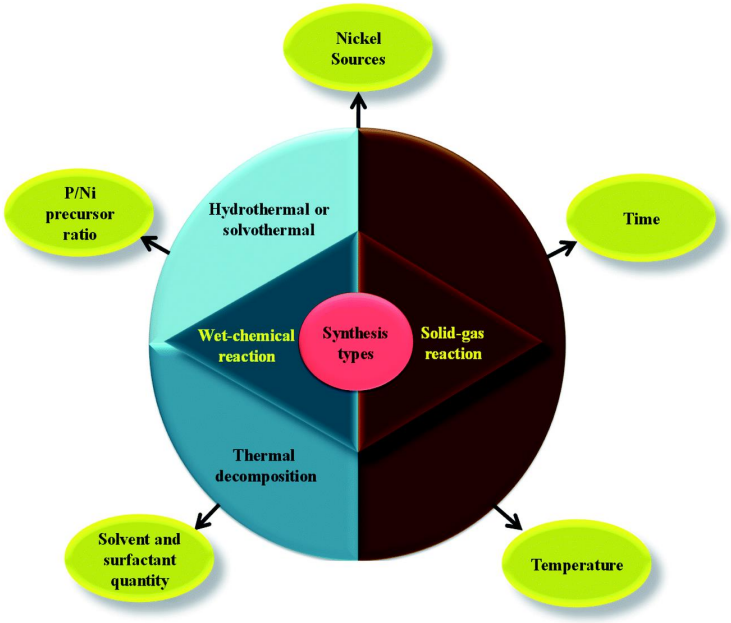

Figure 1-15. Schematic representation of the different synthetic routes of obtaining nickel phosphides. Reproduced from ref. [106] with the permission of Royal Society of Chemistry.

In recent years, numerous synthetic procedures have been developed to achieve nickel phosphide with desirable morphology and crystal structure. The most commonly used are the (a) thermal decomposition [112,113], (b) hydrothermal or solvothermal reaction [114,115], and (c) the solid-gas method [116,117], see **Figure 1-15**. The thermal decomposition synthetic method relies on decomposing precursors in the liquid phase, making it the most efficient approach for obtaining nickel phosphides. In this method, metal salts or metallic nickel react with a phosphorus source in an organic solvent under inert atmosphere conditions. This synthetic approach offers the advantage of producing nickel phosphides in the nanoscale with diverse morphologies, such as nanoparticles and nanowires. Another wet chemical process is the hydrothermal or solvothermal reaction. Here, metal precursors react with the inorganic phosphorous source (red P, white P, or yellow P) under elevated pressure and temperature conditions. The P/Ni ratio, choice of solvent, and reaction conditions all significantly influence

the isolation of the desired phase structure of nickel phosphide. This method is particularly favored for synthesizing Ni_2P and $Ni_{12}P_5$ in a range of morphologies, including nanoparticles and nanosheets. In addition to wet chemical synthetic routes, the solid-gas method is also popular. Here, Ni-based precursors react with phosphorus sources (such as NaH_2PO_2 or $NH_4H_2PO_2$) through a phosphidation process, during which the phosphorus sources decompose to form highly active PH_3 gas (**Figure 1-16**). This synthetic protocol is commonly employed for the production of Ni_2P and $Ni_{12}P_5$ phosphides, yielding materials with diverse sizes and morphologies. In general, Ni_2P co-catalyst enhances light absorption (due to its narrow energy gap), while also accelerating charge transfer and reinforcing photostability. [118,119].

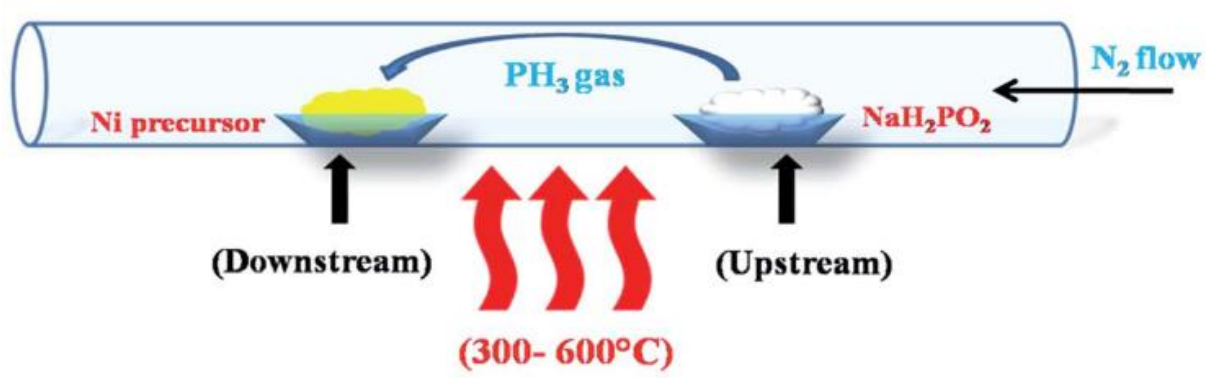

Figure 1-16. Schematic representation of the solid-gas method to obtain nickel phosphide materials. Reproduced from ref. [106] with the permission of Royal Society of Chemistry.

Cobalt phosphides

Cobalt phosphides (Co_xP_y) have received less attention compared to nickel phosphides (Ni_xP_y), but they also exhibit significant catalytic potential [120–122]. Similar to Ni_xP_y, Co_xP_y displays a range of crystal structures, spanning from the metal-rich compositions such as Co_2P and CoP, to phosphorus-rich variants like CoP_3 and CoP_4. The Co atoms that are in the cobalt phosphide structure can function as hydride-acceptors, while P atoms act as proton-acceptors; this synergy results in remarkable activity for the hydrogen evolution reaction. Metal-rich Co_xP_y usually exhibit metallic properties, featuring an electronic structure similar to noble metals. On the other hand, phosphorous-rich Co_xP_y demonstrates semiconductor properties and falls in terms of electrical conductivity compared to their metal-rich counterparts. The synthetic methods currently employed to obtain Co_xP_y are identical to those used for nickel phosphides, including thermal decomposition, hydrothermal or solvothermal reactions, and the solid-gas method. Further analysis of these methods will not be pursued here.

Overall, TMPs represent an intriguing class of materials with significant catalytic potential. While predominantly utilized in electrocatalytic energy conversion applications, such as the hydrogen and oxygen evolution reactions, their high electrical conductivity and redox capabilities render them excellent candidates for serving as co-catalysts in photocatalytic hydrogen production.

Nickel (oxy)hydroxide materials

Ni-based (oxy)hydroxide material represent an intriguing category of catalysts tailored for energy conversion applications [123,124]. These materials have garnered significant attention from the research community due to their cost-effectiveness in manufacturing, the abundance of nickel in comparison to noble metals, and their remarkable catalytic efficiency. Among them, nickel(II) hydroxides ($Ni(OH)_2$) demonstrate exceptional catalytic potential [125,126]. $Ni(OH)_2$ exists in two crystal polymorphs, known as the α and β structures (**Figure 1-17**) [127,128]. The α-$Ni(OH)_2$ phase comprises $Ni(OH)_2$ layers interspersed with intercalated anions or water molecules and crystallizes in the R-3m space group. The β-$Ni(OH)_2$ phase shares the same crystal structure as brucite ($Mg(OH)_2$) and crystallizes in the hexagonal crystal system (P-3m1). The β-$Ni(OH)_2$ crystal structure is characterized by a hexagonal close-packed arrangement of hydroxyl anion groups. The Ni(II) ions adopt an octahedral geometry, with three oxygen atoms positioned above the plane of the nickel atom and the other three below.

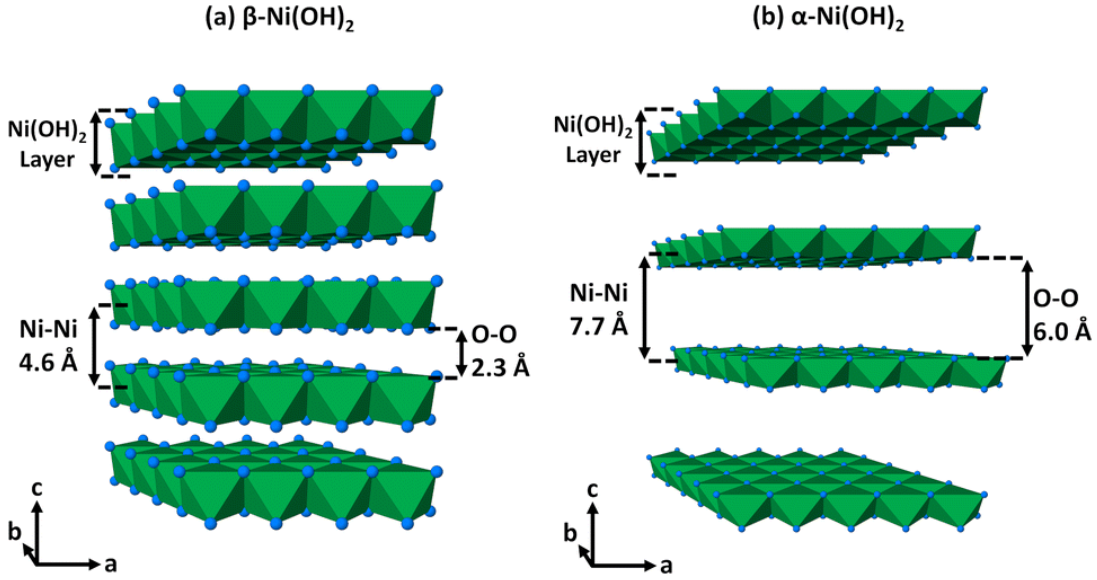

Figure 1-17. Crystal structures of (a) β-$Ni(OH)_2$ and (b) α-$Ni(OH)_2$. Reproduced from ref. [127] with the permission of the Royal Society of Chemistry.

Nickel (II) hydroxide can be synthesized through varioys synthetic methods [129], with the chemical precipitation method being the simplest and most commonly used. Briefly, the chemical precipitation method is a one-step process where the nickel precursor reacts with a basic solution, such as $NaOH_{(aq)}$ or $NH_4OH_{(aq)}$, resulting in the precipitation of the desired $Ni(OH)_2$. The phase structure and crystallinity of $Ni(OH)_2$ are influenced by the choice and concentration of Ni precursor, temperature and pH of the solution. At room temperature conditions, the α phase is typically favored, whereas at higher temperatures, a mixed α/β phase or pure β phase can be obtained. Another method for synthesizing $Ni(OH)_2$ is the electrochemical precipitation method, where nickel cations react with OH^- anions generated from water reduction. The resulting phase of $Ni(OH)_2$ is influenced by the type of Ni precursor and the cathodic current density applied. At low current densities, the α phase is favored, while higher current densities can lead to the formation of the β phase. An interesting synthetic process is the chemical ageing, where α-$Ni(OH)_2$ can transform into β-$Ni(OH)_2$ under alkaline conditions at elevated temperatures (~80 ^oC). This method yields a product with improved structural order and higher crystallinity. Another well-known method for synthesizing nickel hydroxide is the hydrothermal and solvothermal method. This approach is straightforward, requiring only the Ni precursor and solvent in an autoclave. Typically, hydrothermal synthesis is employed to obtain the β phase, while the α phase is achieved through solvothermal reactions with the addition of an intercalation agent. This versatile synthetic process is applicable in the industrial sector for large-scale synthesis and can also produce $Ni(OH)_2$ materials at the nanoscale.

In recent years, $Ni(OH)_2$-based cocatalysts have been widely utilized due to their significant advantages, which can enhance the photocatalytic performance of semiconductor photocatalysts [126]. Specifically, $Ni(OH)_2$ cocatalysts can promote the efficient separation of the photogenerated charge carriers within the semiconductor by forming heterojunctions. Because $Ni(OH)_2$ demonstrates a lower overpotential and reaction energy barrier for the hydrogen evolution reaction compared to most semiconductors, the construction of heterojunctions with $Ni(OH)_2$ leads to an increase in catalytic active sites for photocatalytic hydrogen evolution. Additionally, $Ni(OH)_2$ is renowned for its exceptional stability even under harsh conditions, such as alkaline and acidic environments, thereby offering robust photo-corrosion protection for the semiconductor catalyst. **Figure 1-18** provides a summary of the advantageous utilization of $Ni(OH)_2$-based cocatalysts for photocatalytic applications.

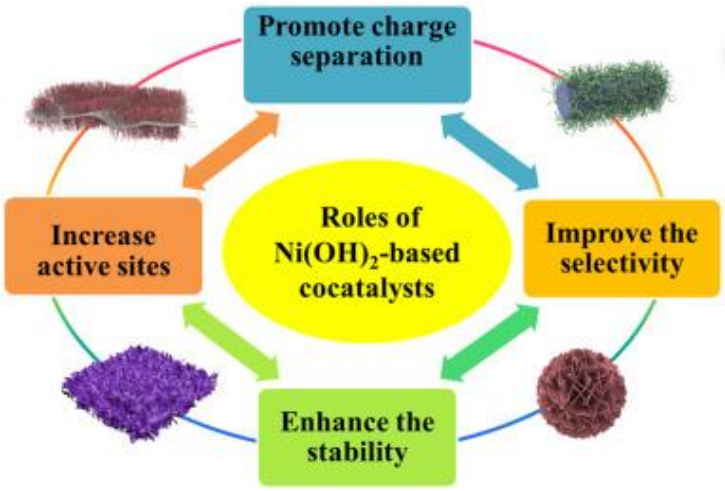

Figure 1-18. $Ni(OH)_2$-based cocatalysts role in photocatalysis. Reproduced from ref. [126] with the permission of Elsevier.

For a better understanding of the crucial role $Ni(OH)_2$ can play as a co-catalyst, it's noted that the photocatalytic performance of the β-$Ni(OH)_2$-modified CdS significantly surpasses that of Pt-loaded CdS [130]. The superior photocatalytic performance of β-$Ni(OH)_2$/CdS heterostructure can be attributed to the formation of a p-n junction between p-type β-$Ni(OH)_2$ and n-type CdS. When exposed to visible light, electrons in the n-type CdS semiconductor get excited, generating electron-hole pairs. The formation of the heterojunction enables photogenerated holes from CdS to transfer to β-$Ni(OH)_2$, leading to an increased electron population in CdS. The increased electron density in CdS subsequently participates in the water reduction reaction, thereby enhancing the photocatalytic performance for the hydrogen evolution reaction. **Figure 1-19** displays a possible photocatalytic mechanism of β-$Ni(OH)_2$/CdS p-n heterojunction for photocatalytic hydrogen evolution.

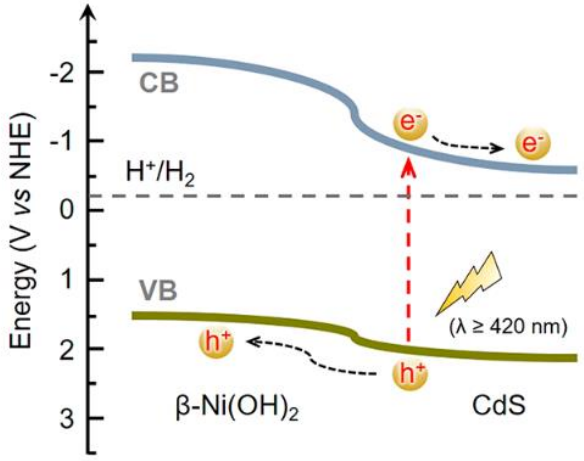

Figure 1-19. Proposed mechanism of the p-n heterojunction between β-$Ni(OH)_2$ and CdS at pH 7. Reproduced from ref. [130] with the permission of American Chemical Society.

1.5 Thesis statement and objectives

The develop of renewable energy sources to replace fossil fuels is of utmost importance. Hydrogen, with its exceptional properties, is recognized as an alternative energy carrier. However, existing hydrogen production technologies suffer from inefficiency and contribute to environmental pollution through the emission of greenhouse gases. Photocatalytic water splitting has emerged as a sustainable technique for generating hydrogen gas from water. During overall water splitting, the simultaneous production of H_2 and O_2 gases poses a challenge for separation. Hence, employing sacrificial reagents as electron donors (hole scavengers) becomes essential. These reagents prevent O_2 generation and exclusively accelerates the water reduction reaction. The last decades, there has been a significant endeavor to develop high-performing semiconductor photocatalysts. However, existing options still suffer from low photocatalytic efficiency and stability. Consequently, there is an urgent need to innovate and explore novel photocatalytic materials capable of simultaneously demonstrating high photoactivity and photochemical stability. Building on this premise, the new photocatalysts should undergo a rational synthetic design to achive optimal photocatalytic activity. The synthetic engineering of three-dimensional (3D) mesoporous architectures, comprising nanoparticles as building blocks, presents numerous advantages. In fact, mesoscopic architectures of nanoscale building blocks could combine disparate functionalities on the same material such as quantum-confined optical absorption and fast interparticle mass transport, not found in traditional porous solids and isolated nanoparticles. Furthermore, nanometer-scale structures can provide a notable boost in intrinsic photoactivity by retarding bulk carrier recombination due to the shortened distance for charge carriers to access the surface-active sites, a notorious problem in photocatalysis.

This dissertation comprises two primary aims. The first is to develop a novel class of 3D mesoscopic structures as potential photocatalysts for the hydrogen evolution reaction. Metal chalcogenides, particularly thiospinel compounds, stand out as excellent candidates due to their intriguing physicochemical and electrochemical properties. Of particular note, 3D mesoporous photocatalysts composed of thiospinel nanoparticles have not yet been reported. The second aim is to enhance the photocatalytic activity of the newly-developed materials by forming heterojunctions (using low-cost materials such as transition metal phosphides and Ni-based materials), and to uncover the role that these cocatalysts in the charge carrier dynamics and the photochemical activity of the semiconductors.

Overall, this Ph.D. thesis encompasses the following research objectives:

(a) The development of a facile synthetic route for producing size-controlled thiospinel nanoparticles ($ZnIn_2S_4$, $CdIn_2S_4$) and their assembly into 3D mesoporous structures.
(b) The structural and physicochemical characterization of these photocatalysts.
(c) The evaluation of their photocatalytic activity towards the hydrogen evolution reaction.
(d) The fabrication of mesoporous heterojunctions comprising thiospinel-based photocatalysts and effective, earth-abundant co-catalysts (e.g., Ni_2P nanosheets, Co_2P, and β-$Ni(OH)_2$ nanoparticles) to achieve superior photocatalytic performance.
(e) To investigate the role of the co-catalysts in the charge carrier dynamics and unveil a possible mechanism for the hydrogen evolution reaction.

Chapter 2: Experimental Section

2.1 Synthesis of $ZnIn_2S_4$ and $CdIn_2S_4$ colloidal nanocrystals

$ZnIn_2S_4$ (ZIS) and $CdIn_2S_4$ (CIS) colloidal nanocrystals (NCs) were prepared though a low-temperature solvothermal reaction [35]. In a typical preparation, $Cd(NO_3)_2{\cdot}4H_2O$ (1 mmol, 237 mg) for $CdIn_2S_4$ NCs or $Zn(NO_3)_2{\cdot}6H_2O$ (297 mg) for $ZnIn_2S_4$ NCs, $In(NO_3)_3{\cdot}6H_2O$ (2 mmol, 818 mg), 3-mercaptopropionic acid (3-MPA, 24 mmol, 3 mL) and NH_4OH (25 % wt. %, 12 mL) were added in 15 mL of ethylene glycol ($C_2H_6O_2$) under vigorous stirring and the resulting mixture was heated at 150 ^oC. Then, thioacetamide (CH_3CSNH_2) (10 mmol, 750 mg) dissolved in 10 mL ethylene glycol was rapidly injected into the above mixture. The resulting yellow colloidal suspension was stirred under reflux conditions for a certain time (see table below). After the mixture reached room temperature, the nanocrystals were isolated through centrifugation with the addition of isopropyl alcohol, washed with copious amounts of water/ethanol (1:1 v/v) mixture and dried at 40 ^oC for 24 hours.

Sample	**Nanocrystal size (nm)**	**Reaction time (hours)**
$ZnIn_2S_4$ NCs	4.5	3
$ZnIn_2S_4$ and $CdIn_2S_4$ NCs	6	6
$ZnIn_2S_4$ and $CdIn_2S_4$ NCs	11	12

For reference studies, bulk $CdIn_2S_4$ and $ZnIn_2S_4$ solids were also prepared by hydrothermal reaction of $Cd(NO_3)_2{\cdot}4H_2O$ (1 mmol, 237 mg) or $Zn(NO_3)_2{\cdot}6H_2O$ (1 mmol, 297 mg) and $In(NO_3)_2{\cdot}6H_2O$ (2 mmol, 818 mg) with thioacetamide (10 mmol, 750 mg) at 150 ^oC for 12 hours. The obtained products were centrifuged, washed with water and ethanol, and dried at 60 ^oC for 24 hours.

2.2 Synthesis of mesoporous $ZnIn_2S_4$ and $CdIn_2S_4$ frameworks

The synthesis of mesoporous nanocrystal frameworks (NCFs) composed of different particle sizes (ca. 4–11 nm) of $CdIn_2S_4$ and $ZnIn_2S_4$ was achieved as follows: 250 mg of 3-MPA-capped $CdIn_2S_4$ or $ZnIn_2S_4$ nanocrystals were suspended in 2.5 mL of deionized (DI) water under vigorous stirring at room temperature. A few drops of 10 M NH_4OH were added to the suspension in order to obtain a stable colloid solution. Then, the colloidal suspension was

transferred in an aqueous solution of polyethylene glycol hexadecyl ether polymer (Pluronic Brij-58, HO-(CH_2CH_2O)$_n$-(CH_2)$_{15}$-CH_3) (10 % w/v, 2.5 mL) and kept under stirring for 1 hour. Then, 1.2 mL of H_2O_2 (3 % v/v) was added dropwise until gelation was observed (typically within 30 min), and the obtained gel suspension was left to slowly evaporate the water at 40 ^oC under static conditions for 4 days. To remove the polymer template, the hybrid product was washed twice with warm ethanol (~40 ^oC) for 2 hours and three times with DI water for 1 hour each time at room temperature. The final product was filtered and washed several times with ethanol and dried at 60 ^oC for 12 hours. For comparison purposes, random aggregates of $CdIn_2S_4$ and $ZnIn_2S_4$ nanocrystals (RNAs) were prepared using the exact synthetic procedure, except the addition of the template.

2.3 Synthesis of transition metal phosphides

2.3.1 Synthesis of Ni_2P nanosheets

Nickel phosphide (Ni_2P) nanosheets were prepared according to a modified literature synthetic procedure [131]. $NiCl_2{\cdot}6H2O$ (1 mmol, 240 mg) and ethylenediamine ($C_2H_8N_2$, 2 mL) were dissolved in 20 mL of DI water, forming a deep violet solution. Then, this solution was transferred in a 50 mL Teflon-lined autoclave and red phosphorus (5 mmol, 150 mg) was added. The autoclave was then sealed and heated at 150 ^oC for 12 hours. The final black product was isolated through centrifugation, washed several times with DI and ethanol and dried at 60 ^oC for 12 hours.

2.3.2 Synthesis of Co_2P nanoparticles

Cobalt phosphide (Co_2P) nanoparticles were prepared via a hydrothermal synthetic method with modifications [132,133]. In a typical reaction, $Co(NO_3)_2{\cdot}6H_2O$ (0.5 mmol, 145 mg) and red phosphorus (5 mmol, 300 mg) were added in 20 mL of DI water and ultra-sonicated for 1 hour to form a homogenous suspension. Then, the resulting solution was transferred in a 25 mL Teflon-lined autoclave and was heated at 210 ^oC for 21 hours. The final product was isolated by centrifugation, washed several times with DI water and ethanol and dried at 60 ^oC for 24 hours.

2.4 Preparation of $CdIn_2S_4$-based heterostructures

2.4.1 Preparation of Ni_2P-modified $CdIn_2S_4$ heterostructures

Mesoporous heterostructures of Ni_2P nanosheets and $CdIn_2S_4$ mesoporous materials were obtained through a wet chemical deposition method. In a typical synthesis of 5 wt. % $Ni_2P/CdIn_2S_4$ sample, 95 mg of mesoporous $CdIn_2S_4$ were dispersed in 50 mL of DI water/isopropyl alcohol mixture (2:1 v/v) at room temperature. In separate vial 5 mg of Ni_2P was suspended in 20 mL of the same mixture (DI water/isopropyl alcohol, 2:1 v/v) by ultrasonication for 2 hours. Then, the Ni_2P solution was added dropwise to $CdIn_2S_4$ suspension and the resulting mixture was left under stirring for 1 hour at room temperature. The product was collected by vacuum filtration, washed with ethanol, and dried at 60 ^oC for 12 hours. A similar procedure was employed for the preparation of 10, 15, 20 and 30 wt. % Ni_2P content (see table below).

Sample	**Ni_2P (wt. %)**	**Ni_2P (mg)**	**Mesoporous $CdIn_2S_4$ (mg)**
5 wt. % $Ni_2P/CdIn_2S_4$	5	5	95
10 wt. % $Ni_2P/CdIn_2S_4$	10	10	90
15 wt. % $Ni_2P/CdIn_2S_4$	15	15	85
20 wt. % $Ni_2P/CdIn_2S_4$	20	20	80
30 wt. % $Ni_2P/CdIn_2S_4$	30	30	70

For comparison, a reference bulk material of $Ni_2P/CdIn_2S_4$ was prepared by wet chemical deposition of 15 mg of Ni_2P nanosheets on 85 mg of bulk $CdIn_2S_4$ (15 wt. % Ni_2P).

2.4.2 Preparation of Co_2P-modified $CdIn_2S_4$ heterojunctions

Mesoporous $Co_2P/CdIn_2S_4$ heterostructures were also prepared via a wet-chemical deposition method. For a typical synthesis of 5 wt. % Co_2P-modified sample, 5 mg of Co_2P nanoparticles were suspended in 50 mL of DI water/isopropanol solution (2:1 v/v) and was ultrasonicated for 1 hour. In a separate beaker, 95 mg of mesoporous assemblies of $CdIn_2S_4$ were suspended under vigorous stirring at room temperature in 50 mL of the DI water/isopropanol (2:1 v/v) mixture. Then, the Co_2P mixture was added to the $CdIn_2S_4$ suspension to form $Co_2P/CdIn_2S_4$ heterojunctions and was left under vigorous stirring for another 1 hour. The Co_2P-modified materials were isolated by vacuum filtration, washed with ethanol, and dried at 60 ^oC for 24

hours. For the synthesis of 7, 10 and 15 wt. % $Co_2P/CdIn_2S_4$ samples, the amounts of Co_2P used was 7, 10 and 15 mg and the amounts of $CdIn_2S_4$ were 93, 90 and 85 mg, respectively.

Also, for comparison purposes, a bulk reference material was also prepared containing 10 wt. % of Co_2P nanoparticles (10 mg Co_2P, 90 mg bulk $CdIn_2S_4$).

2.4.3 Preparation of Ni-modified $CdIn_2S_4$ heterostructures

Ni-modified $CdIn_2S_4$ heterostructures were prepared following a photochemical deposition process with triethylamine (TEA) as hole scavenger [130]. In a typical synthesis, 100 mg of the mesoporous $CdIn_2S_4$ were dispersed in a 20 mL aqueous solution containing triethylamine (10 % v/v). Then, in order to achieve the desired weight loading percentage (5–15 wt. %) of Ni, the amount of Ni precursor was adjusted accordingly ($NiCl_2 \cdot 6H_2O$, 1 mg mL^{-1}). The resulting mixture was sealed in an airtight custom-made photochemical reactor and degasses with Ar gas for 30 minutes. After this, the mixture was illuminated for 90 minutes with a 375 nm light-emitting diode (50-W LED). The final product was collected by centrifugation, washed several times with DI water and ethanol and was left to dry at 60 ^oC for 12 hours.

A reference material, containing 10 wt. % Ni on bulk $CdIn_2S_4$ was also prepared for comparative study. Moreover, bulk β-$Ni(OH)_2$ was prepared by utilizing a chemical precipitation method. In particular, in a 20 mL of 1M $NiCl_2 \cdot 6H_2O$ solution, 20 mL of 4M NaOH were added dropwise until the formation of a light green precipitate is observed. Then, the resulting mixture was transferred into an oven and was heated at 60 ^oC for 24 hours, under static conditions. The final product was isolated by vacuum filtration, washed several times with DI water and ethanol, and dried at 100 ^oC for 12 hours.

2.5 Physical characterization

X-ray diffraction (XRD) patterns were acquired on a PANanalytical X′ pert Pro MPD X-ray diffractometer equipped with Cu Ka radiation (λ=1.5418 Å) in Bragg-Brentano geometry (45 kV and 40 mA).

Small-angle X-ray scattering (SAXS) patterns were collected on a Xeuss 3.0 (Xenocs, France) system equipped with a 2D detector and a Cu (λ = 1.5405 Å) rotating anode. Measurements were performed by transmission in samples that were ground and held in a Kapton capillary. Scattering data were corrected for empty tube scattering.

Filed-emission electron microscopy (FE-SEM) was performed on a JEOL JSM-IT700HR microscopy.

Transmission electron microscopy (TEM) images were obtained with a JEOL JEM-2100 electron microscope (LaB_6 filament) operating at 200 kV. The samples were prepared by suspending fine powders in ethanol using sonication and then drop-casting on a carbon-coated Formvar Cu grid.

Quantitative microprobe analysis was conducted on a JEOL JSM-6390 LV scanning electron microscope (SEM) equipped with an Oxford INCA PnetaFETx3 energy dispersive spectroscopy (EDS) detector (Oxfordshire, UK). Data acquisition was performed on at least ten different regions of every sample, using 20 kV acceleration voltage and 60 s accumulation time.

X-ray Photoelectron Spectroscopy (XPS) was performed on a SPECS spectrometer that was equipped with a Phoibos 100 1D-DLD electron analyzer and a monochromate Al K*a* radiation (1486.6 eV) as an energy source. A low-energy electron flood gun was employed for charge neutralization. Prior to XPS measurements, the samples were pressed to form a pellet. All binding energies were calibrated using the C1s peak of adventitious carbon (284.8 eV) as the reference signal. Peak fitting of XPS spectra was performed using the SpecsLab Prodigy software.

UV-vis/near IR diffusion reflectance spectra were taken using a Shimazu UV-2600 spectrophotometer, with $BaSO_4$ powder as a 100% reflectance reference. Diffuse reflectance data were converted to absorbance (α/S), according to the Kubelka-Munk function: $\alpha/S = (1-R)^2/(2R)$, where R is the reflectance and α, S is the absorption and scattering coefficients, respectively.

Thermogravimetric (TGA) measurements were performed in a Discovery TGA5500 system (TA instruments). The thermal analysis was conducted in a nitrogen atmosphere (under a flow rate of ~200 mL min^{-1}) using a two-step method where the first step the sample was maintained at 100 ^oC to remove the moisture of the sample and the second step was conducted from 100 to 550 ^oC with an increase heating rate of 10 $^oC\ min^{-1}$. Differential scanning calorimetry (DSC) were conducted in a Discovery DSC250 calorimeter (TA instruments).

Raman spectra were recorded on a Thermo Scientific DXR3xi Raman imaging microscope, using a 532 nm laser.

Nitrogen physisorption measurements were performed at –196 ^oC with the use of a Quantachrome NOVA 3200*e* volumetric analyzer. Prior measurement, each sample was degassed at 100 ^oC for 12 hours under vacuum (<10^{-5} Torr). The specific surface areas were

calculated using the Brunauer-Emmet-Teller (BET) method in the relative pressure (P/P_0) range of 0.04–0.24 [134]. The total pore volumes were determined from the N_2 adsorbed amounts at P/P_0 of 0.98. The pore-size distributions were calculated from the adsorption data, using the non-local density functional theory (NLDFT) method [135].

Photoluminescence and decay curve analysis was performed in room temperature conditions using an Edinburgh FSS spectrofluorometer. Time-resolved photoluminescence (TRPL) spectra were acquired at room temperature using 375 nm pulse laser excitation.

High-energy X-ray diffuse scattering (HE-XRDS) plots were collected were collected on a Bruker D8 Venture diffractometer equipped with a PHOTION II CPAD detector at room temperature, using Mo K*a* radiation (λ = 0.7093 Å) under a capillary geometry. Diffraction data were corrected for the empty cell scattering. The X-ray total scattering data ($I(q) = f(q)$, where q is the wavevector) were Fourier transformed to obtain the pair distribution functions (PDFs) using PDFgetX3 [136]. Modelling of PDFs was performed using PDFgui software [137].

2.6 (Photo)electrochemical measurements

The electrochemical experiments were conducted in a single-channel VersaSTAT 4 electrochemical workstation (Princeton Applied Research). The electrochemical cell consists of a working electrode, an Ag/AgCl (saturated KCl solution) reference electrode and a Pt wire counter electrode. The working electrodes were prepared through drop-casting of the samples on a fluorine-doped tin oxide (FTO, 10 Ω sq^{-1}) glass substrates. Briefly, 10 mg of as-synthesized catalyst was homogeneously dispersed in 1 mL ethanol by ultrasonication for about 1 hour. Then, 100 µL of the suspension was drop-casted on a FTO substrate and dried at 60 ºC for 1 hour. Mott-Schottky plots were reordered in 0.5 M Na_2SO_4 aqueous solution (pH = 6.8) using 1 kHz with a 10 mV AC voltage amplitude. All potentials were referred to a reversible hydrogen electrode (RHE), using the following equation:

$$E_{RHE} = E_{Ag/AgCl} + 0.197\ V + 0.059\ V \times pH \quad (12)$$

where, $E_{Ag/AgCl}$ is the measured potential in the Ag/AgCl scale.

The donor concentration (N_D) of the catalysts was calculated from the Mott-Schottky plots, according to the following equation:

$$N_D = \frac{C_{sc}^2 \cdot 2 \cdot (E - E_{FB})}{\varepsilon \cdot \varepsilon_0 \cdot e_0} \quad (13)$$

where, C_{sc} is the space charge capacitance, E is the applied potential, E_{FB} is the flat-band potential, ε is the dielectric permittivity of $CdIn_2S_4$ (6.6) or (4.73) for $ZnIn_2S_4$ (4.73) [74,138], ε_0 is the dielectric permittivity in the vacuum (8.8542 10^{-14} F cm^{-1}) and e_0 is the elementary charge (1.602 10^{-19} C).

The width of the depletion layer (W_D) was calculated as:

$$W_D = \left(\frac{2 \cdot \varepsilon_0 \cdot \varepsilon \cdot (E - E_{FB})}{N_D \cdot e_0}\right)^{1/2} \quad (14)$$

Electrochemical impendence spectroscopy (EIS) measurements were conducted in a frequency range of 1 Hz to 10 kHz under open-circuit potential or with an applied voltage of –1.2 V (vs Ag/AgCl), using a modulation amplitude of 10 mV. The EIS data were fitted using Zview software. Transient photocurrent curves were recorded under chopped visible-light (420–780 nm) irradiation at a fixed bias of −1 V (vs. Ag/AgCl) in 0.5 M Na_2SO_4 electrolyte. Polarization curves were recorded as linear sweep voltammetry (LSV) at a scan rate of 50 mV s^{-1} under visible LED light irradiation. LSV measurements were performed in a three-electrode cell in 0.5 M Na_2SO_4 solution, with the catalyst-modified FTO substrate as a working electrode and Ag/AgCl (saturated KCl solution) and graphite rod as the reference and electrode, respectively. The electrolyte resistance (R_s) was determined using EIS measurements and used for iR correction of corresponding polarization curves. Open circuit potential measurements were performed in a 0.5 M Na_2SO_4 solution under under switching on/off sunlight (AM 1.5G) irradiation. The light was illuminated through the FTO side (back-side illumination).

2.7 Photochemical water splitting study

The photocatalytic hydrogen evolution experiments were conducted in a custom-built gas-tight reaction cell containing 20 mg of photocatalyst suspended in 20 mL aqueous solution of triethanolamine (10% v/v) or 0.35 M $Na_2S \cdot 9H_2O$ and 0.25 M Na_2SO_3 mixture. The suspension was purged with argon for 30 min prior to irradiation. A 300 W Xenon lamp (Variac Cermax) equipped with a UV cut-off filter ($\lambda \geq 420$ nm) was used to irradiate the sample and the temperature of the suspension was maintained at 20 ± 2° C using an external water-cooling system. The evolving H_2 was analyzed using a gas chromatograph (Shimadzu GC-2014) equipped with a thermal conductivity detector (Ar carrier gas).

The apparent quantum yield (AQY) was determined by quantifying the amount of evolved hydrogen at a given wavelength (λ = 375, 420, 460, 520, 620 ±10 nm), according to the

following equation: AQY = (amount of produced H_2 molecules × 2)/(total incident photon flux). The photon flux was measured with a StarLite power meter equipped with a FL400A-BB-50 thermal detector (Ophir Optronics Ltd). The power density of the incident light was 2.55, 14.3, 14.8, 18.8 and 23.4 mW cm^{-2} for 375, 420, 460, 520 and 620 nm wavelengths, respectively.

Chapter 3: Results and Discussion

3.1 Size Dependent Photocatalytic Activity of Mesoporous $ZnIn_2S_4$ Nanocrystal Networks

3.1.1 Synthesis, structural investigation, and morphology

A schematic overview of the synthetic protocol of obtaining $ZnIn_2S_4$ (ZIS) mesoporous materials is depicted in **Figure 3-1**. Briefly, colloidal ZIS nanocrystals (NCs) with adjustable diameters were initially synthesized through a solvothermal reaction between Zn and In nitrates (in 1:2 molar ratio) and thioacetamide as sulfur source. To exert control over the crystal growth kinetics and prevent the formation of large nanoparticles aggregates, we utilized 3-mercaptopropionic acid (3-MPA) as a surface capping agent. By adjusting the reaction time, we succeeded in obtaining ZIS NCs of adjustable particle size (see Experimental Section for details). The gradual growth of ZIS NCs was indicated by the color change of the isolated nanoparticles from light to bright yellow. Afterwards, taking advantage of the chemical self-assembly method we prepared different 3D mesostructured frameworks using ZIS NCs as building block units. This synthetic route involves the oxidative coupling of colloidal ZIS NCs via diluted H_2O_2 through the formation of S-S interparticle bonds around of block copolymer aggregates [35]. Finally, the organic template was extracted from the pores by dissolution in warm ethanol and water (~40 ^oC) to yield a continuous network of linked ZIS NCs with large accessible surface area and well-defined pores (denoted as *n*-ZIS NCFs, where *n* = 4, 6 and 12 refers to the average size (nm) of starting NCs). The thermogravimetric analysis (TGA) profiles of the final products indicated that approximately 9.7–12.2 weight percent (wt. %) of organic residue remains within the porous structure of *n*-ZIS NCFs (**Figure 3-2**).

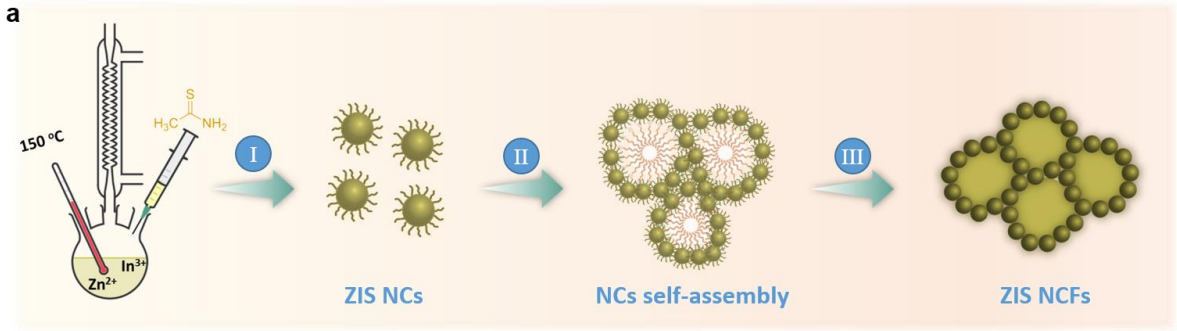

Figure 3-1. Schematic demonstration of the size-control synthesis of ZIS nanocrystal frameworks (NCFs) (step I: reflux synthesis of 3-MPA-capped ZIS NCs, step II: polymer-assisted self-assembly, step III: template extraction resulting to open-pore structures).

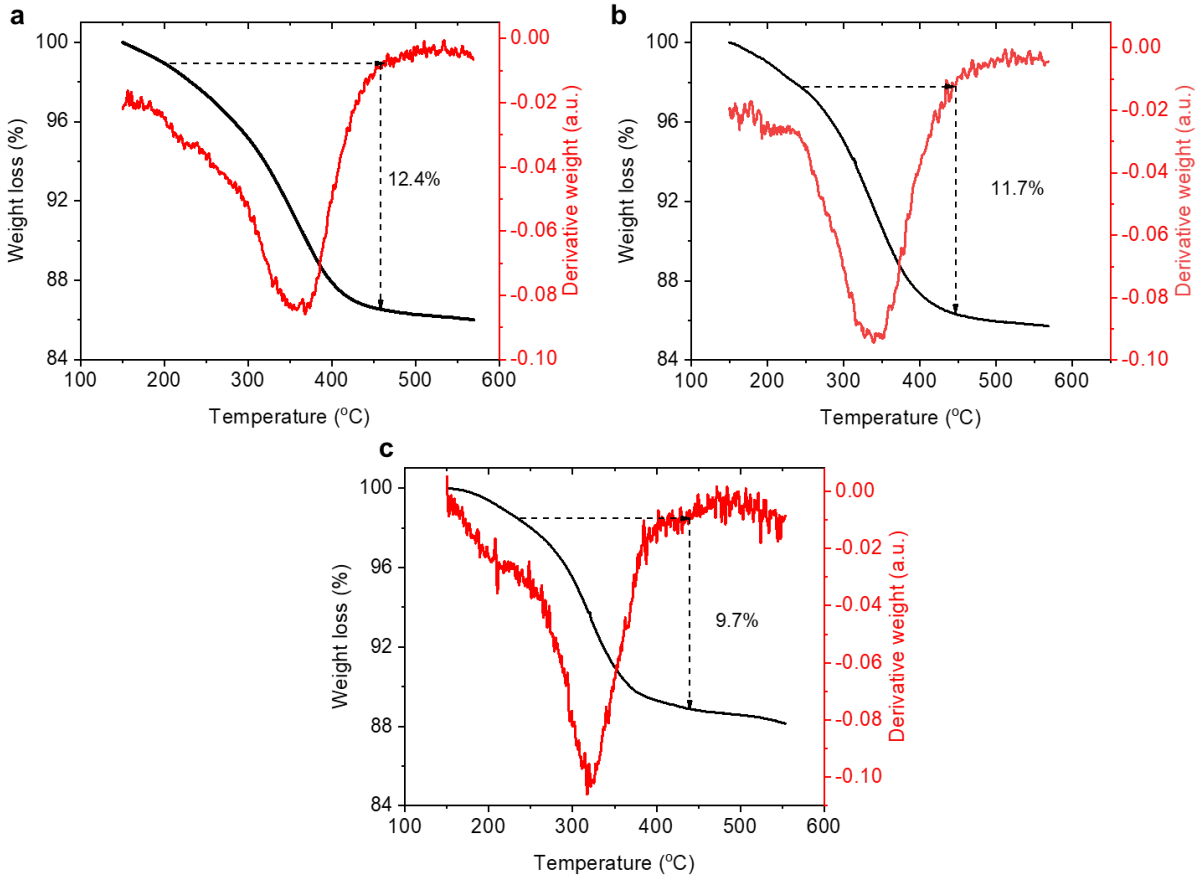

Figure 3-2. TGA profiles (black lines) and the corresponding differential thermogravimetric (DTG) curve (red line) of (a) 4-ZIS, (b) 6-ZIS and (c) 12-ZIS NCFs. The weight loss at the temperature range of 230 to 460 °C is due to the decomposition of the remaining organic molecules in the porous structure.

The chemical composition of the obtained materials was investigated via energy-dispersive X-ray spectroscopy (EDS). The EDS spectra obtained from multiple regions of samples showed a non-stoichiometric structure for the 4-ZIS (Zn/In/S atomic ratios ~ 1.14:2.0:3.9) and a nearly stoichiometric composition (Zn/In/S atomic ratios ~ 1:2:4, within experimental error) for the 6-ZIS and 12-ZIS NCFs (**Figure 3-3**). According to the EDS results the percentage of sulfur-defects in 4-ZIS NCF is ~2.5%. The defective structure of 4-ZIS NCF may result from the slower kinetics of In^{3+} ions in the ethanediol solution compared to the smaller and more labile Zn^{2+}. It is well known that the presence of unsaturated sulfur atoms or low-coordinated metal sites can enhance the photocatalytic properties of metal sulfides. These sites may function as electron-trapping sites, facilitating carrier separation and enhancing photo-absorption as well as highly active sites for photon capture, accelerating the water reduction kinetics (by lowering the overall activation barrier) [139–141]. However, an excess of defect

sites on the catalyst's surface may also serves as electron-hole recombination centers, ultimately resulting in decrease in photocatalytic activity. As a reference sample, we also prepared a polycrystalline bulk ZIS through a well-established hydrothermal method. This material exhibited an elemental composition of Zn/In/S close to 1:2:4 ratio, as confirmed by EDS analysis (**Figure 3-3**). The EDS data and atomic contents of the synthesized ZIS materials are summarized in **Table 3-1**.

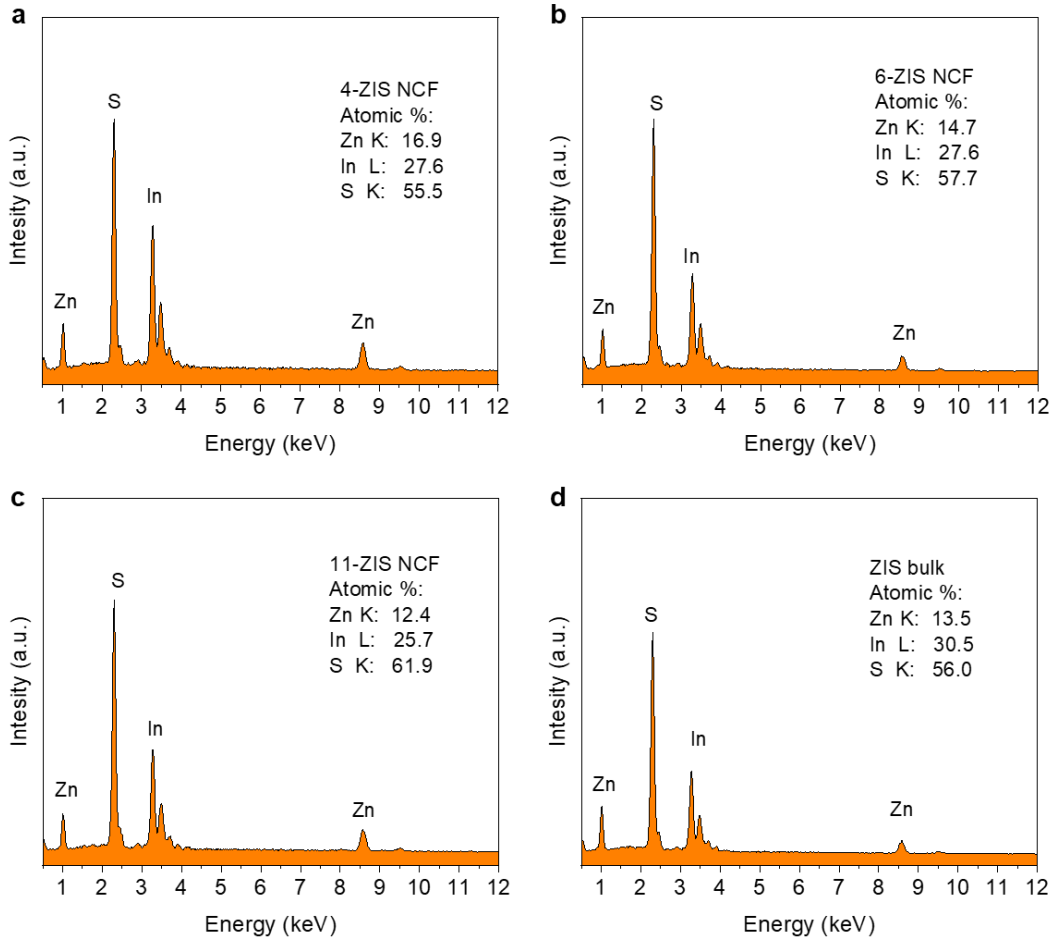

Figure 3-3. Typical EDS spectra of mesoporous *n*-ZIS NCFs and polycrystalline bulk ZIS.

Table 3-1. Chemical composition of mesoporous *n*-ZIS NCFs and polycrystalline bulk ZIS materials.

Sample	**Zn (at.%)**	**In (at.%)**	**S (at.%)**	**Zn:In:S[a]**
4-ZIS NCF	16.2	28.4	55.4	1.14:2.00:3.90
6-ZIS NCF	14.7	27.6	57.7	1.06:2.00:4.14
12-ZIS NCF	14.4	27.2	58.4	1.05:2.00:4.25
ZIS bulk	14.1	28.5	57.4	0.99:2.00:4.03

[a]EDS Zn/In/S atomic ratios based on In atoms.

The surface chemical states of elements of the mesoporous ZIS photocatalysts were characterized with X-ray photoelectron spectroscopy (XPS) (**Figure 3-4**). Consistent with the EDS results, the XPS survey spectra revealed the presence of Zn, In and S elements, whereas the presence of O signal can be attributed to the partial oxidation of the surface atoms upon exposure to air (**Figure 3-4a**). The high-resolution Zn 2p XPS spectra show Zn $2p_{3/2}$ and $2p_{1/2}$ core-level signals at 1024.4 and 1045.5 ± 0.1 eV, respectively, indicating the presence of Zn^{2+} ions (**Figure 3-4b**) [69]. Similarly, the In 3d XPS spectra displays strong subpeaks of the In $3d_{5/2}$ and $3d_{3/2}$ spin-orbit states at 445.3 and 452.9 ± 0.1 eV, respectively, confirming the In-S coordination environment of In^{3+} in $ZnIn_2S_4$ (**Figure 3-4c)** [142]. Meanwhile, a double deconvoluted peak at 162.0 and 163.3 ± 0.2 eV binding energies in the S 2p XPS spectra is consistent with the S $2p_{3/2}$ and $2p_{1/2}$ core-levels of the lattice S^{2-} in $ZnIn_2S_4$ (**Figure 3-4d**) [143]. All these characteristics provide compelling evidence for the formation of $ZnIn_2S_4$ thiospinel structure.

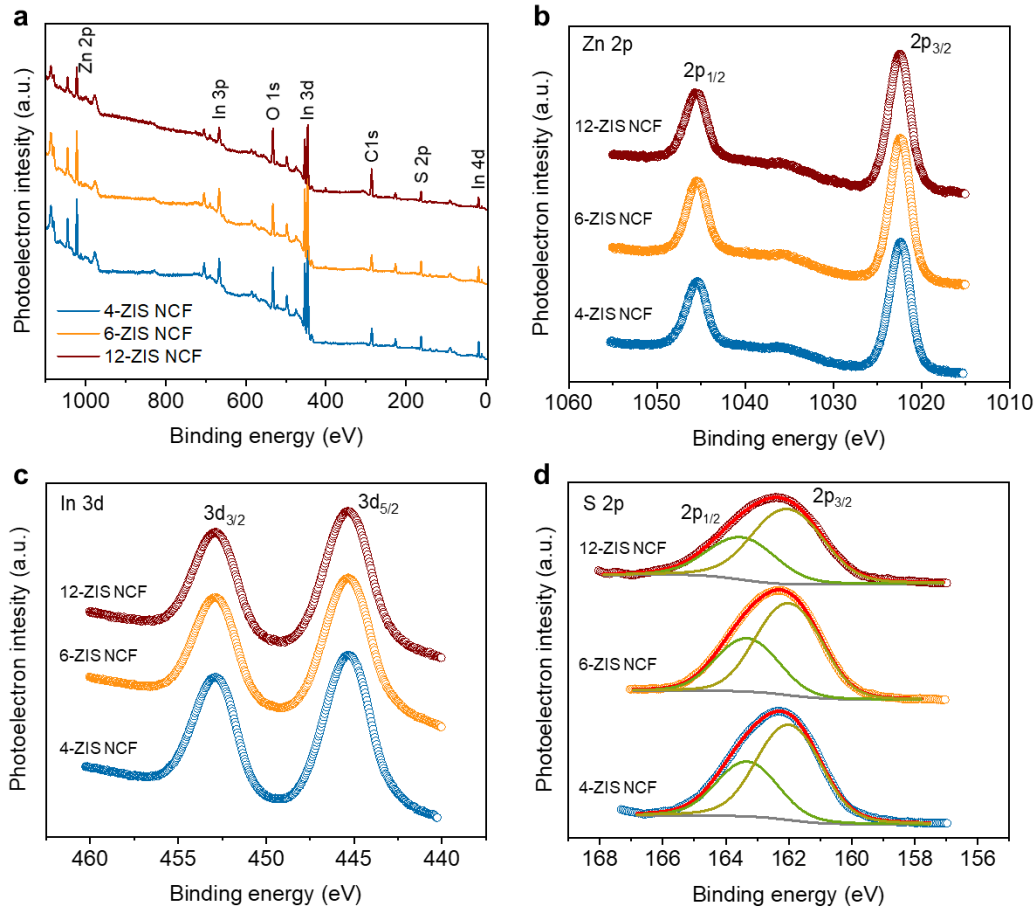

Figure 3-4. (a) XPS survey scans and high-resolution XPS core-levels of (b) Zn 2p, (c) In 3d and (d) S 2p of the mesoporous *n*-ZIS NCFs. In panel d: the XPS S 2p deconvoluted spectra of S $2p_{3/2}$ and S $2p_{1/2}$ core-levels are displayed as yellow and green curves. The red lines are fits to the experimental data.

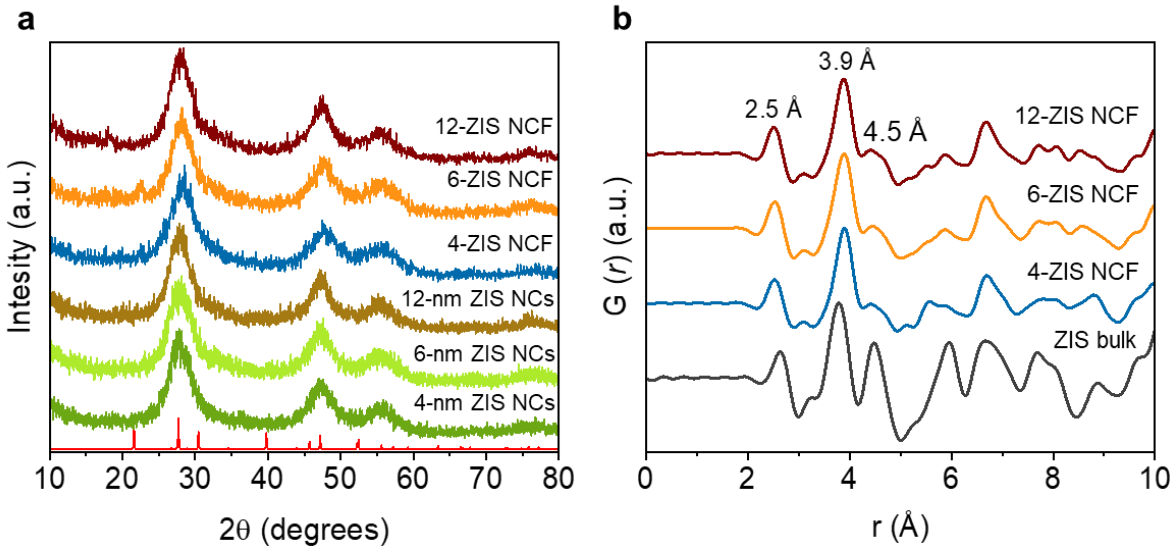

Figure 3-5. (a) Typical XRD patterns of ZIS NCs and mesoporous *n*-ZIS NCFs. (b) Reduced atomic pair distribution functions GI of the mesoporous *n*-ZIS NCFs and polycrystalline bulk ZIS. The standard diffraction pattern of the hexagonal $ZnIn_2S_4$ (JCPDS card no. 65.2023) is also given in red line. a.u. arbitrary units.

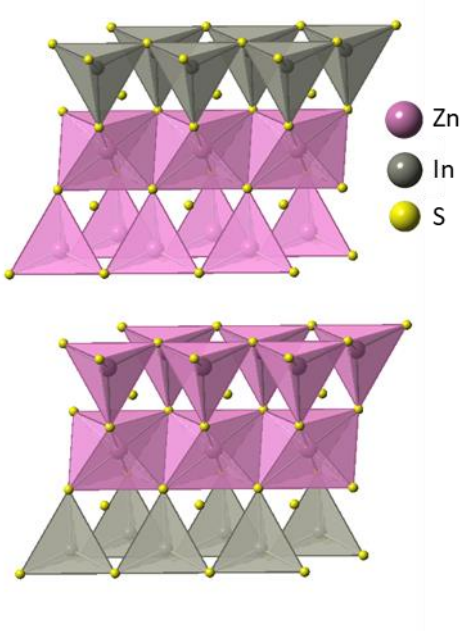

Figure 3-6. Crystal structure of hexagonal $ZnIn_2S_4$ (space group: P-3m1).

Figure 3-5a shows the X-ray diffraction (XRD) patterns of the 3-MPA-caped ZIS NCs and mesoporous *n*-ZIS NCFs. All the XRD plots exhibit three broad diffraction peaks at 2θ scattering angles of 20–60° due to the very small size of crystallites. Because of the broadness of the XRD peaks, however, it is difficult to identify the crystal structure of the samples. Thus,

to figure out the local atomic structure of *n*-ZIS NCFs, we conducted high-energy X-ray diffuse scattering (HE-XRDS) experiments and pair distribution function (PDF) analysis [144]. The corresponding PDF plots as a function of the interatomic distance for the mesoporous ZIS samples along with that polycrystalline ZIS are depicted in **Figure 3-5b**. The PDF plots of *n*-ZIS NCFs are very similar to that of the polycrystalline sample, signifying a similar atomic configuration. Specifically, the PDFs of *n*-ZIS NCFs are consistent with the hexagonal crystal structure of $ZnIn_2S_4$ (space group: P-3m1, **Figure 3-6**), showing intense interatomic vectors at ~2.5, ~3.9 and ~4.5 Å that correspond to the M–S first (M = Zn/In), M···M nearest and Zn···In next nearest neighbor distances, respectively, within the hexagonal $ZnIn_2S_4$. The crystal structure of polycrystalline ZIS was indexed as the hexagonal P-3m1 phase of $ZnIn_2S_4$ (JCPDS card no. 65-2023), according to the XRD data (**Figure 3-7**). Consequently, this analysis offers unequivocal evidence supporting the hexagonal thiospinel structure of the synthesized ZIS NCs. Moreover, a more detailed look at the pair correlation peak for In···In and Zn···Zn second neighbors in mesoporous samples from 11-ZIS to 4-ZIS NCFs reveals a shift from 3.89 to 3.91 Å; in contrast, the position of the Zn/In–S peak remains constant at 2.53 Å. This shift can be attributed to the slight distortions in the In–S–In/Zn–S–Zn bonds in the 4-ZIS NCF lattice, likely caused by the presence of sulfur vacancies as evidenced by EDS analysis (**Figure 3-8**).

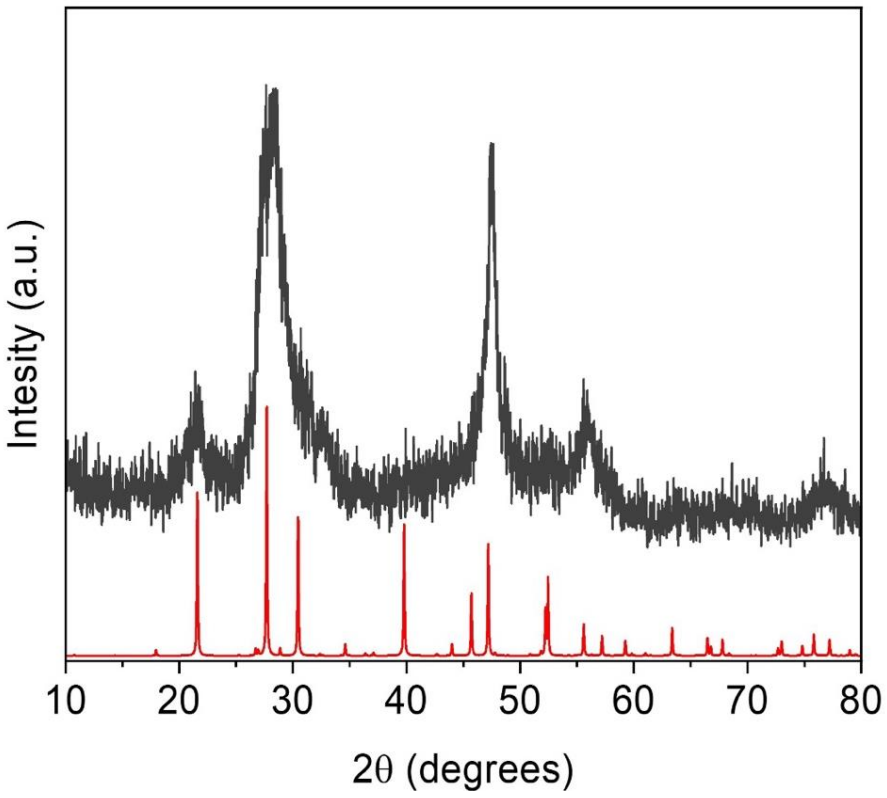

Figure 3-7. Typical XRD pattern of the bulk-like $ZnIn_2S_4$ catalyst. The red line corresponds to the standard diffraction pattern of the hexagonal $ZnIn_2S_4$ (P-3m1, JCPDS card no. 65-2023).

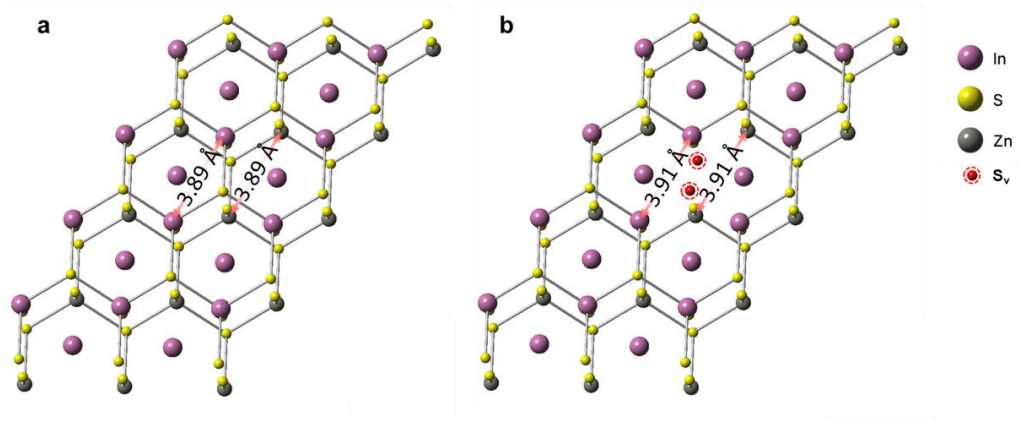

Figure 3-8. The In···In and Zn···Zn interatomic distances in the hexagonal crystal lattice of ZIS (a) without and (b) with sulfur vacancies (S_v).

The crystallinity and morphology of *n*-ZIS NCFs were further investigated with field-emission scanning electron microscopy (FESEM) and transmission electron microscopy (TEM). Representative FESEM images of the 6-ZIS NCF are shown in **Figure 3-9a**. The images reveal that the 6-ZIS NCF sample possesses a 3D porous network consisting of fairly monodisperse nanoparticles with a size smaller than 10 nm. For comparison, the reference polycrystalline ZIS that was synthesized via hydrothermal method consists of individual microspheres of ~3–5 μm diameter, which are composed of plenty of intersecting nanoflakes with an average thickness of about 18–20 nm (**Figure 3-10**). Typical TEM images of mesoporous 6-ZIS NCF are shown in **Figure 3-9b-d**, while the TEM images of 4-ZIS and 12-ZIS NCFs are provided in **Figure 3-11**. According to TEM observations, these samples feature a highly porous framework consisting of closely interconnected nanoparticles, which is beneficial for interparticle electron transfer phenomena. Based on the TEM analysis, we obtained an average size of the constituent ZIS nanoparticles from ~4 to ~12.2 nm in the series of mesoporous *n*-ZIS NCFs materials, which is strongly related with the reaction time of starting NCs (see **Table 3-2**). The nanoparticle sizes obtained from TEM align well with those obtained by independent small-angle X-ray scattering (SAXS) analysis. The SAXS patterns give an estimate of the ZIS NC size from ~4.5 to ~11.3 nm (**Figure 3-12**). Moreover, the crystal structure of *n*-ZIS NCFs was further confirmed by high-resolution TEM (HRTEM). The images support the hexagonal crystal phase of constituent NCs, in agreement with the PDF results, displaying well-resolved lattice fringes with 2.4 Å and 2.9 Å interplanar distances, corresponding to the (107) and (104) crystallographic planes of hexagonal $ZnIn_2S_4$ (JCPDS card no. 65-2023), respectively (**Figure 3-9d**).

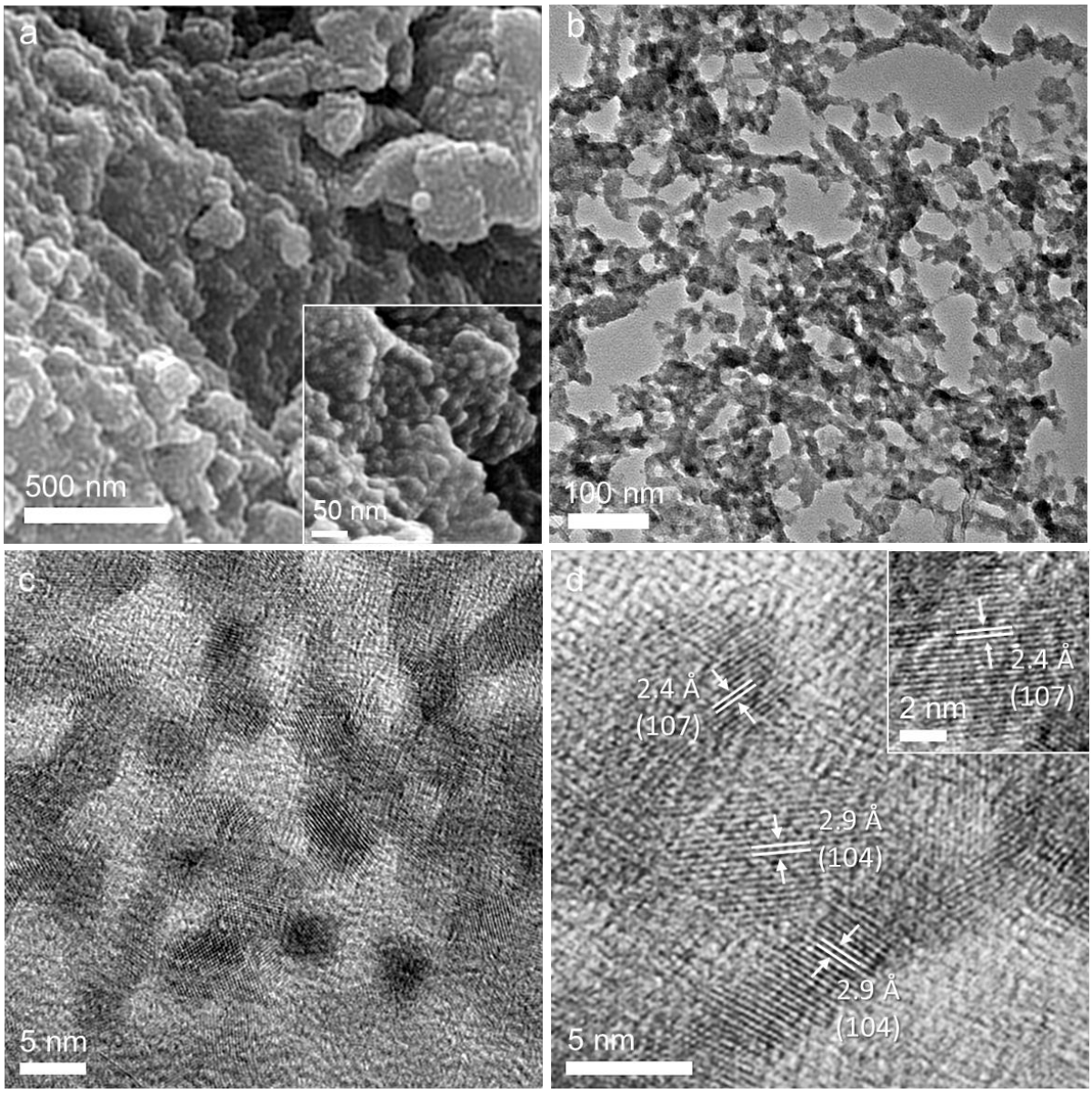

Figure 3-9. Typical (a) FESEM image, (b) TEM and (c and d) high-resolution TEM (HRTEM) images of the mesoporous 6-ZIS NCF catalyst.

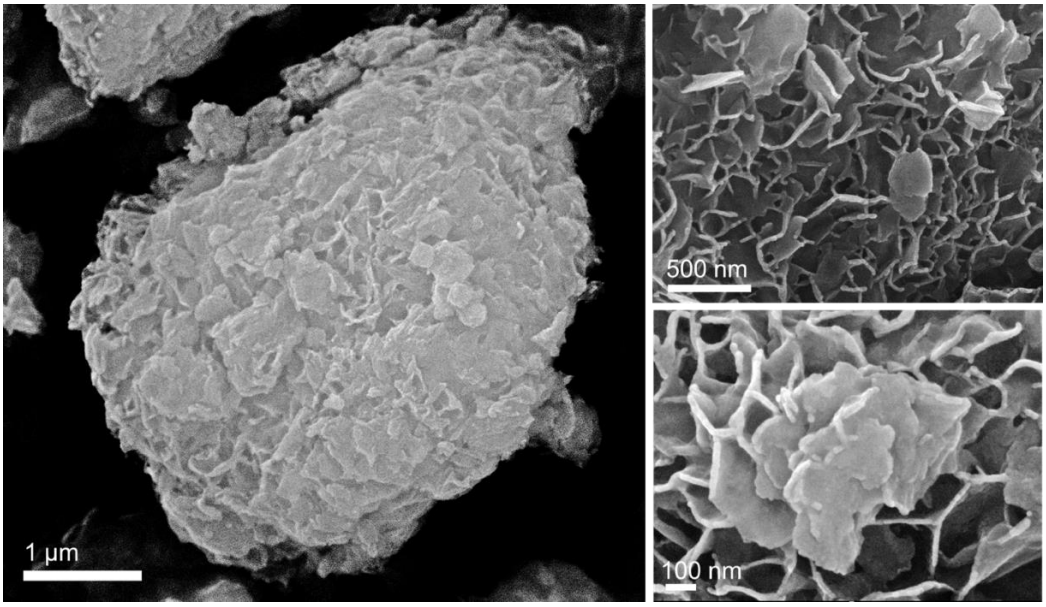

Figure 3-10. Typical FESEM images of the polycrystalline bulk ZIS.

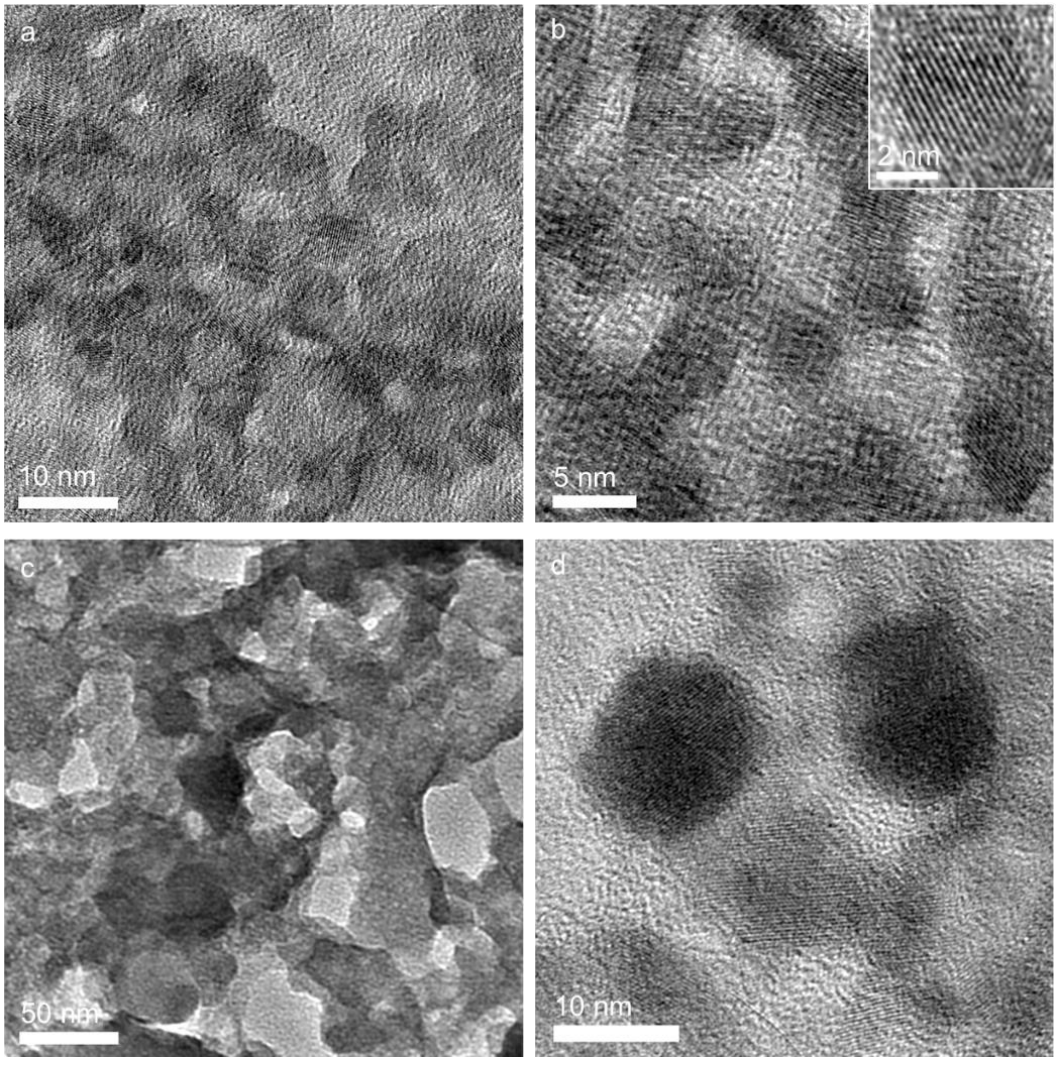

Figure 3-11. Typical TEM images of (a-b) 4-ZIS and (c-d) 12-ZIS NCFs.

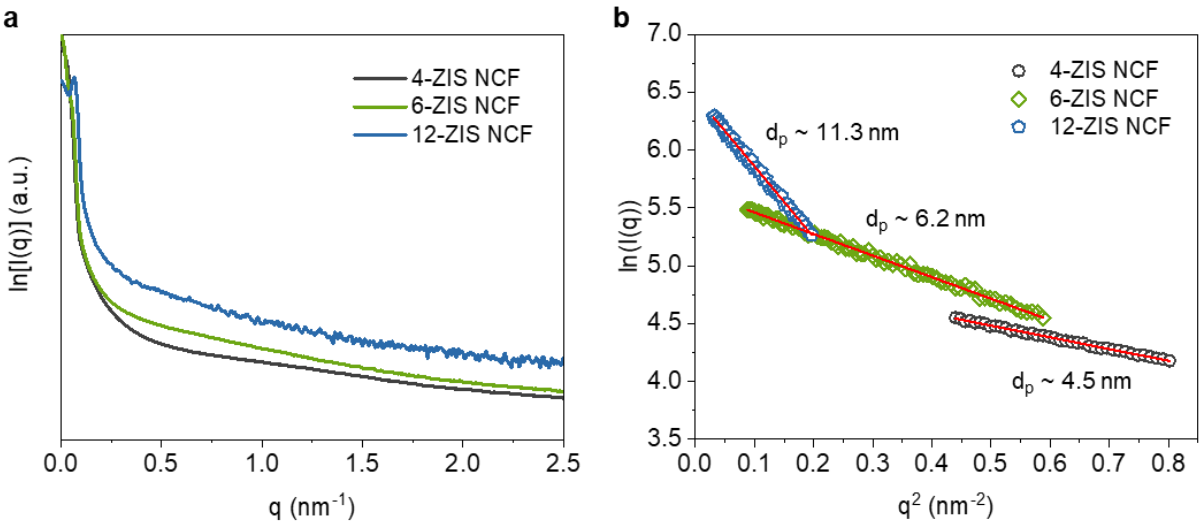

Figure 3-12. (a) SAXS patterns and (b) Guinier plots [$I(q) \propto -q^2R_g^2/3$, where q is the scattering vector and R_g is the radius of gyration] of the mesoporous *n*-ZIS NCFs

Table 3-2. Textural parameters and energy bandgap of mesoporous *n*-ZIS NCFs, ZIS RNAs and polycrystalline ZIS materials.

Sample	Surface area ($m^2\ g^{-1}$)	Pore volume[a] ($cm^3\ g^{-1}$)	Pore size (nm)	D_{TEM} (D_{SAXS})[b] (nm)	Energy bandgap[c] (eV)
4-ZIS NCF	207	0.17	6.4	4.0 (4.5 ±0.1)	2.75 (2.80)
6-ZIS NCF	195	0.17	6.4	6.5 (6.2 ±0.2)	2.66 (2.72)
12-ZIS NCF	187	0.16	6.3	12.2 (11.3 ±0.2)	2.65 (2.66)
ZIS RNAs	76	0.04	1.6	-	2.64
ZIS bulk	47	0.05	-	-	2.50

[a]Cumulative pore volume at relative pressure (P/P_o) equal to 0.98. [b]Particle size of constituent ZIS NCs estimated from TEM and SAXS (in parenthesis) analysis. [c]The energy gap obtained from the corresponding Tauc plots for indirect energy gap semiconductor. In parenthesis: the energy bandgap of the precursor NCs.

The porosity of the prepared materials was probed by N_2 physisorption measurements. All *n*-ZIS NCFs samples display characteristic typical-IV N_2 adsorption-desorption isotherms accompanied by an H_2-type hysteresis loop (**Figure 3-13 and 3-14**), indicating the successful preparation of mesoporous solids with interconnected pores [145]. These materials showed Brunauer-Emmet-Teller (BET) surface areas as high as 187–207 $m^2\ g^{-1}$ and total pore volumes of 0.16–0.17 $cm^3\ g^{-1}$. The slight decrease in surface is attributed to the larger size of ZIS NCs forming the porous framework. However, all *n*-ZIS NCFs materials display an open-pore

structure with a large internal surface area. Compared to the mesoporous samples, the bulk ZIS analogue exhibits a much lower BET surface area of 47 m^2 g^{-1}. Since the mesoporous *n*-ZIS NCFs are obtained as inorganic replicas from the same polymer template, these materials exhibit very similar pore diameters. By applying the nonlocal density functional theory (NLDFT) model to the adsorption isotherms, we obtained narrow size distributions of pores with an average pore size of ~6.3–6.4 nm. It should be stressed that this represents the first example of mesoporous $ZnIn_2S_4$ materials exhibiting such a high internal surface area and well-defined pore structure. For comparative study, we also synthesized a ZIS RNAs reference material (RNAs: random NC-aggregates) through a template-free oxidative coupling of 6-nm-sized ZIS NCs. Compared to the templated counterpart (6-ZIS NCF), ZIS RNAs exhibit a type-I adsorption isotherm (**Figure 3-13**), indicating a microporous structure with a lower BET surface area (ca. 76 m^2 g^{-1}) and small interstitial voids (ca. 1.6 nm in diameter). The aggregation of ZIS nanoparticles is detrimental to catalysis, leading to the formation of dense agglomerates with a reduced number of exposed active sites. All the textural parameters of the prepared ZIS materials are summarized in **Table 3-2**.

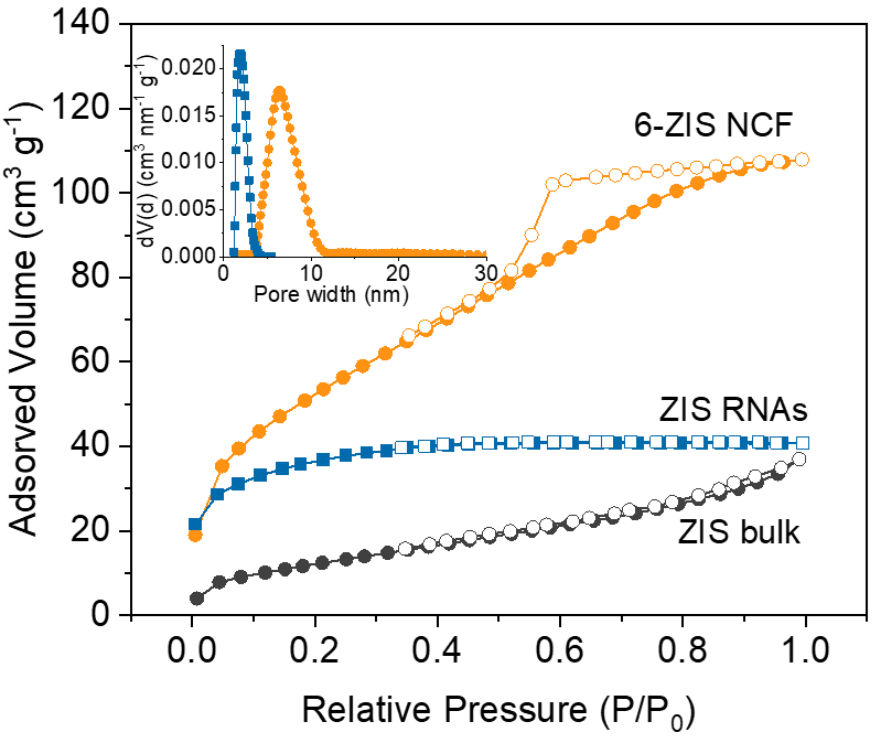

Figure 3-13. Nitrogen adsorption (filled symbols) and desorption (empty symbols) isotherms at –196 ºC for the mesoporous 6-ZIS NCF, random ZIS NC-aggregates (ZIS RNAs) and polycrystalline ZIS bulk. Inset: the corresponding NLDFT pore-size distribution plots calculated from the adsorption data.

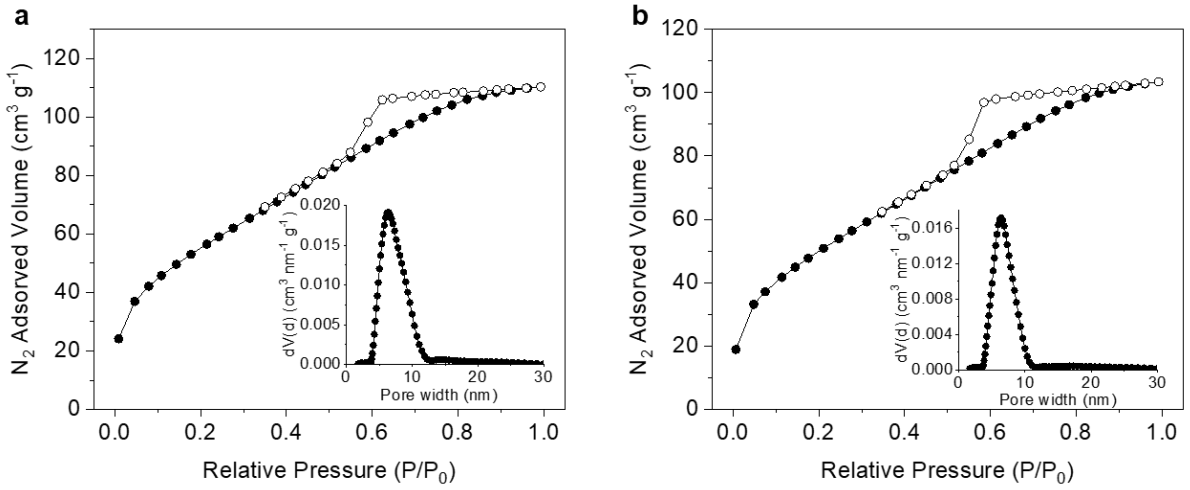

Figure 3-14. Nitrogen adsorption (filled symbols) and desorption (empty symbols) isotherms at –196 ºC for the mesoporous (a) 4-ZIS and (b) 12-ZIS NCFs. Inset: the corresponding NLDFT pore-size distribution plots calculated from the adsorption data.

The ultraviolet-visible (UV-vis) diffuse reflectance spectra of the as-prepared ZIS NCs showed a well-defined electronic structure with sharp optical absorption onsets (**Figure 3-15**). The UV-vis spectra indicated a systematic increase in the energy bandgap of ZIS NCs from ~2.66 eV to ~2.80 eV as the nanoparticle size decreases from 12 to 4 nm, see **Table 3-2**. This energetic shift of the bandgap is attributed to the size-induced quantum confinements transitions, similar to those observed in individual quantum dots and nanoclusters [146]. The optical absorption spectra of the mesoporous samples from 12-ZIS to 4-ZIS NCFs display a similar trend to the starting nanoparticles, signaling a blue shift in the energy gap from 2.65 to 2.75 eV (**see Table 3-2, Figure 3-16**). This blue shift suggests that quantization of the intrinsic band structure of the precursor NCs is well preserved in the assembled structures. The small red-shift (by ~50 meV) in optical absorption from the starting NCs to the mesoporous assemblies suggests strong electronic coupling and delocalization of electrons throughout the mesoporous network. Compared to the bulk ZIS (ca. 2.50 eV), the *n*-ZIS NCFs materials demonstrate a considerably higher bandgap absorption, possibly due to the substantial size reduction of constituent NCs (ca. 4–12 nm in size, as determined from SAXS and TEM results) that enables quantization of the band-edge electronic states. Consistent with its close-packed structure, the bandgap of the ZIS RNAs was found to be slightly lower (by ~20 meV) compared to that of the templated counterpart (6-ZIS NCF) (**Figure 3-17**).

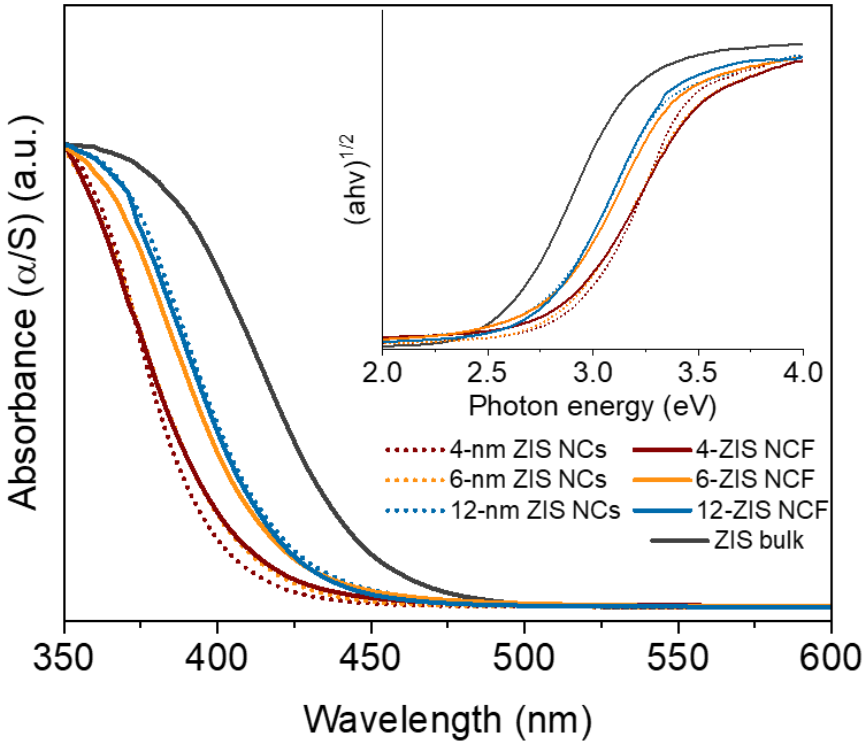

Figure 3-15. UV-vis diffuse reflectance spectra of as-prepared ZIS NCs, mesoporous *n*-ZIS NCFs and polycrystalline bulk ZIS. Inset: the corresponding Tauc plots for indirect gap semiconductors.

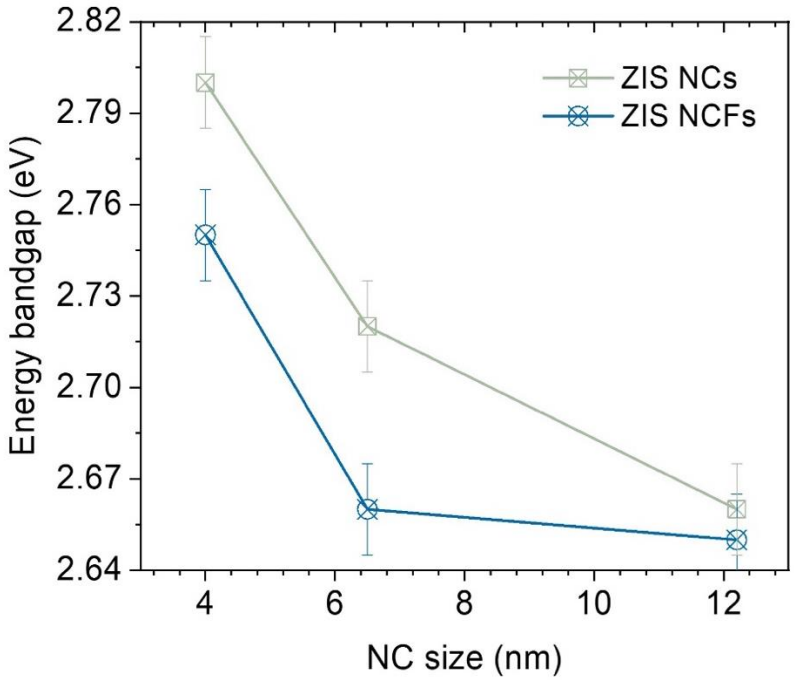

Figure 3-16. The bandgap energy as a function of the NC size for the obtained ZIS NCs and mesoporous *n*-ZIS NCFs materials. The size of the constituent NCs was estimated via TEM analysis.

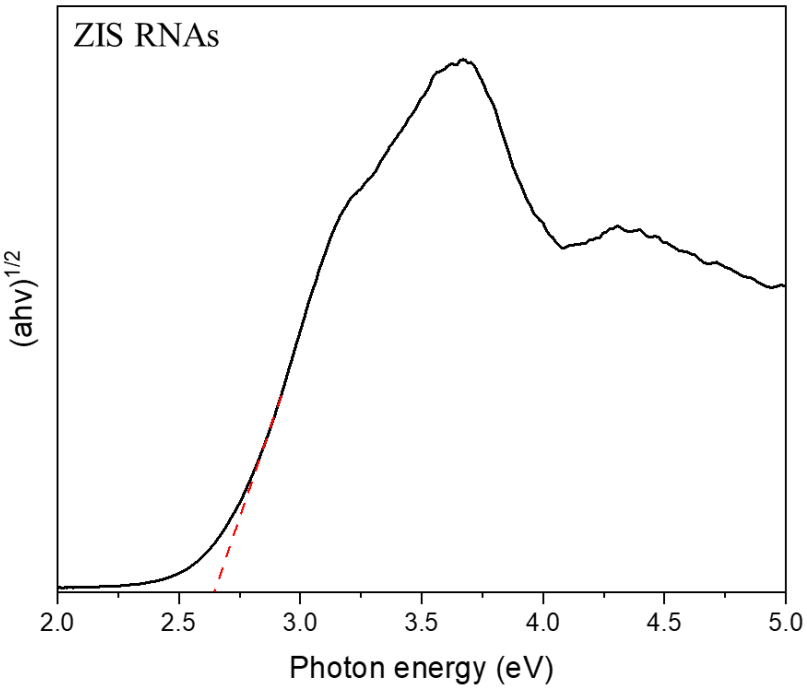

Figure 3-17. The corresponding Tauc plot for indirect gap semiconductors of ZIS RNAs sample.

3.1.2 Photocatalytic hydrogen evolution activity

The photocatalytic hydrogen production activities of the as-prepared ZIS materials were evaluated under $\lambda \geq 380$ nm light irradiation in a custom-made air-tight photocatalytic cell under Ar atmosphere. The photocatalytic H_2 evolution rates of mesoporous ZIS catalysts along with that of ZIS RNAs and polycrystalline ZIS in the presence of Na_2S/Na_2SO_3 pair as sacrificial electron donor are depicted in **Figure 3-18**. Even though, ZIS microparticles display an enhanced visible light absorption (it has an energy gap of ~2.50 eV), they demonstrate limited hydrogen production activity (~3.5 μmol h^{-1}) due to the lower porosity and micro-grain composition. In contrast, the open-pore morphology and large number of catalytic active sites of the mesoporous ZIS materials have a strong impact on adsorption and photochemical reactions. In particular, all *n*-ZIS NCFs exhibited enhanced photocatalytic hydrogen evolution performance, yielding an H_2-production rate ranging from 13.5 to 37.5 μmol h^{-1}. The highest photocatalytic activity is achieved by the 6-ZIS NCF catalyst, which is more than 10-times larger than that of the bulk analogue. As for the lower photoactivity observed for the mesoporous ZIS made of smaller (4 nm) NCs (~13.5 μmol h^{-1}), this is attributed to deficient charge-transfer kinetics induced by the defective structure (see chapter 3.1.3 below). Notably, the hydrogen evolution activity of 6-ZIS NCF also exceeds that of ZIS RNAS (~29.0 μmol h^{-}

[1]), that is obtained through direct coupling of colloidal 6-nm ZIS NCs, by a factor of 1.3x. Altogether, these results explicitly suggest that the small grain size of the constituent nanoparticles and the porous morphology are advantageous characteristics for improving the photocatalytic activity by providing short diffusion pathway of the photoexcited charge carriers and large catalyst/electrolyte interface area. Also, control experiments were conducted in dark conditions and without catalyst, showing no hydrogen evolution. This observation suggests that the detected hydrogen originates from the photocatalytic water splitting reaction.

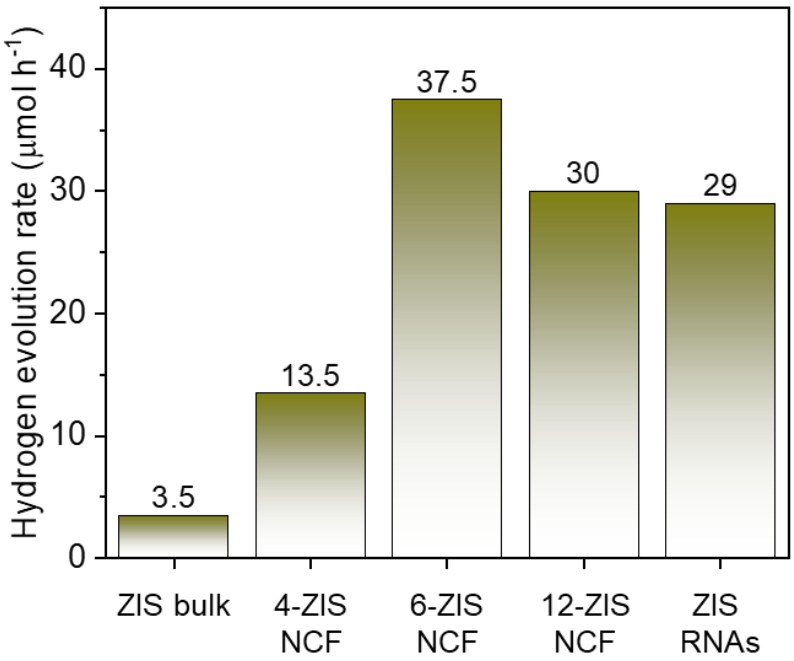

Figure 3-18. Hydrogen production rates of mesoporous *n*-ZIS NCFs, random ZIS NC-aggregates (ZIS RNAs) and polycrystalline ZIS materials under non-optimized conditions (0.35 M Na_2S and 0.25 M Na_2SO_3 mixed solution; UV-vis ($\lambda \geq 380$ nm) irradiation).

To further optimize the catalytic conditions, we performed a series of control experiments employing different hole scavengers and catalyst loads. As can be seen in **Figure 3-19**, triethylamine (TEA, 10% v/v) has the ability to expedite the reaction kinetics of 6-ZIS NCF catalyst, resulting in a H_2 evolution rate of 209 μmol h^{-1} compared to the 58 μmol h^{-1} and 20–42 μmol h^{-1} H_2-evolution rates obtained under triethanolamine (TEOA, 10% v/v) and Na_2S/Na_2SO_3 sacrificial conditions (at fixed catalyst mass), respectively. These results suggest that the interfacial hole transfer for the oxidation process is the rate-determining step of the overall photocatalytic reaction. Furthermore, the H_2-evolution rate experiences an increase with the catalyst load, reaching a maximum efficiency at 1.5 mg mL^{-1} (**Figure 3-20**). Further

increasing the above concentration, the photocatalytic performance slightly declines presumably due to light-scattering effects by the catalyst's particles. Thus, in optimum conditions, 6-ZIS NCF presents an exceptional photocatalytic performance with a respective H_2 evolution rate of 234 μmol h^{-1} (or 7.8 mmol g_{cat}^{-1} h^{-1} mass activity) and apparent quantum yields (AQYs) of 25.0% at 375 ± 10 nm and 17.2 % at 420 ± 10 nm, assuming 100% absorption of the incident light. To the best of our knowledge, this photoactivity is among the highest reported thus far for thiospinel-based catalysts, and vastly higher than previously reported single-component sulfide photocatalysts. Other sulfide-based materials that present such a high H_2-evolution activity usually possess a complex structure of multi-ingredient composition. A comparison of the hydrogen evolution activity of our catalyst with other reported catalyst is given in **Table I** in the **Annex I**.

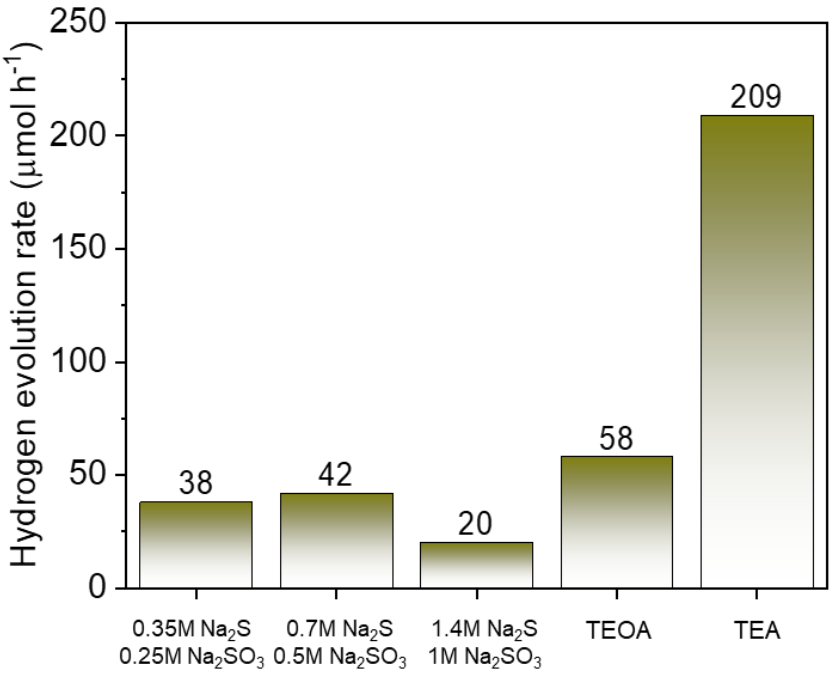

Figure 3-19. Photocatalytic hydrogen production activity of 6-ZIS NCF catalyst using different hole scavengers: 0.35–1.4 M Na_2S/0.25–1 M Na_2SO_3 mixed solution, 10% (v/v) triethanolamine (TEOA) and 10% (v/v) triethylamine (TEA). The photocatalytic experiments were conducted at fixed catalyst loading (1 mg mL^{-1}), under UV-vis (λ ≥ 380 nm) irradiation (300-W Xe lamp) at 20 ± 2 °C.

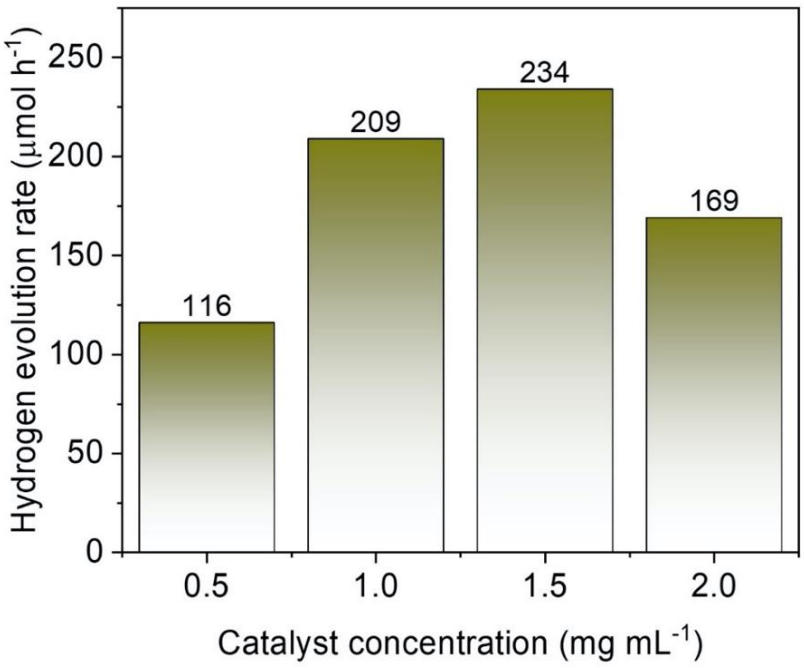

Figure 3-20. Photocatalytic H_2 production activity of 6-ZIS NCF catalyst using different mass concentrations. Reaction conditions: 0.5–2 mg mL^{-1} of catalyst, 20 mL aqueous solution containing 10% (v/v) TEOA, UV-vis ($\lambda \geq 380$ nm) irradiation (300 W Xe lamp), 20 ± 2 °C.

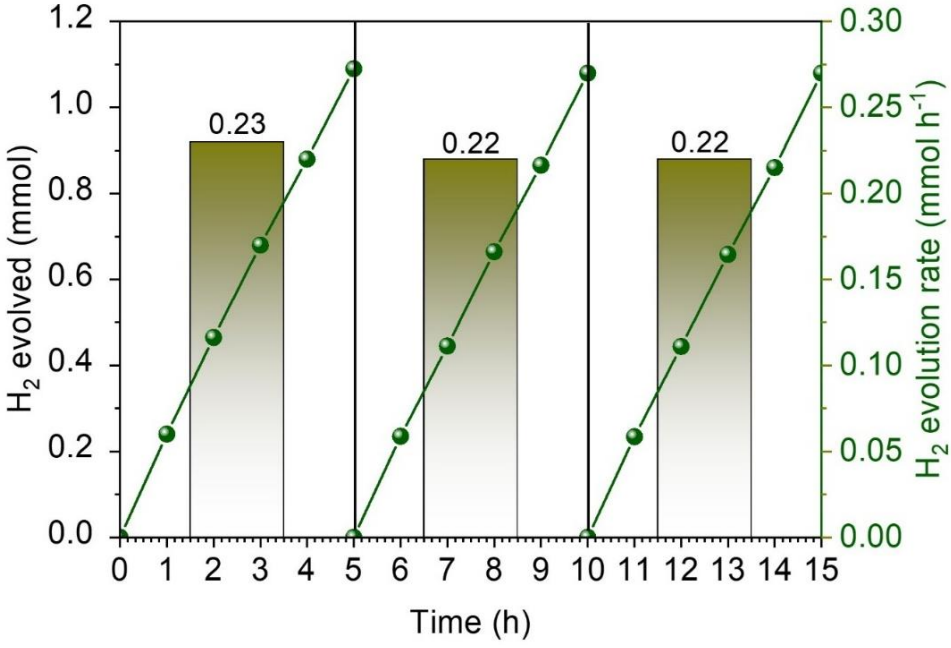

Figure 3-21. Time courses of the photocatalytic hydrogen evolution (lines) and the H_2-evolution rates (column) at the course of the photocatalytic stability study over 6-ZIS NCF catalyst. The H_2-generation rates were averaged over the 5 hours of irradiation. The stability test was conducted with 1.5 mg mL^{-1} catalyst loading in triethylamine (10% v/v) solution, under UV-vis ($\lambda \geq 380$ nm) irradiation (300 W Xe lamp) at 20 ± 2 °C.

The stability of the 6-ZIS NCF catalyst under photocatalytic conditions was assessed through three 5-hour catalytic runs. After each catalytic test, the photocatalyst was obtained from the reaction solution by centrifugation, washed several times with water and re-dispersed in a fresh TEA (10% v/v) solution. The hydrogen production tests showed that 6-ZIS NCF retained an exceptional photo-corrosion resistance, demonstrating no notable catalytic performance decay within 15 hours of photocatalytic reaction (**Figure 3-21**). 6-ZIS NCF exhibits an almost stable photocatalytic activity, yielding a total H_2 evolution of 3.25 mmol (~78.2 mL) after 15 hours of irradiation (average release rate ~0.22 mmol h^{-1}). Furthermore, no obvious changes in chemical composition and oxidation states of 6-ZIS NCF reused catalyst were observed by EDS and XPS analysis (**Figure 3-22**). Specifically, the EDS spectra indicated Zn/In/S atomic ratios ~ 1:1.9:3.9, very close to the composition of the fresh sample.

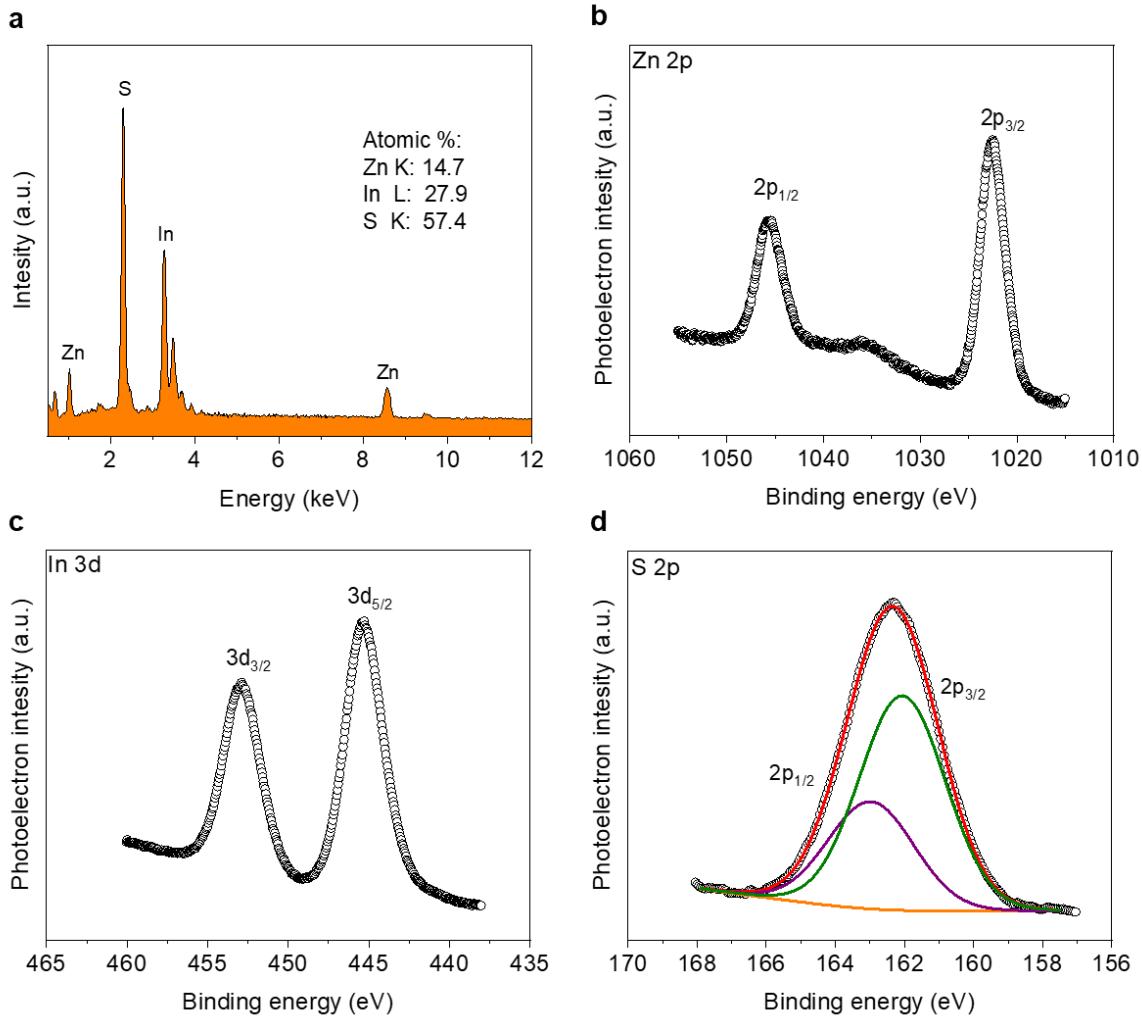

Figure 3-22. (a) Typical EDS spectrum and (b-d) XPS core-level spectra of the (b) Zn 2p, (c) In 3d and (d) S 2p of the reused 6-ZIS NCF catalyst.

The Zn 2p XPS spectrum of the recycled 6-ZIS NCF catalyst depicts a doublet peak at 1022.4 and 1045.5 ± 0.1 eV binding energies, corresponding to the Zn $2p_{3/2}$ and Zn $2p_{1/2}$ core-levels of Zn^{2+} ions, respectively. Also, in the In 3d region, the peaks at 445.4 and 452.9 ± 0.1 eV, are attributed to the In $3d_{5/2}$ and In $3d_{3/2}$ signals of In^{3+} oxidation state. The S 2p XPS spectrum displays two deconvoluted peaks at 162.1 and 163.0 ± 0.2 eV, which are associated with the S $2p_{3/2}$ and S $2p_{1/2}$ core-levels of S^{2-} valence state. Besides, the N_2 physisorption measurements indicate a very slight decrease in surface area (ca. 163 $m^2\ g^{-1}$) and pore diameter (ca. 5.4 nm) after the photocatalytic runs, suggesting the good structural stability of the 6-ZIS NCF catalyst (**Figure 3-23**).

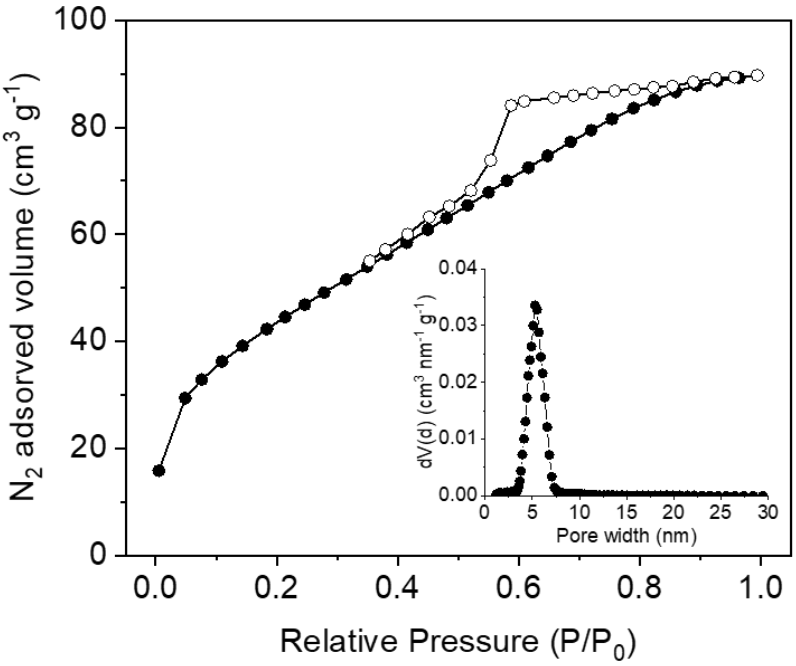

Figure 3-23. Nitrogen adsorption-desorption isotherms at –196 ºC and the corresponding NLDFT pore size distribution plot (inset) of the 6-ZIS NCF catalyst isolated after 15 hours of photocatalytic reaction.

3.1.3 Size-dependent electronic properties of mesoporous $ZnIn_2S_4$ structures

To uncover the effect of the nanoparticle size on the electronic structure of *n*-ZIS NCFs, we performed electrochemical measurements. **Figure 3-24** shows the Mott-Schottky plots, that is, the reciprocal square capacitance ($1/C_{SC}^2$) versus applied potential (E), of the different ZIS catalysts drop-casted as thin film onto fluorine tin oxide (FTO, 10 Ω sq^{-1}) substrates measured in 0.5 M Na_2SO_4 electrolyte. The flat-band potential (E_{FB}) was determined by the intersection point of the linear segment in these plots, and all the measured potentials were converted to

reversible hydrogen electrode (RHE) at pH 7. The positive slope observed in the corresponding Mott-Schottky plots confirms the n-type conductivity of the ZIS materials, consistent with previous reports [147,148]. By combining the E_{FB} potentials and the energy bandgaps (as obtained from UV-vis diffuse reflectance spectra, **Figure 3-15**), the energy levels of the valence band (E_{VB}) for each catalyst were determined, and these results are summarized in **Table 3-3**. In this analysis, E_{FB} serves as a good approximation of the CB edge position, which is quite feasible for heavily n-doped semiconductors (typically with $>10^{18}$ donor density) [46], such as the ZIS. Interestingly, the above analysis showed that the band-edge positions of *n*-ZIS NCFs vary systematically with the NC size. Compared to the polycrystalline ZIS ($E_{FB} \sim -0.78$ V), the mesoporous ZIS samples demonstrate a gradual upshift of the E_{FB} level. In particular, the E_{FB} potential ranges from –0.85 V for the 12-ZIS NCF to –0.91 V for the 4-ZIS NCF. This progressive anodic shift of E_{FB} with decreasing NC size is consistent with the widening of the optical bandgap of *n*-ZIS NCFs (**Figure 3-15**), which is attributed to the quantum size effect of the constituent NCs. These effects can be clearly observed in **Figure 3-25**, where the systematic variation of the band-edge positions (E_{FB} and E_{VB}) with the NC size is depicted.

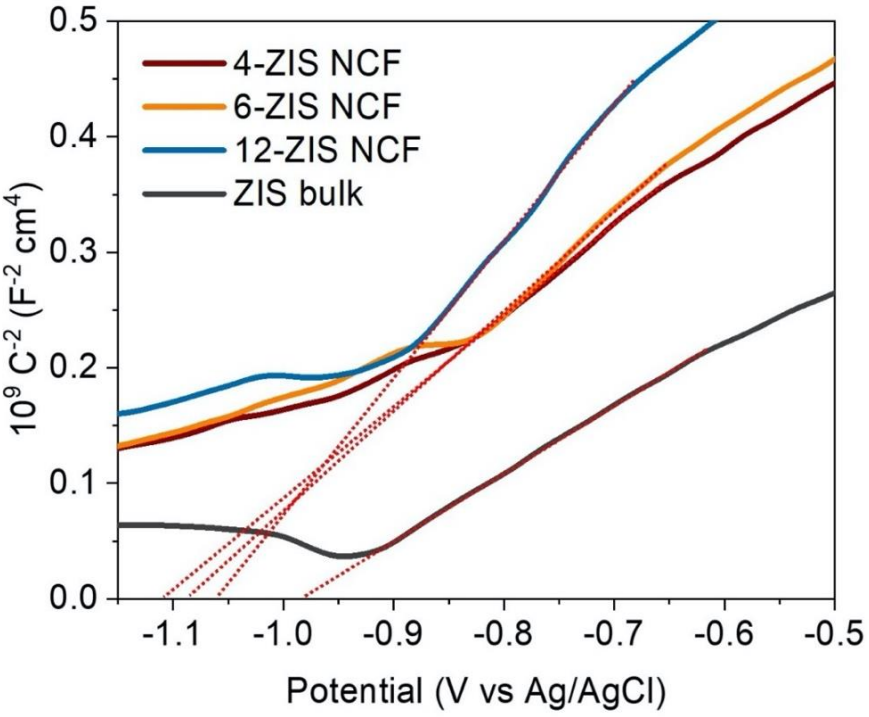

Figure 3-24. Mott-Schottky plots of the as-prepared mesoporous *n*-ZIS NCFs and polycrystalline bulk ZIS catalysts.

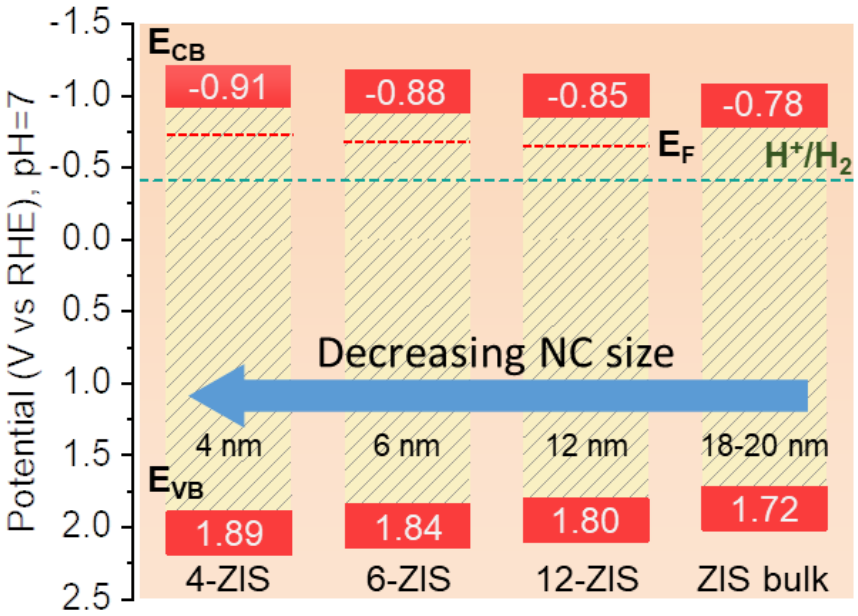

Figure 3-25. Energy band diagrams (E_{CB}: conduction band energy, E_{VB}: valence band energy, E_F: Fermi level, H^+/H_2 redox potential) of different ZIS catalysts.

The shifts in the band-edge positions result from the limited number of electron wavefunctions contributing to the density states of the conduction and valence band due to the substantial reduction in particle size [149,150]. Eventually, this leads to the discretization of the energy levels between electronic states, resulting in the widening of the energy bandgap. Consistent with this assumption, the valence-band (VB) XPS spectra affirm a gradual upshift of the Fermi level (E_F) with decreasing the NC diameter. The results showed that 4-ZIS NCF has the larger Fermi level offset from the VB maximum (2.61 eV), followed by 6-ZIS (2.51 eV) and then 12-ZIS (2.45 eV) NCFs (**Figure 3-26**). In general, the rise of the E_F level as the size of the ZIS NCs decreases is advantageous for the efficient surficial electron transfer. The upshift in the E_F of ZIS nanostructures can be attributed to the sufficient elevation of the CB edge position through quantization of energy states. This assumption aligns well with previous studies on metallic and semiconducting nanoparticles [151]. Also, an electron delocalization in the space charge region of *n*-ZIS NCFs can be inferred by the changes in the charge carrier density (N_D), as determined from the slope of the $1/C_{SC}^2$–E lines (**see Table 3-3**). As the size of ZIS NCs decreases from 12 to 4 nm, the N_D of ZIS mesoporous materials experiences a slight increase from ~2.4 to 3.6 $\times 10^{18}$ cm^{-3}, signifying an increase in n-type doping. The higher N_D values observed in *n*-ZIS NCFs could be attributed to a lower recombination rate of excitons, facilitated by the short depletion width and concomitant increased band bending within the ultrasmall nanoparticles. The depletion layer width (W_D) determined for the ZIS

mesoporous materials ranges from 13.6 to 11.5 nm (as shown in **Table 3-3**) and it is comparable to the size of ZIS NCs. This suggests a pronounced deformation of the band edge at the catalyst/electrolyte interface.

Table 3-3. Electrochemical properties of the mesoporous *n*-ZIS NCFs and bulk ZIS as determined via EIS analysis.

Sample	**E_{FB}**	**E_{VB}**	**Donor density (N_D, cm^{-3})**	**Depletion layer width (W_d, nm)**
	(V vs RHE, pH 7)			
4-ZIS NCF	–0.91	1.89	3.58×10^{18}	11.5
6-ZIS NCF	–0.88	1.84	3.32×10^{18}	11.8
12-ZIS NCF	–0.85	1.80	2.41×10^{18}	13.6
ZIS bulk	–0.78	1.72	4.85×10^{18}	9.2

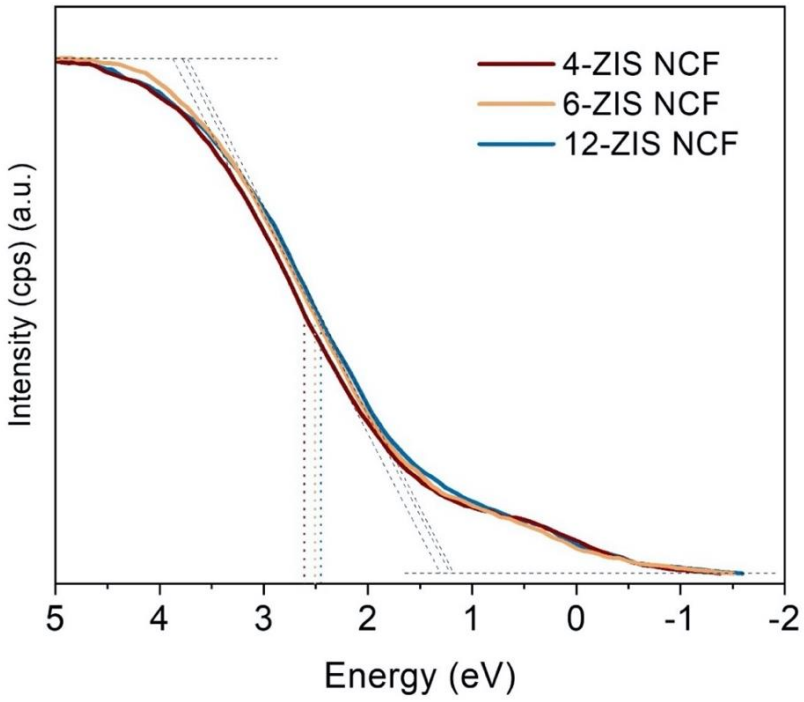

Figure 3-26. Valence band (VB) XPS spectra of mesoporous *n*-ZIS NCFs materials.

The above assumption is also supported by the results of the open circuit potential (V_{OC}) measurements conducted on *n*-ZIS NCFs under solar-light switching on/off transition. In fact, the surface depletion field induced by band bending can be elucidated by the district variations in V_{OC} under dark and illumination conditions ($\Delta V_{OC} = V_{OC,light} - V_{OC,dark}$). As can been seen

in **Figure 3-27**, the light-induced V_{OC} shift (photovoltage) for ZIS mesoporous follows the trend: 6-ZIS (ΔV_{OC} = 211 mV) > 12-ZIS (ΔV_{OC} = 164 mV) > 4-ZIS (ΔV_{OC} = 90 mV). The higher photovoltage generating from 6-ZIS NCF suggest a sharper band bending, which generates a driving force (internal electric field) for the spatial separation of the photoexcited charge carriers, thus amplifying the photocatalytic hydrogen evolution activity. The lower recombination rate of the photoexcited charge carriers in this sample is further evidenced by the gradual decay of V_{OC} signal over time after the light is switched off. On the other hand, the diminished photovoltage amplitude and accelerated V_{OC} decay in 4-ZIS NCF are related to the surface pinning effect induced by midgap interface states (see below). Evidently, these results collectively indicate that the substantial size reduction of the ZIS NCs dictates the electronic structure and, consequent, the photo-redox activity of the resulting catalysts. We conclude that quantization of the band-edge electronic states of ZIS NCs significantly promotes the separation of photogenerated electron-hole pairs within the depletion region, thus enhancing the interfacial charge transfer.

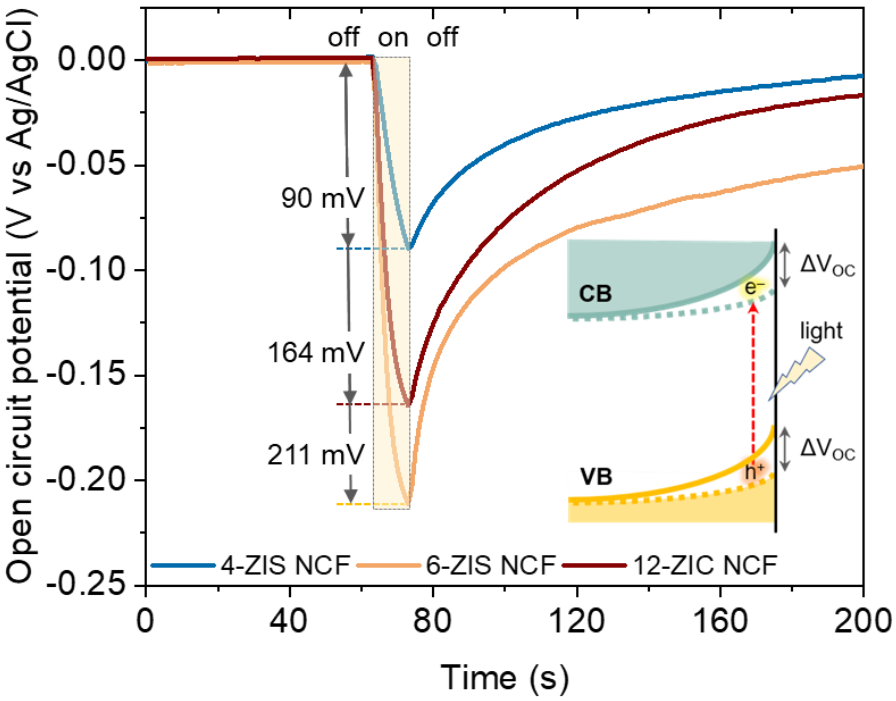

Figure 3-27. Open circuit potential versus elapsed time for mesoporous *n*-ZIS NCFs under switching on/off AM 1.5G illumination (10 s light on). The inset displays the change of the V_{OC} at the catalyst/electrolyte interface under chopped illumination, when the light is switched on, a charge accumulation occurs at the interface of ZIS NCs, mitigating the surface band bending.

More detailed insights on the size-dependent charge carrier recombination and transfer kinetics were obtained by electrochemical impendence spectroscopy (EIS). **Figure 3-28** presents the EIS Nyquist plots of the mesoporous and bulk ZIS materials drop-casted onto FTO substrates. The EIS data were fitted to an equivalent Randles circuit model, consisting of the electrolyte resistance (R_s), double-layer capacitance (C_{dl}) and charge-transfer resistance (R_{ct}) (inset of **Figure 3-28**). This analysis indicated a more efficient migration of electrons withing ZIS mesoporous architectures (R_{ct} ~ 307–377.6 Ω) compared to the bulk ZIS (395.1 Ω). This a direct result of the shorter charge diffusion distance in ZIS NCs. Notably, consistent with its superior photocatalytic activity, 6-ZIS NCF showed the highest charge-transfer efficiency (307.0 Ω) across the catalyst/electrolyte interface, followed by 12-ZIS (359.3 Ω) and 4-ZIS (377.6 Ω) NCFs, see **Table 3-4**. Indeed, the decreasing trend of R_{ct} in *n*-ZIS NCFs catalysts is in good agreement with the photocatalytic hydrogen production experiments shown in **Figure 3-18**. The effect of the surface-active sites of *n*-ZIS NCFs catalysts was also investigated through a comparative analysis of the double-layer capacitances (C_{dl}) obtained from the EIS measurements. The C_{dl} is proportional to the electrochemical active surface area (ECSA) at the catalyst/liquid interface. This analysis showed an improvement of the active surface area compared to the bulk ZIS of 1.2x, 2.8x and 1.5x for the 4-ZIS, 6-ZIS and 12-ZIS NCFs, respectively, which is responsible for the enhanced photocatalytic efficiency and interfacial charge transfer (**Table 3-4**). It is worth noting that the 6-ZIS NCF outperforms all other samples in terms of ECSA, even surpassing the 4-ZIS NCF, despite the latter having a slightly larger specific surface area. Altogether, these results demonstrate that manipulating the $ZnIn_2S_4$ morphology at the nanoscale can significantly improve the charge carrier transfer and separation efficiency and provide an increased exposure of the catalytically active sites at the interface, ultimately resulting in improved photocatalytic activity.

Table 3-4. Nyquist equivalent circuit fitted parameters of the mesoporous *n*-ZIS NCFs and polycrystalline bulk ZIS materials.

Sample	**R_s (Ω)**	**C_{dl} (F cm^{-2})**	**ECSA[a]**	**R_{ct} (Ω)**	**x^2**
4-ZIS NCF	11.6	75.1×10^{-6}	1.2	377.6	1.8×10^{-4}
6-ZIS NCF	11.8	180.0×10^{-6}	2.8	307.0	2.2×10^{-4}
12-ZIS NCF	12.4	96.8×10^{-6}	1.5	359.3	1.7×10^{-4}
ZIS bulk	12.9	64.6×10^{-6}	1	395.1	1.1×10^{-4}

[a]Electrochemically active surface area (ECSA) increment obtained as a ratio of the double-layer capacitance (C_{dl}) relative to that of bulk ZIS.

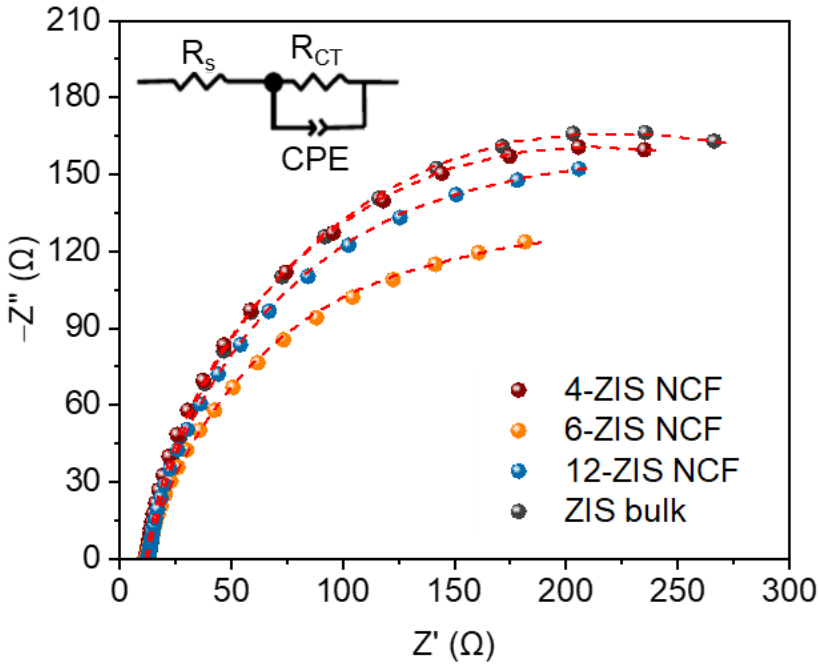

Figure 3-28. EIS Nyquist plots of mesoporous *n*-ZIS NCFs and polycrystalline bulks ZIS measured in 0.5 M Na_2SO_4 aqueous solution using a conventional three-electrode setup. Inset: equivalent Randles circuit model.

The impact of the constituent NCs on charge-carrier delocalization dynamics in mesoporous *n*-ZIS NCFs was also examined by time-resolved photoluminescence (TRPL) spectroscopy. The PL decay data of different ZIS catalysts were recorded at the near band-edge emission and were fitted to a biexponential function: $F(t) = \alpha_1 \cdot e^{-t/\tau 1} + \alpha_2 \cdot e^{-t/\tau 2}$, where α_1 and α_2 are the relative amplitudes of each lifetime component, and τ_1 and τ_2 reflect the surface-mediated (fast) and intrinsic band-to-band (slow) relaxation of excited electrons, respectively (**Figure 3-29**). The average lifetime (τ_{av}) derived from this analysis was found to be 4.20 ns for 6-ZIS NCF, which longer than the fluorescent lifetime of mesoporous 4-ZIS (2.33 ns) and 12-ZIS (4.08 ns) NCFs and bulk ZIS (3.20 ns). This indicates a more efficient charge carrier migration and separation in 6-ZIS NCF mesoporous, in agreement with the above V_{OC} results. Typically, in nanostructures with very small grain sizes, the photogenerated electrons tend to preferentially transfer to the catalyst interface, actively participating in surface reactions rather than undergoing detrimental bulk recombination loss. The unexpected short-lived electron transfer (2.33 ns) of 4-ZIS NCF suggests the presence of additional pathways for fast electron-hole relaxations. This phenomenon can be attributed to the localized defect states introduced by sulfur vacancies (as was evidenced by EDS and PDF analyses), which have the ability to facilitate the trapping of photoexcited electrons, leading to swift transitions from sub-band

levels to the VB. Taking into consideration the above EIS results, this suggests that the presence of sulfur vacancies on the surface of 4-ZIS NCF diminishes electron accessibility at the catalyst interface by promoting the recombination of the photogenerated carrier rather than their separation. In accordance with this, a more cautious observation on the fast and slow decay time constants unveiled an interesting correlation between the NCs size and τ-components of PL decay data. In mesoporous ZIS consisting of smaller (4.5 nm) NCs, the majority of the photogenerated electrons are lost via surface and/or defect-mediated recombination ($\alpha_1 \sim 83.3$ %) due to the high defect trapping. On the other hand, as the NC size increases, the electron-hole transitions associated with surface defect states are overridden ($\alpha_1 \sim 36.4\%$ for 6-ZIS and $\alpha_1 \sim 20\%$ for 12-ZIS NCF), with band-edge relaxation emerging as the more prominent pathway for carrier recombination loss. The fitted TRPL parameters for the *n*-ZIS NCFs and bulk ZIS are summarized in **Table 3-5**.

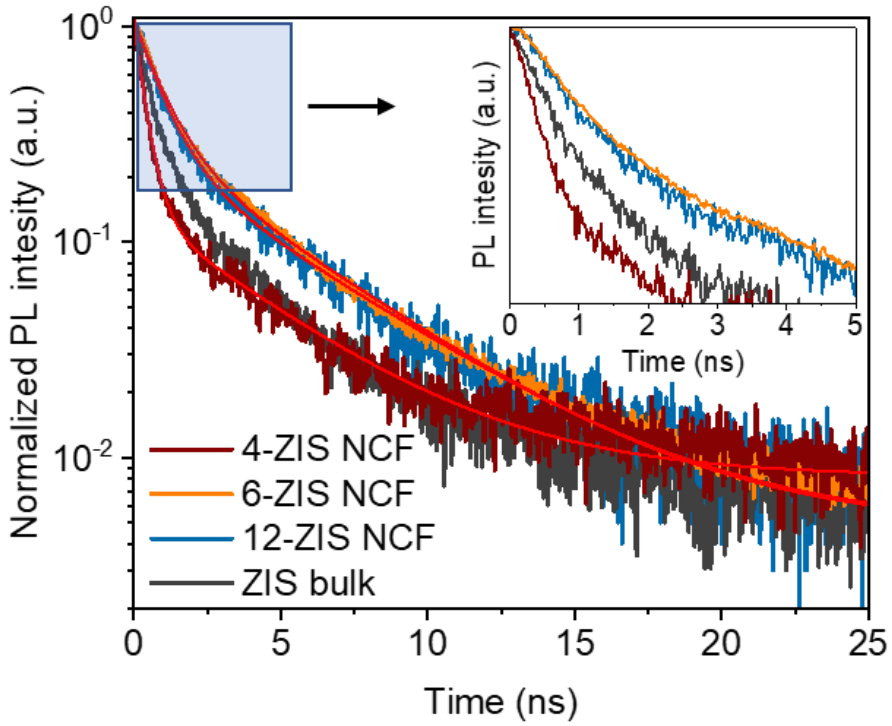

Figure 3-29. Time-resolved photoluminescence (TRPL) spectra under 375 nm pulsed laser excitation of mesoporous *n*-ZIS NCFs and bulk ZIS catalysts. Inset: magnified view of the PL decay spectra.

Table 3-5. Time-resolved photoluminescence decay parameters of mesoporous *n*-ZIS NCFs and bulk ZIS materials.

Sample	τ_1 (ns)	τ_2 (ns)	α_1 (%)	α_2 (%)	τ_{av}[a] (ns)
4-ZIS NCF	0.60	3.73	83.3	16.7	2.33
6-ZIS NCF	0.90	4.57	36.4	63.6	4.20
12-ZIS NCF	0.37	4.17	20.0	80.0	4.08
ZIS bulk	0.86	4.75	23.2	76.8	3.29

[a]The average lifetime (τ_{av}) was determined using the following equation: $\tau_{av} = (\sum_i \alpha_i \tau_i^2)/(\sum_i \alpha_i \tau_i)$ (i = 1, 2).

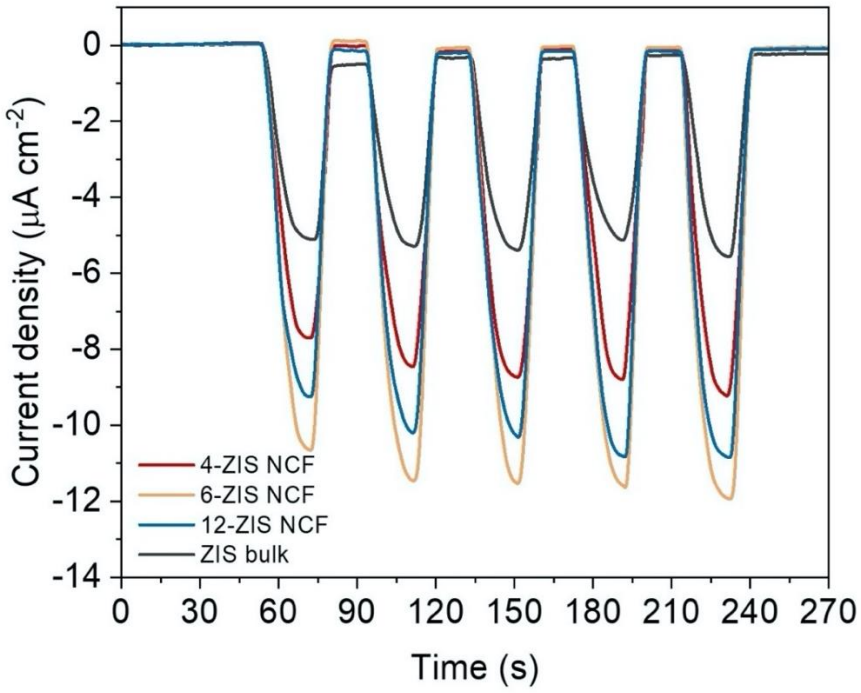

Figure 3-30. Transient photocurrent response at –1 V bias (vs. Ag/AgCl reference electrode) for the mesoporous *n*-ZIS NCFs and bulk ZIS under visible-light (420–720 nm) illumination.

The migration of the photogenerated carriers in mesoporous ZIS structures was further confirmed by transient photocurrent (TPC) experiments. The current-potential (J–V) curves were obtained using visible light (420–720 nm) illumination. The results showed that 6-ZIS NCF generates higher photocurrent (11.6 μA cm^{-2}) than the other mesoporous samples (8.4–10.2 μA cm^{-2}) and polycrystalline ZIS (5.2 μA cm^{-2}) (**Figure 3-30**), suggesting an efficient separation and interfacial transfer of the photoexcited carriers. Taken together, all the above results suggest that the photocurrent improvement and superior photocatalytic activity of the

n-ZIS NCFs family primarily result from the enhanced charge separation and transfer facilitated by the low dimensionality of the ZIS NC building blocks, rather than the increased photon absorption or beneficial effect of surface trap states. Clearly, these charge separation processes have significant implication for hydrogen evolution reaction as they facilitate the dissociation of charge carrier under light irradiation, enabling more electrons and holes to actively participate in electrochemical reactions at the catalyst's surface.

3.1.4 Conclusions

In this project, we present the synthesis of new mesoporous frameworks consisting of interconnected $ZnIn_2S_4$ nanocrystals with variable diameter (ranging from ~4 nm to ~12 nm) using a low-temperature colloidal synthetic method, followed by a polymer-templated self-assembly approach. To our knowledge this is the first example of porous thiospinel structures with tunable grain composition and large internal surface area (up to 207 $m^2\ g^{-1}$). Significantly, these ensemble structures provide a unique opportunity for studying the size effect on charge-transfer dynamics and catalytic performance in this system. Through comprehensive physicochemical and (photo)electrochemical investigations, we unveiled an understanding on the interplay between size-dependent electronic structure, interfacial charge transport and intrinsic photocatalytic activity in these porous materials. The results suggest that the size decrease of ZIS nanocrystal provides high interfacial charge-transfer kinetics, improving the ability of the photoexcited carriers to initiate water-splitting reaction. For ultrasmall nanocrystals (ca. 4.5 nm in size), the charge transfer and separation rates confirm the dominant effect of the surface sulfur vacancies on carrier recombination loss, which is a fundamental reason for depressed photocurrent and reduced photoactivity. Benefiting from proper charge transport and separation phenomena within the NCs, the mesoporous assembles made of 6-nm-sized ZIS NCs exhibit a remarkable photocatalytic performance towards the hydrogen evolution reaction, yielding a 7.8 mmol $g_{cat}^{-1}\ h^{-1}$ H_2-evolution rate and a photon-to-hydrogen conversion efficiency of 25.0 % at 375 and 17.2 % at 420 nm. The above findings highlight the importance of rational design of photocatalysts and provide fundamental insights into the charge-transfer dynamics and electronic properties of nanoscale catalysts for clean energy conversion applications. Moreover, the open-pore architecture of thiospinel nanostructures offers significant opportunities for surface modification, thereby expanding the synthesis of multi-component semiconductors with improved interfacial charge-carrier transport.

3.2 Mesoporous Catalysts of Hexagonal $CdIn_2S_4$ Nanocrystals Decorated with Ni_2P Nanosheets

3.2.1 Synthesis, phase structure and morphology

The synthetic process for obtaining mesoporous networks of linked $CdIn_2S_4$ nanocrystals is depicted in **Figure 3-31**. Initially, fairly monodisperse thiol-capped $CdIn_2S_4$ nanocrystals (denoted as CIS NCs) were obtained through a one-pot reflux reaction of Cd^{2+} and In^{3+} nitrates (in 1:2 molar ratio) and thioacetamide as sulfur source. To achieve kinetic control over the formation of CIS NCs, a thiol-terminated ligand (3-mercaptopropionic acid) was used as a capping agent. The use of the 3-mercaptopropionic acid is essential for impending crystal growth and effectively stabilizing the colloidal nanoparticles in polar solvents. This synthetic approach provides precise control over the grain size of the resultant CIS NCs, allowing the particle size to be adjusted simply by modifying the reaction time. Small-angle X-ray scattering (SAXS) analysis of the CIS NCs obtained after 6 and 12 hours of growing time revealed mean Guinier diameters of approximately 6 nm and 11 nm, respectively. (**Figure 3-32**).

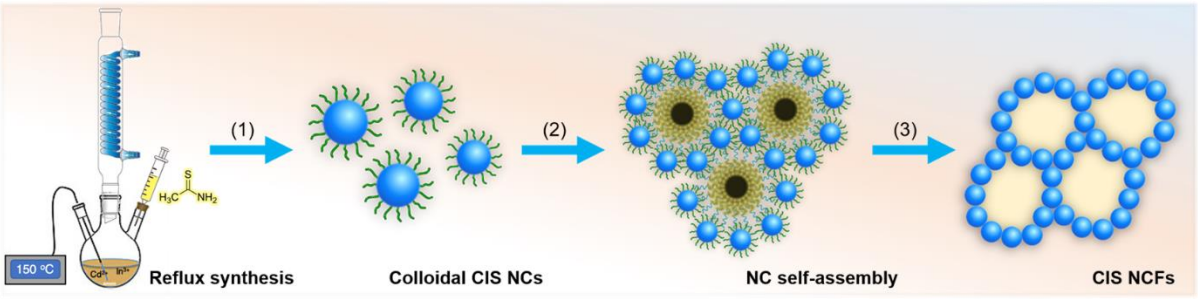

Figure 3-31. Schematic illustration of the synthesis of CIS NC-linked frameworks (NCFs) (step 1: reflux synthesis of thiol-capped CIS NCs; step 2: polymer-templated NC self-assembly; step 3: template removal toward open-pore structures).

After obtaining the CIS NCs, they were utilized as building block units to assemble three-dimensional (3D) polymeric networks thought a surfactant-directed coupling method. Briefly, this method involves the self-assembly and slow oxidative polymerization of thiol-capped CIS NCs in the presence of the commercially available polyoxyethylene-*block*-cetyl ether (Pluronic Brij-58) copolymer as a structure-directing agent. A small addition of H_2O_2 (3% v/v) into the mixture of polymer/CIS NCs was employed to induce the formation of extended mesostructures through cross-linking the thiospinel NCs via S–S bonding [33,35,152]. The removal of the polymer template from the pores of the hybrid mesostructures was accomplished

using a water/isopropyl alcohol (1:1 v/v) solution, resulting in the formation of mesoporous CIS NC-linked frameworks (denoted as CIS (*n*) NCFs, where *n* represents the particle size (nm) of starting NCs). This post-treatment method is quite effective in removing the organic molecules and thermogravimetric analysis (TGA) indicated that only ~9–9.5 wt. % of organic residual remains in the porous structure (**Figure 3-33**). The TGA profiles of the mesoporous products exhibited a weight loss bellow 230 ^{o}C due to the liberation of solvent and a gradual weight loss within the range of 230–425 ^{o}C due to the decomposition of the organic molecules remaining in the porous structure.

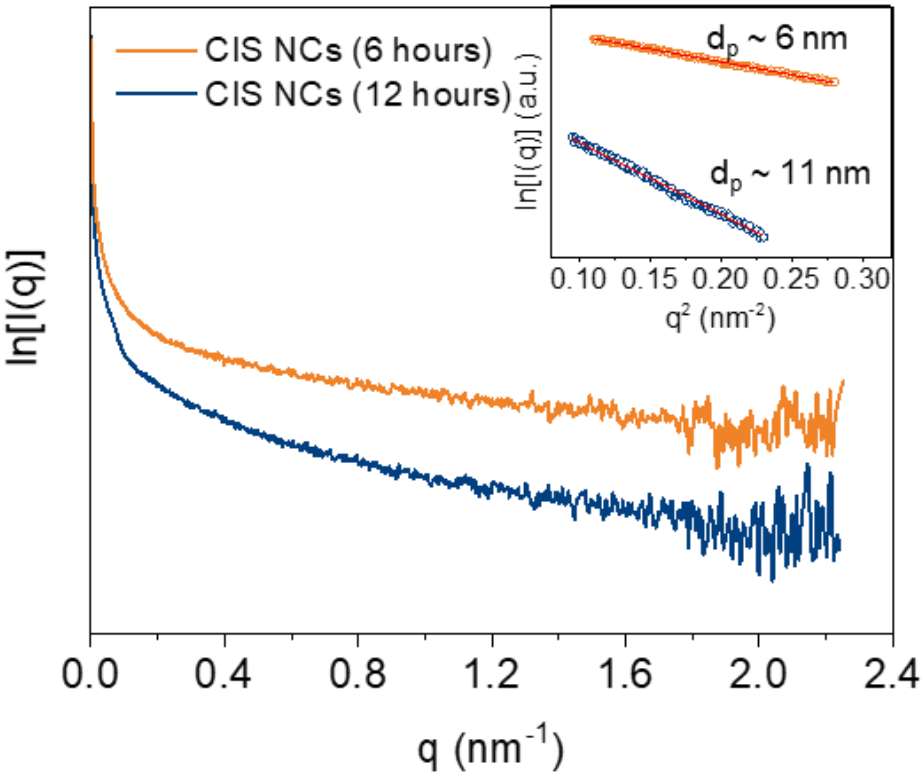

Figure 3-32. SAXS pattens and Guinier plots [$I(q) \propto -q^2R_g^2/3$, where q is the scattering vector and R_g is the radius of gyration] (inset) of the as-synthesized CIS NCs obtained after 6 hours (orange) and 12 hours (blue) of growing time. The Guinier analysis for the two different colloidal NCs yields an average particle size (d_p) of ~6 nm and ~11 nm.

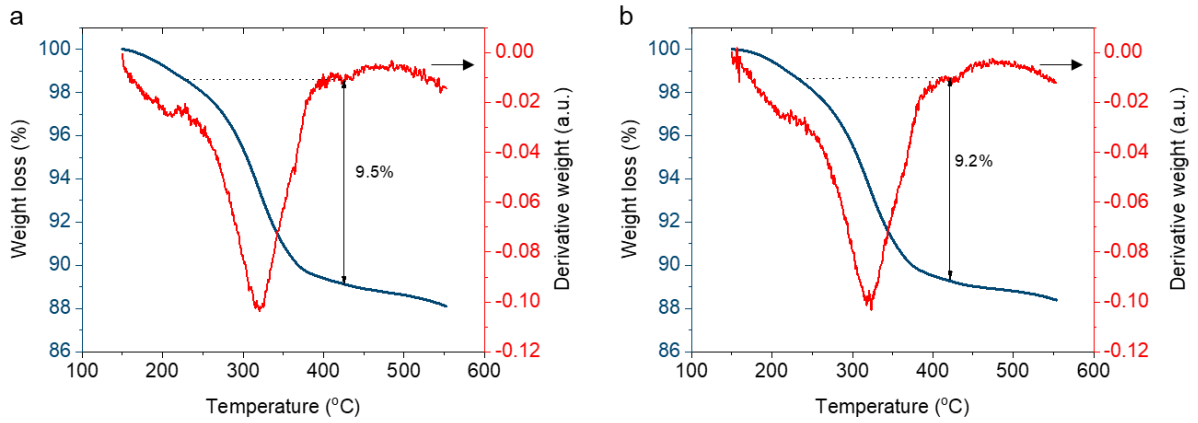

Figure 3-33. TGA profiles (blue lines) of the post-treated mesoporous CIS NCFs consisting of NCs building blocks of (a) 6 nm and (b) 11 nm size. The differential thermogravimetric (DTG) curves (red lines), highlight the weight loss from the decomposition of the organic molecules in the mesostructure.

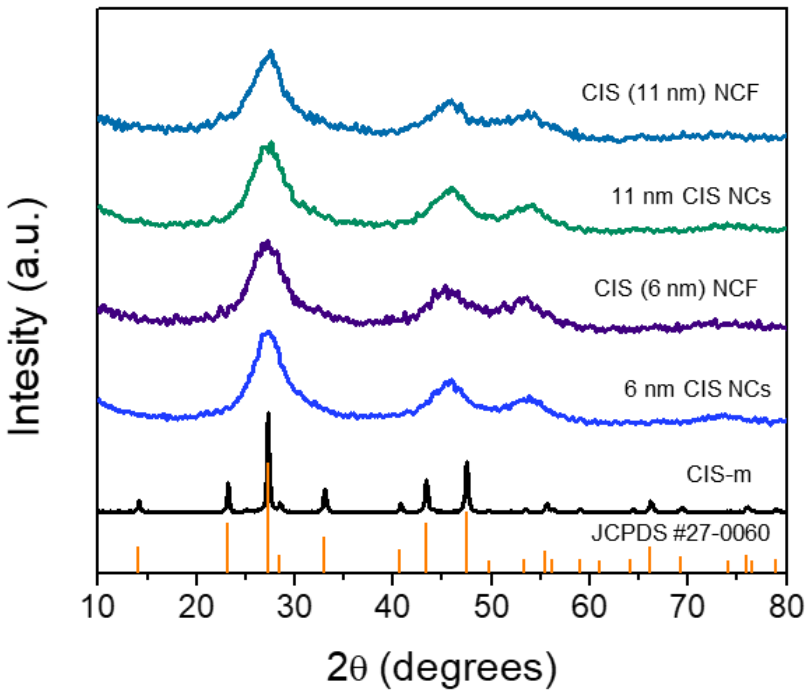

Figure 3-34. XRD patterns of the resulting 6 and 11-nm CIS NCs along with their mesoporous materials. The XRD pattern of the polycrystalline bulk CIS and the standard X-ray diffraction pattern of cubic $CdIn_2S_4$ (JCPDs card no. 27-0060) are also given.

The X-ray diffraction (XRD) patterns of the as-prepared NCs and mesoporous CIS NCFs materials are shown in **Figure 3-34**. The XRD profiles of the samples display three wide Bragg reflections in 2θ scattering angle range of 20–60°, highlighting the existence of very small

crystallite sizes. For comparative studies, a polycrystalline bulk CIS material (denotes as CIS-*m*) was also prepared through a hydrothermal method. The XRD pattern of bulk CIS shows several diffraction peaks that are readily assigned to the cubic crystal phase (Fd3m) of $CdIn_2S_4$ (JCPDs card no. 27-0060). However, due to the broadening of the XRD peaks makes it difficult to conclusively determine the crystal phase of the CIS NCs. To this end, the local atomic structure of CIS NCs was investigated by X-ray total scattering measurements and pair distribution function (PDF) analysis. This method is sensitive to the distribution of interatomic distances and can provide information about the atomic configuration in well-defined structures, such as the CIS nanoparticles [144]. The PDF plots as a function of interatomic distances for the 6-nm CIS NCs and bulk CIS material are depicted in **Figure 3-35**. While preserving the chemical integrity and atomic displacement parameters of appropriate atomic structural models, the calculated PDF plots were refined until they matched the experimental data. Concerning the polycrystalline CIS, the modeled PDF plot is well consistent with the face-centered cubic (*fcc*) structure of $CdIn_2S_4$ (Fd3m) with unit cell parameters $\alpha = 10.805(8)$ Å. Particularly, the PDF plot of bulk CIS shows three intense interatomic vectors at ~2.6, ~3.8 and ~4.5 Å, which can be assigned to the M–S (M = Cd/In) bonds, and In···In and Cd···In next nearest-neighbor distances of the cubic $CdIn_2S_4$, respectively. Compared to bulk CIS, the PDF profile of CIS NCs is very different, indicating a distinct atomic configuration. By using the *fcc* model refinement to describe the positions and relative intensities of the PDF peaks of CIS NCs, the PDF fit shows unsatisfactory agreement across the entire range of 2–10 Å (**Figure 3-36**). Therefore, there is an imminent need to elucidate the atomic structure of CIS NCs using an alternative structural model. The thiospinel materials, apart from the cubic phase, exhibit an additional polymorphic phase, the hexagonal close-packed (*hcp*) structure. While $CdIn_2S_4$ has been experimentally identified in the cubic crystal phase, $ZnIn_2S_4$ thiospinel exhibits both cubic and hexagonal ($P6_3mc$) polymorphs. Here, our *hcp* structural model was derived from the known crystallographic data of hexagonal $ZnIn_2S_4$, in which Zn atoms were substituted by Cd atoms. As can be observed in **Figure 3-37**, the calculated PDF of the hexagonal $ZnIn_2S_4$ closely resembles that of CIS NCs, suggesting a similar atomic structure [153].

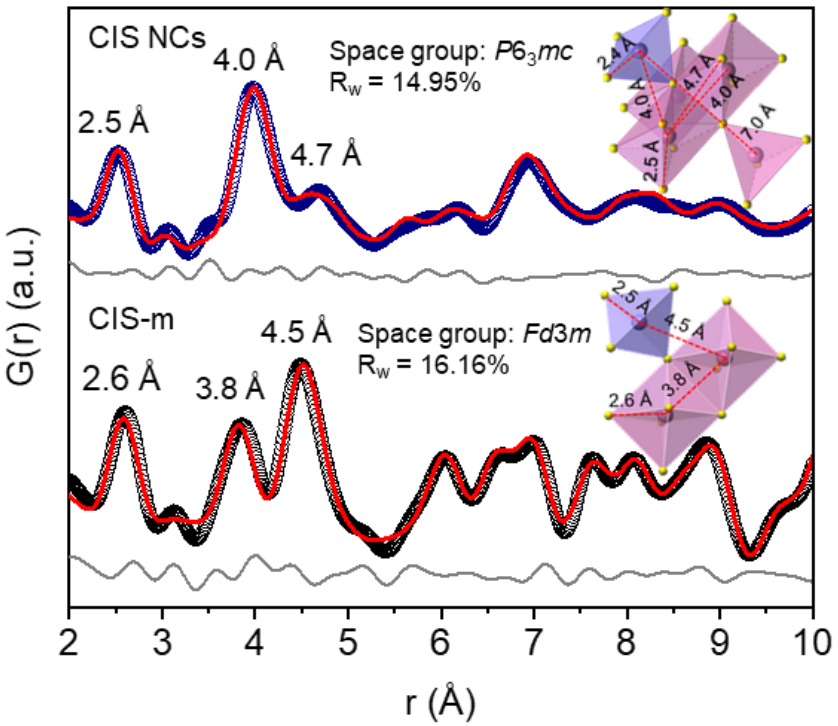

Figure 3-35. Reduced atomic pair distribution functions G(r) of the 6-nm sized CIS NCs and polycrystalline bulk CIS.

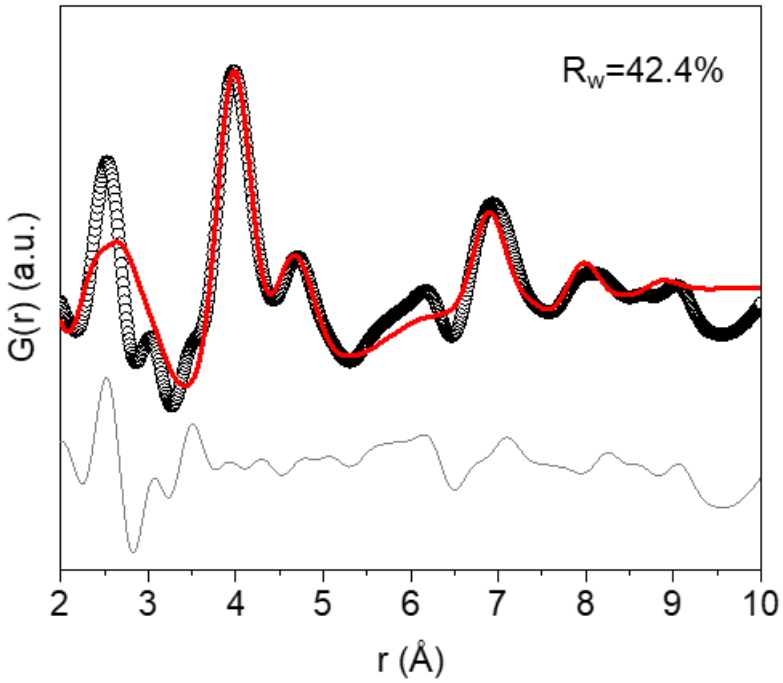

Figure 3-36. Real-space refinement of the PDF plot of CIS NCs (6 nm), using a face-centered cubic (*fcc*) model (space group, Fd3m). The corresponding black symbols are the experimental data, the red line is the simulated PDF, and the bottom gray line is the fit residual. The *fcc* model refinement does not correctly describe all positions and relative intensities of the PDF peaks.

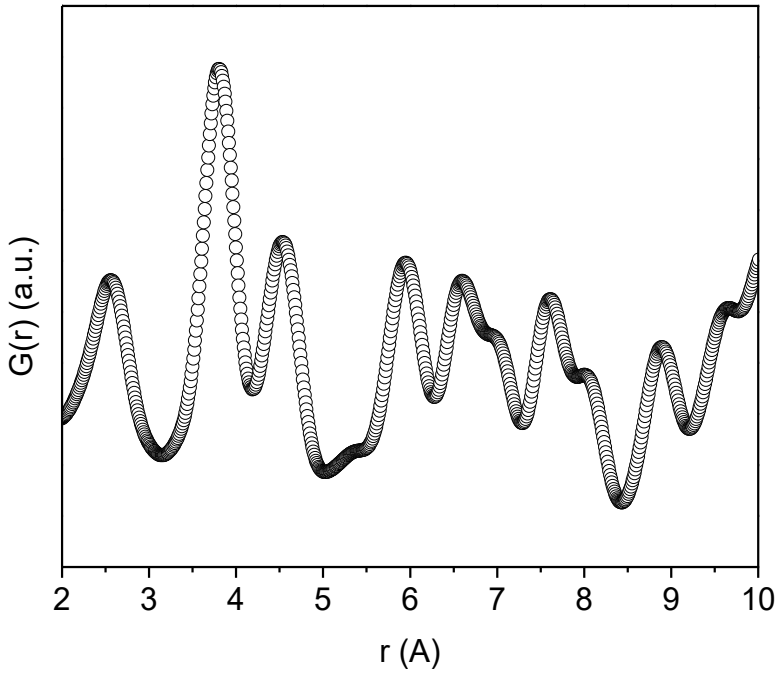

Figure 3-37. Calculated PDF plot of the hexagonal $ZnIn_2S_4$ (space group $P6_3mc$).

Interestingly, the *hcp* model produced excellent results, effectively capturing the structural characteristics of 6-nm CIS NCs. Specifically, the interatomic vector at ~2.5 Å corresponds to the M–S (M = Cd/In) bonds, while those at ~4.0 and ~4.7 Å arise from the M···M and Cd···In next-nearest distances of the hexagonal CIS (**Figure 3-35**). The unit cell parameters obtained from the PDF refinement were a = b = 3.976(9) Å and c = 20.281(0) Å. As for the larger (11 nm) CIS NCs, the PDF refinement (using a *hcp* structural model) yielded unit cell parameters of a = b = 3.968(5) Å and c = 20.615(8) Å (**Figure 3-38**). It should be stressed that these structural models describe the average structural arrangements and do account for potentially defective lattice sites and locally disordered structural domains (as likely reflected by the fast damping of the PDF peaks at r > 8 Å distances).

To get further insight into the atomic structure of CIS, we conducted comparative analysis between the theoretical I(q) versus scattering wavevector ($q = 2\pi \cdot \sin\theta/\lambda$, where 2θ is the scattering angle) patterns derived from the refined structural models with the experimental XRD data of 6-nm NCs obtained using Mo Kα (λ = 0.7107 Å) radiation. As can be seen in **Figure 3-39**, all X-ray reflections of 6-nm NCs can be indexed to the hexagonal CIS crystal structure ($P6_3mc$), validating the credibility of the above analysis. In particular, the XRD pattern shows a broad peak at ~1.93 $Å^{-1}$ scattering vector, which can be assigned to either the $\bar{1}13$ cubic (Fd3m) reflection or the (006) and (013) overlapped hexagonal ($P6_3mc$) reflections

of CIS. Nevertheless, the distinct Bragg peaks at ~3.16 $Å^{-1}$ and ~3.67 $Å^{-1}$ scattering vectors clearly correspond to the (110) and (116) reflections of the hexagonal CIS.

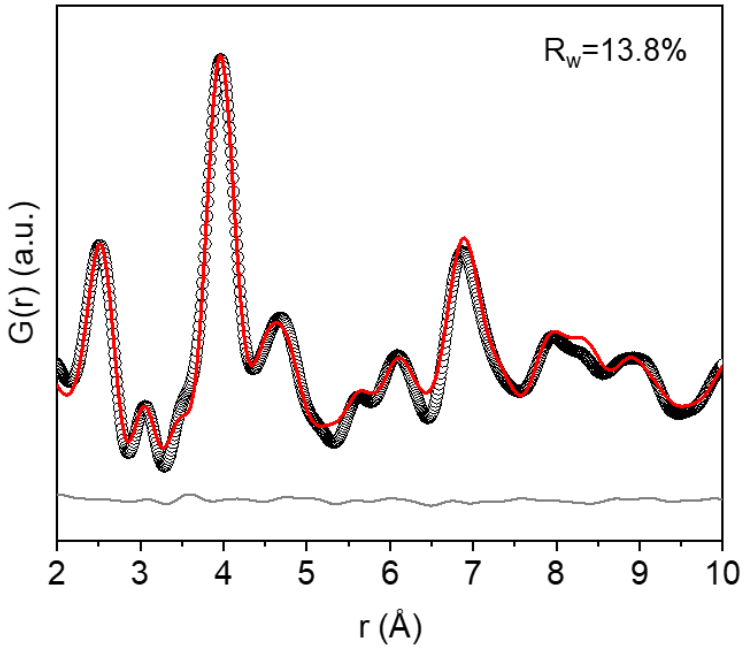

Figure 3-38. PDF refinement of 11-nm size CIS NCs using an *hcp* structure model. The back symbols are the experimental data, the red line is the simulated PDF and the bottom gray line is the fit residual.

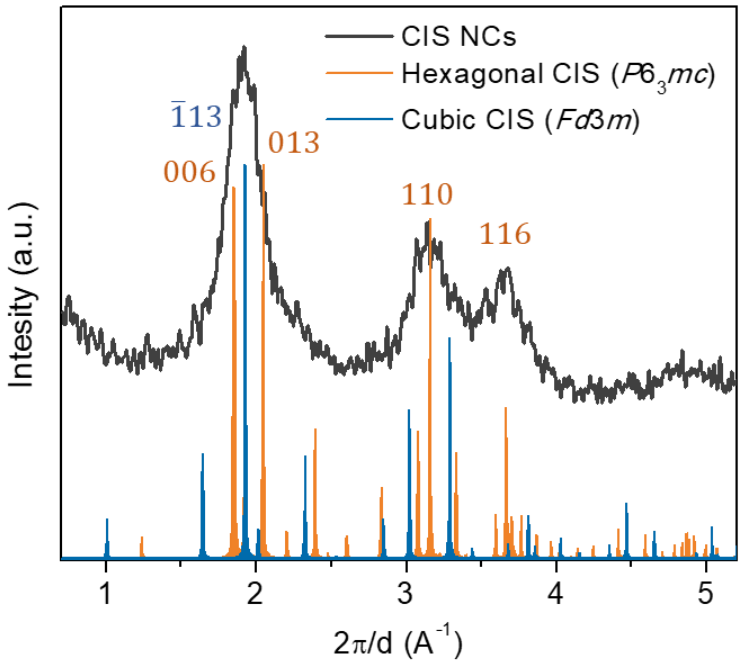

Figure 3-39. X-ray diffraction intensity versus scattering wave vector (q) of 6-nm CIS NCs. The orange and blue lines depict the simulated XRD patterns obtained from the refined hexagonal ($P6_3mc$) and cubic (Fd3m) structural models, respectively.

The coordination geometry of metal ions in CIS NCs and bulk CIS crystal lattice was also investigated by Raman spectroscopy (**Figure 3-40**). For bulk CIS, the Raman shifts in the 215–235 cm^{-1} region and at ~346 cm^{-1} are attributed to the breathing vibrations of the [CdS_4] and [InS_6] edge-sharing polyhedral of the cubic $CdIn_2S_4$, in agreement with previous $ZnIn_2S_4$ and $CdIn_2S_4$ Raman investigations [154–156]. On the contrary, the Raman spectrum of CIS NCs exhibited distinct characteristics, with pronounced shifts at ~219 cm^{-1} and 300–340 cm^{-1} region; these shifts can be assigned to the vibrational modes of the four-fold coordinated [Cd/InS_4] tetrahedral geometry (T_d) and six-fold coordinated [InS_6] octahedral geometry (O_h), respectively. Remarkably, this Raman signature closely resemble that of hexagonal $ZnIn_2S_4$ [68]. Overall, these spectroscopic changes serve as a distinctive fingerprint indicating the presence of mixed In T_d and O_h symmetries in CIS NCs, as collaborated by the PDF structural refinements described above. Thus, it is strongly suggested that the CIS NCs indeed exhibit a hexagonal spinel structure, which to our knowledge is the first example of hexagonal $CdIn_2S_4$ phase being reported so far. This crystal polymorph of $CdIn_2S_4$ has only been predicted theoretically, primarily for its intriguing electronic properties [157].

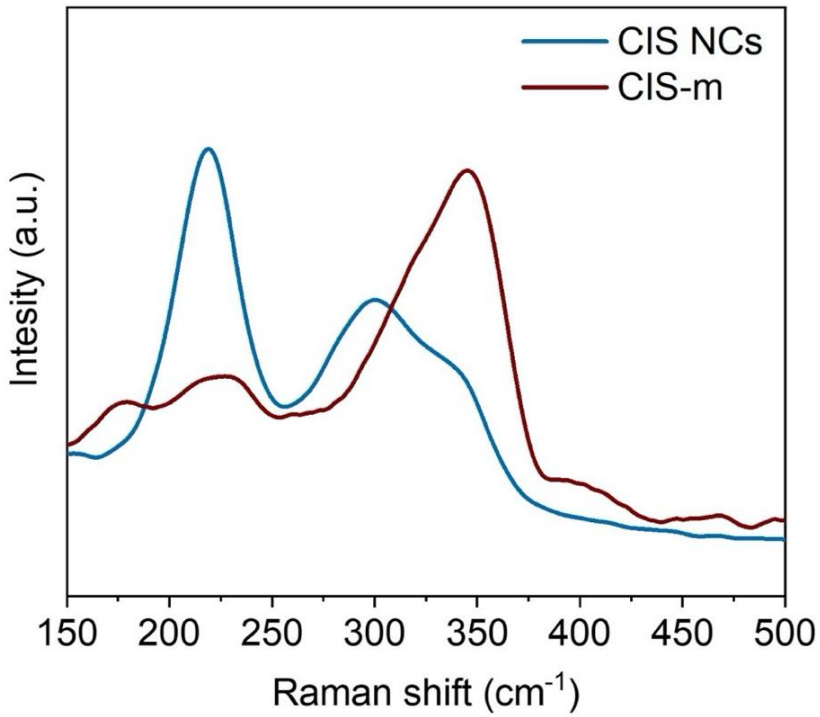

Figure 3-40. Raman spectra of 6 nm CIS NCs and bulk CIS.

After annealing the 6-nm CIS NCs at various temperatures, the X-ray total scattering data of these samples revealed intriguing findings. (**Figure 3-41a**). It appears that the crystal structure of CIS NCs undergoes a phase transition from hexagonal to cubic spinel phase at

elevated temperature. The simulation results unveiled a gradual decrease in the c/a ratio from 5.10 to 5.05 and further to 4.99 as the temperature increases from 25 to 200 °C. This suggests a progressive transformation of the thiospinel structure. Additionally, the PDF refinements yielded an inward distortion of the [InS_4] polyhedral, leading to a reduction in the In–S bond lengths from ~2.341 Å (25 °C) to 2.329 (200 °C) (**Figure 3-41b**). At a heating temperature of 250 °C, the resulting PDF plot is identical to that of the bulk CIS, suggesting similar atomic configuration. Hence, this sample was effectivelly fitted using the *fcc* model, yielding a calculated lattice parameter of α = 10.849(8) Å. Furthermore, we observed that with increasing annealing temperature, the intensity of PDF peaks at larger interatomic distances also increases. This phenomenon occurs due to the expansion of the scattering domain size upon heating. The results of PDF refinements with different structural models are listed in **Table 3-6**.

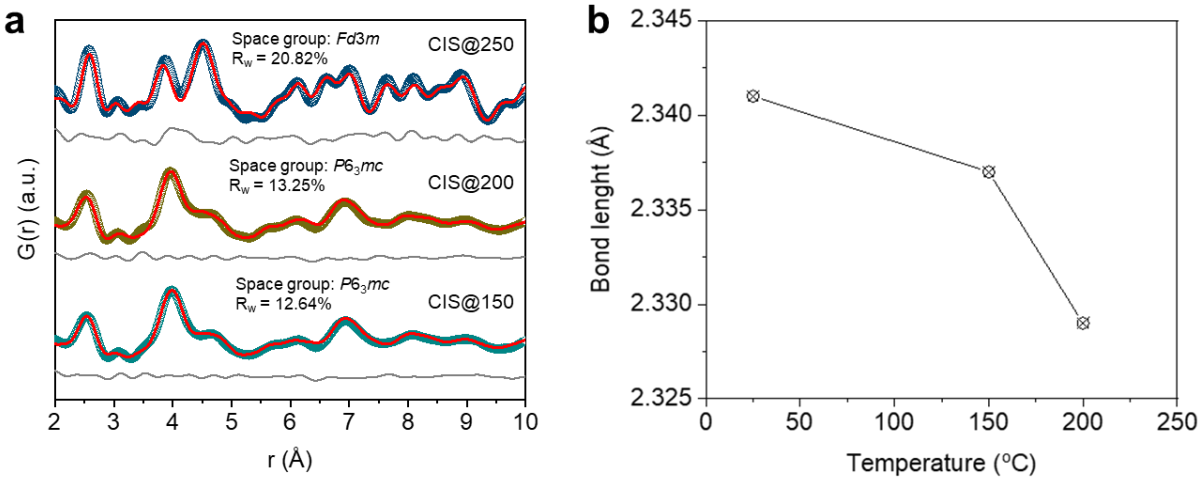

Figure 3-41. (a) G(r) plots of the 6-nm CIS NCs annealed at various temperatures. The back symbols are the experimental data, the red line is the simulated PDF and the bottom gray line is the fit residual. (b) Mean In–S bond length of [InS_4] tetrahedral units versus heating temperature of 6-nm CIS NCs obtained from PDF analysis using the *hcp* structural model.

To provide further support for the phase transition of CIS NCs, we conducted differential scanning calorimetry (DSC) measurements. (**Figure 3-42a**). The DSC profile of the 6-nm CIS NCs showed a broad endothermic peak around 200–250 °C, which corresponds to the phase transition from the hexagonal to the cubic crystal phase, in agreement with previous studies on hexagonal Mn, Fe and Co-based thioindicates [158]. Moreover, the XRD patterns of the annealed samples further confirm this phase transition. As can be seen in **Figure 3-42b**, the crystallinity of CIS NCs is retained until 200 °C, displaying the characteristic broad reflections of hexagonal $CdIn_2S_4$. In stark contrast, the sample annealed at 250 °C exhibited a distinct XRD

profile, which can be readily assigned to the cubic phase of $CdIn_2S_4$ (Fd3m, JCPDs card no. 27-0060).

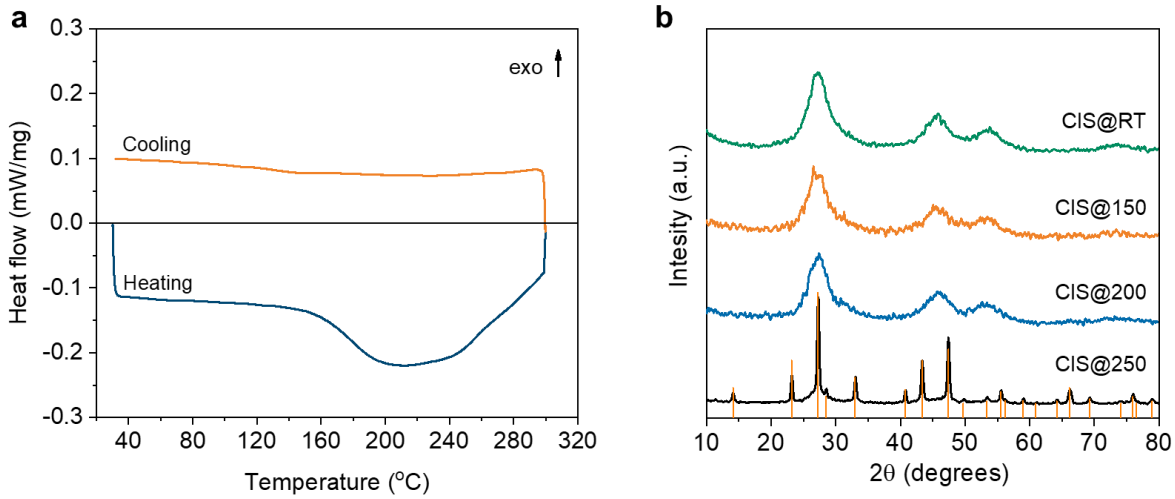

Figure 3-42. (a) DSC profile of 6-nm CIS NCs using heating and cooling rate of 5 °C min^{-1}. (b) XRD patterns of 6-nm CIS NCs annealed at various temperatures (from 25 to 250 °C).

Table 3-6. PDF refinement results for bulk CIS and CIS NCs annealed at various temperatures.

Sample Name	**CIS NCs (11 nm)**	**CIS NCs (6 nm)**	**CIS NCs@150C**	**CIS NCs@200C**	**CIS NCs@250C**	**CIS-*m***
Sample Temp.	RT	RT	150 °C	200 °C	250 °C	RT
Space group	*P*6$_3$*mc*	*P*6$_3$*mc*	*P*6$_3$*mc*	*P*6$_3$*mc*	*Fd*3*m*	*Fd*3*m*
Lattice constants						
a (Å)	3.9685	3.9769	3.9933	3.9970	10.8498	10.8058
b (Å)	3.9685	3.9769	3.9933	3.9970	10.8498	10.8058
c (Å)	20.6158	20.2810	20.1771	19.9258	10.8498	10.8058
α (°)	90	90	90	90	90	90
β (°)	90	90	90	90	90	90
γ (°)	120	120	120	120	90	90
Atomic positions and thermal parameter						
Cd01						
x	0.0	0.0	0.0	0.0	0.0	0.0
y	0.0	0.0	0.0	0.0	0.0	0.0
z	0.4335	0.4204	0.4144	0.4074	0.0	0.0
U_{Cd01} (eqv)	0.0014	0.0134	0.0049	0.0084	0.0751	0.0344
In01						
x	0.3333	0.3333	0.3333	0.3333	0.6250	0.6250
y	0.6667	0.6667	0.6667	0.6666	0.6250	0.6250
z	0.0961	0.0943	0.0953	0.0931	0.6250	0.6250
U_{In01} (eqv)	0.0664	0.0566	0.0725	0.0427	0.0198	0.0201
In02						
x	0.3333	0.3333	0.3333	0.3333	-	-
y	0.6667	0.6667	0.6667	0.6666	-	-
z	0.7539	0.7569	0.7561	0.7566	-	-
U_{In02} (eqv)	0.0664	0.0566	0.0725	0.0427	-	-
S01						
x	0.3333	0.3333	0.3333	0.3333	0.3868	0.3834
y	0.6667	0.6667	0.6667	0.6666	0.3868	0.3834

z	0.9520	0.9489	0.9646	0.9641	0.3868	0.3834
U_{S01} (eqv)	0.0209	0.0305	0.0641	0.0310	0.0004	0.0096
S02						
x	0.0	0.0	0.0	0.0	-	-
y	0.0	0.0	0.0	0.0	-	-
z	0.0446	0.0470	0.0433	0.0671	-	-
U_{S02} (eqv)	0.0209	0.0305	0.0641	0.0310	-	-
S03						
x	0.3333	0.3333	0.3333	0.3333	-	-
y	0.6667	0.6667	0.6667	0.6666	-	-
z	0.2017	0.1977	0.2037	0.2006	-	-
U_{S03} (eqv)	0.0209	0.0305	0.0641	0.0310	-	-
S04						
x	0.0	0.0	0.0	0.0	-	-
y	0.0	0.0	0.0	0.0	-	-
z	0.3138	0.3138	0.3068	0.3149	-	-
U_{S04} (eqv)	0.0209	0.0305	0.0641	0.0310	-	-
R_w (%)	13.76	14.95	12.64	13.25	20.82	16.16

To improve the photocatalytic efficiency of CIS NCFs, we modified the CIS mesostructure (made of 6-nm sized CIS NCs) with Ni_2P nanosheets via a straightforward wet chemical process. The high charge carrier mobility and electron withdrawal ability of Ni_2P (its Fermi level lies at 4.8–4.9 eV) can synergistically enhance the photocatalytic activity of CIS NCFs [159]. The coupling of Ni_2P and CIS semiconductors to form heterojunctions may provide multiple electron transfer pathways across the Ni_2P/CIS heterointerface, which are anticipated to enhance the separation and migration efficiency of charge carriers to the surface. The Ni_2P content on the Ni_2P/CIS heterostructures was determined via energy dispersive X-ray spectroscopy (EDS). On the basis of Ni/Cd atomic ratio, the Ni_2P weight loading was found to be approximately 5, 10, 15 and 20 wt. %, which is very close to the nominal compositions (within ~8% deviation). Furthermore, the atomic ratios of Cd/In/S in all samples were found to be ~1:2:4, indicating that stoichiometric $CdIn_2S_4$ was synthesized (**Table 3-7**, **Figure 3-43**).

Table 3-7. Elemental composition of CIS and Ni_2P/CIS materials.

Sample	**Cd (at. %)**	**In (at. %)**	**S (at. %)**	**Ni (at. %)**	**P (at. %)**	**Ni_2P content (wt. %)**
CIS (6 nm) NCF	14.1	27.9	58.0	-	-	-
CIS (11 nm) NCF	14.4	29.1	56.5	-	-	-
5-Ni_2P/CIS NCF	11.3	22.7	57.8	3.9	4.3	5.06
10-Ni_2P/CIS NCF	10.9	21.8	53.8	7.2	6.3	9.45
15-Ni_2P/CIS NCF	10.5	21.1	43.9	11.5	13.0	14.75
20-Ni_2P/CIS NCF	9.3	18.7	40.0	14.8	17.2	19.98
15-Ni_2P/CIS-*m*	11.4	22.8	47.0	12.8	6.0	15.07
CIS-*m*	13.8	27.5	58.7	-	-	-

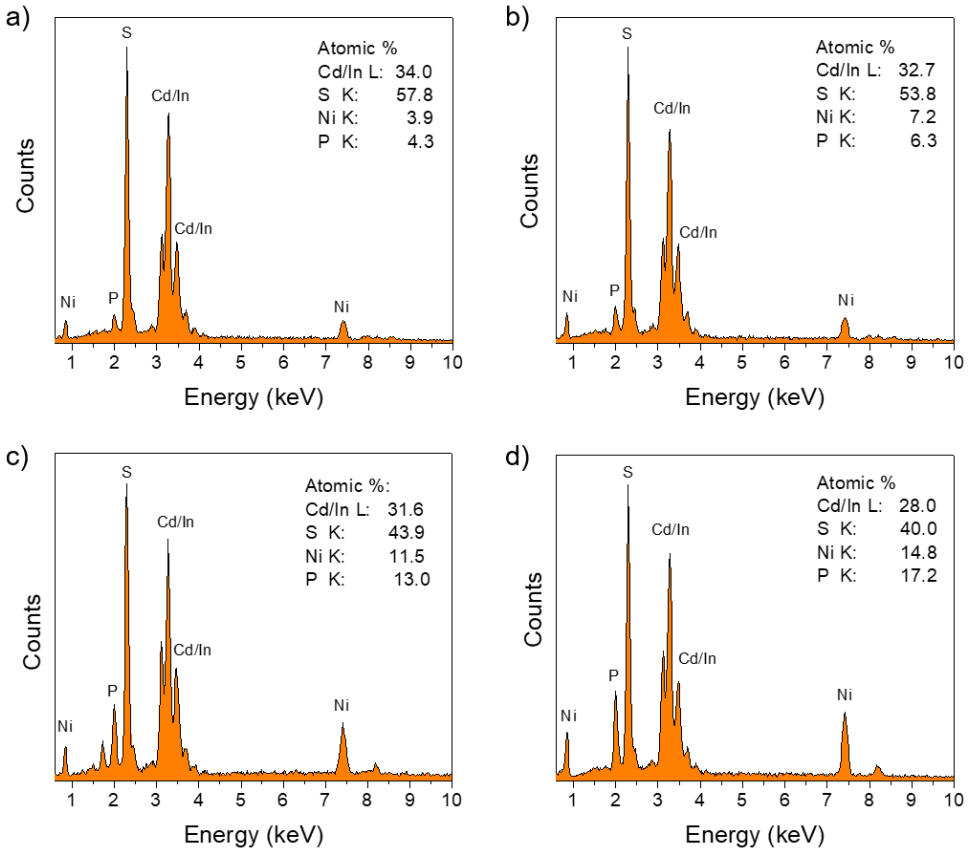

Figure 3-43. Typical EDS spectra of mesoporous assemblies of Ni_2P/CIS NCFs with (a) 5, (b) 10, (c) 15 and (d) 20 wt. % Ni_2P content.

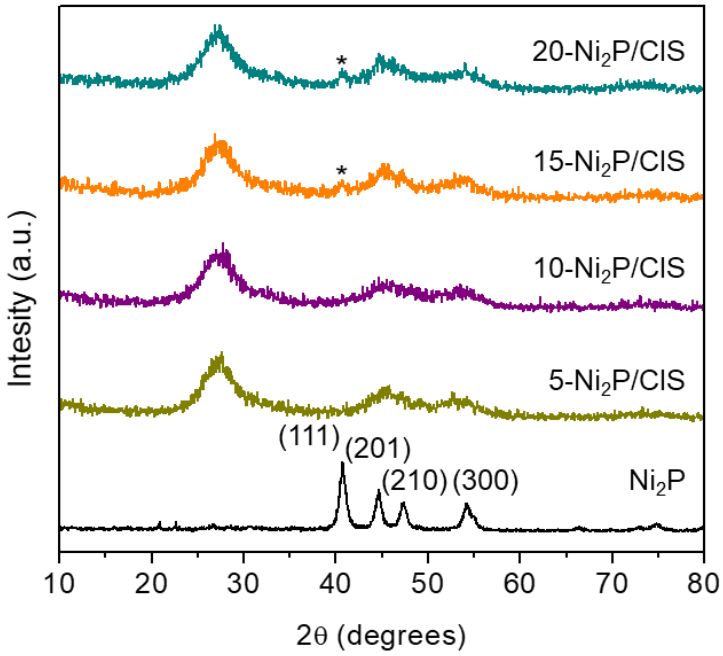

Figure 3-44. X-ray diffraction patterns of different mesoporous Ni_2P/CIS NCFs and Ni_2P nanosheets. The indexing of the diffraction peaks of Ni_2P nanosheets was performed using the standard JCPDS file of Ni_2P (card no. 74-1385).

The X-ray diffraction (XRD) patterns of Ni_2P/CIS NCFs exhibited the broad characteristic reflections of the CIS host matrix, along with an additional weak yet well-resolved diffraction peak at ~ 40.7°. This peak, which becomes more pronounced in samples with higher Ni_2P content, corresponds to the (111) diffraction of the hexagonal Ni_2P (space group $P\bar{6}2m$, JCPDS card no. 74-1385) (**Figure 3-44**).

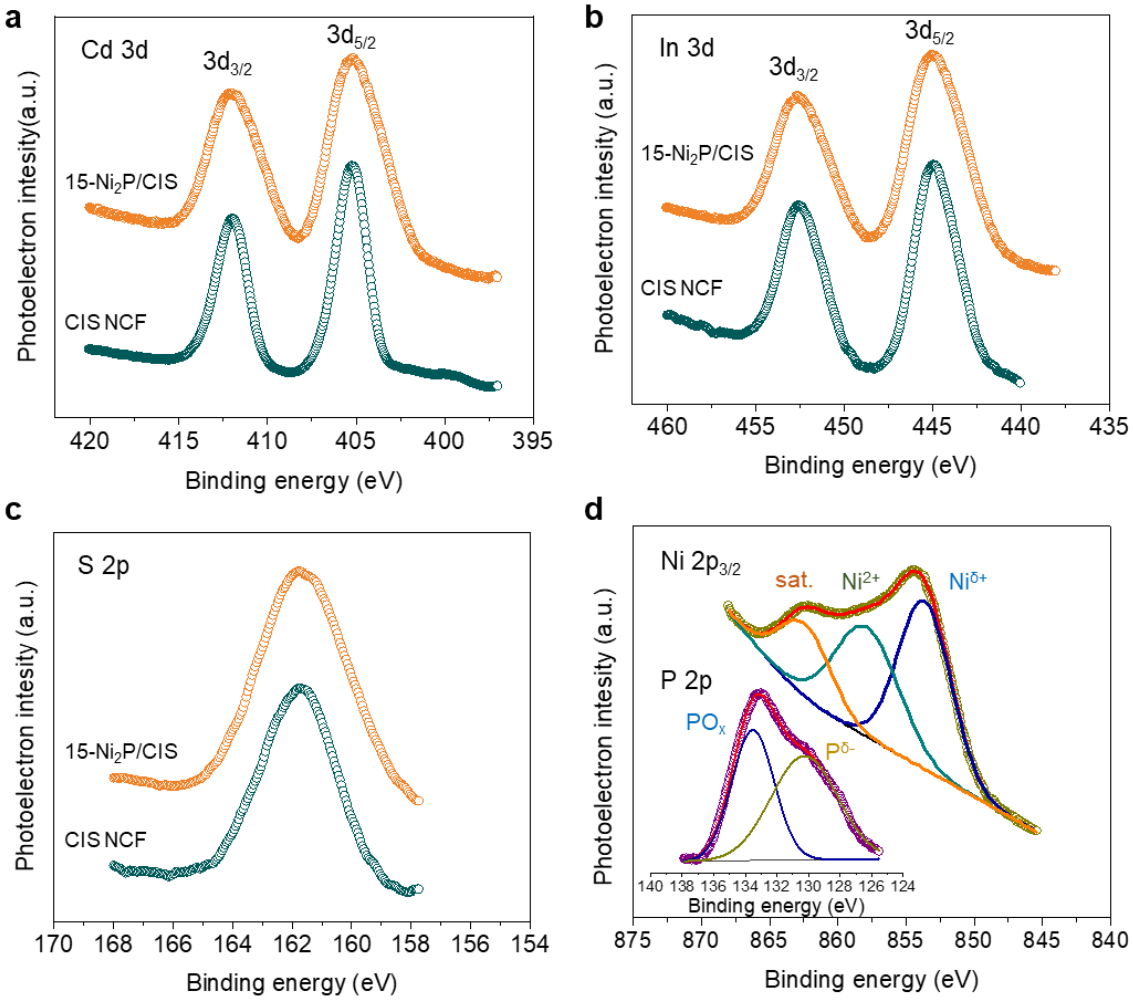

Figure 3-45. (a) Cd 3d, (b) In 3d and (c) S 2p XPS spectra of mesoporous CIS (made of 6-nm CIS NCs) and 15-Ni_2P/CIS (15 wt. % Ni_2P loading) NCFs. (d) Ni $2p_{3/2}$ and P 2p XPS core-level spectra of 15-Ni_2P/CIS NCF material. The XPS deconvoluted spectra of the different chemical state of elements are displayed as blue, green, orange, and yellow lines. The red lines are fit to the experimental data.

The chemical state of elements in the pristine CIS and 15% Ni_2P-modified CIS (15-Ni_2P/CIS) NCFs was investigated by X-ray photoelectron spectroscopy (XPS) (**Figure 3-45**). In particular, the Cd 3d XPS spectrum of mesoporous CIS (6 nm) NCF showed a spin-orbit

doublet at 405.3 and 412.1 ± 0.1 eV due to the Cd $3d_{5/2}$ and Cd $3d_{3/2}$ core-levels of Cd^{2+} ions [87]. In the In 3d core-level spectrum, the peaks at 444.8 and 452.5 ± 0.1 eV are attributed to the In $3d_{5/2}$ and In $3d_{3/2}$ peaks of In^{3+} ions [160]. The S 2p spectrum exhibited a prominent peak at 161.7 ± 0.2 eV, corresponding to the S^{2-} valence state [161]. For the 15-Ni_2P/CIS NCF sample, the Cd 3d spectrum showed a double peak at 405.1 and 411.9 ± 0.1 eV, assigned to the Cd $3d_{5/2}$ and Cd $3d_{3/2}$ core-levels of Cd^{2+} ions. In the In 3d XPS spectrum, the peaks at 444.7 and 452.4 ± 0.1 eV are attributed to the In $3d_{5/2}$ and In $3d_{3/2}$ of In^{3+} oxidation state. The prominent peak of the S 2p spectrum at 161.6 ± 0.2 eV is due to the metal sulfide phase in CIS. Regarding the Ni_2P chemical state, the Ni $2p_{3/2}$ XPS spectrum showed a peak at 853.6 ± 0.2 eV, which is assigned to the partially charged $Ni^{\delta+}$ ($0 < \delta < 2$) in Ni_2P, and a peak at 857.9 ± 0.2 eV along with the satellite feature at 862.4 ± 0.2 eV, which is assigned to the oxidized Ni species on the surface of catalyst (most likely as Ni–OH/PO_x species) [162]. The peak at 130.3 ± 0.1 eV and the broad signal at 133.5 ± 0.2 eV in the P 2p core-level spectrum correspond respectively to the slightly negatively charged $P^{\delta-}$ atoms in the Ni_2P structure and the oxidized species (PO_x) at the surface of the catalysts, possibly due to air exposure [163]. Also, XPS quantitively analysis indicated Cd/In/S atomic ratios of ~1:2:3.8 for the mesoporous CIS (6 nm) NCF and ~1.1:2:3.9 for the 15-Ni_2P/CIS NCF, which is in good agreement with the previous EDS results (**Table 3-7**). Moreover, from the In $3d_{5/2}$ and Ni $2p_{3/2}$ spectra, the surface weight content of Ni_2P was determined to be ~14.7%.

The morphology of the mesoporous CIS and 15-Ni_2P/CIS NCFs was examined with field-emission scanning electron microscopy (FESEM). Both materials consist of fairly monodisperse nanoparticles with diameters of approximately 5–10 nm (**Figure 3-46a-b**), which are interconnected to form a 3D porous network (**Figure 3-49a**). The grain size of mesoporous CIS is significantly smaller than that of bulk CIS, which comprises microparticles with diameters ranging from 8 to 10 μm, as indicated by FESEM (**Figure 3-46c-d**). Indeed, these microparticles feature a flake-like morphology composed by a plethora of intersecting nanoflakes. SEM-EDS mapping of the Cd, In, S, Ni and P elements revealed the presence of Ni_2P small flakes on the surface of CIS (**Figure 3-47**). The mapping images show a homogenous distribution of Cd, In and S atoms throughout the Ni_2P/CIS composite structure, whereas Ni and P atoms are localized in certain regions. The nanoflake morphology of Ni_2P was further verified by FESEM observation (**Figure 3-48**). In **Figure 3-49b**, representative TEM images of the Ni_2P-modified sample (15-Ni_2P/CIS NCF) reveal closely interconnected NCs forming a porous structure, which is beneficial for enhancing interparticle electron

conductivity. The particle size of CIS NCs was estimated to be ~5–7 nm, in very good agreement with SAXs measurement (ca. 6 nm). The crystal structure of constituent NCs is also confirmed by the well-resolved lattice fringes in the high-resolution TEM (HRTEM) image in **Figure 3-49c**. In particular, the lattice plane distance of the crystallites measures approximately 3.3 Å, which combined with previous PDF investigations, could be attributed to the (011) crystallographic plane of hexagonal CIS. Moreover, **Figure 3-49d** provides additional confirmation that Ni_2P nanoflakes, with lateral sizes ranging from 15 to 20 nm, are indeed deposited on the surface of CIS. The interplanar distances of 2.0 and 5.0 Å are attributed to the (021) and (010) lattice planes of hexagonal Ni_2P. Overall, the above results confirm the successful decoration of the CIS mesoscopic assemblies with Ni_2P nanosheets, leading to the formation of a robust Ni_2P-CIS porous network.

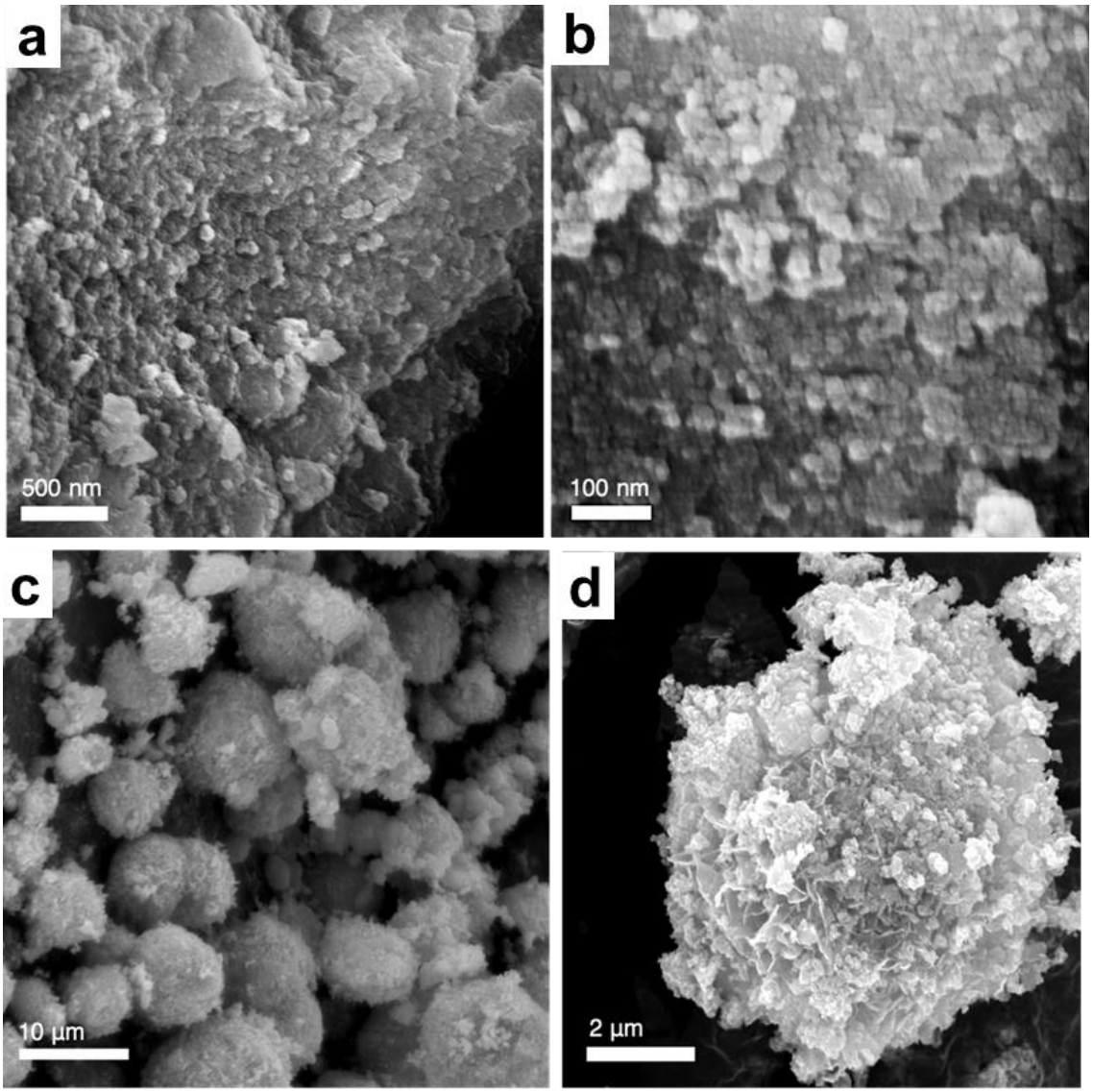

Figure 3-46. Typical FESEM images of (a-b) mesoporous CIS NCF and (c-d) polycrystalline bulk CIS.

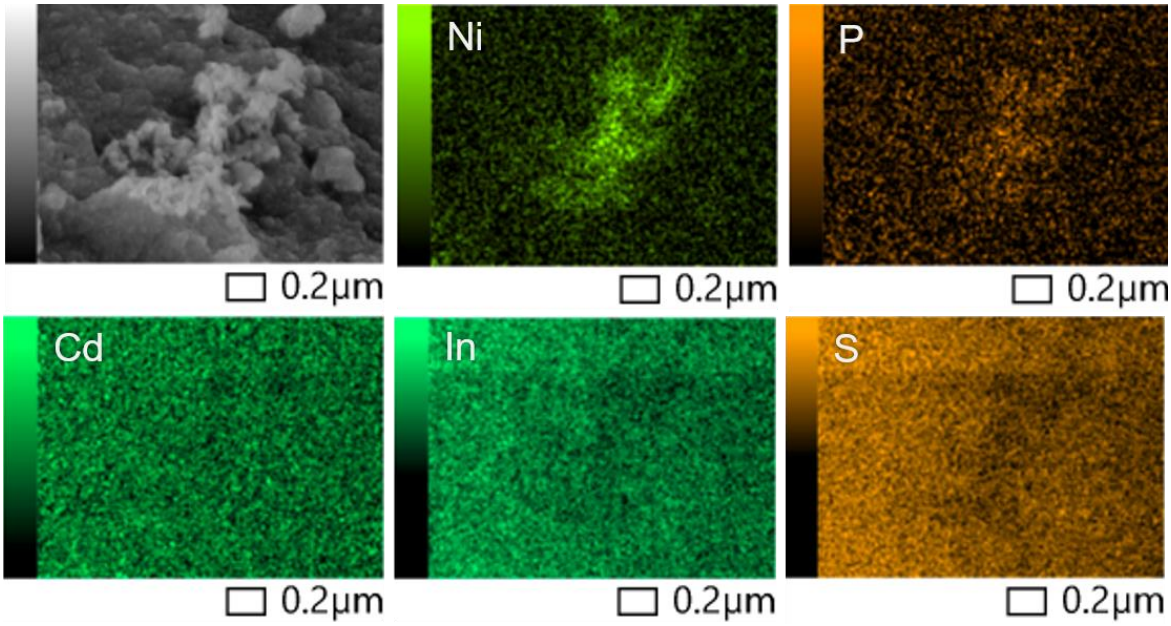

Figure 3-47. SEM-EDS mapping images of Ni, P, Cd, In and S elements of 15-Ni_2P/CIS NCF catalyst.

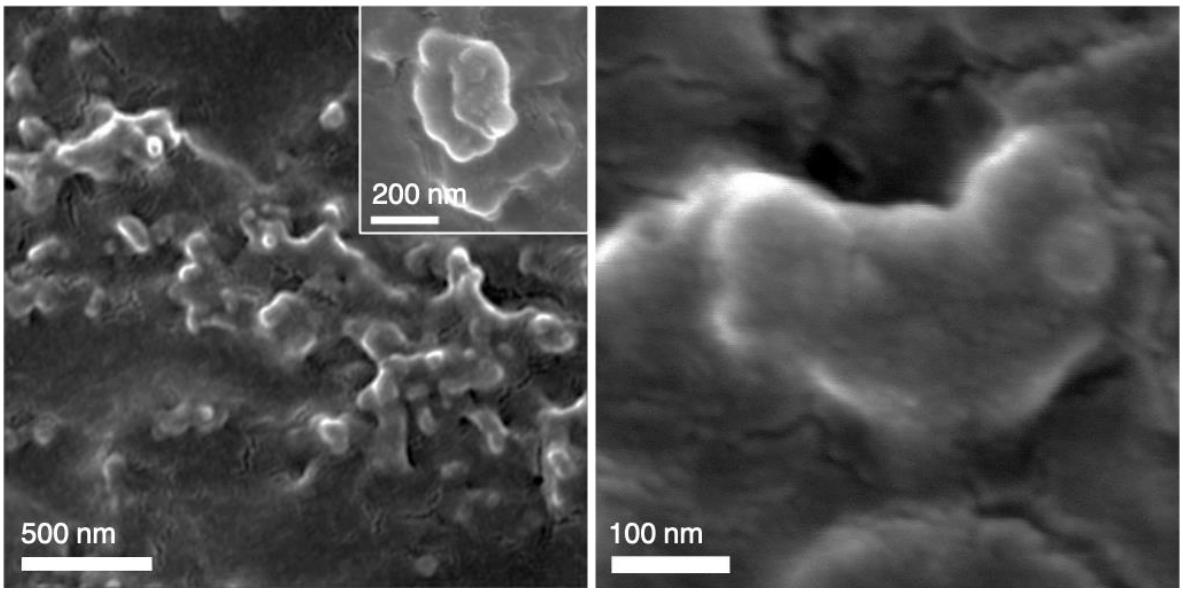

Figure 3-48. FESEM images of Ni_2P co-catalyst, displaying a nanoflake-like morphology with intersecting nanosheets forming a layered-assembled structure.

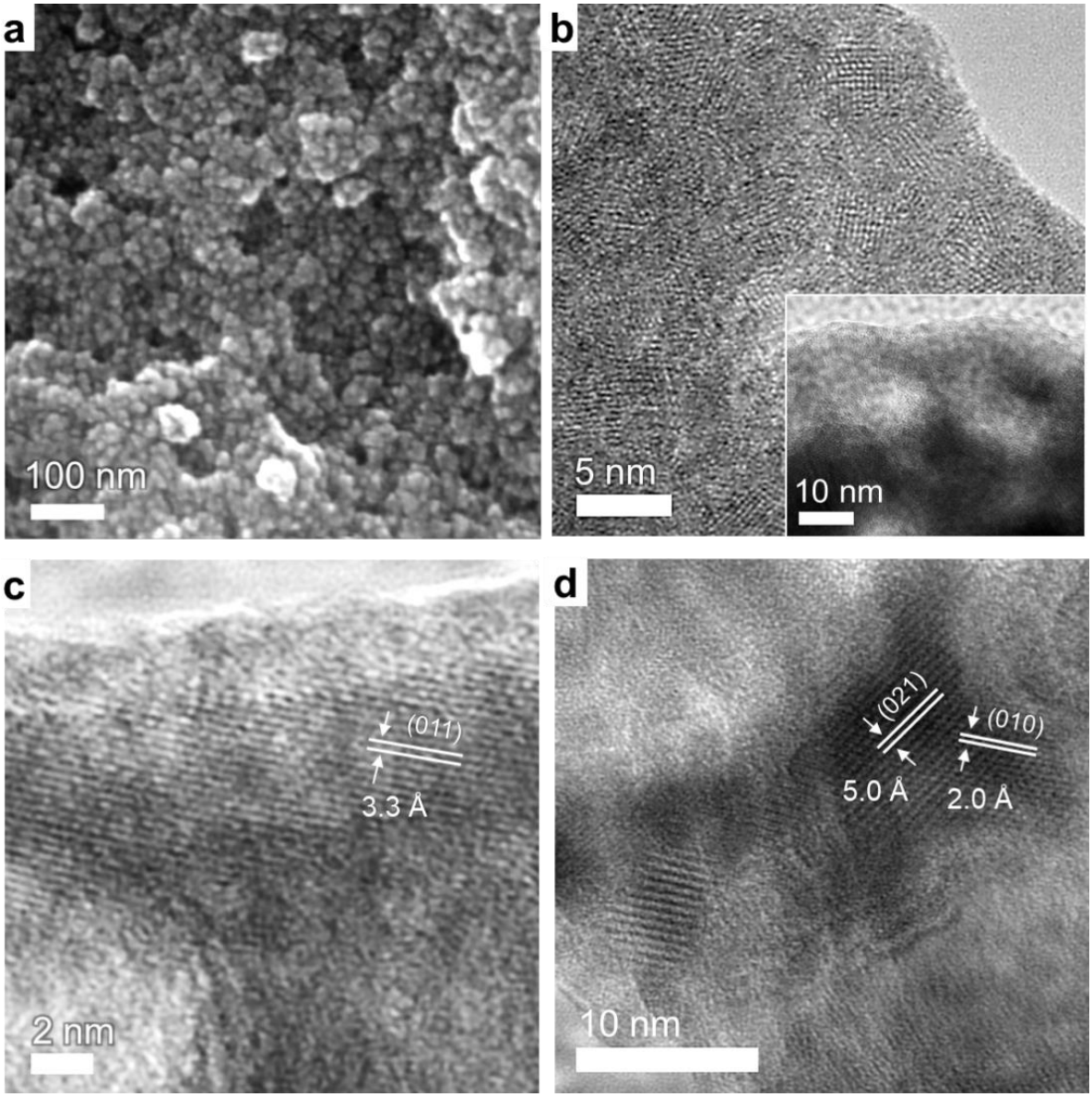

Figure 3-49. Representative (a) FESEM and (b-d) HRTEM images of mesoporous 15-Ni_2P/CIS NCF (15 wt. % Ni_2P content).

The porosity of the prepared samples was determined by nitrogen physisorption experiments. The CIS NCFs exhibited a typical type-IV N_2 adsorption-desorption isotherm accompanied with a H_2-type hysteresis loop, being characteristic of mesoporous solids with interconnected pores (**Figure 3-50**). In addition, the weak but notable steep adsorption in the relative pressure (P/P_0) range of ~0.5–0.6 indicates N_2 adsorption and condensation within narrow-size mesopores [145]. The CIS NCFs made of 6 and 11-nm sized CIS NCs exhibited a Brunaeur-Emmet-Teller (BET) surface area of 135 and 107 $m^2\ g^{-1}$ and total pore volumes of 0.13 and 0.10 $cm^3\ g^{-1}$, respectively. These values are significantly higher than those of the bulk analogue (25 $m^2\ g^{-1}$ and 0.03 $cm^3\ g^{-1}$). Also, a reference material of self-assembled CIS NCs

was prepared through the template-free oxidative coupling of 6-nm sized CIS NCs (denoted as CIS RNAs). Compared to the templated analogue, this sample shows a type-I adsorption isotherm, being characteristic of a microporous structure, and features a smaller BET surface area of 63 m^2 g^{-1} and narrow pore width of approximately 1.5 nm. These results suggest the formation of randomly agglomerated NCs, which comprise small interstitial voids (micropores) between the inorganic nanoparticles. The Ni_2P-modified heterostructures exhibited surface areas ranging from 25 to 90 cm^2 g^{-1} and total pore volumes between 0.02 and 0.07 cm^3 g^{-1}. The lower porosity observed in Ni_2P/CIS NCFs is attributed to the deposition of Ni_2P sheets on the surface of CIS. The N_2 adsorption-desorption isotherms of the Ni_2P/CIS heterostructures are depicted in **Figures 3-50** and **3-51**. By applying the nonlocal density function theory (NLDFT) model to the adsorption data, we obtained narrow size distributions of pores with a maximum peak at ~5.6–5.8 nm for CIS NCFs and ~3.8–4 nm for Ni_2P/CIS NCFs.

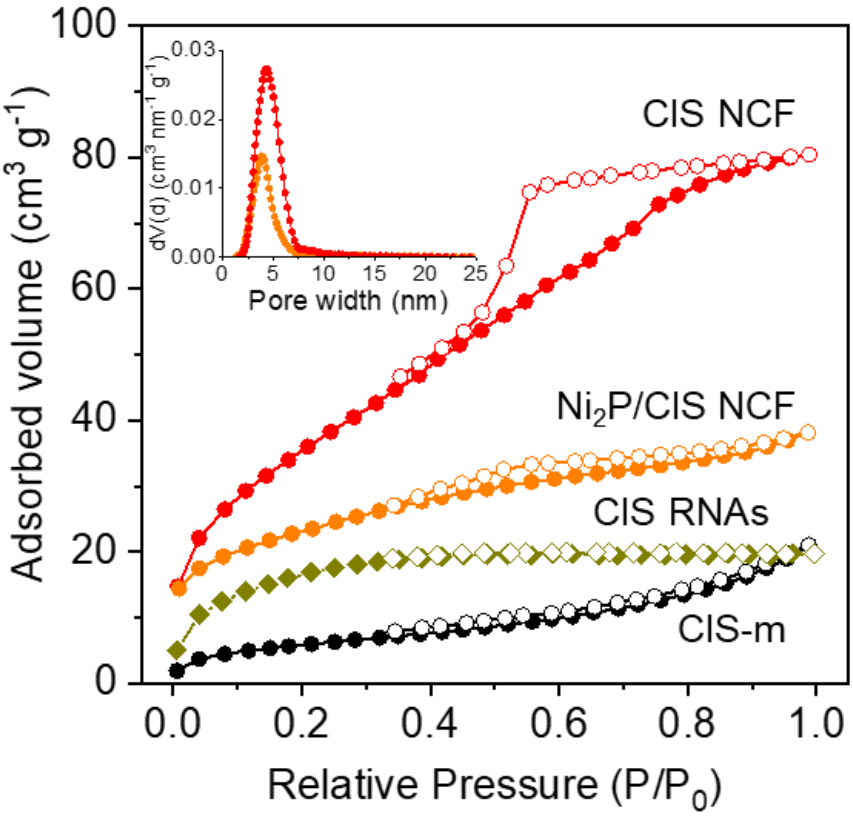

Figure 3-50. N_2 adsorption (filled symbols) and desorption (open symbols) isotherms at –196 ^oC for mesoporous CIS (6 nm) and 15-Ni_2P/CIS NCFs, random NC agglomerates (CIS RNAs) and bulk CIS. Inset: The corresponding NLDFT pore size distribution plots acquired from the adsorption data.

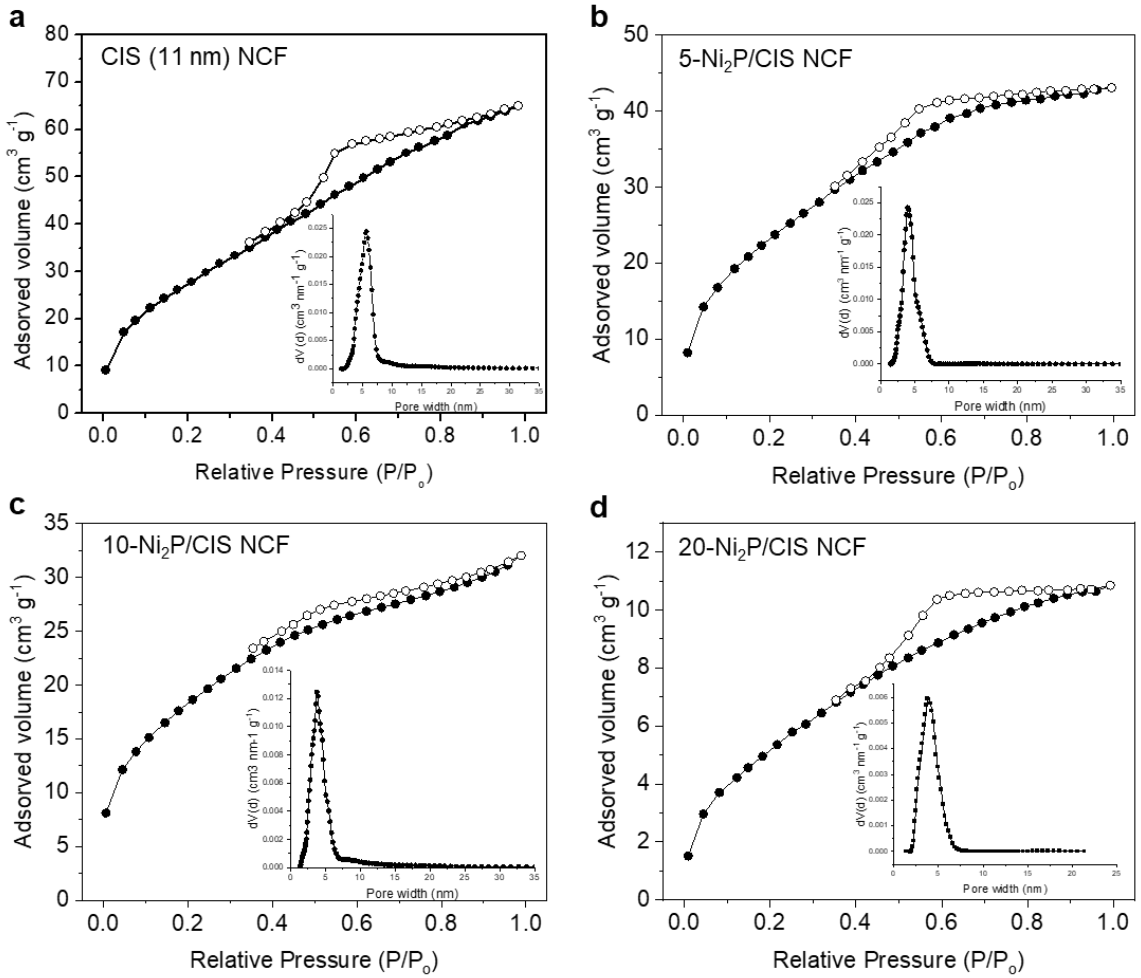

Figure 3-51. N_2 adsorption (filled symbols) and desorption (open symbols) isotherms at –196 ^oC for mesoporous CIS (11 nm) and Ni_2P/CIS composites with 5, 10 and 20 wt. % Ni_2P content. Inset: The corresponding NLDFT pore size distribution plots calculated from the adsorption isotherms.

The CIS nanostructures exhibited a well-defined electronic structure that differs from that of bulk CIS solid (**Figure 3-52**). Compared to CIS microparticles (they show an absorption edge at 2.35 eV), the ultraviolet-visible/near IR (UV-vis/NIR) diffuse reflectance spectrum of 6-nm sized NCs showed a notable blue shift in the absorption edge, indicating the intrinsic excitonic (inter-band) transition (E_g) in CIS occurring at 2.56 eV. This blue-shift in energy gap is related to the very small size of CIS NCs (ca. 5–7 nm, according to SAX and TEM results), which results in strong quantization of the electronic states. In line with this, the bandgap of larger (11 nm) CIS NCs also shifts to higher energy (2.51 eV) relative to bulk CIS, attributed to size-induced quantum confinement effects. A similar behavior is observed in the mesoporous materials consisting of different size NCs. In particular, the mesoporous architectures

composed of 6 and 11-nm NCs preserve the quantum-confined properties of the starting NCs to the mesoporous structures. The small shift (by ~20 meV) in the energy gap going from isolated NCs to mesoporous materials could be attributed to the efficient delocalization of excitons within the porous structure. Although, the change in the dielectric environment of colloidal NCs resulting from the removal of capping agents is also a plausible explanation. The modification of CIS mesostructure with Ni_2P results in altered optical and electronic properties of Ni_2P/CIS heterostructures (**Figure 3-53**). The bandgap energy of the composite materials ranges from 2.55 to 2.52 eV, depending on the Ni_2P content. The strong change in the electronic properties of CIS due to Ni_2P deposition suggests intense electronic interactions and thus efficient charge transfer between Ni_2P nanosheets and CIS host matrix (see below). A summary of optical and textural properties of the pristine and Ni_2P-modified CIS NCFs are given in **Table 3-8**.

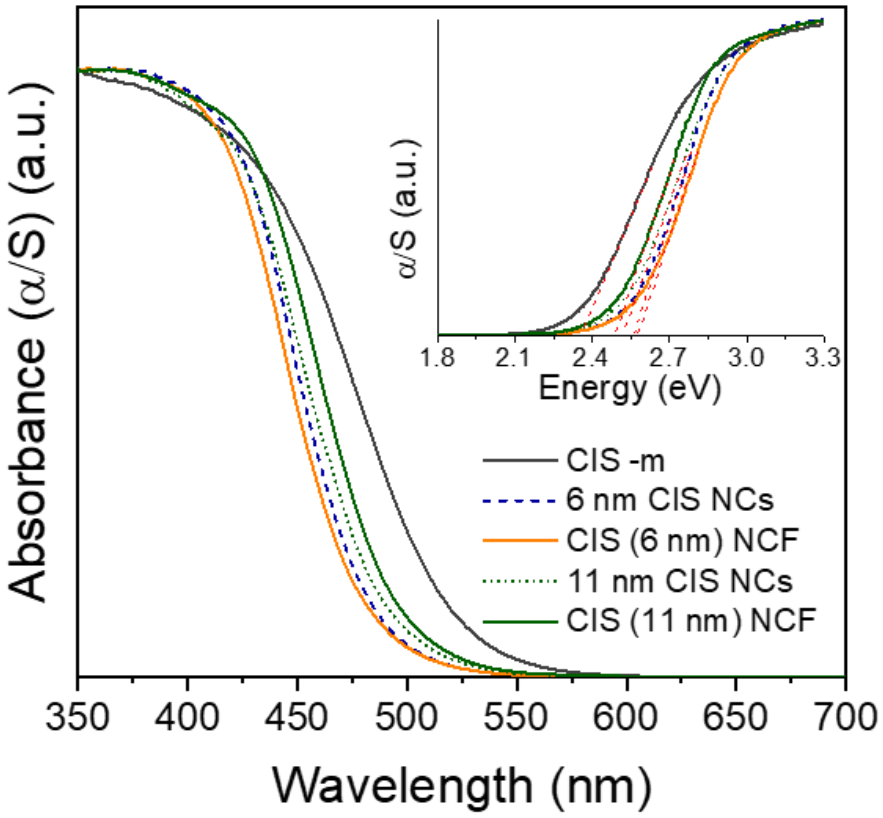

Figure 3-52. UV-vis/NIR diffuse reflectance spectra of as-prepared CIS NCs, mesoporous CIS NCFs and CIS microparticles (CIS-*m*). Inset: The corresponding Kubelka-Munk plots.

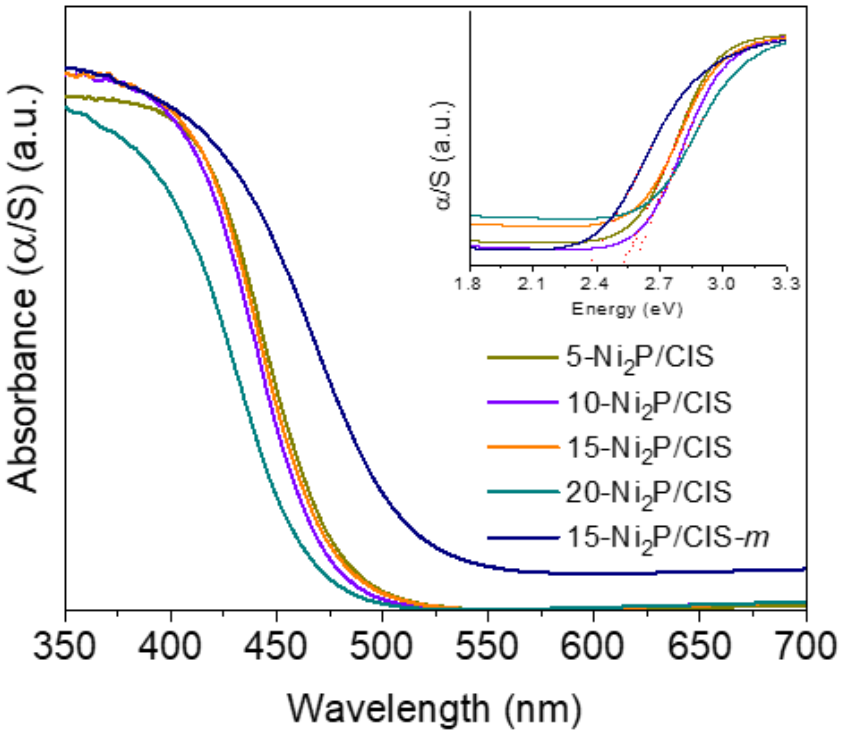

Figure 3-53. UV-vis/NIR diffuse reflectance spectra of mesoporous Ni_2P/CIS NCFs and 15 wt. % Ni_2P-loaded CIS microparticles (15-Ni_2P/CIS-*m*). Inset: The corresponding Kubelka-Munk plots.

Table 3-8. Textural and optical properties of as-prepared CIS NCs, mesoporous CIS and Ni_2P/CIS NCFs, and pure (CIS-*m*) and 15 wt. % Ni_2P-loaded (15-Ni_2P/CIS-*m*) CIS microparticles.

Sample	**BET surface area (m^2 g^{-1})**	**Pore volume (cm^3 g^{-1})**	**Pore size (nm)**	**Energy gap[a)] (eV)**
6-nm CIS NCs	-	-	-	2.56
11-nm CIS NCs	-	-	-	2.51
CIS (6 nm) NCF	135	0.13	5.8	2.58
CIS (11 nm) NCF	107	0.10	5.6	2.49
5-Ni_2P/CIS NCF	90	0.07	4.0	2.54
10-Ni_2P/CIS NCF	68	0.05	3.9	2.55
15-Ni_2P/CIS NCF	52	0.04	3.8	2.53
20-Ni_2P/CIS NCF	25	0.02	3.9	2.52
15-Ni_2P/CIS-*m*	12	0.03	-	2.37
CIS-*m*	25	0.03	-	2.35

[a)]Optical bandgap estimated from the Kubelka-Munk plots.

3.2.2 Photocatalytic study

The photocatalytic activity towards hydrogen production of the prepared materials was assessed under visible light ($\lambda \geq 420$ nm) irradiation. The photocatalytic experiments were conducted in an air-tight quartz reactor, using triethanolamine (TEOA, 10 % v/v) as electron donor. As can be seen in **Figure 3-54**, the mesoporous CIS NCF consisting of 6 nm NCs exhibits a remarkable enhancement in the photocatalytic performance, yielding a H_2 evolution rate of 71 μmol h^{-1}, which is approximately 142 times higher than the photocatalytic activity of bulk CIS (0.5 μmol h^{-1}) under the same experimental conditions. Remarkably, the mesoporous CIS composed of larger (11 nm) NCs exhibited poorer photoactivity (29 μmol h^{-1}) compared to the CIS (6 nm) NCF sample, possibly due to depressed charge transfer process (see below) and low concentration of surface-active sites. It should be noted, that the photocatalytic H_2 production activity of CIS NCF (made up of 6-nm NCs) is superior to that of the random aggregates of NCs (CIS RNAs, ~45 μmol h^{-1}). These results signify the importance of the porous morphology and small grain size composition in enhancing photocatalytic H_2 production efficiency. These attributes induce a short diffusion pathway of the charge carriers to reach the surface, a large catalyst/electrolyte interface, high density of catalytic active sites, and improved mass transport characteristics. The modification of CIS mesoscopic ensembles with Ni_2P significantly enhances H_2 production, highlighting the pivotal role of Ni_2P nanosheets as a co-catalyst. The photocatalytic experiments demonstrated a significant increase in the H_2 production rate with increasing Ni_2P content up to 15 wt. %. Specifically, the H_2 production rate of 15-Ni_2P/CIS NCF is ~586 μmol h^{-1} (or 29.3 mmol g_{cat}^{-1} h^{-1} mass activity), which is approximately 1172 and 8 times higher than that of bulk and mesoporous CIS, respectively. Comparatively, the other Ni_2P-modified catalysts (with 5, 10 and 20 wt. % Ni_2P content) exhibited hydrogen evolution rates between 299 to 541 μmol h^{-1}, which is ~4–8 times higher than that of pristine CIS NCF sample. Moreover, the 15-Ni_2P/CIS catalyst also outperformed the Ni_2P-modified CIS microparticles with the same Ni_2P content (denoted as 15% Ni_2P/CIS-*m*, ~8.5 μmol h^{-1}) by 69 times. As it will be discussed below, the large exposure surface due to the very small grain size of CIS NCs (NCs with particle size smaller than 10 nm have almost all atoms exposed to the surface) and the strong built-in electric field at the Ni_2P/CIS interface lead to rapid surface photocatalytic reactions and efficient delocalization of excitons through electron injection from CIS to the Ni_2P co-catalyst.

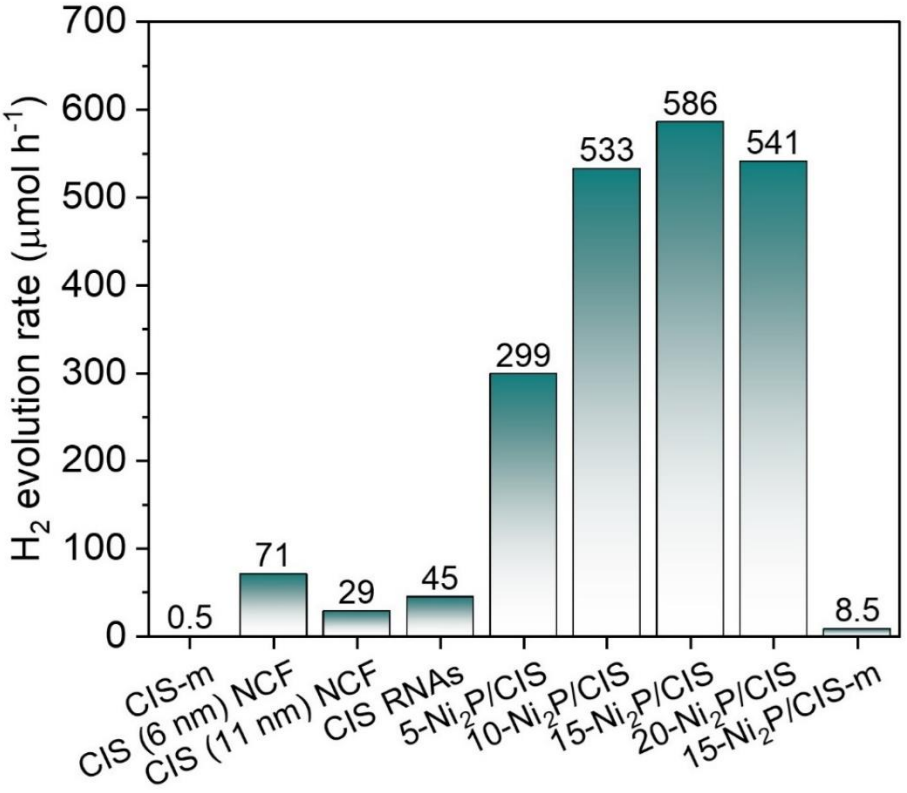

Figure 3-54. Photocatalytic H_2 production activities of different mesoporous CIS and Ni_2P/CIS NCFs, random CIS NCs aggregates (CIS RNAs), and pure and 15 % Ni_2P-loaded (15 % Ni_2P/CIS-*m*) CIS microparticles.

The optimal photocatalytic conditions of the best photocatalyst (15-Ni_2P/CIS NCF) were also determined. Interestingly, the hydrogen evolution activity of 15-Ni_2P/CIS NCF is closely related to the mass loading (**Figure 3-55**). The optimum activity was found at a concentration of 1 mg mL^{-1}, while lower concentrations (0.5 mg mL^{-1}) resulted in inferior activity, likely due to the low density of active sites. Also, at higher catalyst mass loads (1.5 and 2 mg mL^{-1}), the poorer photocatalytic activity can be attributed to the light scattering effect of the catalyst's particles. Also, when TEOA is replaced by several other common sacrificial reagents, such as isopropyl alcohol (10% v/v), 2 M NaOH-10% (v/v) ethanol (OH^-/$^{\bullet}OH$ redox pair) and triethylamine (10% v/v) at a fixed catalyst concertation of 1 mg mL^{-1}, the H_2 evolution rates observed are approximately 45, 36, and 125 μmol h^{-1}, respectively. (**Figure 3-56**). These findings suggest that the photogenerated hole transfer process is the decisive step for the catalytic efficiency of the catalyst. The apparent quantum yields (AQYs) were also determined under monochromatic light sources. In particular, 15-Ni_2P/CIS NCF display AQYs of 81.5%, 61.7%, 22.4% and 0.7% at 375, 420. 460 and 520 nm, assuming 100% absorption of the

incident light. To the best of our knowledge, this photocatalytic efficiency is one of the highest so far reported for $CdIn_2S_4$-based catalyst (see **Table I** in **Annex I**). Remarkably, the wavelength-dependent AQYs values of H_2 evolution closely follow the optical absorbance of the 15-Ni_2P/CIS NCF catalyst, suggesting that the photocatalytic reaction proceeds via band-edge transition (**Figure 3-57**).

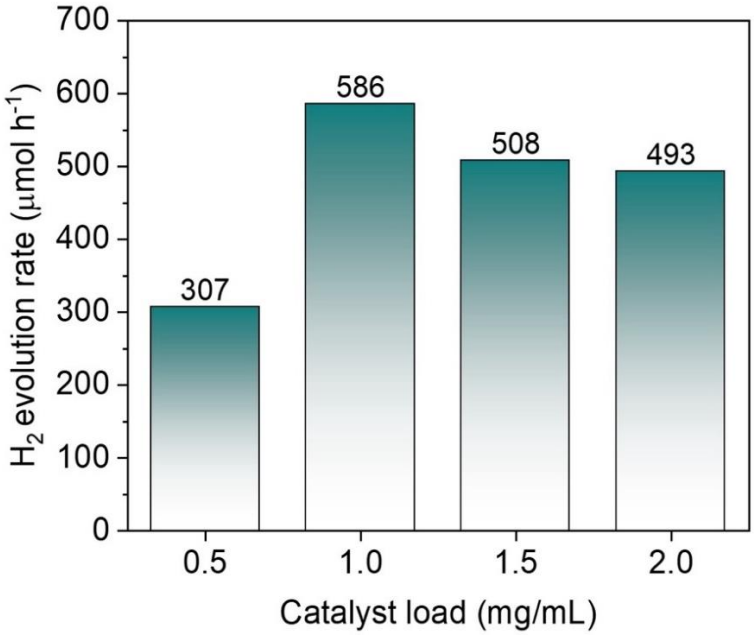

Figure 3-55. Photocatalytic H_2 production activities at different concentrations of 15-Ni_2P/CIS NCF catalyst.

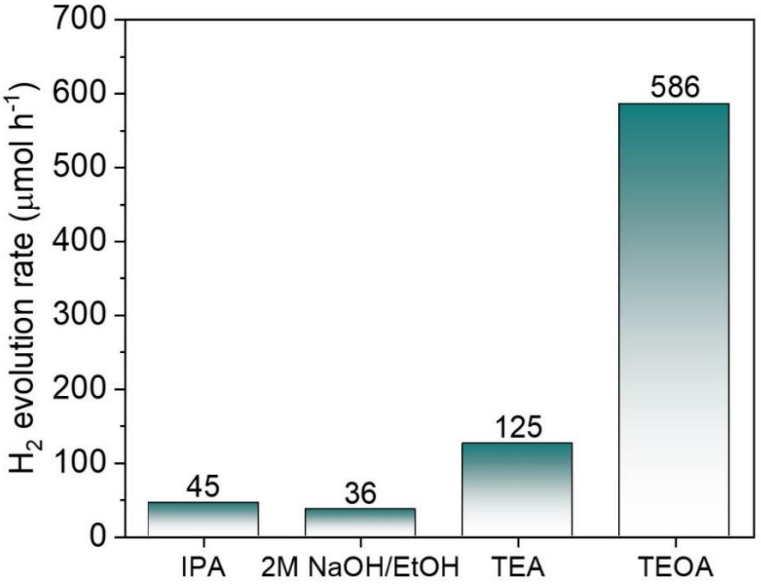

Figure 3-56. Photocatalytic H_2 production activities of 15-Ni_2P/CIS NCF using different hole scavengers: isopropyl alcohol (IPA, 10% v/v), 2 M NaOH/ethanol (EtOH, 10% v/v) mixed solution, triethylamine (TEA, 10% v/v) and triethanolamine (TEOA, 10% v/v).

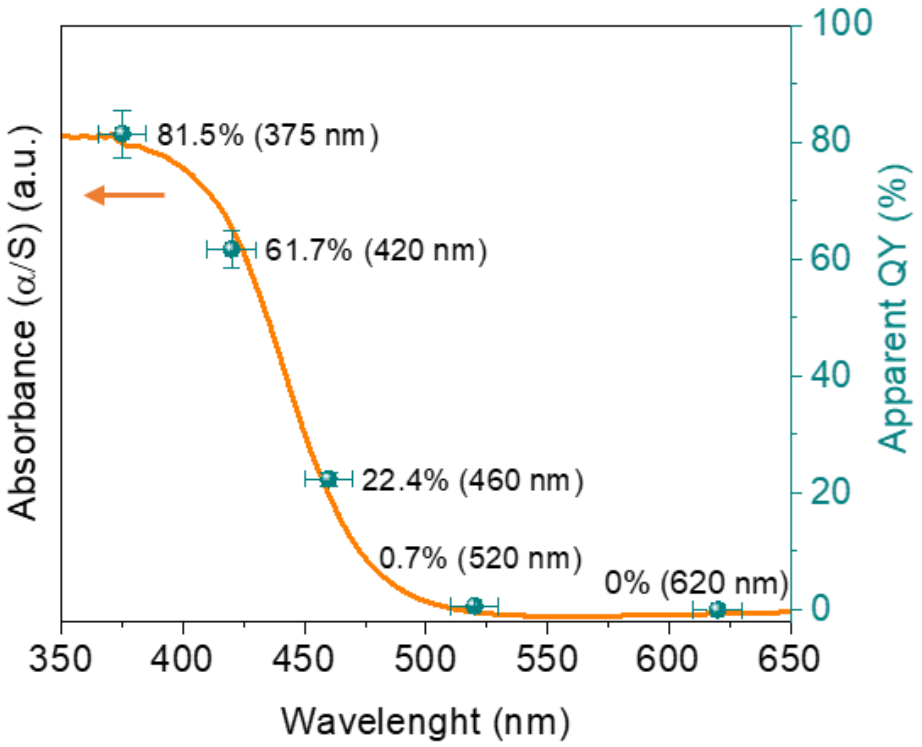

Figure 3-57. UV-vis diffuse reflectance spectrum of mesoporous 15-Ni_2P/CIS NCF catalyst and AQYs of H_2 evolution under different incident light irradiations.

The stability of our best photocatalyst in optimized conditions was assessed under four five-hour catalytic runs. After each run, the catalyst was isolated from the reaction mixture by centrifugation, washed several times with water and reinserted in a fresh TEOA (10% v/v) solution. Prior to each test, the photocatalytic reactor was degassed with Ar gas for at least 30 minutes to eliminate the presence of oxygen gas. As can be seen in **Figure 3-58**, the photocatalytic activity of 15-Ni_2P/CIS NCF showed no detectable deterioration after 20 hours of visible-light irradiation. During this period, the catalyst produced 11.7 mmol of H_2 or ~280 mL at 20 ^{o}C, corresponding to an average hydrogen production rate of ~580 μmol h^{-1}. The chemical and structural integrity of the reused catalyst was investigated with EDS microanalysis and XRD measurements. The EDS spectra indicated that the chemical composition of the catalyst is well retained after catalysis and no leaching of the Ni_2P co-catalyst is observed (~14.7 wt. % Ni_2P). Also, the XRD pattern of the reused catalyst indicated no obvious structural changes (**Figure 3-59**). The porosity of the recycled catalyst was examined by N_2 physisorption (**Figure 3-60**), revealing a BET surface area of 35 m^2 g^{-1}, a total pore volume of 0.03 cm^3 g^{-1} and a mean pore width of 4.9 nm, slightly smaller than those of

the fresh sample. The slight decrease in porosity of the catalyst after reactions could be attributed to mild photo-corrosion of the mesoporous structure.

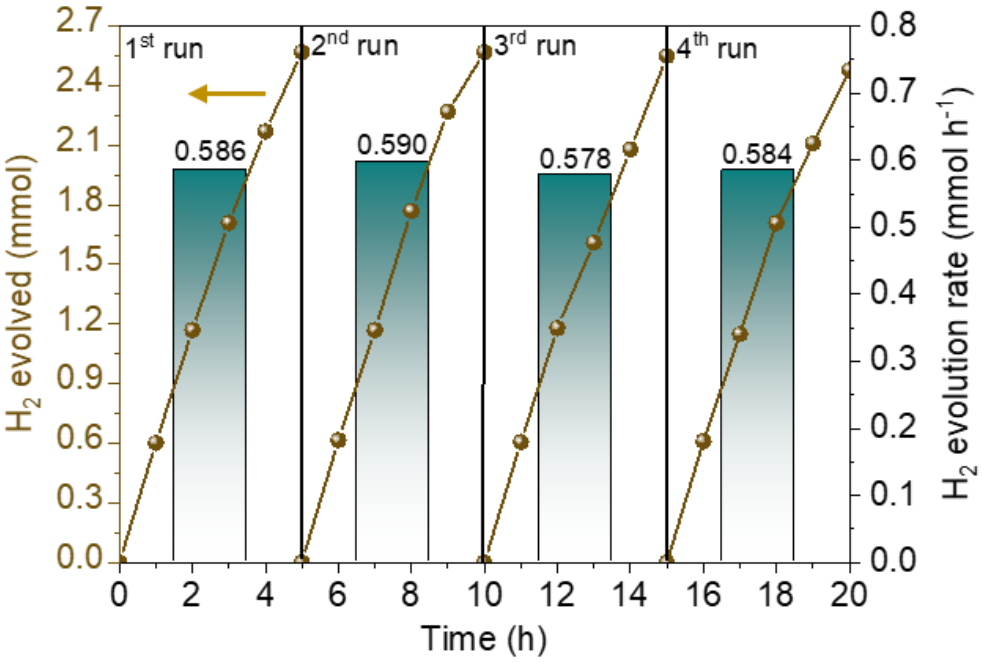

Figure 3-58. Time courses of the photocatalytic hydrogen evolution (lines) and the H_2-evolution rates (column) at the course of the photocatalytic stability study over 15-Ni_2P/CIS NCF catalyst. The H_2-generation rates were averaged over the 5 hours of irradiation. The stability test was conducted with 1 mg mL^{-1} catalyst loading in triethanolamine (10% v/v) solution, under visible-light ($\lambda \geq 420$ nm) irradiation (300 W Xe lamp) at 20 ± 2 °C.

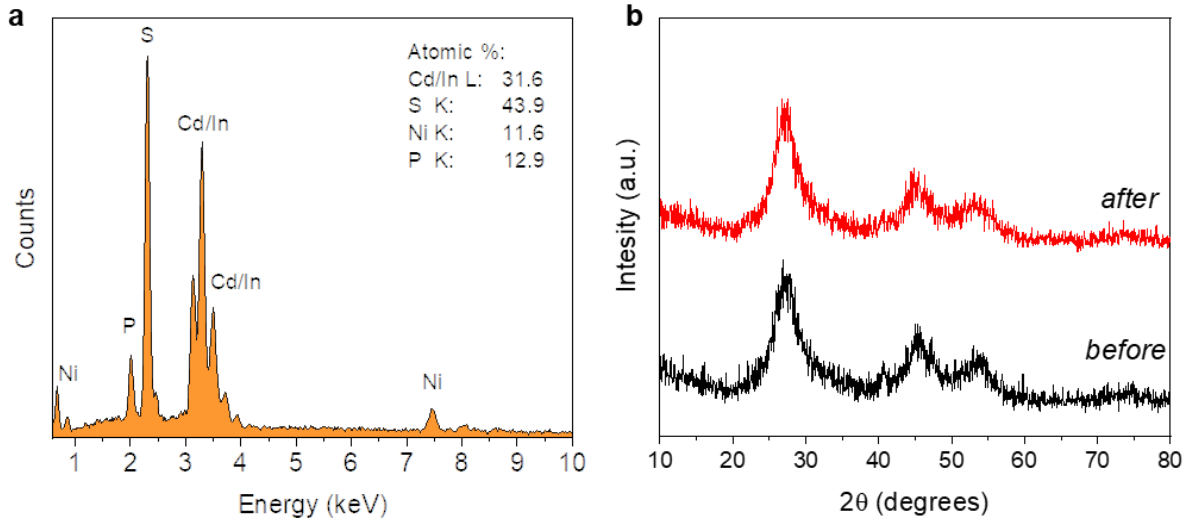

Figure 3-59. (a) Typical EDS spectrum and (b) XRD pattern (red line) of 15-Ni_2P/CIS NCF catalyst after 20 hours of photocatalytic reaction. In panel (b), the XRD pattern (black line) of the fresh catalyst is also given.

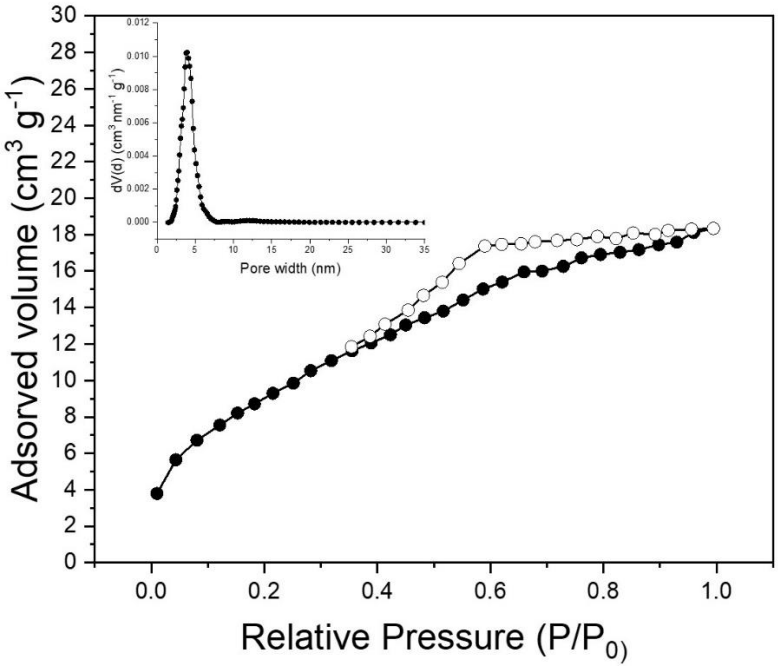

Figure 3-60. N_2 adsorption-desorption isotherm at –196 ^oC and the corresponding NLDFT pore-size distribution plot (inset) of the 15-Ni_2P/CIS NCF catalyst retrieved after 20 hours of photocatalytic reaction.

The chemical state of elements of the recycled catalyst was also investigated via X-ray photoelectron spectroscopy (XPS). The XPS results suggests that the chemical integrity of the 15-Ni_2P/CIS NCF is preserved after the stability tests (**Figure 3-61**), In particular, the Cd 3d spectrum exhibited a spin-orbit doublet signal at 405.0 and 411.8 ± 0.1 eV, corresponding to the Cd $3d_{5/2}$ and Cd $3d_{3/2}$ of Cd^{2+} ions. The In 3d XPS core-level spectrum displayed a doublet peak at binding energies of 444.8 and 452.4 ± 0.1 eV, which are assigned to the In $3d_{5/2}$ and In $3d_{3/2}$ signals of In^{3+} ions in $CdIn_2S_4$. The S 2p XPS spectrum showed a single peak at 161.7 ± 0.2 eV due to the S^{2-} valence state. As for the Ni $2p_{3/2}$ XPS spectrum, the peak at 853.8 eV ± 0.1 is characteristic of the partially charged $Ni^{\delta+}$ ($0 < \delta < 2$) of Ni_2P, while the peak at 857.2 ± 0.1 eV and the satellite feature at 861.1 ± 0.2 eV originate from the Ni^{2+} oxidized species (Ni–OH/Ni–PO_x) on the catalyst surface. Similar to this, the P 2p XPS spectrum shows a peak at 130.1 ± 0.1 eV, corresponding to slightly negatively charged $P^{\delta-}$ atoms in Ni_2P, and a peak at 133.4 ± 0.1 eV due to the oxidized PO_x species at the surface. Furthermore, XPS quantitative analysis of the recycled catalyst showed Cd/In/S atomic ratios close to ~1.2:2:3.9, consistent with the stoichiometry of $CdIn_2S_4$ (1:2:4), along with a Ni_2P weight percentage of ~14.5 % (as determined from the Ni $2p_{3/2}$ and In $3d_{5/2}$ signals). Thus, the above findings suggest that the

15-Ni_2P/CIS NCF catalyst exhibits splendid photocatalytic performance towards hydrogen evolution, along with remarkable photo-corrosion resistance and photo-chemical stability.

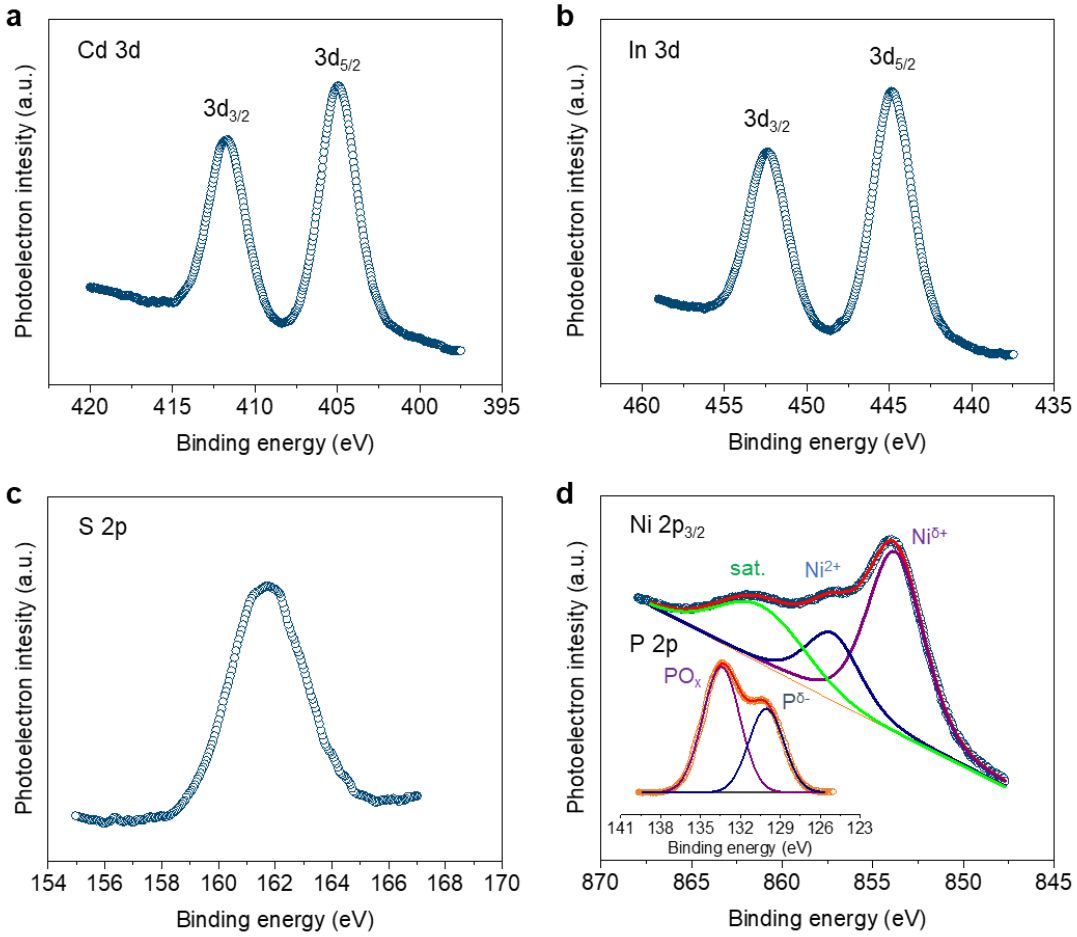

Figure 3-61. High-resolution XPS spectra of (a) Cd 3d, (b) In 3d, (c) S 2p and (d) Ni $2p_{3/2}$ and P 2p of the recycled 15-Ni_2P/CIS NCF catalyst.

3.2.3 Effect of Ni_2P on the photocatalytic activity

In order to understand the charge transfer dynamics in Ni_2P/CIS heterojunctions, Mott-Schottky experiments were performed. **Figure 3-62a** depicts the inverse square-charge capacitance ($1/C_{SC}^2$) as a function of the applied potential (E) plot for the mesoporous CIS and Ni_2P/CIS NCFs. The samples were drop-casted as thin-films on fluorine-doped tin oxide (FTO, 10 Ω sq^{-1}) glass substrates and the flat band (E_{FB}) potentials were determined by the tangent lines of the $1/C_{SC}^2$–E plots. All the reported electrochemical potentials were converted to the reversible hydrogen electrode (RHE) at pH 7. The E_{FB} potential combined with the optical bandgap (as determined from UV-vis/NIR spectra, see **Table 3-8**) can provide the valence band energy level (E_{VB}) of the catalysts (**Table 3-9**, **Figure 3-62b**). This interpretation provides a

good estimation of the conduction band (CB) edge position, which is quite feasible for heavily n-type dope semiconductors [164], where the E_{FB} typically is typically located ~0.1–0.3 eV below the CB edge [46]. All Mott-Schottky plots exhibited positive slopes, indicating n-type conductivity in our catalysts. The Mott-Schottky results revealed that the E_{FB} level of CIS NCFs consisting of 6-nm NCs undergoes an energetic elevation by 130 mV compared to the bulk CIS, that is, from –0.77 V to –0.90 V. The shift in E_{FB} is in good agreement with the widening of the bandgap and the size-dependent optical absorption observed in UV-vis/NIR experiments, highlighting the presence of quantized band-edge electronic states due to the considerable particle size reduction of CIS. Similarly, the mesoporous CIS composed of 11-nm CIS NCs exhibited a E_{FB} of ~ –0.81 V, further confirming that the quantum confinement effects in the electronic band structure originate from the CIS NCs building blocks. The employment of Ni_2P nanosheets on the surface of CIS NCFs, has an immediate effect on the electronic band structure of CIS. Specifically, the E_{FB} gradually shifts from –0.83 V to –0.60 V as the Ni_2P loading increases from 5 to 20 wt. %. The continuous down-shift of the E_{FB} position in the Ni_2P/CIS heterojunctions can be attributed to the electron capture ability of Ni_2P and the rearrangement of the band-edge positions of the Ni_2P and CIS semiconductors. The energetic level alignment between Ni_2P and CIS can result to a potential drop across the Ni_2P/CIS interface, leading to electron migration from CIS, which has a higher Fermi level, to Ni_2P until their Fermi level reach equilibrium. The E_{FB} potential of Ni_2P nanosheets was found to be –0.41 V, significantly lower than that of CIS NCFs. Combined with its bandgap (E_g ~ 1.05 eV), the energy band structure of Ni_2P was also determined (**Figure 3-62b**, **Figure 3-63**).

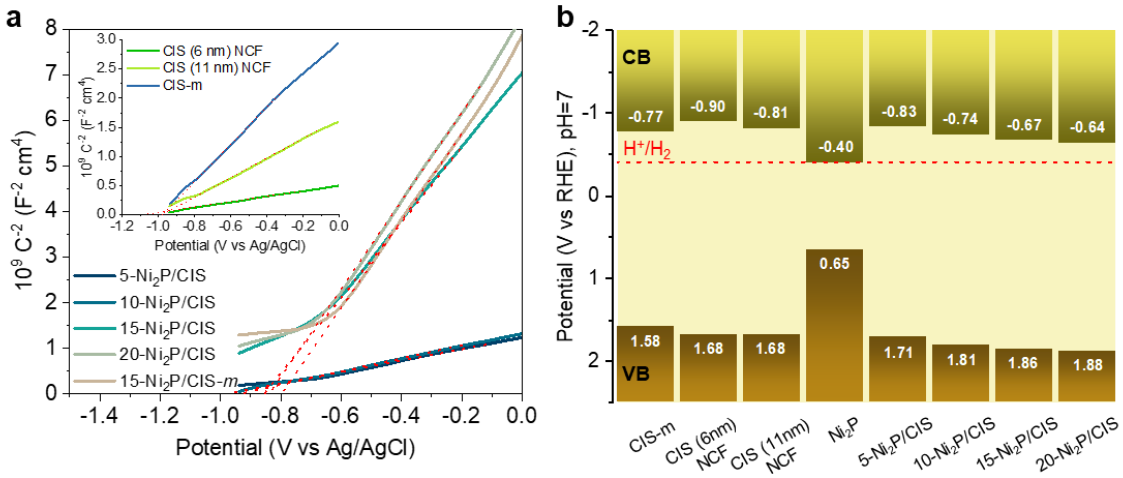

Figure 3-62. (a) Mott-Schottky plots and (b) electronic band structures of the mesoporous CIS and Ni_2P/CIS NCFs, bulk CIS and 15-Ni_2P/CIS-*m* microparticles (VB: valence band, CB: conduction band, red line: H^+/H_2 redox potential).

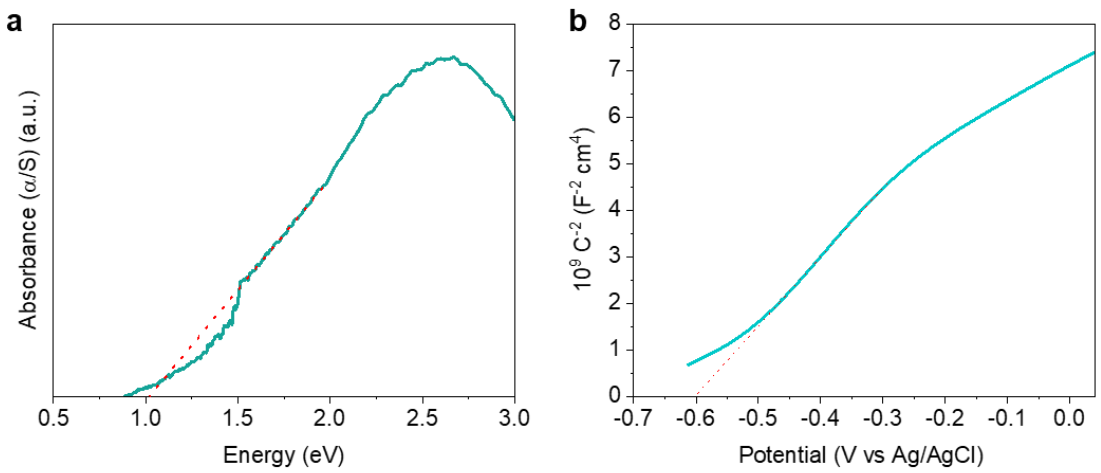

Figure 3-63. (a) UV-vis/NIR diffuse reflectance spectrum and (b) Mott-Schottky plot of Ni_2P nanosheets. In panel (b), the linear fit (red line) indicates a E_{FB} potential of –0.41 V (vs RHE) at pH 7.

Table 3-9. Electrochemical properties of mesoporous CIS and Ni_2P/CIS NCFs, pure CIS and 15% Ni_2P-loaded CIS (15-Ni_2P/CIS-*m*) microparticles, and Ni_2P nanosheets obtained from Mott-Schottky experiments.

Sample	**E_{FB}**	**E_{VB}**	**Donor density**
	(V vs RHE, pH 7)		**(N_D, cm^{-3})**
CIS (6 nm) NCF	–0.90	1.68	4.73×10^{18}
CIS (11 nm) NCF	–0.81	1.68	1.26×10^{18}
5-Ni_2P/CIS NCF	–0.83	1.71	1.74×10^{18}
10-Ni_2P/CIS NCF	–0.74	1.81	1.49×10^{18}
15-Ni_2P/CIS NCF	–0.67	1.86	2.63×10^{17}
20-Ni_2P/CIS NCF	–0.64	1.88	2.20×10^{17}
15-Ni_2P/CIS-*m*	–0.60	1.77	2.28×10^{17}
CIS microparticles	–0.77	1.58	6.65×10^{17}
Ni_2P nanosheets	–0.41	0.64	-

The progressive electron migration from CIS to Ni_2P and the observed E_{FB} shift of CIS are further supported by the change in the slope of the $1/C_{SC}^2$ vs E lines. The charge donor densities (N_D) of CIS NCFs made of 6-nm and 11-nm CIS NCs are approximately 4.73×10^{18} and 1.26×10^{18} cm^{-3}, respectively. The bulk CIS sample exhibited a much lower N_D concentration

(~6.65 × 10^{17} cm^{-3}) compared to the mesoporous CIS, which is attributed to the large grain size of CIS microspheres. Upon Ni_2P decoration, the charge donor densities range between ~1.74 × 10^{18} to ~2.20 × 10^{17} cm^{-3} with increasing Ni_2P content (**Table 3-9**). Overall, the Mott-Schottky results demonstrate that the band-edge alignment at Ni_2P/CIS heterojunctions determines the charge transport processes and the redox ability of the obtained catalysts. These charge transfer pathways can enhance the efficient separation of photogenerated electron-hole pairs and their migration to the catalytic active sites.

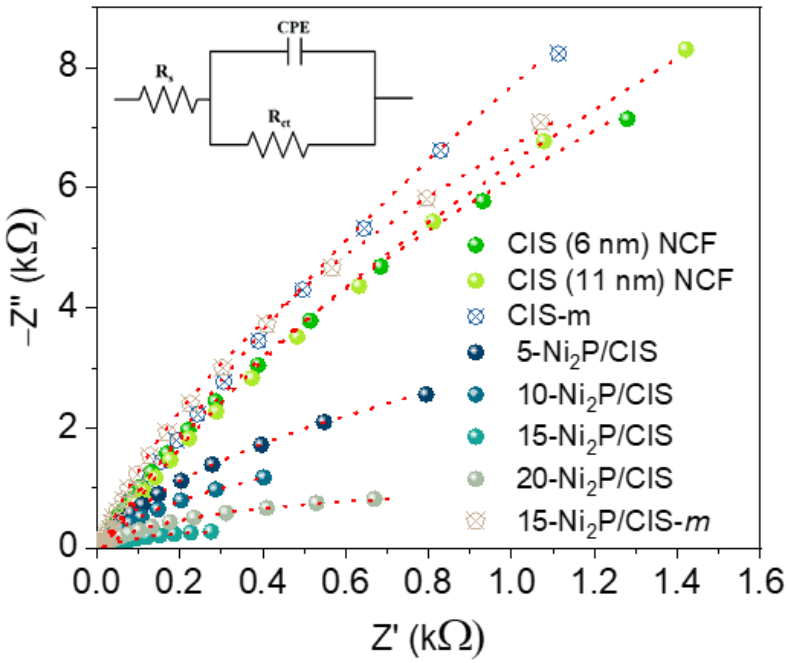

Figure 3-64. EIS Nyquist plots (Inset: equivalent Randles circuit model [R_s (CPE/R_{ct})], used for the simulation of EIS data) for mesoporous CIS and Ni_2P/CIS NCFs, and polycrystalline bulk CIS and 15-Ni_2P/CIS-*m* materials. The red dotted lines are fit to the experimental data.

The charge-transfer dynamics upon Ni_2P functionalization were also investigated via electrochemical impedance (EIS) and time-resolved photoluminescence (TR-PL) spectroscopy. The obtained Nyquist data were fitted using an equivalent Randles circuit model. The mesoporous CIS NCF composed of 6-nm NCs exhibited much lower charge-transfer resistance (R_{ct} ~ 79.3 kΩ) compared to the mesoporous CIS sample made of larger (11 nm) NCs (~110.6 kΩ) and the bulk analogue (~187.2 kΩ), indicating less resistive interfacial charge-transfer kinetics (**Figure 3-64**). The high photocatalytic activity of Ni_2P/CIS catalysts stems from their efficient charge-transfer properties, characterized by markedly lower R_{ct} values. The best photocatalyst (15-Ni_2P/CIS NCF) showed the lowest R_{ct} resistance (~0.7 kΩ)

followed by 20-Ni_2P/CIS (~2.0 kΩ), 10-Ni_2P/CIS (~4.9 kΩ) and 5-Ni_2P/CIS (~12.3 kΩ) NCFs (**Table 3-10**). The significant decrease in charge-transfer resistance observed in Ni_2P/CIS composites correlates well with the hydrogen evolution reaction results (**Figure 3-54**). Of note, the bulk reference 15-Ni_2P/CIS-*m* catalyst, although it possesses a similar electronic structure to the mesoporous 15-Ni_2P/CIS NCF counterpart (E_{FB} ~ –0.6 V and $N_D \sim 2.28 \times 10^{17}$ cm^{-3}, see **Table-3-9**), exhibits less efficient charge transport properties (R_{ct} ~ 69.2 kΩ). These results thus explicitly indicate that the formation of Ni_2P/CIS nanojunctions provides a more efficient interfacial charge carrier pathway and an enhanced separation ability, leading to improved photocatalytic activity.

Table 3-10. EIS Nyquist equivalent circuit model fitted parameters of different CIS-based catalysts.

Sample	**R_s (Ω)**	**C_{dl} (F)**	**R_{ct} (kΩ)**	**x^2**
CIS (6 nm) NCF	13.36	15.53×10^{-6}	79.3	1.8×10^{-4}
CIS (11 nm) NCF	19.04	21.43×10^{-6}	110.6	5.4×10^{-4}
5-Ni_2P/CIS NCF	16.71	40.96×10^{-6}	12.3	1.1×10^{-3}
10-Ni_2P/CIS NCF	14.28	44.53×10^{-6}	4.9	2.8×10^{-4}
15-Ni_2P/CIS NCF	14.92	25.45×10^{-6}	0.66	2.7×10^{-4}
20-Ni_2P/CIS NCF	13.39	24.38×10^{-6}	1.95	3.3×10^{-4}
15-Ni_2P/CIS-*m*	15.01	11.73×10^{-6}	69.2	8.5×10^{-5}
CIS microparticles	19.21	13.79×10^{-6}	187.2	2.4×10^{-3}

TRPL studies were conducted to elucidate the role of the Ni_2P/CIS interface in charge delocalization and transfer phenomena. **Figure 3-65** depicts the TRPL emission decay curves for different CIS catalysts measured upon 375 nm excitation. To properly fit the PL decay and obtain the carrier lifetimes, we utilized a biexponential function: $F(t) = y_0 + \Sigma_i a_i e^{-t/\tau i}$ (i =1, 2), where a_i is the amplitude fraction and τ_i is the carrier lifetime of each component ($\Sigma_i \alpha_i = 1$). The τ_1 an τ_2 charge-carrier lifetimes correspond to the surface-mediated (fast) and band-to-band (slow) recombination of excitons, respectively. The obtained TRPL decay fitting parameters are listed in **Table 3-11**. The catalyst containing 15 wt. % Ni_2P (15-Ni_2P/CIS NCF) exhibits an average lifetime (τ_{av}) of ~3.57 ns, which is approximately 1.4 times larger than that of mesoporous CIS (~2.55 ns) and bulk CIS (~2.53 ns). The combined results from TRPL and

EIS Nyquist measurements advocate for an extensive electronic contact throughout the assembles structure and a more efficient utilization of the photoexcited electrons in the H_2 evolution reaction, which is attributed to faster electron migration through the Ni_2P/CIS nanojunction. Furthermore, a cautious observation of the decay parameters of bulk CIS revealed a dominant recombination of localized carriers within the CIS structure. On the other hand, the mesoporous CIS and Ni_2P/CIS NCFs exhibited a higher contribution of the surface-related radiative transitions (fast), which justifies lower bulk carrier recombination losses due to the rapid electron migration to the surface. This is attributed to the increased band-bending in the CIS mesostructures (due to the low dimensionality of the constituent nanoparticles) and the deposition of Ni_2P nanosheets, which act as "electron pumps" reducing the recombination rate of excitons through spatial separation of the charge carriers.

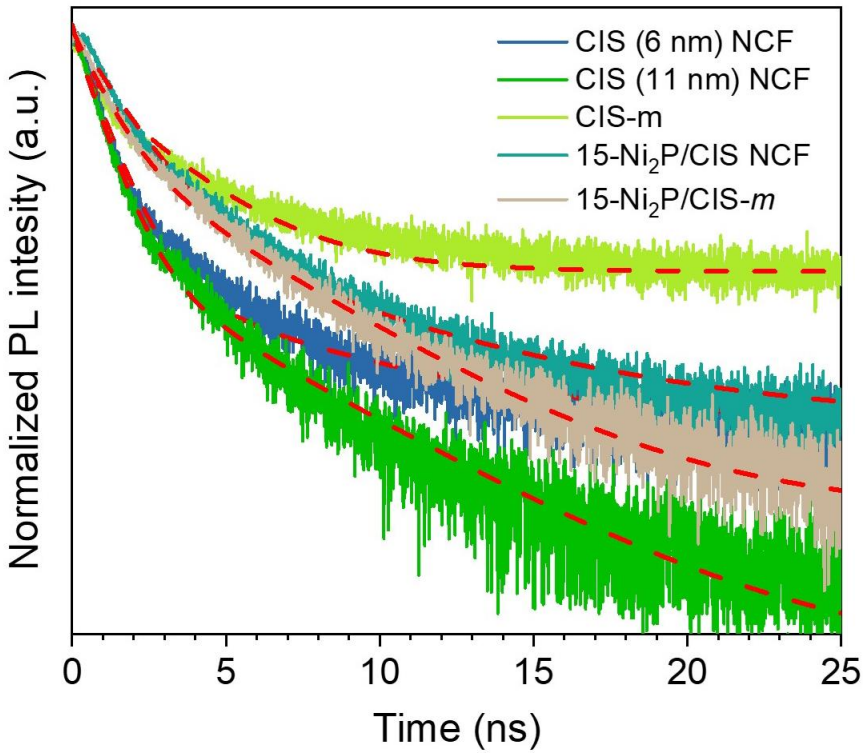

Figure 3-65. TRPL emission decay curves of mesoporous CIS and 15-Ni_2P/CIS NCFs, and pure (CIS-*m*) and 15% Ni_2P-loaded (15-Ni_2P/CIS-*m*) CIS microparticles excited under 375 nm light. The red lines are fit to the experimental data.

Table 3-11. Time-resolved PL decay parameters of mesoporous CIS and 15-Ni_2P/CIS NCFs, and pure (CIS-*m*) and 15% Ni_2P-loaded (15-Ni_2P/CIS-*m*) CIS microparticles.

Sample	**τ_1 (ns)**	**τ_2 (ns)**	**α_1 (%)**	**α_2 (%)**	**τ_{av}[a] (ns)**
CIS (6 nm) NCF	0.94	6.32	94.5	5.5	2.55
CIS (11 nm) NCF	0.84	4.94	91.8	8.2	2.22
15-Ni_2P/CIS NCF	1.62	7.15	89.3	10.7	3.57
15-Ni_2P/CIS-*m*	1.05	4.59	74.1	25.9	3.19
CIS microparticles	0.34	2.73	42.4	57.6	2.53

[a]The average lifetime (τ_{av}) was determined by the equation: $\tau_{av} = (\sum_i \alpha_i \tau_i^2)/(\sum_i \alpha_i \tau_i)$ (i = 1, 2).

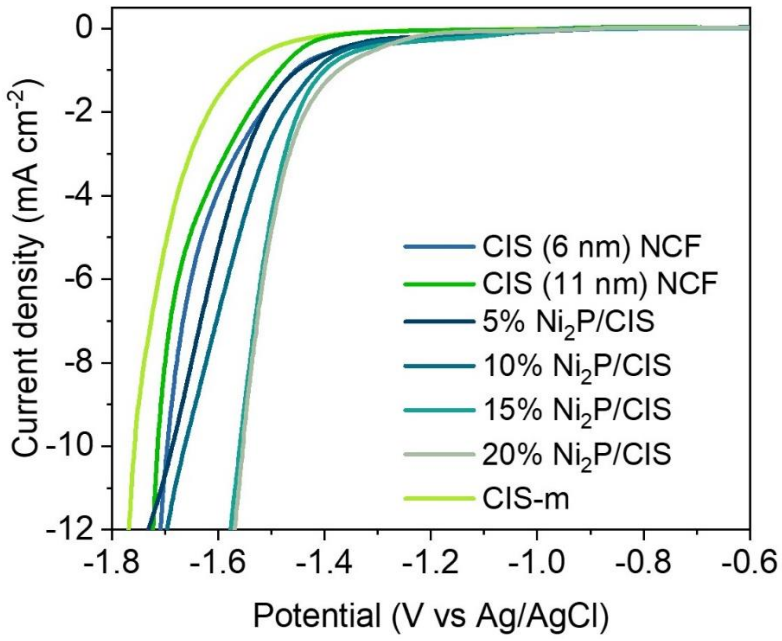

Figure 3-66. J–V plots of mesoporous CIS and Ni_2P/CIS NCFs, and bulk CIS drop-casted as thin-films on FTO glass substrates.

The rapid scavenging of the surface-reaching electron by proton in Ni_2P/CIS heterojunctions is further elucidated by current-potential (J–V) experiments (**Figure 3-66**). The J–V curves showed an earlier onset potential (by ~100–200 mV) and a steeper current response for the Ni_2P/CIS composites compared to the unmodified mesoporous and bulk CIS materials, illustrating improved charge-transfer kinetics and lower energy barrier for H_2 production. For instance, the 15-Ni_2P/CIS NCF catalyst yielded a current density of 4.85 mA cm^{-2} at –1.5 V

(vs Ag/AgCl), while mesoporous and bulk CIS showed current densities of 1.28 and 0.52 mA cm^{-2} at the same potential, respectively. Also, the efficient migration of photoexcited charge carriers due to Ni_2P modification is further confirmed via photocurrent measurements (**Figure 3-67**). In particular, 15-Ni_2P/CIS NCF exhibited a higher cathodic photocurrent (ca. –0.16 mA cm^{-2}) than the mesoporous CIS NCF (ca. –0.09 mA cm^{-2}) under visible light irradiation, indicating better utilization of the photogenerated charge carriers due to the enhanced charge migration at the Ni_2P/CIS interface.

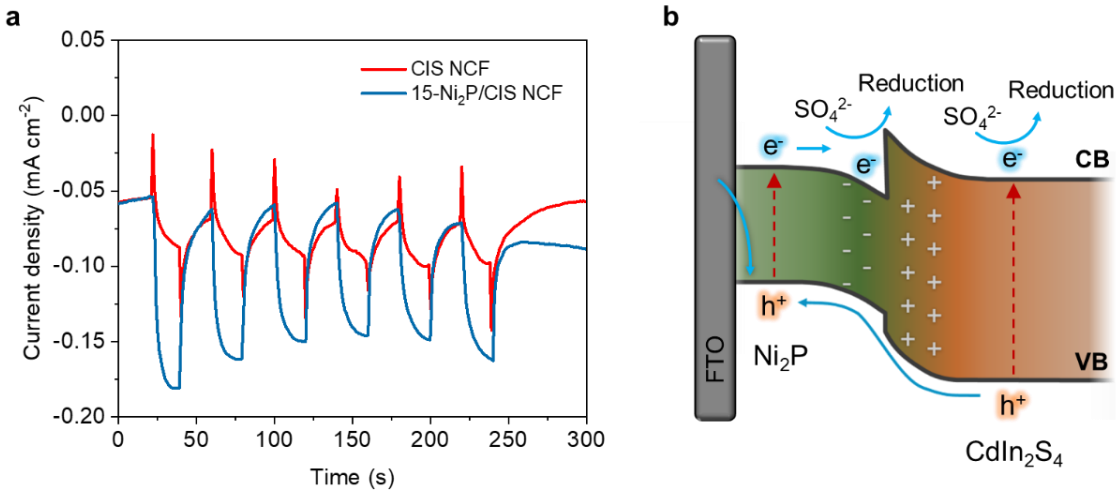

Figure 3-67. (a) Transient photocurrent response of mesoporous CIS and 15-Ni_2P/CIS NCFs measured at a constant potential of –1 V (vs Ag/AgCl) under visible light irradiation ($\lambda \geq 420$ nm). (b) Mechanism of cathodic photocurrent generation at the FTO/15-Ni_2P/CIS NCF electrode. Cathodic photocurrent generation occurs when the electrode potential facilitates electron accumulation in the conduction band (CB) of Ni_2P and CIS semiconductors, and simultaneously promotes hole migration from the valence band (VB) of these semiconductors to the electrode (FTO).

Figure 3-68 illustrates a potential band bending model and reaction mechanism of mesoporous Ni_2P/CIS NCFs. Specifically, the equilibration of Fermi levels and the subsequent electron flow creates a band-bending at the Ni_2P/CIS interface, in which both CB and VB edges of CIS shift upwards, while the band-edges of Ni_2P nanosheets simultaneously descend. In the case of the 15-Ni_2P/CIS NCF catalyst, a CB offset of about 0.5 eV is established between Ni_2P and CIS semiconductors (as determined by the electron affinity (x) difference between the two semiconductors) that results in a notched CB grading near the heterointerface, as depicted in **Figure 3-68**. This leads to the formation of a potential barrier at the CB that impedes the

electron flow from CIS to Ni_2P side, even though the Ni_2P CB is more favorable for electron injection. Thus, the photogenerated electrons from CIS remain in the CB of CIS, whereas the free electrons of Ni_2P tend to accumulate at the Ni_2P interface (accumulation region). These localized interfacial states can act as electron traps in the vicinity of the heterointerface (forming a 2D electron gas), facilitating the proton reduction reaction. At the same time, the built-in electric field that has formed at the Ni_2P/CIS contact can thermodynamically facilitate the hole transfer from the CIS VB to Ni_2P where they can oxidize the sacrificial reagent (TEOA). Considering that the VB potential of isolated Ni_2P is ~0.65 V (**Table 3-9**) and accounting for an expected VB banding of about 0.2–0.3 eV, the VB maximum of Ni_2P is estimated to be ~0.4–0.5 V (vs RHE) after equilibrium with CIS, which is far above the VB position of CIS (ca 1.86 V vs RHE). The net effect of this procedure is expected to generate a migration and separation of excitons at the interface of Ni_2P/CIS. The built-in potential (V_{bi}) at the Ni_2P/CIS interface, which is defined at the energy difference between the Fermi levels of Ni_2P (ca. –0.4 V vs RHE) and CIS NCF (ca. –0.9 V vs RHE) is approximately 0.5 eV, which is sufficient enough to induce the charge pair separation. The separation and migration pathway of photoexcited carriers seen in the above EIS and TR-PL spectroscopic analyses is consistent with this mechanism.

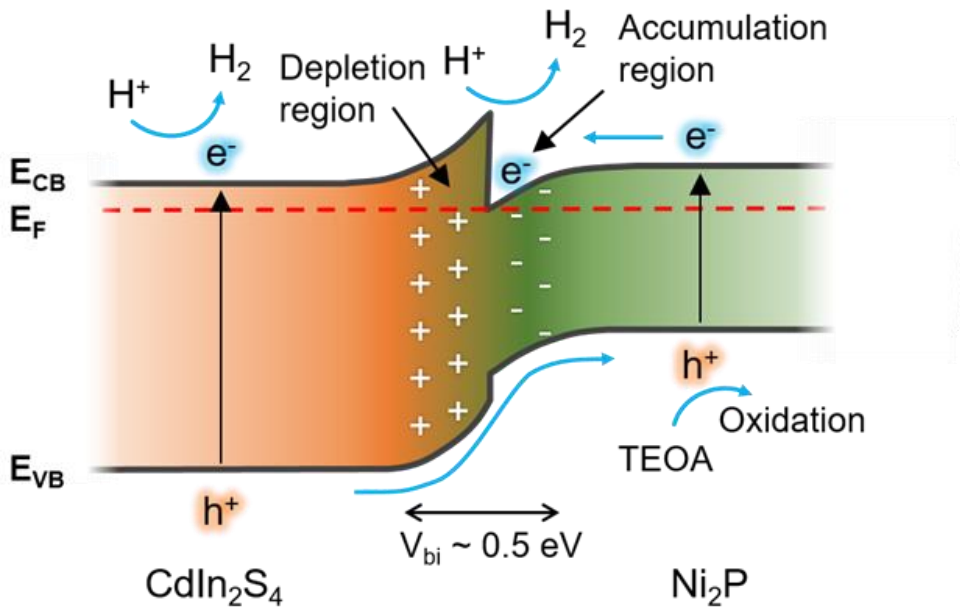

Figure 3-68. Proposed band-bending model, displaying a typical type-I (straddling) n-n Ni_2P/CIS heterojunction and possible photocatalytic H_2 production mechanism over Ni_2P/CIS catalysts (E_{CB}: conduction band energy, E_{VB}: valence band energy, E_F: Fermi level).

3.2.4 Conclusions

A low-temperature synthetic protocol of obtaining high-surface-area 3D mesoporous networks of unique hexagonally CIS NCs was demonstrated. Importantly, this synthetic method provides the ability to construct mesoporous architectures of CIS nanoparticles with different size. The combination of mesoporosity along with the small grain size of CIS (ca. 6 and 11 nm in diameter) results to significant advantages towards the photocatalytic activity, deriving from the enhanced migration of charge carriers and interparticle mass transport. Functionalizing the CIS nanostructures with Ni_2P nanosheets significantly enhances the photocatalytic activity of CIS by facilitating increased charge transfer that promote hole transfer across the Ni_2P/CIS interface (from CIS to Ni_2P). As a result, the mesoporous Ni_2P/CIS catalyst containing 15 wt. % Ni_2P demonstrates a remarkable photocatalytic activity for the water reduction reaction, exhibiting a 29.3 mmol h^{-1} g_{cat}^{-1} H_2 production rate under visible light irradiation with AQYs of 81.5% and 61.7% at 375 nm and 420 nm monochromatic light, respectively. This photocatalytic activity is among the highest reported for $CdIn_2S_4$-based photocatalytic systems.

3.3 Mesoporous Mott-Schottky heterojunctions of Co_2P-modified $CdIn_2S_4$ nanocrystals

3.3.1 Synthesis and structural characterization

The mesoporous framework of linked $CdIn_2S_4$ nanocrystal (denoted as CIS NCF) was synthesized via the oxidative coupling of colloidal CIS nanocrystals (with 6 nm in size) in the presence of polyoxothylene-*block*-cetyl ether (Brij-58) copolymer, which is sufficient to mediate the assembly of individual nanocrystals into a continuous 3D porous structure. The polymer template was then removed from the pores by solvent extraction in warm ethanol and water (~40 ^oC). This process produces a robust network of connected CIS nanocrystals with large internal surface area and well-defined pores. The sufficient removal of the organic mold was verified by thermogravimetric analysis (TGA), which indicated an inevitable ~9.3 wt. % of organic residual remaining in the mesoporous CIS sample (**Figure 3-69**).

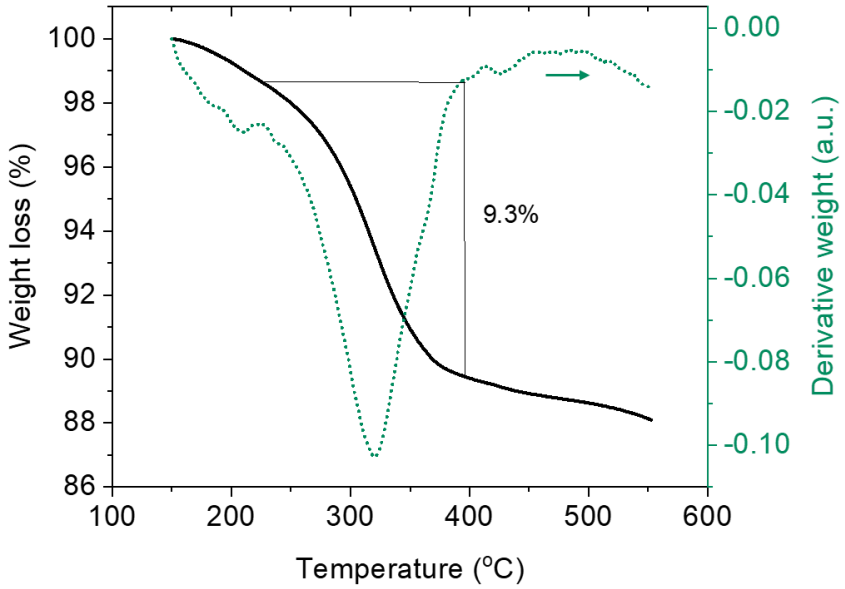

Figure 3-69. TGA profile (black line) and the corresponding differential thermogravimetric (DTG) curve (green line) of mesoporous CIS NCF.

Then, mesoporous Co_2P-modified CIS heterostructures (denoted as *n*-CP/CIS NCFs, where *n* refers to the weight percentage of Co_2P) with adjustable composition of Co_2P, that is, from 5 to 15 wt %, were prepared by chemical deposition of pre-formed Co_2P nanoparticles on the surface of CIS mesoporous. Also, a reference material was synthesized by chemical deposition of 10 wt. % Co_2P on the surface of CIS microparticles (denoted as 10-CP/CIS-*m*). The chemical composition of the prepared materials was determined by energy dispersive X-ray spectroscopy

(EDS). The EDS results confirmed that the resultant CP/CIS NCFs have a stoichiometric composition of Cd:In:S = 1:2:4 and Co_2P loadings very close to those expected from the stoichiometry of reactions (within a ~5-8 % standard deviation) (**Figure 3-70**). The analytical data and the estimated Co_2P loadings of mesoporous samples are given in **Table 3-12**.

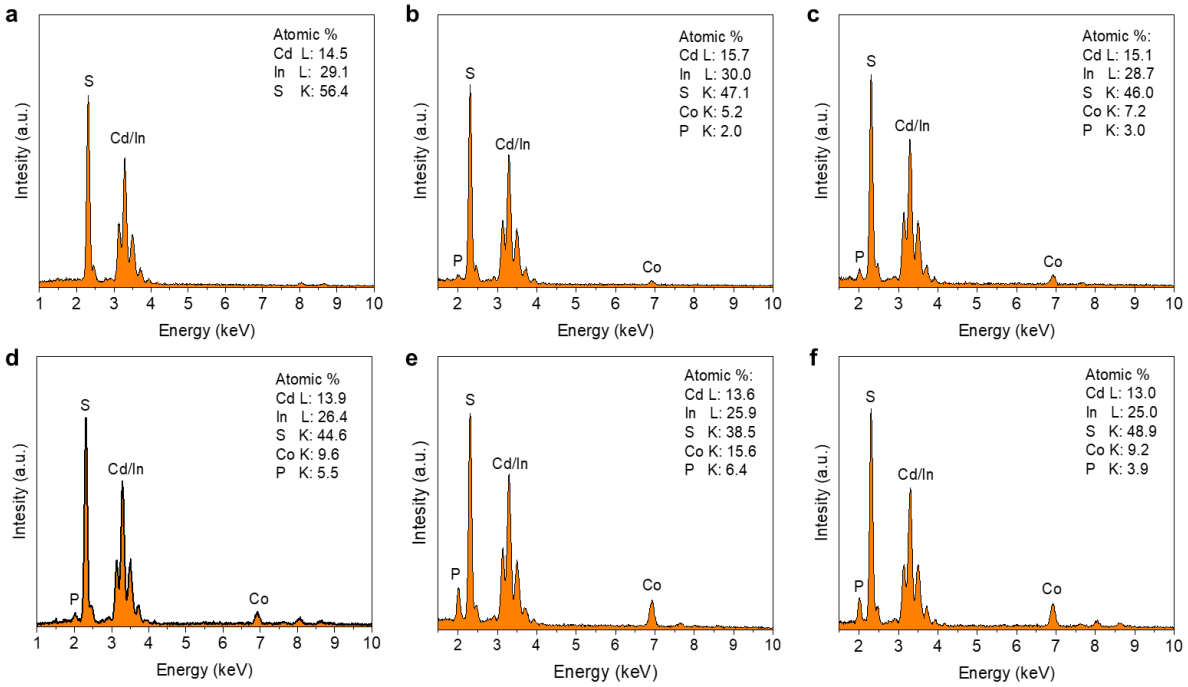

Figure 3-70. Typical EDS spectra of the mesoporous (a) CIS and CP/CIS NCFs with (b) 5, (c) 7, (d) 10 and (e) 15 wt. % Co_2P loading, and (f) 10% Co_2P-loaded CIS microparticles.

Table-3-12. Element composition of Co_2P nanoparticles and mesoporous CIS and Co_2P/CIS samples.

Sample	**Cd (at. %)**	**In (at. %)**	**S (at. %)**	**Co (at. %)**	**P (at. %)**	**Co_2P loading[a)] (wt.%)**
Co_2P NPs	-	-	-	61.4	38.6	-
CIS NCF	14.5	29.1	56.4	-	-	-
5-CP/CIS NCF	15.7	30.0	47.1	5.2	2.0	4.98
7-CP/CIS NCF	15.1	28.7	46.0	7.2	3.0	7.02
10-CP/CIS NCF	13.9	26.4	44.6	9.6	5.5	9.84
15-CP/CIS NCF	13.6	25.9	38.5	15.6	6.4	15.32
10-CP/CIS-*m*	13.0	25.0	48.9	9.2	3.9	10.03

[a)] Based on the EDS Co to Cd atomic ratio.

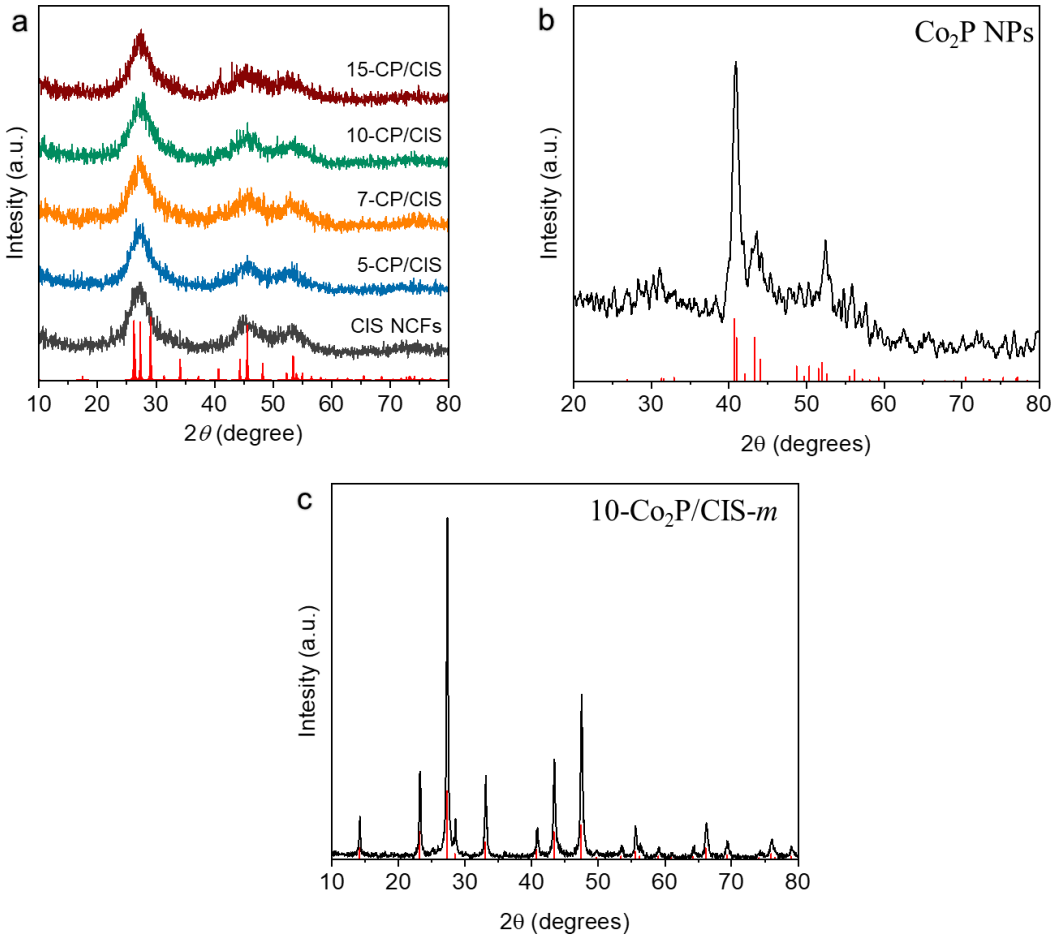

Figure 3-71. XRD patterns of (a) CIS NCFs and CP/CIS samples, (b) Co_2P nanoparticles and (c) 10 wt. % Co_2P-modified CIS microparticles. The standard diffraction lines of (a) hexagonal $CdIn_2S_4$, (b) orthorhombic Co_2P (JCPDs card no. 32-0306) and (c) cubic $CdIn_2S_4$ (JCPDs card no. 27-0060) are also given.

The crystal structure of mesoporous CIS and CP/CIS NCFs was examined with X-ray diffraction (XRD) analysis. The CIS NCF showed three broad diffraction peaks at 2θ scattering angles between 20° to 60° (**Figure 3-71a**), which can be assigned to the hexagonal phase of $CdIn_2S_4$ (see chapter 3.2). The broadness of the diffraction peaks implies the nanocrystalline nature of the samples. The Co_2P-modified samples with Co_2P content up to the 10 wt. % exhibited identical XRD patterns to the pristine CIS sample, with no detectable Co_2P crystallites due to the small grain size and low content of Co_2P. In higher concentration of Co_2P (15 wt. %), however, the Co_2P/CIS heterostructures showed an additional diffraction peak at 2θ ~ 40.7°, which can be assigned to the (112) lattice planes of orthorhombic Co_2P, further confirming the formation of Co_2P/CIS heterostructures. The crystal phase of as-prepared Co_2P

was identified via XRD as can be seen in **Figure 3-71b**, in which all the diffraction peaks correlate well with the orthorhombic phase of Co_2P (JCPDS card. No 32-0306). No other distinguishable XRD peaks were observed, suggesting the high phase purity of Co_2P. The XRD pattern of the reference 10-CP/CIS-*m* material showed only the characteristic diffraction peaks of the cubic $CdIn_2S_4$ (JCPDs card no. 27-0060), with no additional Co_2P XRD peaks due to the low content and small grain size (**Figure 3-71c**).

The morphology of the mesoporous sample with 10 wt. % Co_2P loading (10-CP/CIS) was observed by field-emission scanning electron microscopy (FESEM). The FESEM images show the formation of a 3D mesoporous network composed of fairly monodisperse CIS nanoparticles of size ~5–10 nm (**Figure 3-72a**). Comparatively, the reference sample 10-CP/CIS-*m*, synthesized via a simple hydrothermal method, is composed of microparticles of 5–10 μm diameter that consist of numerous intersecting ~250-nm-sized nanoflakes (**Figure 3-72b**). SEM-EDS mapping on 10-CP/CIS mesoporous indicated a homogenously distribution of Co, Cd, In and S element throughout the porous framework (**Figure 3-72c**), suggesting that Co_2P deposits uniformly on the CIS surface. Further structural characterization of 10-CP/CIS NCF with transmission electron microscopy (TEM) display plenty of tightly interconnected nanoparticles of 5–7 nm diameter forming the porous framework (**Figure 3-72d-e**), in accordance with the results from XRD and FESEM. Such an intimate particle-to-particle contact is crucial to maximize the electrical conductivity of the mesoporous structure. In addition, uniform pores of about ~4–5 nm in size between the assembled structure can be observed in the TEM images, which is beneficial to mass transport processes. The hexagonal crystal structure of CIS was also verified by high-resolution TEM (HRTEM). The lattice fringes with interplanar distance of 3.3 Å in **Figure 3-72e** are assigned to the (001) crystal planes of hexagonal $CdIn_2S_4$ (space group $P6_3mc$). The presence of different orientations of the lattice planes suggests the polycrystalline nature of CIS. Moreover, HRTEM observation also confirms the uniform distribution of Co_2P nanoparticles on the CIS surface, clearly showing Co_2P nanocrystals (appeared as dark regions) with lattice planes of 2.8 Å, which agree well with the (200) crystal planes of the orthorhombic Co_2P (space group Pnma). A more careful analysis of the TEM images shows that Co_2P comprises nanocrystallites with an average size of ~6–7 nm. Also, the HRTEM images depict distinct heterointerfaces between the Co_2P and CIS materials (highlighted with white lines in **Figure 3-72f**), which are expected to be beneficial for the dissociative adsorption of water molecules during the hydrogen evolution reaction [165]. Overall, the chemical composition and crystal structure of the obtained materials was confirmed through EDS and XRD analysis. The corresponding results

suggest the successful preparation of mesoporous frameworks comprising of interconnected Co_2P and CIS nanoparticles with internal porosity, which allows for an efficient interparticle contact and maximizes the electrical conductivity.

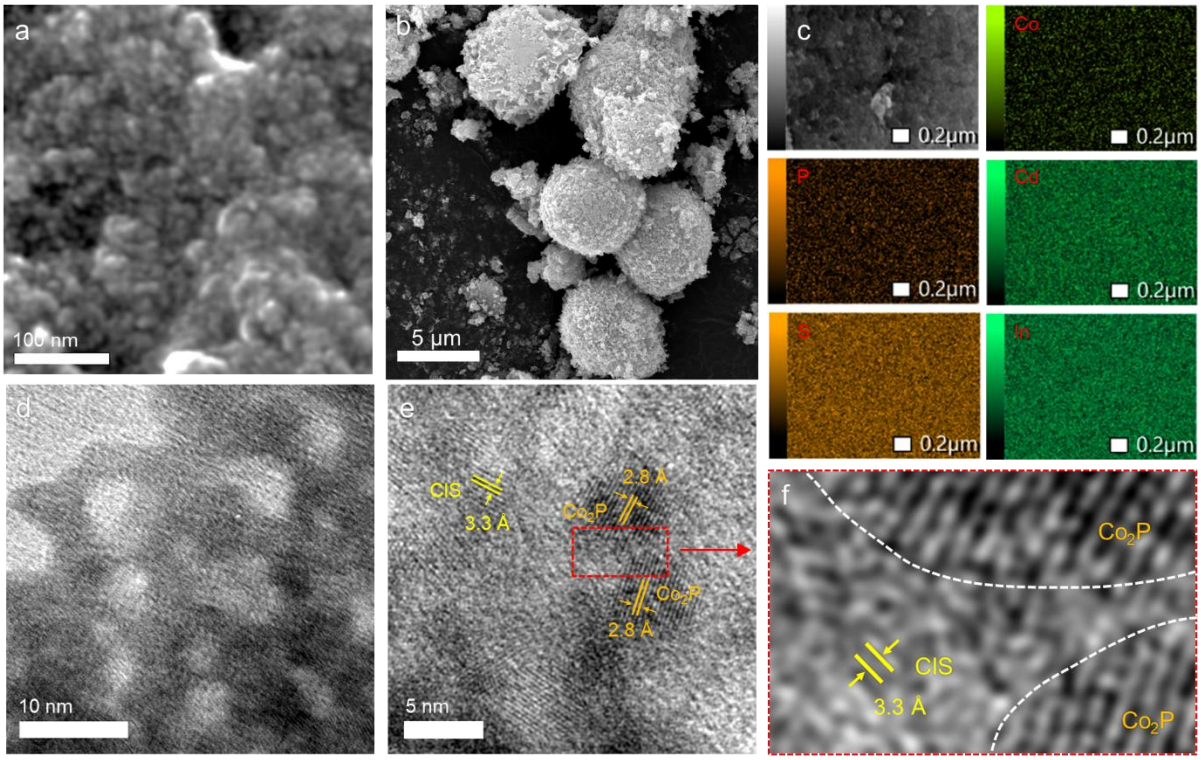

Figure 3-72. (a-b) FE-SEM images of (a) mesoporous 10-CP/CIS and (b) bulk 10-CP/CIS-*m* materials. (c) EDS elemental mapping of Cd, In, S, Co and P elements of 10-CP/CIS NCF. (d) TEM and (e-f) high-resolution TEM (HRTEM) images of mesoporous 10-CP/CIS NCF.

The successful synthesis of Co_2P/CIS composites was further confirmed by X-ray photoelectron spectroscopy (XPS). The XPS survey spectrum of 10-CP/CIS NCF verified the presence of Cd, In, S, Co and P elements (**Figure 3-73a**), in agreement with the results of EDS analysis. It should be noted that the presence of O could due to the partial oxidation of surface atoms as a result of exposure to air. The Cd 3d core-level XPS spectrum of 10-CP/CIS NCF showed a doublet peak of Cd $3d_{5/2}$ and Cd $3d_{3/2}$ spin-orbit states at 405.1 and 411.8 ± 0.1 eV, respectively (**Figure 3-73b**), corresponding to the divalent Cd in metal sulfides [61,88]. Likewise, the In 3d XPS spectrum showed two peaks at 444.8 and 452.4 ± 0.1 eV, corresponding to the In $3d_{5/2}$ and In $3d_{3/2}$ spin-orbit signals of In^{3+} ions, respectively (**Figure 3-73c**). The deconvolution of the S 2p XPS spectrum revealed two signals at 161.7 and 163.3 ± 0.2 eV binding energies, consistent with the metal–S and S–O(OH) bonds, respectively (**Figure 3-73d**) [90]. The low-valence states of $Co^{\delta+}$ and $P^{\delta-}$ elements in Co_2P can be affirmed

by the Co $2p_{3/2}$ and P 2p core-levels at 778.2 eV and 129.6 ± 0.1 eV, respectively. Also, the presence of an additional Co $2p_{3/2}$ and P 2p sub-signals at 780.8 eV and 133.4 ± 0.1 eV refers to the Co–OH/Co–PO_x species, indicating that the surface of Co_2P is partially oxidized likely due to air exposure (**Figure 3-73e-f)** [133,166,167]. The XPS quantitative analysis indicated the nominal composition of 10-CP/CIS NCF, in accord with EDS results, showing a surface Co/In ratio of ~0.28 that corresponds to a ~8.3 wt. % Co_2P loading amount. We also measured in-situ irradiated XPS (ISI-XPS) to understand the charge transfer interactions between the CIS and Co_2P under light irradiation. As can be seen in **Figure 3-73**, when photoexcitation of 10-CP/CIS NCF occurs, a positive shift (by ~0.2 eV) of Cd $3d_{5/2}$ (405.2 eV) and In $3d_{5/2}$ (445.0 eV) XPS spectra and a simultaneously negative shift (by ~0.3-0.5 eV) of Co $2p_{3/2}$ (777.9 eV) and P 2p (129.1 eV) XPS spectra, in comparison to the corresponding ex-situ XPS spectra can be observed. These binding energy shifts clearly confirm a photoelectron transition from Cd/In 3d states of CIS to Co/P 2p states to Co_2P at the interface. These charge redistribution phenomena are beneficial for the separation of photoexcited carriers, leading to improved photocatalytic efficiency.

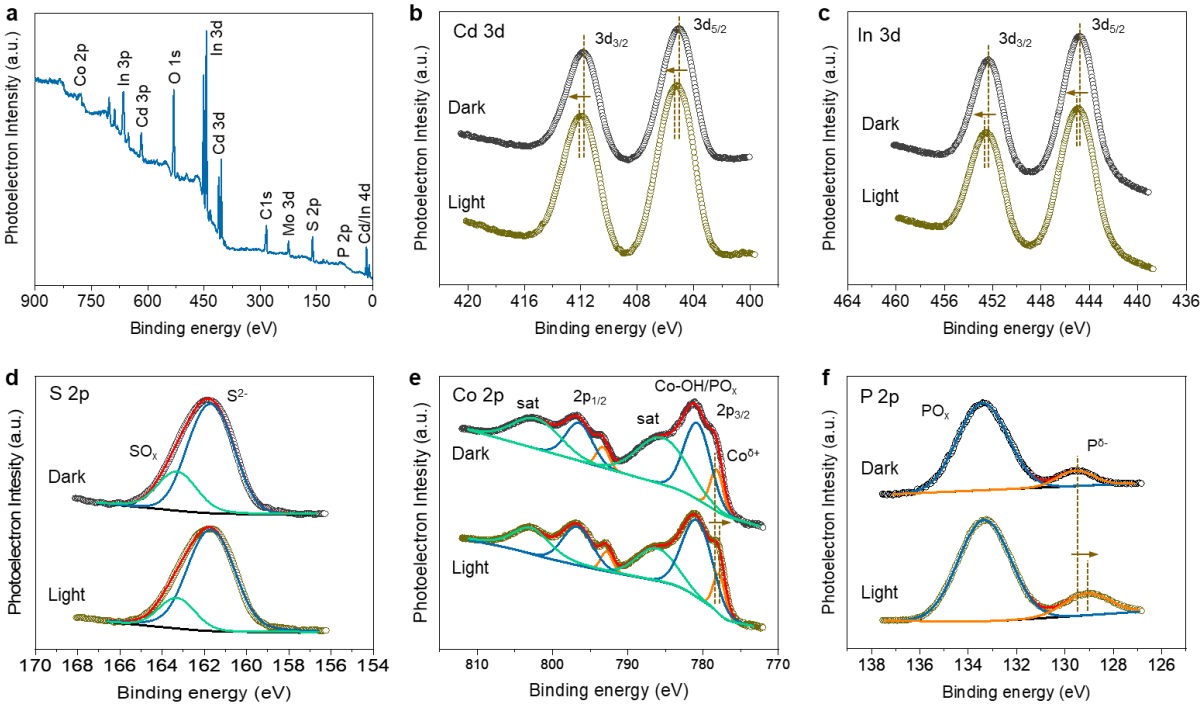

Figure 3-73. (a) XPS survey and high-resolution XPS spectra of (b) Cd 3d, (c) In 3d, (d) S 2p, (e) Co 2p and (f) P 2p core-levels of mesoporous 10-CP/CIS NCF. In-situ XPS spectra were collected under visible light irradiation. The signal of Mo 3d in panel (a) is from the sample holder. The XPS deconvoluted spectra of different chemical species are shown as blue, green and orange curves. The red lines are fits to the experimental data.

The nitrogen adsorption-desorption isotherms of mesoporous CIS and 10-CP/CIS NCFs are compared in **Figure 3-74**, while the N_2 isotherms of the other CP/CIS heterostructures are displayed in **Figure 3-75**. All samples exhibited typical type-IV isotherms with an H_2-type hysteresis loop, according to the IUPAC classification, indicating mesoporous structures with interconnected pores [145]. The hysteresis loop between the adsorption and desorption branches is attributed to the pore blocking effects from cage-type or slit-shaped pores. The CIS NCF exhibited a Brunauer-Emmet-Teller (BET) surface area of 132 $m^2\ g^{-1}$ and a pore volume of 0.12 $cm^3\ g^{-1}$. Upon Co_2P modification, the BET surface area ranges from 55 to 106 $m^2\ g^{-1}$ and pore volume ranges from 0.05 to 0.08 $cm^3\ g^{-1}$ depending on the Co_2P content. Analysis of the adsorption data with non-local density functional theory (NLDFT) method gave quite narrow size distributions of pores with an average diameter of ~5 nm for CIS NCF and ~3.8–4.0 nm for CP/CIS NCFs, in agreement with the interstitial pore spaces observed by TEM (ca. 4–5 nm). The gradual decrease in surface area and pore size for the Co_2P-modified materials is due to the deposition of Co_2P nanoparticles inside the pores of CIS NCF. Nevertheless, all the CP/CIS heterostructures still display an open-pore structure with highly accessible surface area. Comparatively, the surface area of bulk CIS and 10-CP/CIS-*m* microparticles obtained by hydrothermal synthesis is significant low (ca. 25 and 9 $m^2\ g^{-1}$, respectively) (**Figure-3-74**), suggesting the formation of a non-porous structure.

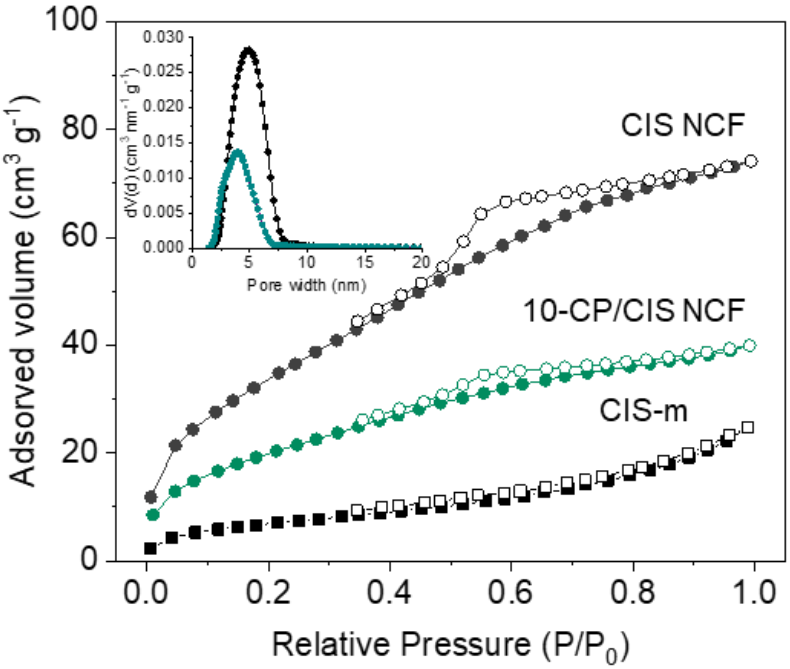

Figure 3-74. N_2 adsorption (filled cycles) and desorption (open cycles) isotherms at –196 ^oC for the mesoporous CIS and 10-CP/CIS NCFs and bulk CIS. Inset shows the corresponding NLDFT pore size distributions calculated from the adsorption isotherms.

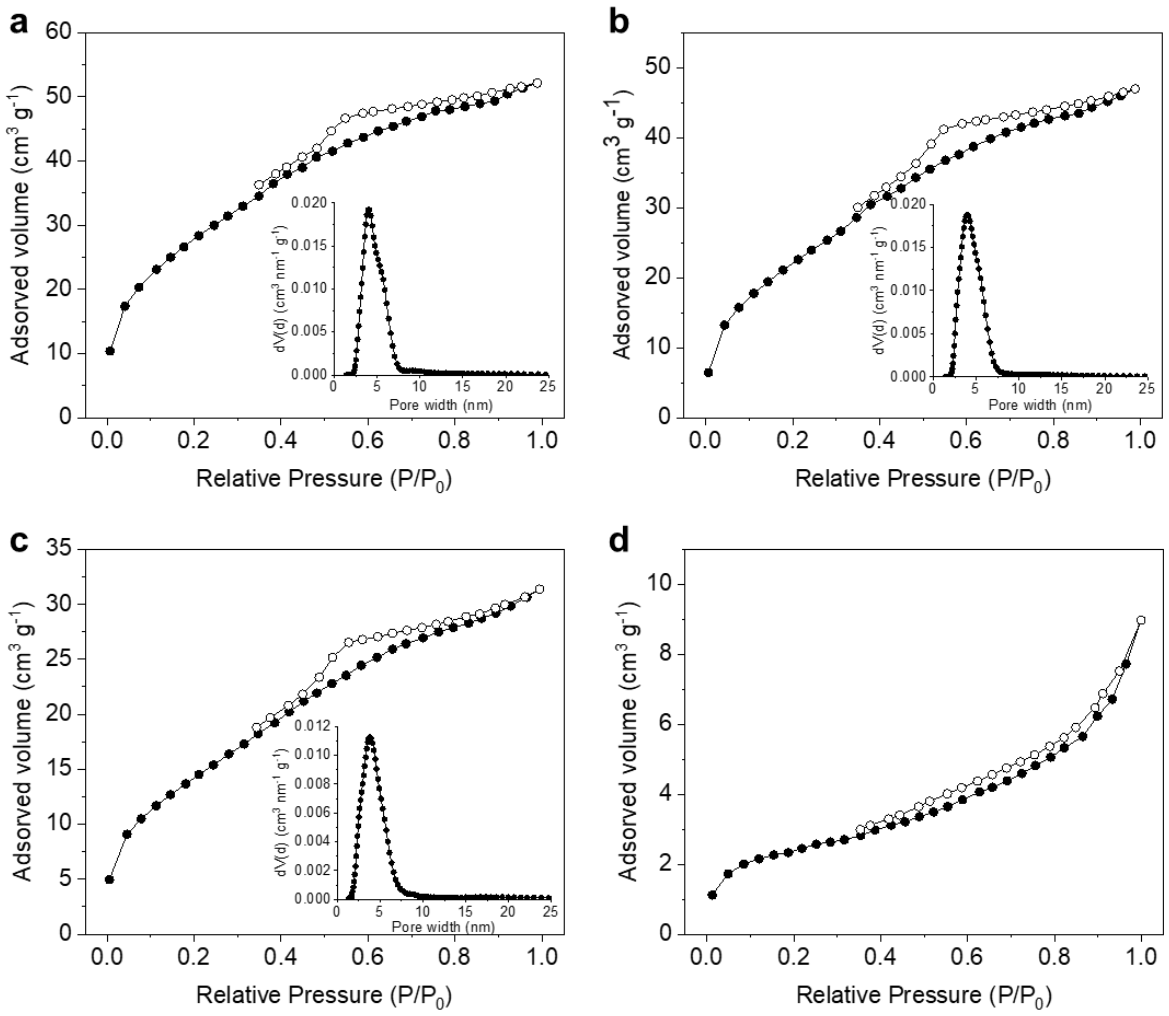

Figure 3-75. N_2 adsorption (filled cycles) and desorption (open cycles) isotherms at –196 ºC for the mesoporous CP/CIS heterostructures containing (a) 5, (b) 7 and (c) 15 wt. % Co_2P content, and (d) 10 wt. % Co_2P-loaded CIS microparticles (10-CP/CIS-*m*). Inset: the corresponding pore-size distribution plots.

The optical properties of the mesoporous samples were investigated with ultraviolet-visible/near IR (UV-vis/NIR) diffuse reflectance spectroscopy. The CIS NCF exhibited a strong optical absorption onset at ~471 nm (2.63 eV), corresponding to the band-edge transition in $CdIn_2S_4$ (**Figure 3-76**). The small grain size of the constituent CIS nanocrystals (ca. 5–7 nm according to TEM analysis) has a considerable effect on the bandgap energy (E_g), which gives rise to larger E_g values than the bulk CIS (2.30 eV). In general, such a blue shift in the optical absorption spectra is a fascinating phenomenon of nanomaterials and it can be explained by the size-induced quantum confinement effects, analogous to those realized in discrete nanoparticles and nano-sized frameworks [146]. On the other hand, the Co_2P-decorated

materials showed a narrower energy gap by ~100–200 meV, which depends on the Co_2P content. Specifically, the E_g of CP/CIS NCFs varies systematically with the Co_2P composition from 2.51 eV for the 5 wt. % Co_2P to 2.42 eV for the 15 wt. % Co_2P-modified sample. This red shift of the energy gap arises from strong interfacial electronic interaction between Co_2P and CIS materials after Co_2P deposition. Besides, the incorporation of Co_2P onto the CIS structure leads to an increase in the visible/near-IR light absorption owing to the light harvesting capability (d-d charge-transfer transitions of tetrahedral Co clusters) of Co_2P [168]. Notably, the as-prepared Co_2P exhibited a systematic absorption over the entire UV-vis/NIR spectrum, which indicates a metallic behavior (**Figure 3-77**). The metallic nature of Co_2P is also confirmed by electrochemical measurements (see chapter 3.2.3). It is worth noting that the E_g of 10-CP/CIS_*m* is about 300 meV smaller (2.26 eV) than the energy bandgap of mesoporous 10-CP/CIS NCF, reasonably due to the larger grain-size composition (ca. 8–10 μm in diameter, see **Figure 3-72b**). The textural and optical properties of the prepared materials are summarized in **Table 3-13**.

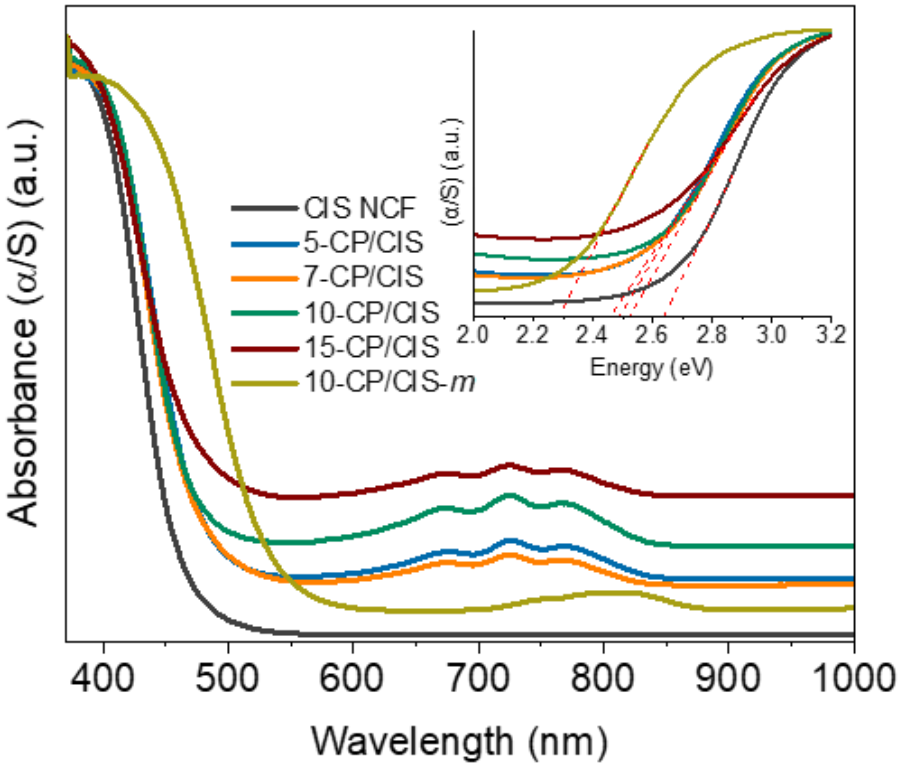

Figure 3-76. UV-vis diffuse reflectance spectra of mesoporous CIS and CP/CIS NCFs, and bulk 10-CP/CIS-*m* material. Inset: the corresponding Kubelka-Munk plots.

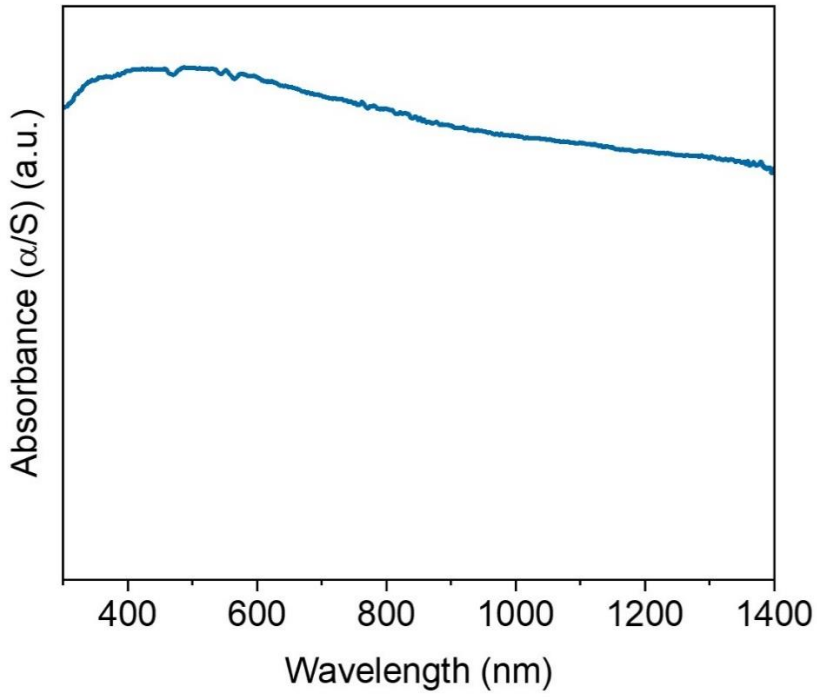

Figure 3-77. UV-vis diffuse reflectance spectra of as-prepared Co_2P nanoparticles.

Table 3-13. Textural and optical properties of mesoporous CIS and CP/CIS NCFs, and 10% Co_2P-modified CIS microparticles (10-CP/CIS-*m*).

Catalyst	**BET surface area ($m^2\ g^{-1}$)**	**Pore volume ($cm^3\ g^{-1}$)**	**Pore size (nm)**	**Energy gap (eV)**
CIS NCF	132	0.12	5.0	2.63
5-CP/CIS NCF	106	0.08	4.0	2.51
7-CP/CIS NCF	87	0.07	3.9	2.49
10-CP/CIS NCF	75	0.06	4.0	2.50
15-CP/CIS NCF	55	0.05	3.8	2.42
CIS bulk	25	0.03	-	2.30
10-CP/CIS-*m*	9	<0.01	-	2.26

3.3.2 Photocatalytic study

The photocatalytic H_2 production activity of the prepared materials was investigated under visible light irradiation ($\lambda \geq 420$ nm) in an air-tight photocatalytic reactor cell, using triethanolamine (TEOA, 10% v/v) as the hole scavenger. A comparison of the photocatalytic activities of mesoporous CIS decorated with different amount of Co_2P is shown in **Figure-3-**

78. For comparative studies, the photocatalytic H_2-evolution activities of CIS microparticles and 10-CP/CIS-*m* bulk catalysts were also investigated under identical conditions. Interestingly, the CIS NCF exhibited a H_2 evolution rate of 110 μmol h^{-1}, which is 220 times larger than the bulk analogue (~0.5 μmol h^{-1}), demonstrating a remarkable enhancement of the H_2 evolution efficiency. Upon Co_2P modification, the evolution rate of H_2 is significantly raised to 417 μmol h^{-1} by deposition of 10 wt. % amount of Co_2P. This activity is an enhancement by a factor of 3.8x compared to the pristine CIS sample. It should be noted that, even a small amount of Co_2P (5 wt. %) has a crucial impact in the photocatalytic activity, affording a H_2 evolution rate of ~250 μmol h^{-1}. Deposition of higher concentration of Co_2P (15 wt. %) results to a slight decrease in the photocatalytic performance (~205 μmol h^{-1}), likely due to the light-shielding effect of Co_2P (incident light absorbed by Co_2P and not by CIS) and rapid electron-hole recombination at the catalyst's interface. Evidently, coupling of Co_2P and CIS materials remarkably enhances the charge separation efficiency and increases the availability of catalytic active sites for water reduction, as confirmed by photoluminescence and electrochemical measurements (see chapter 3.3.3). The refence 10-CP/CIS-*m* catalyst exhibited poor photocatalytic performance, yielding a H_2 evolution rate of only 4.5 μmol h^{-1}. All these results consistently indicate that the formation of Co_2P-CIS heterostructures with large internal surface area and nano-grain composition increases the number of active sites and shorten the diffusion path of photoexcited carriers to the solid/liquid interface, thereby increasing the photocatalytic performance. Furthermore, the presence of organic molecules in the porous structure (ca. 9 wt. %) has a negligible effect on the accessibility of the pore surface and active sites of the catalyst. As a comparison sample, the as-prepared Co_2P particles showed no photocatalytic hydrogen evolution activity under the same experimental conditions (results not shown). Also, photocatalytic control experiments showed that no hydrogen evolution was observed in the absence of the catalyst or in the dark, confirming that the catalyst and light irradiation were indispensable for the photocatalytic water reduction reaction. The origin of hydrogen evolution was also verified by a controlled photocatalytic reaction over the best catalyst (10-CP/CIS NCF) in the presence of 0.1 M sodium iodate ($NaIO_3$) and 10% (v/v) TEOA, which acted as electron and hole scavengers, respectively. The reduction of $NaIO_3$ is thermodynamically more favorable reaction than the reduction of water (the reduction potential is 1.2 V for $NaIO_3$ versus 0 V for water, at pH 0), offering the potential to investigate the competitive TEOA oxidation effect on the hydrogen generation. It has been suggested that TEOA oxidation may produce acetaldehyde (CH_3CHO) and diethanolamine ($HN(CH_2CH_2OH)_2$), where sequential oxidation of these products could generate hydrogen [169,170]. Interestingly, through this photocatalytic

experiment no hydrogen production was observed (by gas chromatography) even after a 3-hour illumination period, confirming that the hydrogen evolution exactly generated by water reduction reaction.

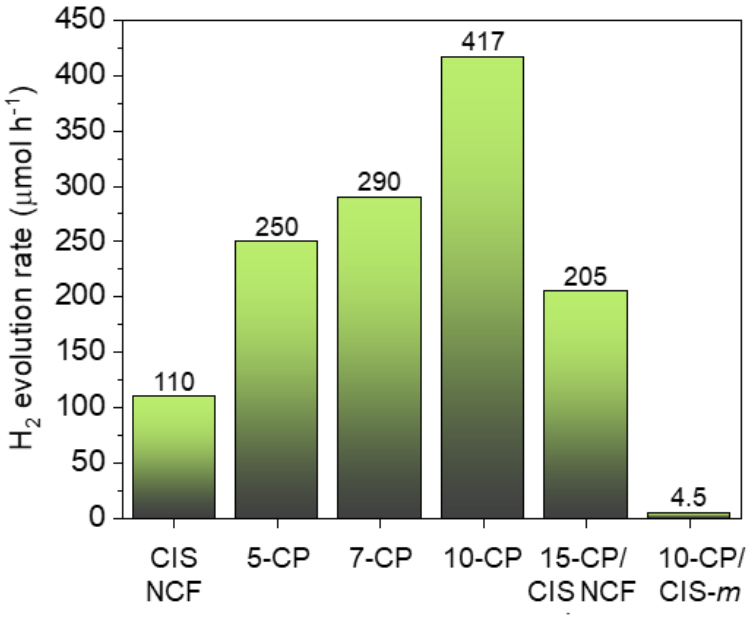

Figure 3-78. Comparison of photocatalytic hydrogen production rates of mesoporous CIS and CP/CIS NCFs. The corresponding H_2 production rate of 10-CP/CIS-*m* is also given.

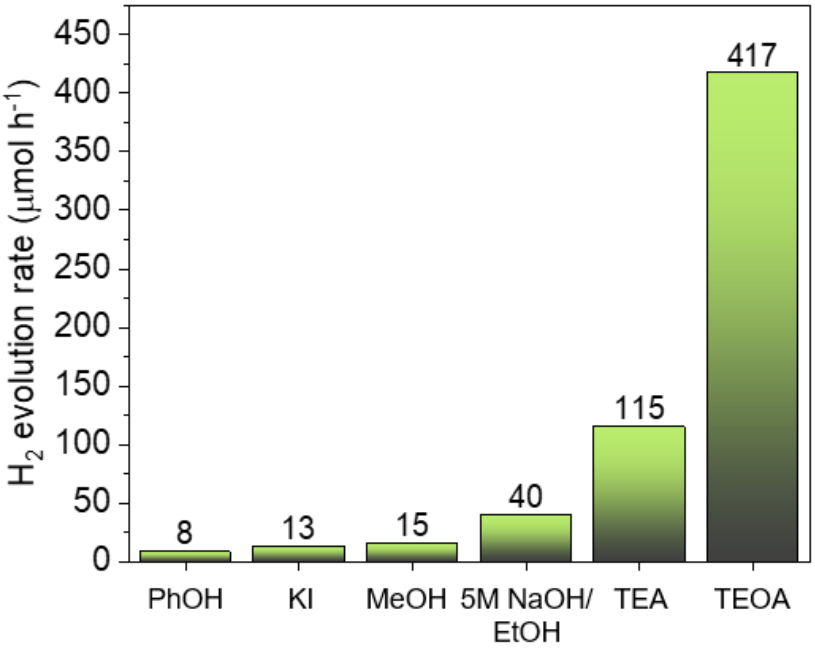

Figure 3-79. Photocatalytic hydrogen generation activity of mesoporous 10-CP/CIS NCF (1 mg mL^{-1}) using various sacrificial reagents: phenol (PhOH, 0.35 M), KI (0.05 M), methanol (MeOH, 10% v/v), 5 M NaOH/ethanol (10% v/v), triethylamine (TEA, 10% v/v) and triethanolamine (TEOA, 10% v/v).

The influence of difference sacrificial reagents and catalyst concentration on the photocatalytic hydrogen evolution activity was also investigated. The photocatalytic reactions with various hole scavengers (at fixed catalyst load), such as phenol (0.35 M), KI (0.05 M), methanol (10% v/v), 5 M NaOH/ethanol (10% v/v), triethylamine (10% v/v) and triethanolamine (10% v/v), produced notable variations in the H_2 production rates (**Figure 3-79**), indicating that the oxidation process is the rate-limiting step in the overall photocatalytic reaction. It was found that the photocatalytic reaction proceeds at a faster rate with TEOA as sacrificial reagent. Also, the photocatalytic performance of 10-CP/CIS NCF over different mass loadings of catalyst was investigated (**Figure 3-80**). A substantial increase of H_2 generation rate was observed with increasing the catalyst load, until reacting a maximum rate at 1 mg mL^{-1}. When exceeding this concentration, the photocatalytic activity declines due to the increased light scattering effect by the catalyst's particles. Overall, the 10-CP/CIS NCF catalyst at the optimal conditions exhibits an exception photocatalytic H_2 evolution rate of 20.9 mmol g_{cat}^{-1} h^{-1} with an apparent quantum yield (AQY) of 56.1% under 420 ± 10 nm monochromatic light excitation, assuming 100% absorption of incident photons. To our knowledge, the photocatalytic activity of 10-CP/CIS NCF is among the highest reported activities for other high-performance thiospinel based-catalysts. **Table I** in annex I provides a comparison of the H_2 evolution activity of our catalysts with previously reported catalysts.

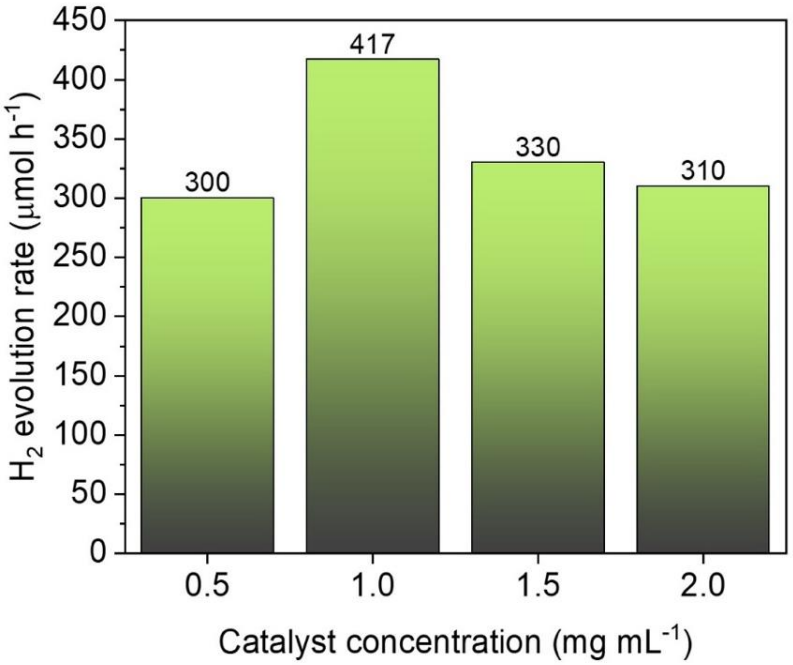

Figure 3-80. Photocatalytic hydrogen generation activity of mesoporous 10-CP/CIS NCF in various catalyst's concentrations. Reaction conditions: 10–40 mg of catalyst, 20 mL of TEOA solution (10% v/v), visible-light irradiation (300 W Xe lamp, $\lambda \geq 420$ nm), 20 ± 2 °C.

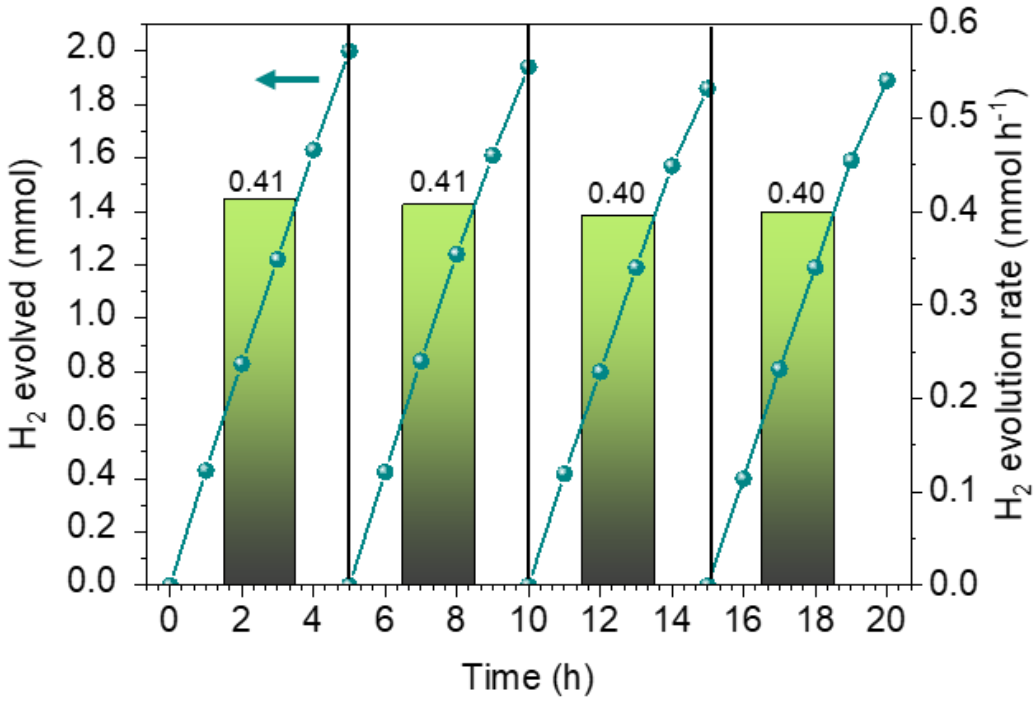

Figure 3-81. Time courses of photocatalytic hydrogen evolution (lines) and hydrogen production rates (columns) during the stability experiments over 10-CP/CIS NCF. The H_2 evolution rates were averaged over 5 h of visible-light irradiation.

The stability of 10-CP/CIS NCF catalyst was evaluated by recycling photocatalytic reactions. After each photocatalytic test, the catalyst was isolated by centrifugation and then re-dispersed in a newly prepared TEOA solution (10% v/v). As can be seen in **Figure 3-81**, 10-CP/CIS NCF shows a remarkable photo-corrosion resistance with no detectable H_2 evolution decay even after four 5-hour runs. During this period, the catalyst affords a constant H_2 evolution rate of ~406 μmol h^{-1} (within 3% experimental error), thus indicating high photochemical stability and recyclability. A small discrepancy in photoactivity after two runs may be attributed to minor photo-corrosion and/or mass loss during the recycling process. In addition, the chemical and structural stability of 10-CP/CIS NCF after photocatalysis was studied with various analytic techniques. Elemental EDS analysis revealed that the reused catalyst maintained its chemical composition, displaying Cd:In:S atomic ratios of ~1:2:4 and a Co_2P weight loading percentage (wt. %) of 9.87% (**Figure 3-82a**). Also, the XRD analysis of the recycled catalyst showed no obvious charges in the crystal structure (**Figure 3-81b**). Moreover, XPS measurements further supported the high photochemical stability of the Co_2P-$CdIn_2S_4$ heterostructure (**Figure 3-83**). Specifically, the Cd 3d spectrum of the reused 10-CP/CIS NCF catalyst displayed a doublet peak at 404.9 and 411.7 ± 0.1 eV binding energies,

corresponding to the Cd $3d_{5/2}$ and Cd $3d_{3/2}$ core levels of Cd^{2+} ions. The In 3d XPS spectrum showed two peaks at 444.9 and 452.5 ± 0.1 eV due to the In $3d_{5/2}$ and In $3d_{3/2}$ core-level peaks of In^{3+} chemical state. The S 2p spectrum displayed a prominent peak at 161.5 ± 0.1 eV due to the S^{2-} valence state and a shoulder peak at 162.4 ± 0.2 eV, corresponding to the surface SO_x species. In the Co 2p region, the spin-orbit doublet signal at 778.2 and 792.7 ± 0.1 eV was assigned to the Co $2p_{3/2}$ and Co $2p_{1/2}$ core-levels of the partially charged $Co^{\delta+}$ ($0 < \delta < 2$) in Co_2P, while the signals at 781.6 and 797.0 ± 0.1 eV, along with the satellite peaks at 786.5 and 803.1 ± 0.2 eV, were attributed to the partially oxidized Co species (Co–OH/PO_x) at the surface of catalyst.

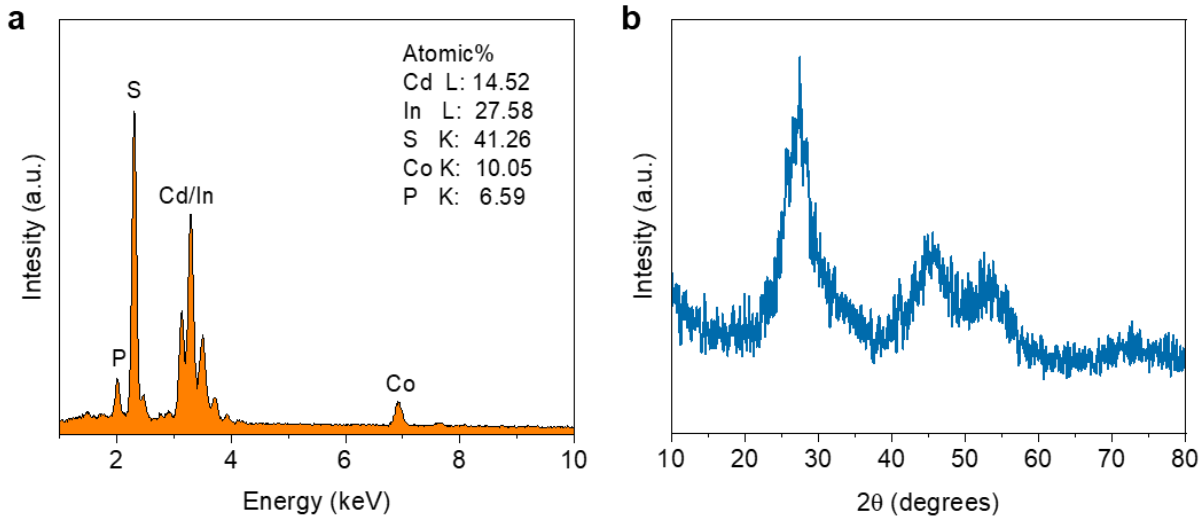

Figure 3-82. (a) (a) Typical EDS spectrum and (b) XRD pattern of the 10-CP/CIS NCF catalyst retrieved after 20 hours of photocatalytic reaction. EDS analysis indicates a 9.87 wt % Co_2P content.

Similar to this, the P 2p XPS spectrum showed a peak at 131.0 ± 0.1 eV and a broad signal at 133.6 ± 0.2 eV, which can be assigned to the slightly negatively charged $P^{\delta-}$ atoms and surface oxidized PO_x species of Co_2P, resulting from air exposure. The presence of Co suboxide ($CoO(OH)_x$) and phosphate-like (PO_x) species has been suggested to play an important role towards hydrogen evolution reaction [171,172]. In particular, such oxide complexes may favor the dissociative adsorption of water (through nucleophilic attack of OH^- on Co–O/OH) and the electrochemical hydrogen evolution reaction (by donating electrons to the adsorbed H^+), thus providing more active sites to the catalyst. Nevertheless, the N_2 physisorption isotherms indicated a minor reduction in porosity after catalysis (**Figure 3-84**). The recycled catalyst exhibited a slightly lower BET surface area of 59 m^2 g^{-1} and narrower pore sizes of ~3.8 nm

compared to the fresh one (ca. 75 m^2 g^{-1} surface area; ~4 nm pore size). This slight decrease in porosity can be attributed to minor photo-corrosion of the sulfide lattice and/or rearrangement of CIS nanocrystals in the mesoporous structure. Overall, the 10-CP/CIS NCF photocatalyst attains a remarkable photocatalytic performance, giving an average hydrogen evolution rate of ~417 μmol h^{-1} (or 20.9 mmol g_{cat}^{-1} h^{-1}) and an AQYs of 56.1% at 420 nm.

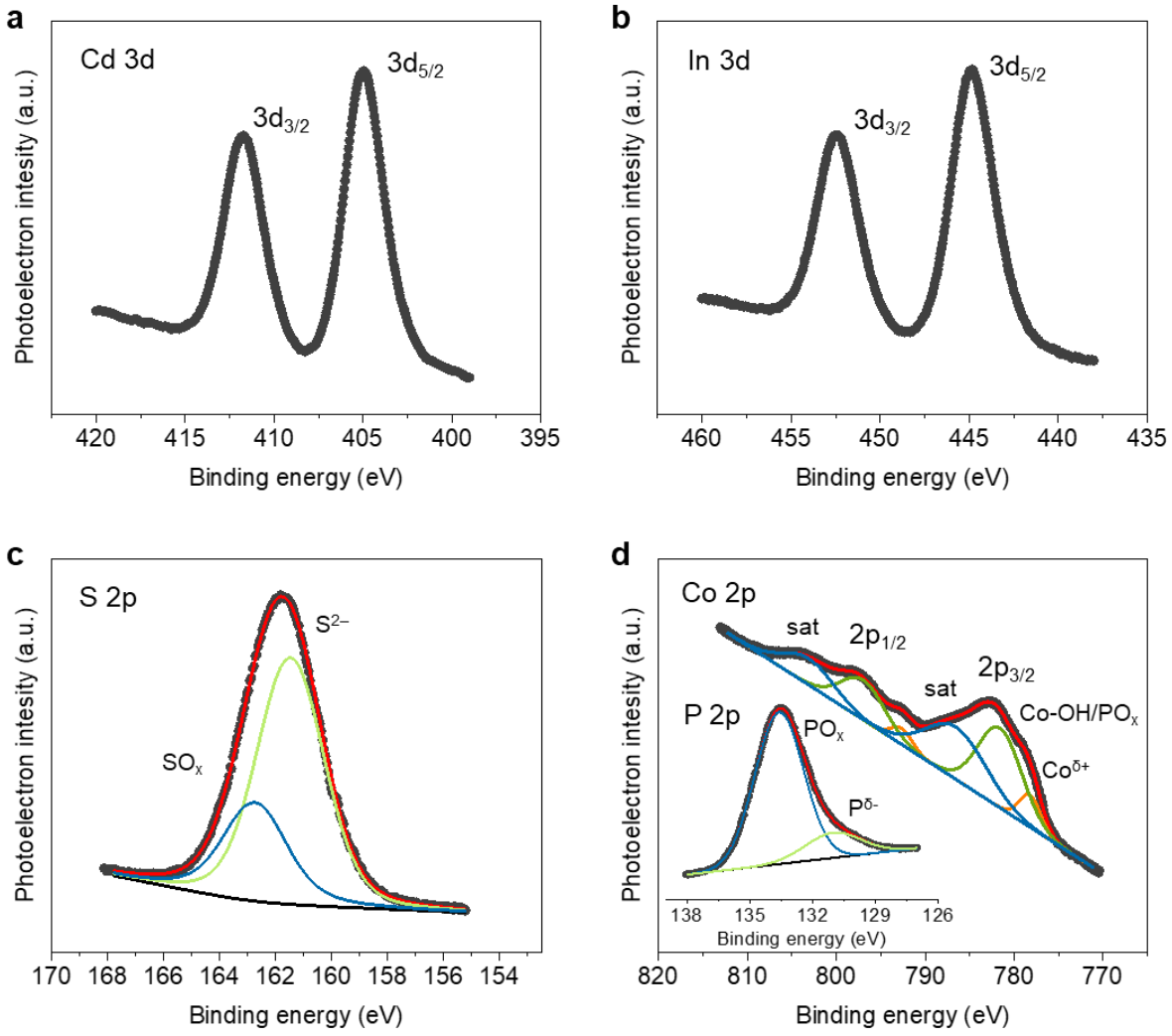

Figure 3-83. High-resolution XPS spectra of (a) Cd 3d, (b) In 3d, (c) S 2p and (d) Cp 2p and P 2p core-levels of the reused 10-CP/CIS NCF catalyst. The XPS deconvoluted spectra of different chemical species are represented as blue, green and orange curves. The red lines are fits to the experimental data.

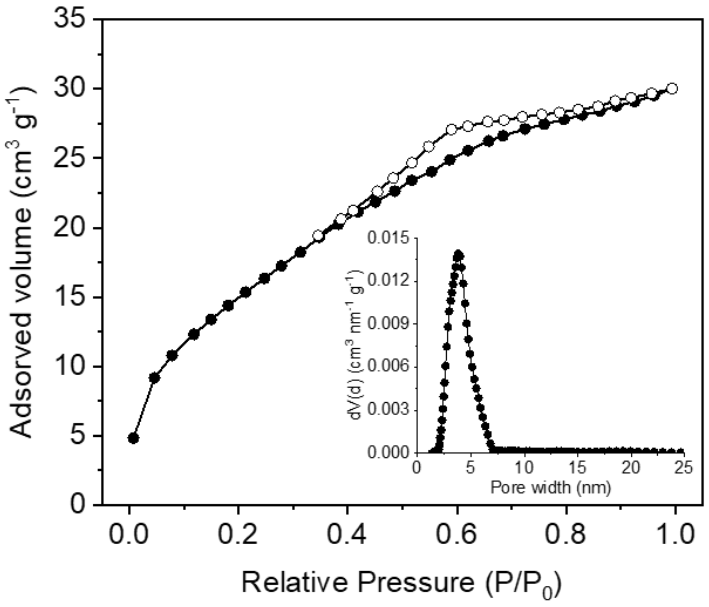

Figure 3-84. Nitrogen adsorption and desorption isotherms at –196 ºC of 10-CP/CIS NCF catalyst after 20 hours of hydrogen evolution reaction. Inset: The corresponding NLDFT pore size distribution calculated from the adsorption isotherm.

3.3.3 Charge transfer and reaction mechanism

The electronic properties of the prepared catalysts were assessed via Mott-Schottky plots, that is, the reciprocal square capacitance ($1/C_{sc}^2$) versus the applied potential (E). The flat-band potential (E_{FB}) of the catalysts was determined by measuring the x-axis intercept of the $1/C_{sc}^2$–E lines, as can be seen in **Figure 3-85a**. All the E_{FB} values are referred to the reversible hydrogen electrode (RHE) at pH 7 (**Table 3-14**). The positive slope of Mott-Schottky plots in all samples indicates that CIS is an n-type semiconductor, in agreement to previous reports [61,64,173]. Considering that in heavily doped n-type semiconductors the E_{FB} is positioned slightly more positive (~0.1–0.3 eV) relative to the conduction band (CB), a rational band-edge structure diagram for each catalyst can be obtained. The valence band energy (E_{VB}) of the catalysts was determined by subtracting the bandgap energy (as estimated from UV-vis/NIR spectra) from the E_{FB}. The results indicated that the mesoporous CIS NCF has an E_{FB} of –0.88 V, which is well above the reduction potential for hydrogen, whereas Co_2P modification of the surface of CIS leads to a remarkable change in the band-edge structure of $Co_2P/CdIn_2S_4$ heterostructures (**Figure 3-85b**). In particular, a downward tendency of the E_{FB} level can be inferred from –0.79 to –0.60 V with increasing the loading amount of Co_2P from 5 to 15 wt.

%. The anodic shift of E_{FB} is due to the formation of Mott-Schottky nanojunctions between Co_2P and CIS nanoparticles upon contact, leading to an electron migration from CIS to Co_2P until their Fermi levels (E_F) reach equilibrium. The work function of Co_2P is ~4.6 eV vs vacuum level [133,174], which is much lower than the electrochemical potential of CIS NCF (ca. 4.1 eV vs vacuum level). Overall, the CIS-to-Co_2P electron injection can cause a potential drop at the $Co_2P/CdIn_2S_4$ interface (from CIS to Co_2P), resulting in a decrease in the donor density (N_D) within the CIS semiconductor. Such charge-carrier redistribution between CIS and Co_2P could raise the Fermi level of Co_2P, thereby facilitating a better electron transfer from the Co_2P surface to participate in redox reactions. In accord with this, the inferred N_D values determined from the Mott-Schottky plots showed the following trend: ~1.1×10^{18} cm^{-3} for CIS NCF and ~$1.8–9.1 \times 10^{17}$ cm^{-3} for Co_2P-modified catalysts (**Table 3-14**). The gradual decrease of N_D with the deposition of Co_2P confirms that an electron delocalization from mesoporous CIS to metallic Co_2P occurs, which is in good agreement with the observed anodic shift of the CIS's E_{FB} level. In comparison with the mesoporous 10-CP/CIS NCF, the 10-CP/CIS-*m* bulk reference sample exhibited a less anodic shift of the E_{FB} level (~ –0.67 V) and a lower N_D concentration loss (~1.3×10^{17} cm^{-3}) compared to the pristine bulk CIS (E_{FB} ~ –0.77 V, N_D ~ 6.6×10^{17} cm^{-3}, see **Figure 3-62**), indicating that the electronic interactions between the Co_2P and CIS microparticles are weak. Such a poor electronic communication results in a depressed charge transfer from CIS to Co_2P.

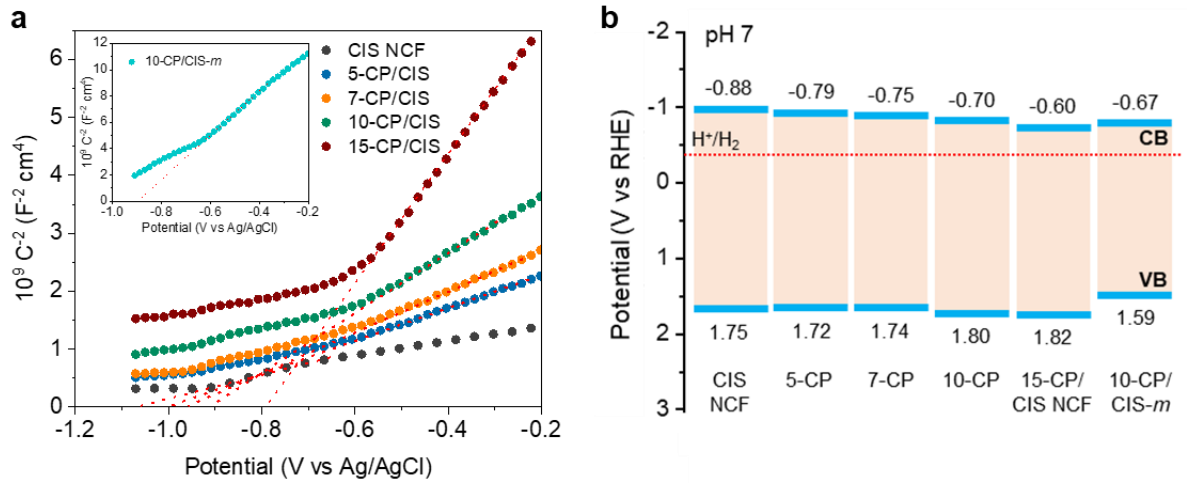

Figure 3-85. (a) Mott-Schottky plots, (b) energy band diagrams for the mesoporous CIS and CP/CIS NCFs and 10-CP/CIS_*m* samples (VB: valence band, CB: conduction band, red line: H^+/H_2 redox potential).

Table 3-14. Electrochemical properties determined from EIS analysis for the mesoporous CIS and CP/CIS NCFs, and bulk CIS and 10-CP/CIS-*m* microparticles.

Sample	E_{FB}	E_{VB}[a)]	Donor density	R_{ct} (Ω)
	(V vs RHE, pH 7)		(N_D, cm^{-3})	
CIS NCF	–0.88	1.75	1.1×10^{18}	3464
5-CP/CIS NCF	–0.79	1.72	9.1×10^{17}	226
7-CP/CIS NCF	–0.75	1.74	6.5×10^{17}	174
10-CP/CIS NCF	–0.70	1.80	4.3×10^{17}	129
15-CP/CIS NCF	–0.60	1.82	1.8×10^{17}	282
10-CP/CIS-*m*	–0.67	1.59	1.3×10^{17}	10925
CIS-m	–0.77	1.58	6.6×10^{17}	-

[a)] The valence band energy (E_{VB}) was calculated from E_{FB}–E_g.

The charge-transfer kinetics at the interface of catalysts were investigated with electrochemical impendence spectroscopy (EIS). The EIS Nyquist plots of the catalysts (drop-casted on FTO substrate) measured in 0.5 M Na_2SO_4 aqueous solutions are depicted in **Figure 3-86**. The corresponding EIS spectra were fitted using a simple equivalent circuit model composed of the electrolyte resistance (R_s), constant phase element (CPE) and charge-transfer resistance (R_{ct}) (**Figure 3-86**, **inset**). All the Co_2P-modified samples exhibited a much smaller R_{ct} values, ranging from 129 to 282 Ω, than the pristine CIS NCF sample (3464 Ω) (**Table 3-15**). The decrease of the R_{ct} resistance indicates that coupling of CIS mesoporous with highly conductive Co_2P nanoparticles provides improved interfacial charge-transfer kinetics, which promotes the photocatalytic hydrogen evolution reaction. Specifically, the Co_2P acts as an effective electronic mediator to facilitate the transfer of photogenerated electrons from CIS to the active sites. The ultra-high conductivity of Co_2P is unveiled by EIS and voltage-current (J–V) experiments. The EIS analysis of Co_2P showed a very low R_{ct} resistance of about 33 Ω (**Figure 3-87a**), suggesting high electronic conductivity, which is crucial for improved catalytic performance. Similarly, four-probe J–V measurements performed on a pressed pellet of Co_2P showed a linear response in the current range of –100 to +100 mA (**Figure 3-87b**), further confirming the ohmic conduction [175]. By comparison with the other prepared catalysts, 10-CP/CIS NCF exhibited the lowest R_{ct} value (129 Ω), which indicates a superior interfacial charge transfer in this catalyst, consistent with its superior photocatalytic activity. On the other hand, 10-CP/CIS-*m* bulk catalysts suffers from enormous charge transfer inefficiency, as evidenced by its high R_{ct} value of 10925 Ω (**Figure 3-86**). This accounts for poor electronic contact between Co_2P and CIS microparticles – a behavior less relevant to the mesoporous

CP/CIS materials due to the existing nanoscale junctions. Apparently, the above results highlight the importance of the synthetic method in modulating the electronic interactions and interfacial charge-transfer kinetics of $Co_2P/CdIn_2S_4$ catalysts.

Table 3-15. Nyquist equivalent circuit fitted parameters of the prepared catalysts.

Sample	**R_s (Ω)**	**C_{dl} (F)**	**R_{ct} (Ω)**	**x^2**
CIS NCF	15.12	37.24×10^{-6}	3464	2.2×10^{-4}
5-CP/CIS NCF	15.30	55.37×10^{-6}	226	3.9×10^{-4}
7-CP/CIS NCF	16.57	47.82×10^{-6}	174	1.2×10^{-4}
10-CP/CIS NCF	18.64	54.26×10^{-6}	129	7.5×10^{-4}
15-CP/CIS NCF	15.27	30.68×10^{-6}	282	1.5×10^{-4}
10-CP/CIS-*m*	14.68	86.82×10^{-6}	10925	2.5×10^{-4}
Co_2P nanoparticles	15.28	90.94×10^{-6}	33	7.2×10^{-4}

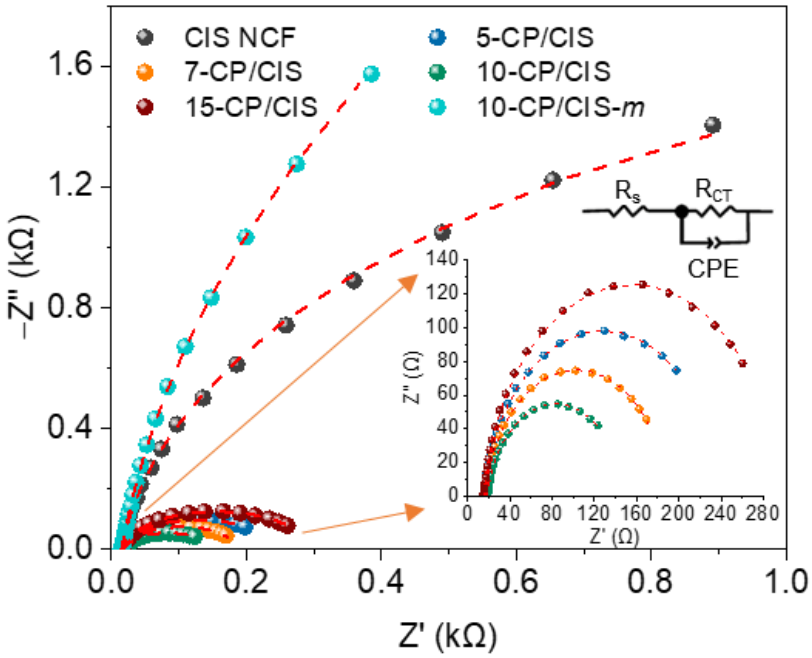

Figure 3-86. Nyquist plots (Inset: magnification of the Nyquist plots and equivalent circuit model used to fit the EIS data) for the mesoporous CIS and CP/CIS NCFs, and bulk 10-CP/CIS-*m* catalysts.

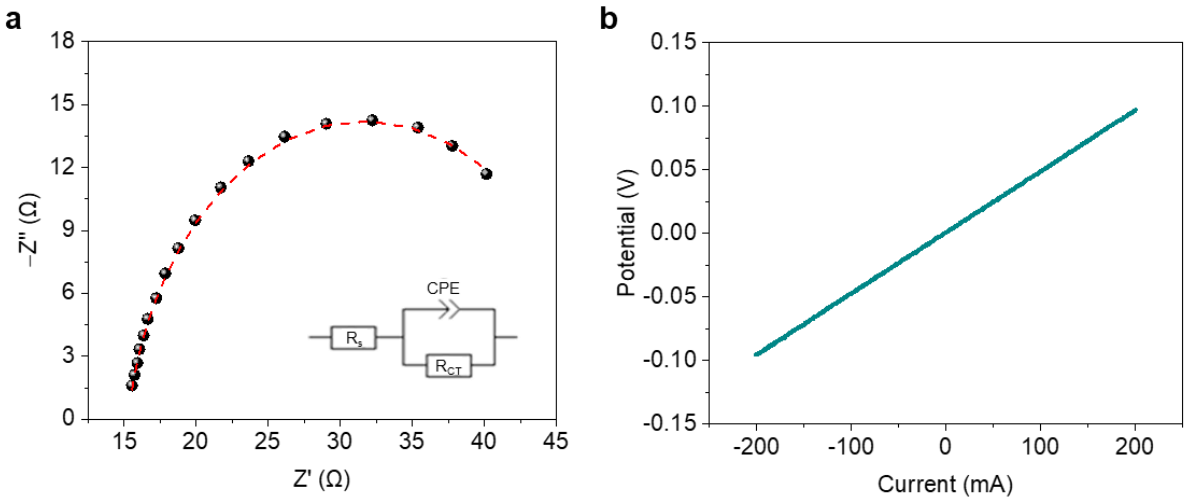

Figure 3-87. (a) EIS Nyquist plot of Co_2P nanoparticles. Inset: equivalent Randles circuit model [R_s(CPE/R_{ct})] used to fit the EIS data. (b) Voltage-current (I–V) curve of Co_2P nanoparticles. The I–V measurement was carried out on compressed pellet by a four-probe method.

The dynamics of the photogenerated charge carrier recombination and migration were investigated by steady-state photoluminescence (PL) and time-resolved PL (TRPL) spectroscopy. The PL spectrum of CIS NCF is depicted in **Figure 3-88a**, in which the intense peak at 468 nm (2.65 eV) is due to the band-edge emission and the weak features at 483 nm (2.57 eV) and 494 nm (2.51 eV) correspond to the radiative relaxations of excitons through sub-bandgap trap states. **Figure 3-88b** shows a comparison of the TRPL spectra measured near the band-edge emission (E_w) of the mesoporous CIS and CP/CIS NCFs and bulk 10-CP/CIS-*m* at 468 nm and 545 nm emission wavelength, respectively. Assuming negligible Auger-type recombination, the lifetime of the photoexcited charge carriers could be determined by fitting the PL decay data with a biexponential function: $I(t) = \alpha_1 \cdot e^{-(\tau/\tau 1)} + \alpha_2 \cdot e^{-(\tau/\tau 2)}$, where the parameters α_1 and α_2 are the relative amplitudes of each lifetime component, and τ_1 and τ_2 are the radiative recombination lifetimes of the trap-assisted (fast) and band-to-band (slow) decay components, respectively. From the TRPL data, the average charge carrier lifetime (τ_{av}) of 10-CP/CIS NCF was found to be 4.06 ns, which is significantly longer than that of unmodified CIS NCF (2.89 ns). Furthermore, the deposition of Co_2P significantly inhibits the electron-hole recombination due to efficient electron migration from the bulk region to the surface. Using the average PL decay times of the samples, we further calculated the rate constant of Co_2P/CIS interfacial electron transfer as $k_{et} = 1/\tau_{10\text{-CP/CIS}} - 1/\tau_{CIS}$, where $1/\tau_{CIS}$ is the exciton recombination rate (k_r) and $1/\tau_{10\text{-CP/CIS}}$ corresponds to the sum of the rate recombination and electron transfer processes

[176,177]. From the above analysis, the band-edge k_{et} (electron-transfer pathway 1, ET1) was estimated to be ~0.1×10^9 s^{-1}. Also, the corresponding electron transfer efficiency (n_{et}) from CIS to Co_2P, which is defined as $n_{et} = k_{et}/(k_{et}+k_r)$, was found to be ~29%. Notably, the PL decay kinetics of the band-edge bleaching of bulk 10-CP/CIS-*m* (3.57 ns) shows a remarkably shorter average lifetime than mesoporous 10-CP/CIS NCF, suggesting that the nanoporous nature and the formation of Co_2P/CIS nanojunctions are very effective for suppressing the bulk carrier recombination. A careful examination of the mesoporous 10-CP/CIS NCF photoluminescence (PL) decay results revealed a significantly smaller τ_1-component of PL decay (32.8%) compared to the pristine CIS NCF (79.0%) and bulk 10-CP/CIS-*m* analogues (70.0%), which is attributed to its lower defect trapping. The TRPL decay parameters are summarized in **Table 3-16**. To better understand the inter-band photoemission processes, PL decay measurements at the emission channels attributed to the trapping states were also performed. The trap-state PL lifetimes measured at E_W= 483 (ET2) and 494 (ET3) nm wavelengths for 10-CP/CIS NCF were found to be 0.94 and 0.92 ns, respectively (**Figure 3-88b**, **inset**), which are about two times longer than those for unmodified CIS NCF (0.44 and 0.51 ns). The CIS trap-mediated electron transfer rate (k_{et}) and efficiency (n_{et}) into Co_2P were determined to be ~1.21×10^9 s^{-1} and 53% for ET2 and ~0.87×10^9 s^{-1} and 45% for ET3, respectively, which are markedly higher than those observed by direct CB edge electron injection. The acceleration of both band-edge and trap-state PL decay kinetics indicates that passivation of CIS surface with Co_2P creates specific electronic interactions between the Co_2P nanoparticles and CIS surface-related emission centers. These interactions facilitate the separation of electron-hole pairs by enabling ultrafast electron transfer from CIS to Co_2P. The CP/CIS NCFs heterostructures undergo this phenomenon in a matter consistent with their efficient separation and migration of photoinduced carriers by virtue of their multi-pathway interfacial electron-transfer processes. These results were also confirmed by transient photocurrent (TPC) measurements. Specifically, **Figure 3-89** shows that mesoporous 10-CP/CIS NCF exhibits a higher photocurrent response compared to both the mesoporous CIS NCF and the bulk 10-CP/CIS-*m*. These charge-transfer dynamics have important implications for the water reduction reaction, as they facilitate the delocalization of electron-hole pairs under light irradiation, enabling them to participate effectively in surface redox reactions.

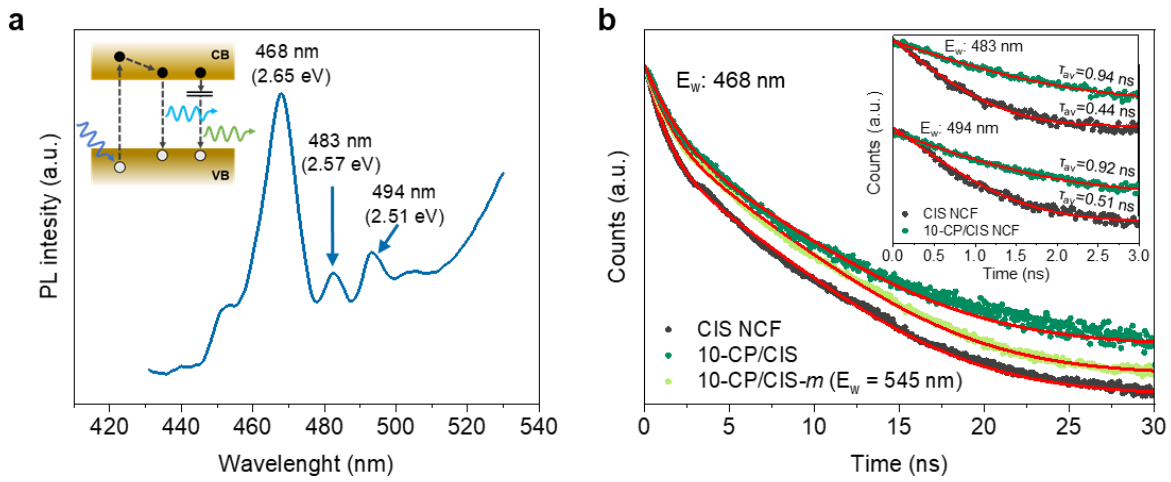

Figure 3-88. (a) Room-temperature steady-state PL spectrum of mesoporous CIS NCF (excitation 380 nm). Inset: electron-hole recombination pathways in CIS. (b) TRPL spectra of mesoporous CIS and 10-CP/CIS NCFs at 468 nm and bulk 10-CP/CIS-*m* at 545 nm emission wavelength using a 375 nm laser pulse excitation. Inset: TRPL spectra of mesoporous CIS and 10-CP/CIS NCFs measured at 483 nm and 494 nm emission wavelengths. The red lines are fit to the experimental data.

Table 3-16. Time-resolved photoluminescence decay parameters of mesoporous CIS and 10-CP/CIS NCFs, and bulk 10-CP/CIS-*m*.

Sample	**τ_1 (ns)**	**τ_2 (ns)**	**α_1 (%)**	**α_2 (%)**	**τ_{av}[a] (ns)**
CIS NCF	0.74	4.28	79.0	21.0	2.89
10-CP/CIS NCF	0.90	4.38	32.8	67.2	4.06
10-CP/CIS-*m*	1.10	4.85	70.0	30.0	3.57

[a]The average lifetime (τ_{av}) was determined by the equation: $\tau_{av} = (\sum_i \alpha_i \tau_i^2)/(\sum_i \alpha_i \tau_i)$ (i = 1, 2).

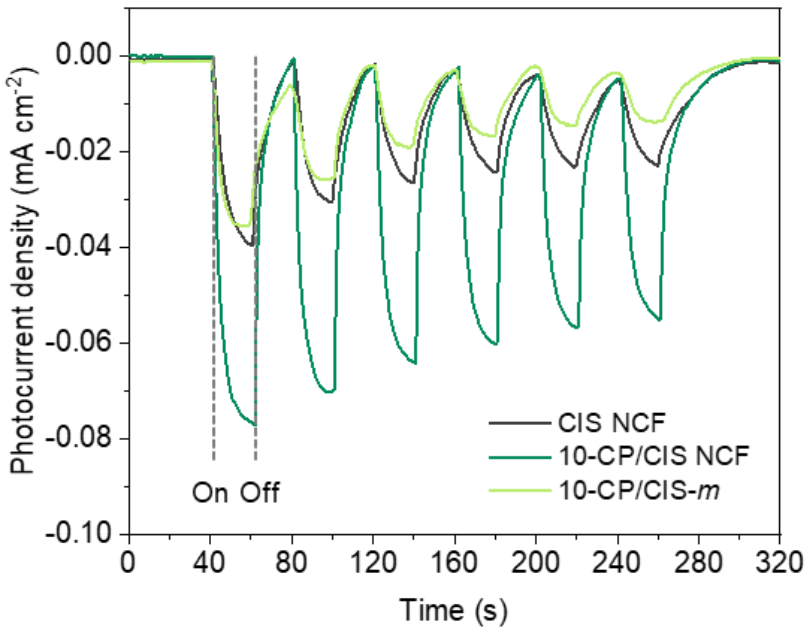

Figure 3-89. Transient photocurrent response of mesoporous CIS and 10-CP/CIS NCFs, and bulk 10-CP/CIS-*m* conducted at a constant potential of –1 V (vs Ag/AgCl) under visible-light irradiation ($\lambda \geq 420$ nm).

The highly porous structures formed through the synthetic method have the potential to possess a high density of catalytically active sites and facilitate efficient mass transfer kinetics, thereby enhancing photocatalytic hydrogen production efficiency. Evidence of the high permeability of 10-CP/CIS NCF catalyst to electrolyte was obtained from contact angle measurements. **Figure 3-90** indicates a higher diffusion rate and better penetration of water through the mesoporous architecture of 10-CP/CIS NCF compared to the bulk 10-CP/CIS-*m* cognate. The water contact angle is almost 0º for 10-CP/CIS NCF and ~32º for 10-CP/CIS-*m* after diffusion for 170 μs. This confirms that the open-pore mesostructured is a vital feature for increasing the electrolyte-catalyst interface area and, consequently, enhancing the wettability of the catalyst. Linear sweep voltammetry (LSV) measurements were also conducted on mesoporous CIS and 10-CP/CIS NCFs and bulk 10-CP/CIS-*m* photocatalysts under visible light irradiation (λ = 420–780 nm) to assess the impact of the 3D mesoporous architecture on the reaction kinetics. Figure **3-91a** displays typical cathodic LSV curves obtained by using a three-electrode setup, consisting of sample-deposited working electrode, an Ag/AgCl reference electrode and a graphite rod counter electrode in 0.5 M Na_2SO_4 electrolyte. The LSV plots reveal a significantly improved photocurrent density and lower onset potential for the hydrogen evolution reaction over the 10-CP/CIS NCF compared to the CIS NCF and 10-CP/CIS-*m*

electrodes. Specifically, at a potential of 1.4 V versus RHE (pH 7), 10-CP/CIS NCF yields a photocurrent density of –13.1 mA cm^{-2} versus –4.0 and –1.9 mA cm^{-2} for CIS NCF and 10-CP/CIS-*m*, respectively. Consistent with this observation, the calculated Tafel slope of the photocatalysts, which is strongly related with the reaction kinetics, follows the order: 10-CP/CIS NCF (192 mV dec^{-1}) < CIS NCF (237 mv dec^{-1}) < 10-CP/CIS-*m* (332 mV dec^{-1}) (**Figure 3-91b**). The lower Tafel slope of 10-CP/CIS NCF highlights better reaction kinetics for hydrogen evolution, which is consistent with the observed superior photocatalytic activity. Notably, because the Tafel slope values are above 120 mV dec^{-1}, these studies confirm that hydrogen evolution reaction over CP/CIS NCFs photocatalysts is mainly governed by the Volmer process ($H_2O + e^- + M \leftrightharpoons M–H_{ads} + OH^-$) in neutral condition, which is related to water dissociation step, followed by the desorption step of Heyrovsky reaction ($M–H_{ads} + H_2O + e^- \leftrightharpoons H_2 + OH^- + M$).

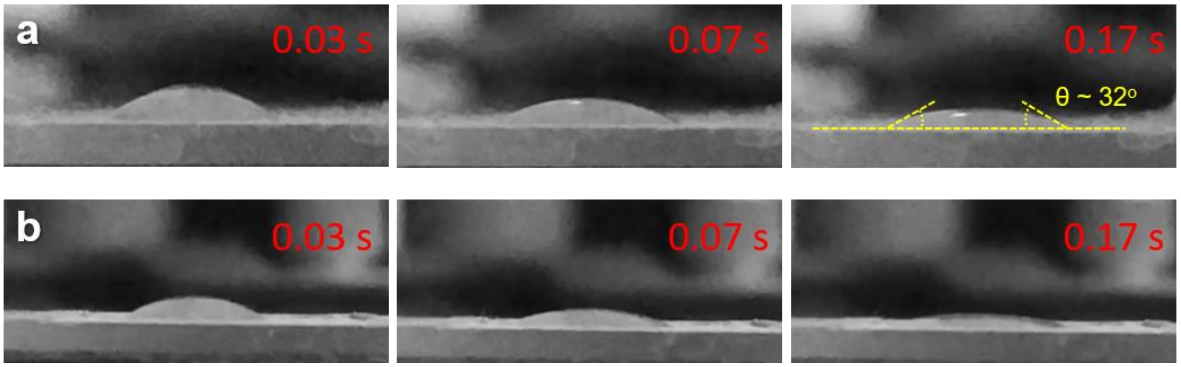

Figure 3-90. Contact angle measurements of the (a) bulk 10-CP/CIS_*m* and (b) mesoporous 10-CP/CIS NCF. The diameter of the water droplet was approximately 2 nm.

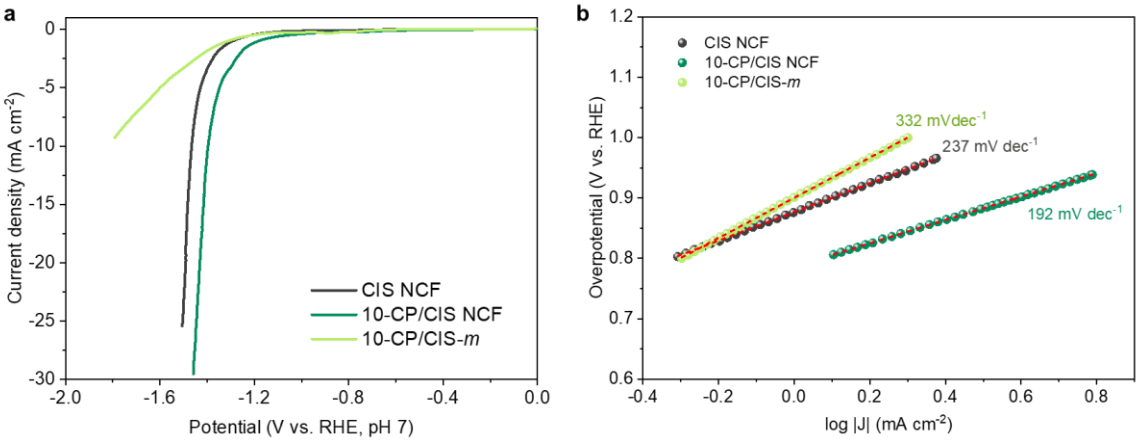

Figure 3-91. (a) iR-corrected polarization curves (scan rate: 50 mV s^{-1}) and (b) the corresponding Tafel plots of the mesoporous CIS and 10-CP/CIS NCFs and bulk 10-CP/CIS-*m* measured under visible light irradiation (λ ≥ 420 nm).

Based on the above results, we propose a mechanistic model for the hydrogen evolution reaction, as illustrated in **Figure 3-92**. Upon photoexcitation, the electrons at the CB of CIS tend to migrate to the Co_2P surface. This electron transfer pathway is thermodynamically feasible due to the formation of Mott-Schottky contact between the semiconductive CIS mesoporous framework and the metallic Co_2P nanoparticles, which results to a potential drop across the interface. Taking into consideration the electron affinity (x) of mesoporous CIS NCF (ca. 4.1 eV) and the work function (ϕ) of Co_2P (ca. 4.6 eV), a Schottky barrier (ϕ_{SB}) of about 0.5 eV is established near the interface of the heterojunction that results to a band-edge deformation. Driven by the interfacial potential drop and the high-electron-withdrawing ability of metallic Co_2P, photoexcited electrons can migrate though the metal/semiconductor nano-junction and transfer from the photoactivated CIS to Co_2P, where the hydrogen evolution reaction occurs, as can be seen in **Figure 3-92**. Moreover, the surface passivation of CIS with Co_2P can retard to a great extent the thermal relaxation of the surface-reaching electrons to lower energy states (trapping states). This process may provide additional pathways for interfacial electron injection from trap (acceptor) states of CIS to Co_2P nanoparticles. Here, we assumed the trap states are located ~0.1–0.15 eV bellow the CB edge of CIS NCF, as inferred by PL spectroscopy (**Figure 3-88**, **inset**). Such unique multi-pathway discharging events across the Co_2P-$CdIn_2S_4$ interface can effectively separate the photoexcited electron-hole pairs and lead to an accumulation of the photoelectron on the Co_2P surface. During photocatalysis, the Co_2P nanoparticles act as high-conductive electron mediators, which boost the separation and utilization of photogenerated carriers for the hydrogen evolution reaction. A comprehension of the CIS-to-Co_2P electron transfer routes under light illumination was confirmed by ISI-XPS, TRPL and TPC experiments. It should be noted that Co atoms in Co_2P have been identified as the active sites for H_2 evolution. This supported by DFT calculations showing that Co d bands contribute to the density of states near the Fermi level and Co sites exhibit optimal H^+ adsorption strength [178]. Meanwhile, the photogenerated holes left on the VB of CIS NCF transfer to oxidize the sacrificial agent (TEOA).

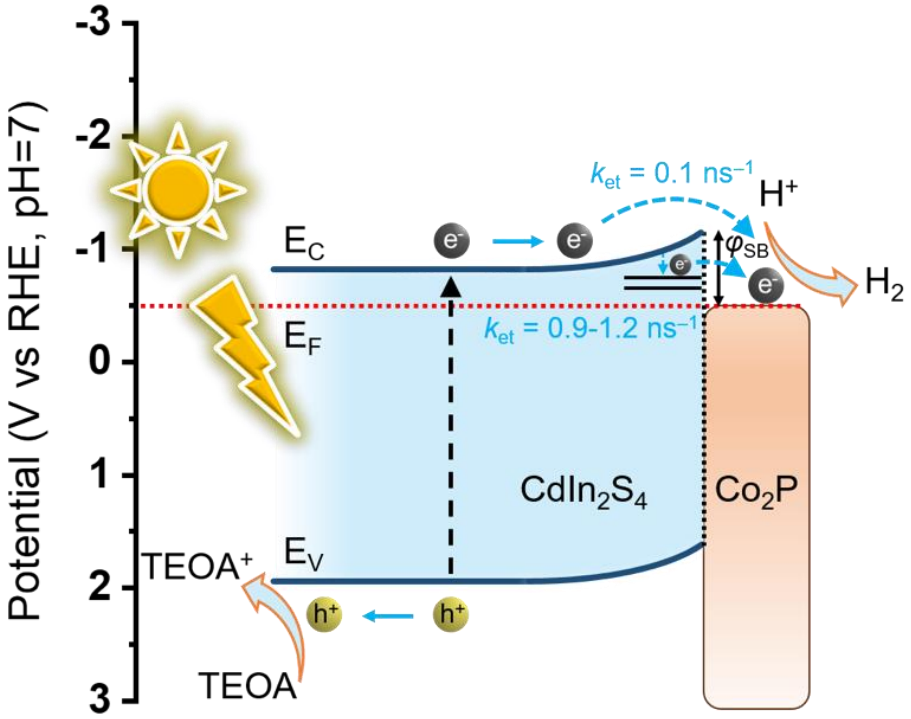

Figure 3-92. Proposed photocatalytic H_2 production mechanism and charge-transfer pathways in $Co_2P/CdIn_2S_4$ mesoporous heterostructures under visible light irradiation (ϕ_{SB}: Schottky barrier formed at the semiconductor/metal interface, k_{et}: interfacial electron-transfer rate, E_V: valence band energy, E_C: conduction band energy, E_F: Fermi level).

3.3.4 Conclusions

In this project, we demonstrated the synthesis of highly dispersed metallic Co_2P nanoparticles on mesoporous $CdIn_2S_4$ nanocrystal frameworks to maximize their photocatalytic performance for water splitting and hydrogen evolution. The combined effect of large accessible surface area and small grain sizes (ca. 5–7 nm diameter) of $CdIn_2S_4$, along with the metallic Co_2P nanoparticles (ca. 6–7 nm in diameter), results in high efficiency in charge carrier separation and migration. Through spectroscopic and (photo)electrochemical characterization techniques, we unveiled the formation of Mott-Schottky heterojunctions at the $Co_2P/CdIn_2S_4$ interfaces. These heterojunctions significantly enhance the migration of photogenerated electrons from both the valence band and surface states of semiconductive $CdIn_2S_4$ to metallic Co_2P, enabling a more efficient utilization of charge carriers for photo-redox reactions. As a result, the optimized photocatalyst containing 10 wt % Co_2P demonstrates an excellent photocatalytic performance with a respective H_2 evolution rate of 20.9 mmol g_{cat}^{-1} h^{-1} and an AQE of 56.1% at 420 nm, which is among the highest reported for thiospinel-based photocatalysts.

Furthermore, the mesoporous ensembles of Co_2P/CIS nanocrystals demonstrate outstanding chemical and structural stability, leading to a sufficient preservation of its catalytic activity in long-term operation.

3.4 Mesoporous networks of p-n β-$Ni(OH)_2$-$CdIn_2S_4$ nano-heterojunctions

3.4.1 Synthesis, structural characterization and morphology

Mesoporous Ni-modified $CdIn_2S_4$ materials were obtained through a two-step synthesis. The first step includes the synthesis of thiol-capped $CdIn_2S_4$ NCs and their integration into three-dimensional (3D) mesoporous frameworks (CIS NCF) via an oxidative polymerization process in the presence of a polyoxoethylene-*block*-cetyl ether (Brij-58) block copolymer. In the second step, $Ni(OH)_2$ nanoparticles were deposited onto the surface of CIS through the photo-deposition of soluble Ni(II) precursor in the presence of triethylamine as a base and sacrificial reagent. It has been demonstrated that upon light irradiation, photoexcited electrons in semiconductors with suitable CB-edge position have the ability to reduce the Ni(II) precursors in the solution, resulting to the formation of Ni nanoparticles. Then, these nanoparticles undergo a transformation into $Ni(OH)_2$ in the presence of alkaline conditions [130]. In general, the photochemical deposition method offers notable advantages over the most commonly used wet-chemical deposition methods. These include the growth of small-sized nanoparticles characterized by uniform distribution and, equally importance, intimate contact with the host surface. By altering the concentration of the Ni(II) precursor, we successfully prepared a series of Ni-modified CIS materials, denoted as *n*-Ni/CIS NCFs, where *n* represents the weight percentage (wt. %) of Ni. The Ni content of the as-prepared materials was determined by energy dispersive spectroscopy (EDS) (**Figure 3-93**). The EDS spectra revealed the presence of Cd, In, S and Ni atoms, which can be quantified to a Ni content (based on Ni/Cd atomic ratio) ranging from approximately 5 to 15 wt. % (**Table 3-17**). Notably, the experimental Ni loading is in good agreement with the targeted composition of each sample (within 8% deviation), suggesting that all nickel atoms were effectively deposited on the surface of mesoporous CIS.

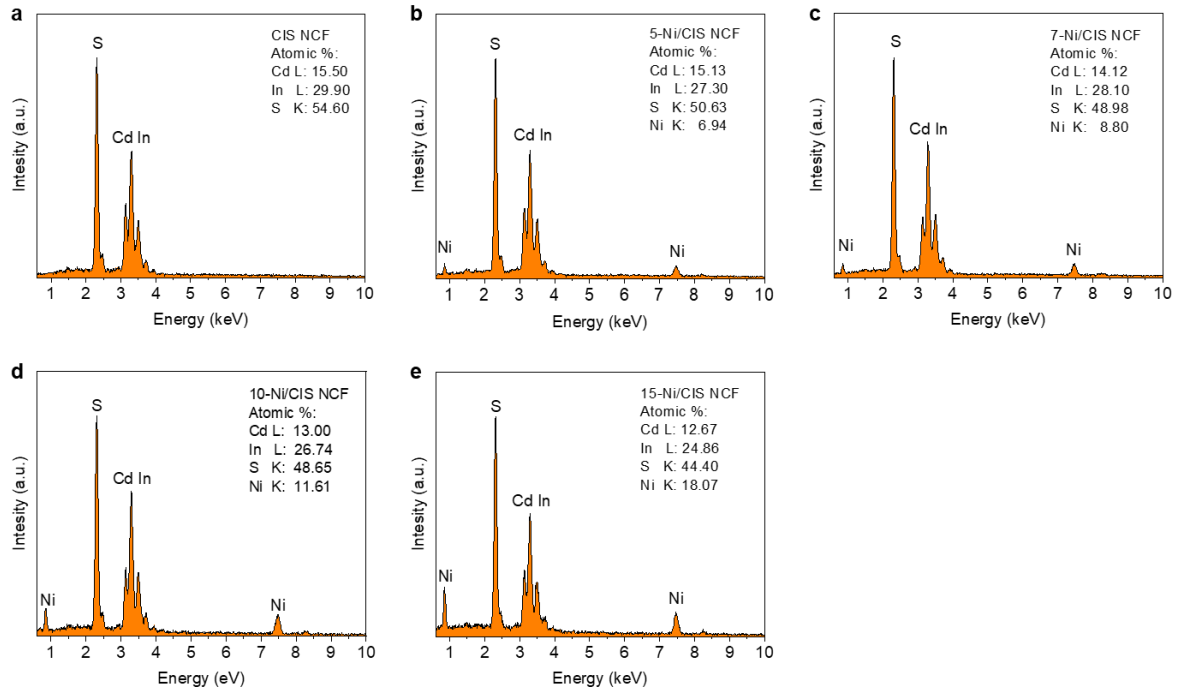

Figure 3-93. Typical EDS spectra of the mesoporous CIS and Ni-modified CIS NCFs materials.

Table 3-17. Elemental composition of mesoporous CIS and Ni-modified CIS NCFs, and 10 % Ni-modified CIS microparticles.

Sample	**Cd (at. %)**	**In (at. %)**	**S (at. %)**	**Ni (at. %)**	**Ni loading[a] (wt. %)**
CIS NCF	15.50	29.90	54.60	-	-
5-Ni/CIS NCF	15.13	27.30	50.63	6.94	5.40
7-Ni/CIS NCF	14.12	28.10	48.98	8.80	7.22
10-Ni/CIS NCF	13.00	26.74	48.65	11.61	10.02
15-Ni/CIS NCF	12.67	24.86	44.40	18.07	15.11
10-Ni/CIS-*m*	13.07	26.68	48.33	11.92	10.20

[a] Based on the EDS Ni to Cd atomic ratio.

The X-ray diffraction (XRD) patterns of the obtained materials are depicted in **Figure 3-94**. All samples exhibited three broad diffraction peaks in the range of 20–60º 2θ scattering angles, indicating the presence of very small crystalline grains. These diffractions can be attributed to the hexagonal ($P6_3mc$) crystal phase of $CdIn_2S_4$ based on previous studies. Notably, the XRD patterns of the Ni/CIS NCFs heterostructures are very similar to that of CIS NCF, without exhibiting extra diffraction peaks of Ni species. The absence of Ni XRD peaks is related to the

very small grain size and homogenous dispersion of Ni complexes on the surface of CIS. To obtain a clear picture over the crystal structure of the deposited Ni-species, a Ni-modified CIS sample with high Ni content (30 wt. %) was also prepared through a similar photochemical deposition method (30-Ni/CIS NCF) and characterized by X-ray diffraction. Compared with the unmodified CIS, 30-Ni/CIS NCF exhibited two additional XRD peaks at 33º and 59º 2θ scattering angles, which can be attributed to the (100) and (110) reflections of the hexagonal (P-3m1) β-$Ni(OH)_2$ (**Figure 3-95**). The XRD pattern of the isolated $Ni(OH)_2$ microparticles obtained by a simple wet-chemical precipitation method showed well-defined diffraction peaks consistent with the hexagonal phase of β-$Ni(OH)_2$ (JCPDS card no. 14-0117).

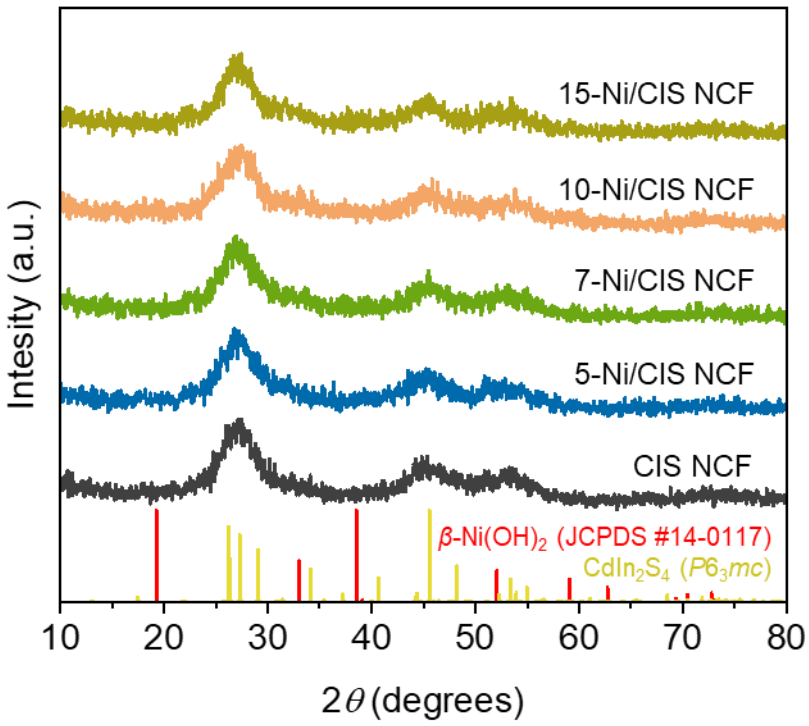

Figure 3-94. X-ray diffraction patterns of mesoporous CIS and Ni-modified CIS NCFs materials. The standard diffraction data of the hexagonal $CdIn_2S_4$ and β-$Ni(OH)_2$ (JCPDS card no. 14-0117) are also given.

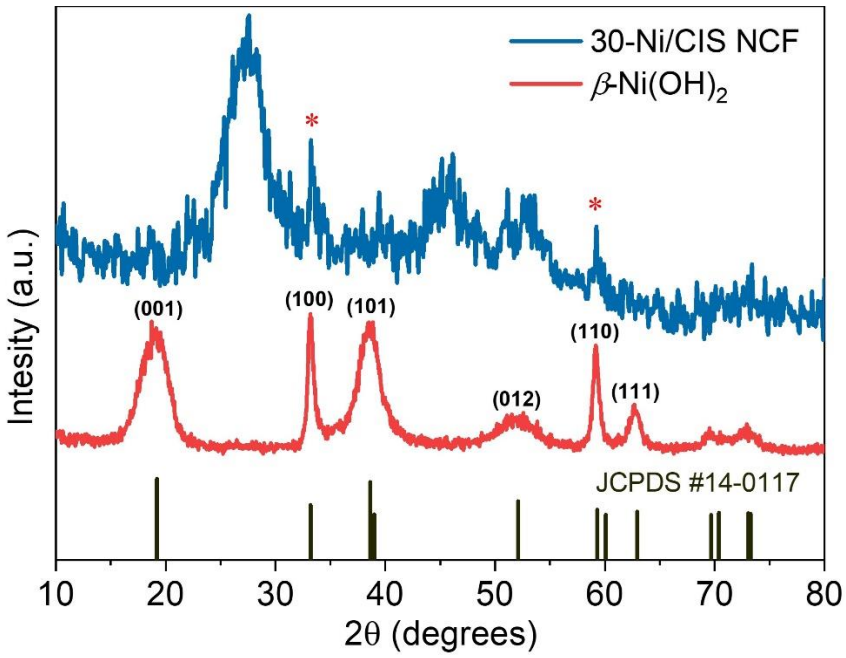

Figure 3-95. XRD patterns of the as-prepared 30 wt. % Ni-loaded CIS (30-Ni/CIS NCF) and isolated β-$Ni(OH)_2$ microparticles. The diffraction peaks at 2θ = 33° and 59° scattering angles (marked with symbol *) in the XRD pattern of 30-Ni/CIS NCF correspond to the hexagonal crystal phase of β-$Ni(OH)_2$. The standard diffraction data of JCPDs card no. 14-1017 reference card of hexagonal β-$Ni(OH)_2$ is also given.

Furthermore, the atomic configuration of 30-Ni/CIS NCF was also characterized by X-ray total scattering and pair distribution function analysis (PDF). The PDF analysis can provide information on the local atomic structure of Ni species and CIS host material [144]. As can be observed in **Figure 3-96**, the PDF plot of CIS NCF fully correlated with that of the hexagonal (P63mc) $CdIn_2S_4$. Specifically, the distinct interatomic vectors at ~2.5, ~4.0 and ~4.7 Å are assigned to the Cd/In–S bonds, and Cd···Cd/In···In and Cd/In···S next-nearest-neighbor distances of hexagonal $CdIn_2S_4$, respectively. Compared with mesoporous CIS, the 30-Ni/CIS NCF displayed a similar PDF profile, indicating similar atomic configuration, although same additional correlations in the short-range order (up to 8 Å) can be resolved. Key structural features of the Ni species can be obtained by differential PDF (d-PDF) analysis, which entails subtracting the CIS PDF from that of the 30-Ni/CIS NCF sample. This analysis yielded a PDF plot which resembles that of the isolated β-$Ni(OH)_2$ particles, providing clear evidence that the chemical identity of the deposited Ni species is hexagonal β-$Ni(OH)_2$. In the d-PDF plot, the scattering vector at ~2.1 Å corresponds to the Ni–O bond, while those at ~2.6 and ~3.1 Å are consistent with the nearest O···O and Ni···Ni distances of the hexagonal *β*-$Ni(OH)_2$,

respectively. These findings are in good agreement with the PDF plot of β-$Ni(OH)_2$ microparticles. Thus, these findings provide clear evidence that hexagonal β-$Ni(OH)_2$ crystallites grown on the surface of CIS NCF during the photochemical deposition method.

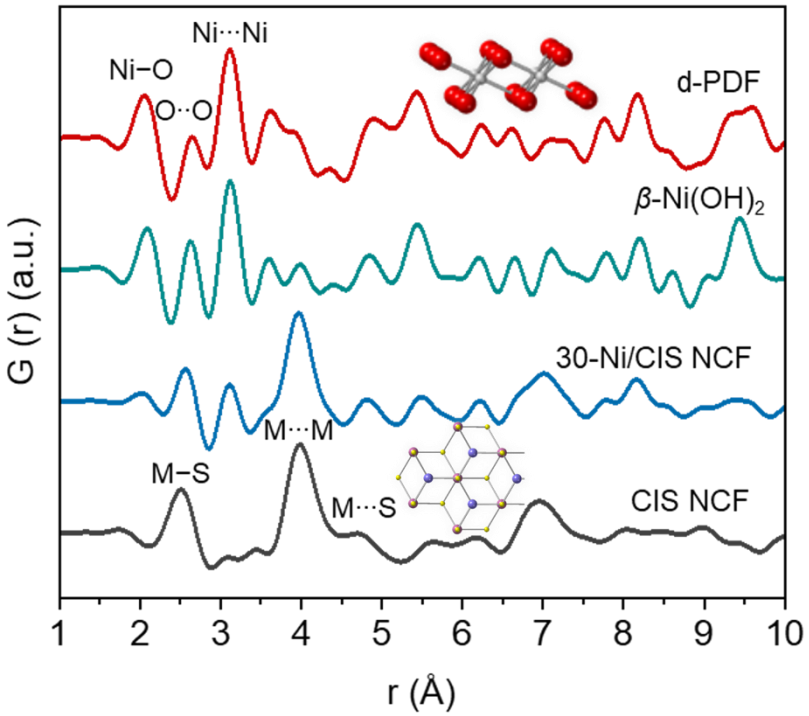

Figure 3-96. Reduced atomic pair distribution function G(r) of the mesoporous CIS and 30 % Ni-loaded CIS (30-Ni/CIS) NCFs and β-$Ni(OH)_2$ microparticles (M = Cd, In). The red line corresponds to the differential PDF (d-PDF) plot obtained by subtracting the CIS PDF from that of 30-Ni/CIS NCF.

The chemical state of elements of the 10-Ni/CIS NCF, which is the best catalyst in this study, was characterized by X-ray photoelectron spectroscopy (XPS). **Figure 3-97** depicts typical high-resolution XPS spectra of Cd 3d, In 3d, S 2p, Ni 2p and O 1s lines. In XPS spectrum of Cd 3d, the doublet peak at 412.0 and 405.1 ± 0.1 eV binding energies correspond to Cd $3d_{3/2}$ and $3d_{5/2}$ spin-orbit components of Cd^{2+} (**Figure 3-97a**), while the signals at 452.5 and 444.9 ± 0.1 eV in the In 3d region (**Figure 3-97b**) are attributed to the In $3d_{3/2}$ and $3d_{5/2}$ peaks of In^{3+} chemical state, respectively, in $CdIn_2S_4$ [161,166,179]. Also, the S-metal (Cd or In) bonding can be proven by the intense peak at 161.9 ± 0.2 eV in the S 2p spectrum, while the peak at 168.3 ± 0.2 eV reveals the presence of some surface SO_x species, likely due to air exposure of the sample (**Figure 3-97c**) [180]. The paramagnetic Ni(II) state was further confirmed by the deconvoluted Ni $2p_{3/2}$ and $2p_{1/2}$ peaks at 856.1 and 862.2 ± 0.2 eV (**Figure 3-97d**). The O 1s signal at 531.8 ± 0.2 eV further confirms the presence of Ni hydroxide on the

surface of mesoporous CIS NCF (**Figure 3-97d**, **inset**) [130]. Meanwhile, the O 1s peak at 534.0 ± 0.2 eV indicates the presence of adsorbed moisture (H_2O) on the sample.

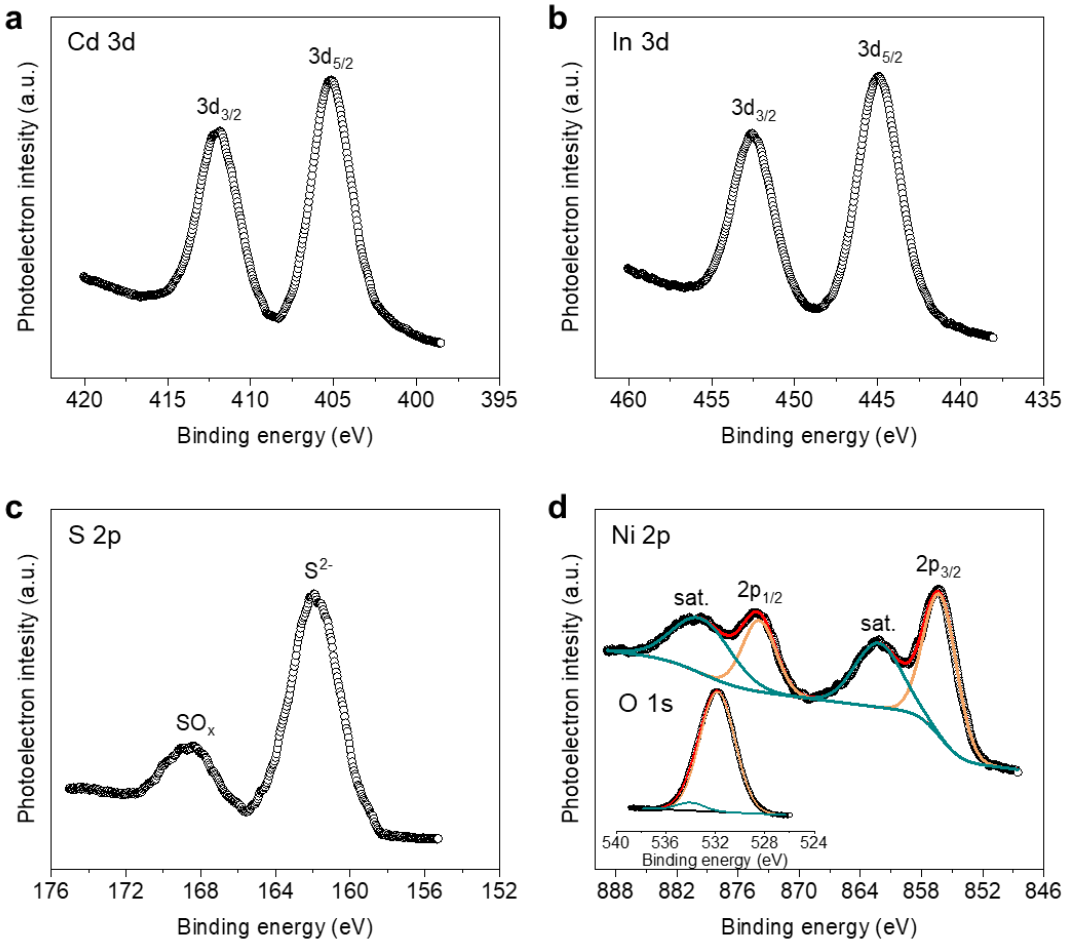

Figure 3-97. Typical XPS core-level of the (a) Cd 3d, (b) In 3d, (c) S 2p, and (d) Ni 2p and O 1s (inset) region of the 10-Ni/CIS NCF catalyst.

The morphology of 10-Ni/CIS NCF catalyst was characterized by field emission scanning electron microscopy (FESEM) and transmission electron microscopy (TEM). Typical FESEM images, shown in **Figure 3-98a**, display a network structure consisting of aggregated nanoparticles with size smaller than 10 nm. Also, EDS mapping images confirm a homogenous distribution of Cd, In, S and Ni atoms throughout the mesoporous structure, highlighting that β-$Ni(OH)_2$ deposition follows a homogenous growth on the surface of CIS (**Figure 3-99**). TEM imaging further confirms the existence of a mesoporous network consisting of interconnected nanoparticles as building blocks (**Figure 3-98b**). TEM and high-resolution TEM (HRTEM) images show ~7–8 nm-sized β-$Ni(OH)_2$ nanoparticles in close contact with CIS NCs of ~5–7 nm diameter (**Figure 3-98b-c**). This morphology is advantageous for promoting interfacial electronic interactions among the components. The structural identification of $CdIn_2S_4$ and β-

$Ni(OH)_2$ was also confirmed via HRTEM analysis. In particular, in **Figure 3-98d**, the interplanar distance of 3.3 Å corresponds to the (011) crystal planes of hexagonal $CdIn_2S_4$ ($P6_3mc$), while the 2.7 Å lattice plane distances are attributed to the (100) and (010) facets along the [001] crystal direction of hexagonal β-$Ni(OH)_2$ (P-3m1). Ultimately, we can conclude to the successful preparation of a 3D porous heterostructure consisting of close contact β-$Ni(OH)_2$ and $CdIn_2S_4$ NCs, which is anticipated to induce enhanced charge carrier delocalization and mass transfer kinetics.

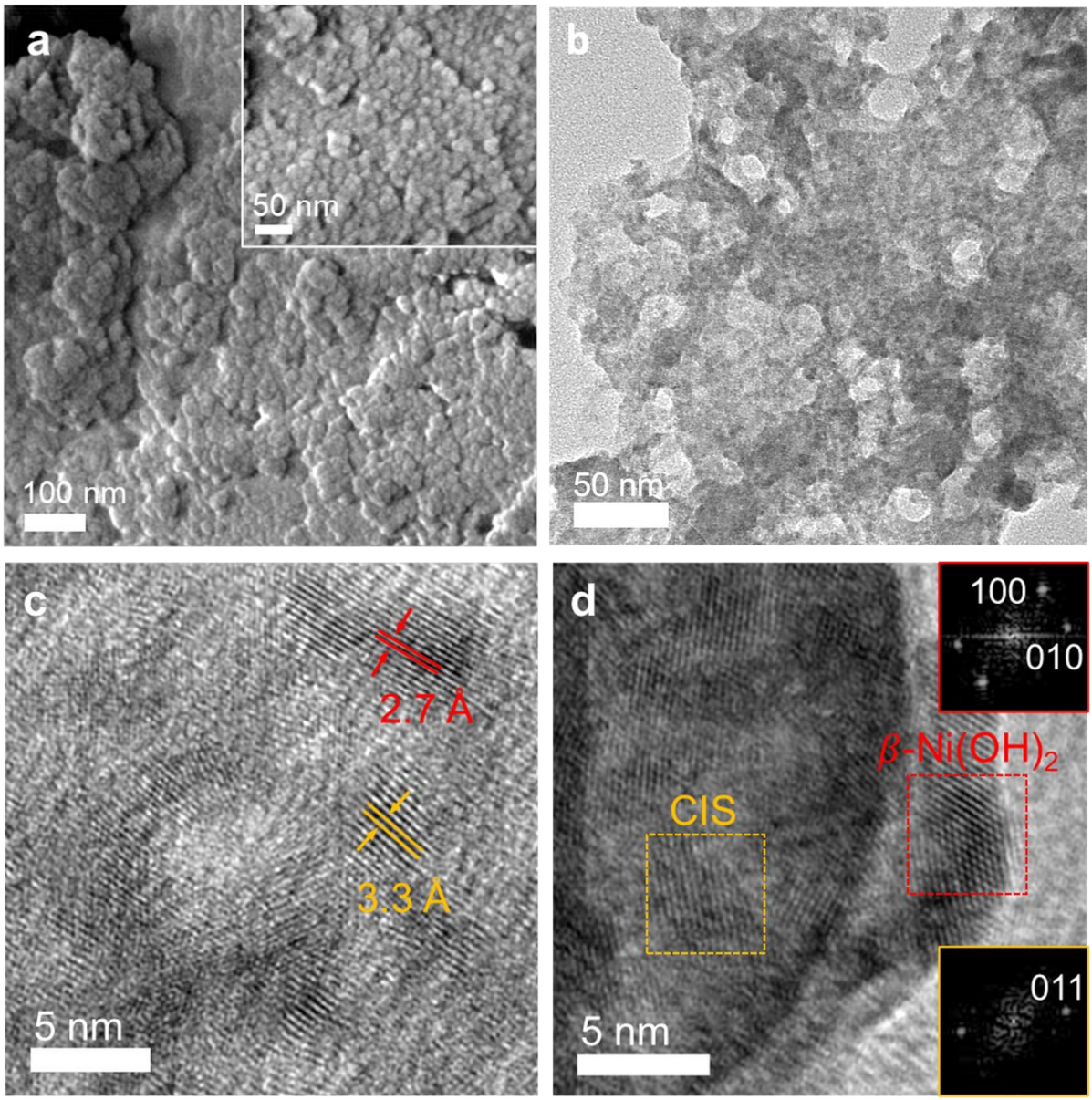

Figure 3-98. (a) Representative FESEM (inset: high-magnification SEM image), (b) TEM and (c-d) high-resolution TEM (HRTEM) images of 10-Ni/CIS NCF. Inset of panel (d): fast Fourier transform (FFT) patterns indexed to the hexagonal $CdIn_2S_4$ ($P6_3mc$, orange outline) and hexagonal β-$Ni(OH)_2$ (P-3m1, red outline).

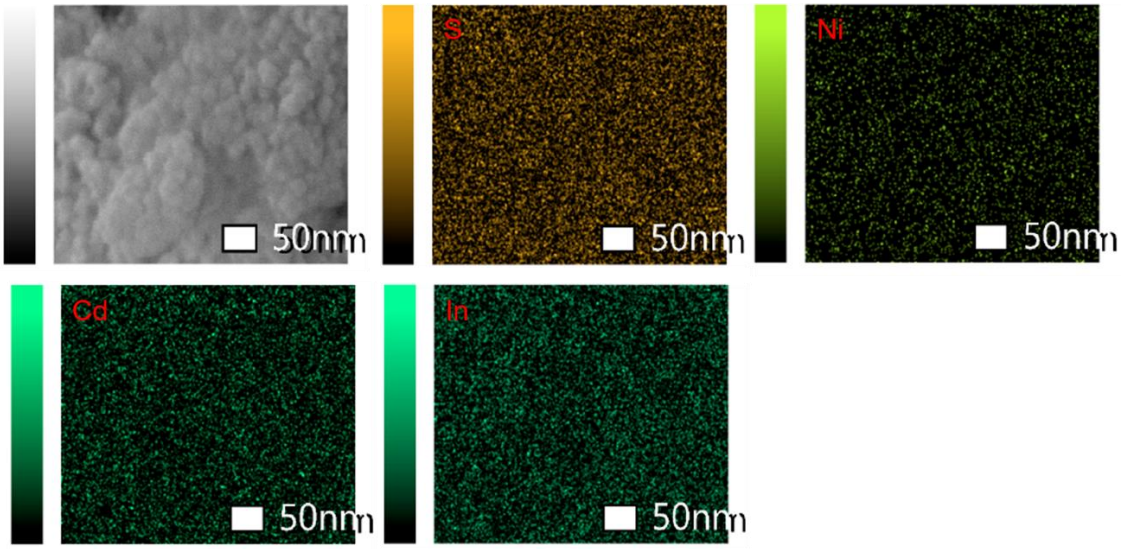

Figure 3-99. EDS elemental mapping of 10-Ni/CIS NCF catalyst.

The porosity of the samples was probed by N_2 physisorption measurements. **Figure 3-100** depicts the N_2 adsorption-desorption isotherms of mesoporous CIS and 10-Ni/CIS NCFs along with that of bulk CIS microparticles (CIS-*m*). The N_2 isotherms of the other Ni-modified catalysts are shown in **Figure 3-101**. The CIS NCF exhibited a typical type-IV adsorption isotherm accompanied with an H_2-type hysteresis loop, which is characteristic for mesoporous solids with interconnected pores [145]. Upon modification with β-$Ni(OH)_2$, the obtained materials exhibited N_2 adsorption-desorption isotherms with a H_3-type hysteresis loop, suggesting slit-shaped pore morphology. The Brunauer-Emmet-Teller (BET) surface area and pore volume of the mesoporous CIS were determined to be 137 $m^2\ g^{-1}$ and 0.12 $cm^3\ g^{-1}$, respectively. Comparatively, the surface area and pore volume of CIS microparticles are limited (ca. 25 $m^2\ g^{-1}$ and 0.03 $cm^3\ g^{-1}$, respectively), suggesting non-porous morphology. Upon β-$Ni(OH)_2$ deposition, an increasing trend in surface area (from 139 to 185 $m^2\ g^{-1}$) and pore volume (from 0.17 to 0.23 $cm^3\ g^{-1}$) is observed, indicating that β-$Ni(OH)_2$ layered nanostructures on the surface of CIS contribute to the overall porosity. The mean pore size of the samples was calculated by the non-local density functional theory (NLDFT) method. All the materials exhibited narrow pore-size distributions (insets of **Figures 3-100** and **3-101**) with an average pore size of ~6 nm for CIS NCF and ~3.6–4.0 nm for Ni/CIS NCFs. Compared to CIS NCF, the reduced pore size observed in the Ni-modified samples suggests the possible growth of β-$Ni(OH)_2$ nanoclusters within the pores of the CIS mesoporous framework. All the textural parameters for the mesoporous CIS and Ni-modified CIS NCFs are summarized in **Table 3-18**.

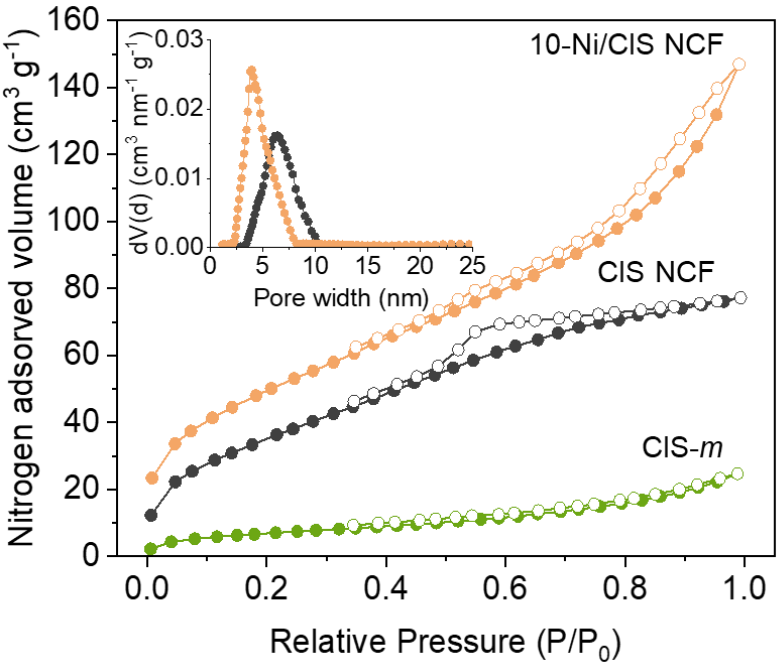

Figure 3-100. Nitrogen adsorption (filled cycles) and desorption (open cycles) isotherms at – 196 ºC of mesoporous CIS and 10-Ni/CIS NCF and CIS microparticles (CIS-*m*). Inset: the corresponding NLDFT pore-size distribution plots calculated from the adsorption isotherms.

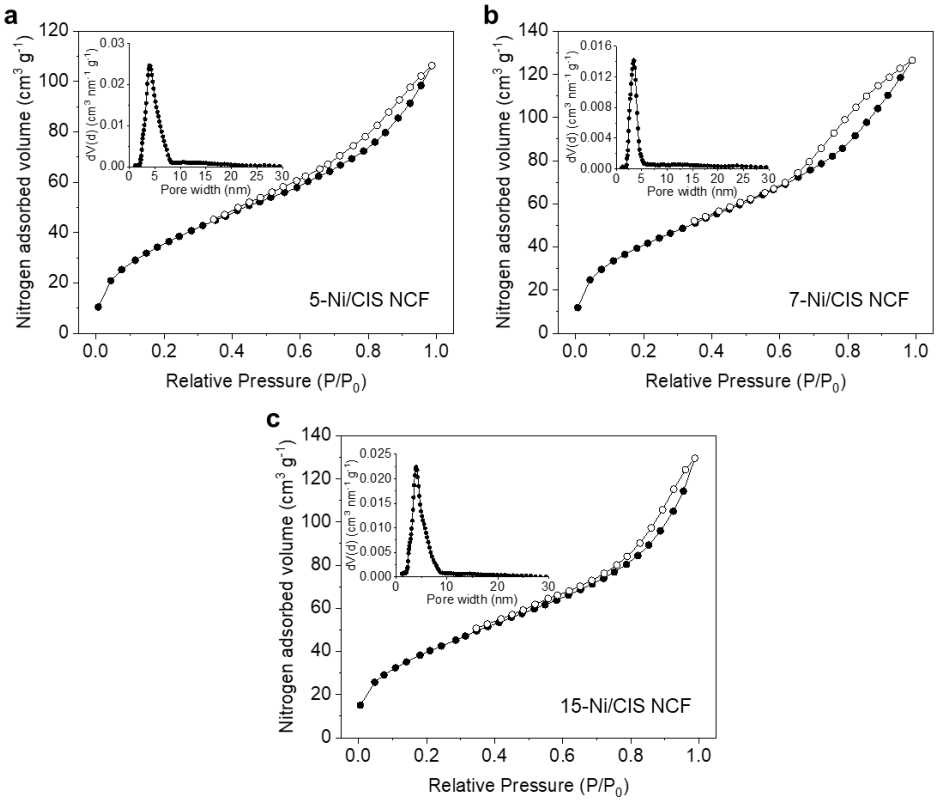

Figure 3-101. Nitrogen adsorption (filled cycles) and desorption (open cycles) isotherms at – 196 ºC for the Ni-modified CIS NCFs with 5, 7 and 15 wt. % Ni content. Inset: the corresponding NLDFT pore-size distribution plots calculated from the adsorption isotherms.

Table 3-18. Textural and optical properties of the mesoporous CIS and Ni-modified CIS NCFs and bulk 10 wt. % Ni-loaded (10-Ni/CIS-*m*) sample.

Sample	BET surface ($m^2\ g^{-1}$)	Pore volume ($cm^3\ g^{-1}$)	Pore size (nm)	Energy gap[a)] (eV)
CIS NCF	137	0.12	6.3	2.57
5-Ni/CIS NCF	139	0.17	4.0	2.59
7-Ni/CIS NCF	156	0.20	3.6	2.52
10-Ni/CIS NCF	185	0.23	3.9	2.48
15-Ni/CIS NCF	150	0.20	3.9	2.45
10-Ni/CIS-*m*	68	0.14	-	2.33

[a)] The energy bandgap was obtained from the corresponding Kubelka-Munk plots.

The optical properties of the prepared materials were investigated with ultraviolet-visible (UV-vis) diffuse reflectance spectroscopy. The mesoporous CIS NCF exhibited a strong absorption onset at 483 nm, which corresponds to the interband electron transition (**Figure 3-102**). The energy bandgap (E_g) of CIS NCF, derived from the corresponding Kubelka-Munk plot, was determined to be 2.57 eV (inset **Figure 3-102**). Compared to bulk CIS (2.35 eV, **Figure 3-52**), the mesoporous CIS displayed a significant hypsochromic shift of the energy gap, probably due to quantization effects in the electronic structure of the constituent CIS NCs (ca. 5–7 nm in diameter, as determined from TEM images). The modification of the CIS surface with β-$Ni(OH)_2$ appears to have a considerable effect on the optical properties. In particular, the E_g of the Ni-modified materials was progressively reduced from 2.59 eV to 2.45 eV with increasing Ni content from 5 to 15 wt. % (**Table 3-18**). This variation in the energy gap suggests strong electronic interactions between the two components within the mesoporous framework. Moreover, the increased light absorption in the visible and near-IR region (~550–1200 nm) observed for the Ni/CIS samples is attributed with the d-d interband transitions (peaks at ~670 and ~1150 nm) of Ni(II) in β-$Ni(OH)_2$, as inferred from the UV-vis spectrum of pure β-$Ni(OH)_2$ (**Figure 3-103**) [129,181]. Thus, the above results are entirely consistent with the growth of β-$Ni(OH)_2$ nanoparticles on the surface of CIS NCF, and importantly, with strong electronic communication across the interface.

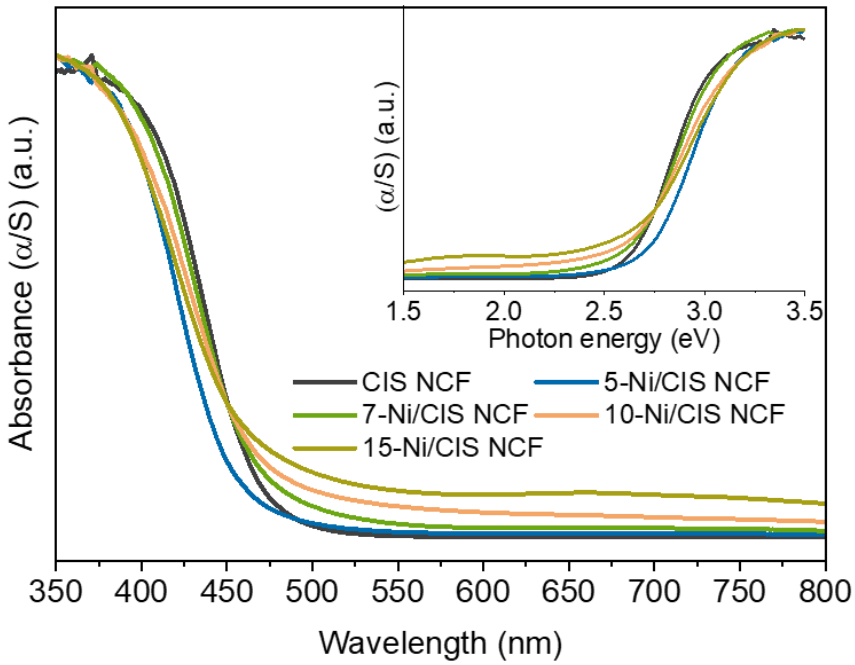

Figure 3-102. UV-vis spectra of mesoporous CIS and Ni-modified CIS NCFs. Inset: the corresponding Kubelka-Munk plots.

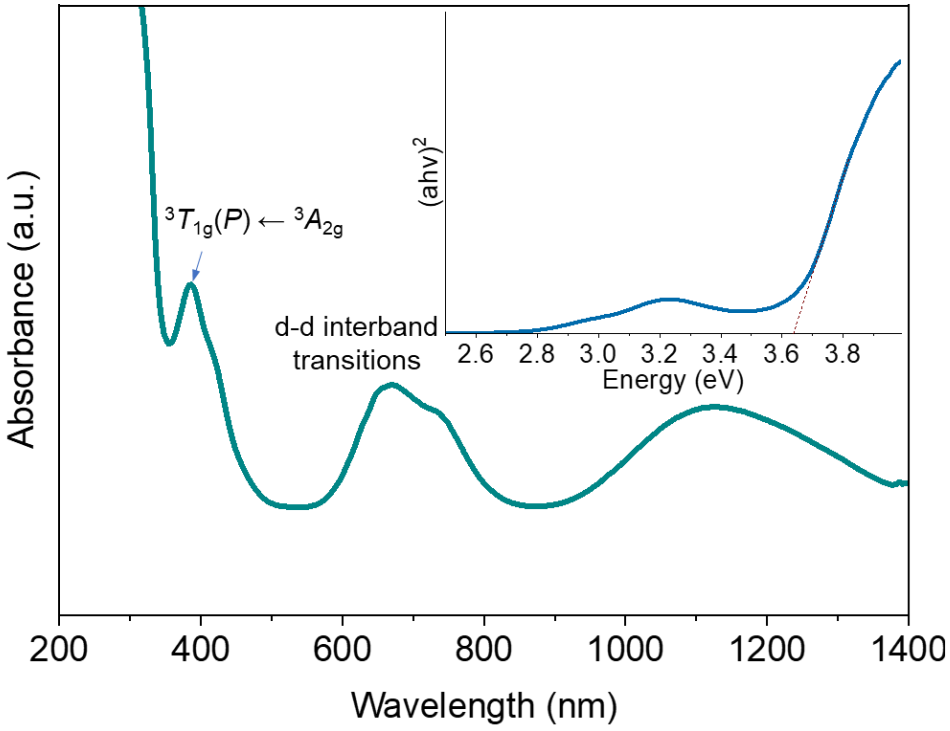

Figure 3-103. Optical absorption spectrum of the as-prepared β-$Ni(OH)_2$ microparticles, showing characteristic d-d interband transitions at ~385, ~670 and ~1120 nm. The steep absorption below 350 nm is attributed to the band-gap transition. Inset: the corresponding Tauc plot for direct band gap semiconductor, showing an energy bandgap of ~3.65 eV.

3.4.2 Photocatalytic hydrogen evolution study

The photocatalytic hydrogen production activities of the different catalysts were assessed under visible-light irradiation ($\lambda \geq 420$ nm), using triethanolamine (TEOA, 10% v/v) as sacrificial reagent. As can be observed in **Figure 3-104**, the mesoporous CIS NCF displays a moderate hydrogen evolution activity (~110 μmol h^{-1}), encountering fast charge carrier recombination. Interestingly, modification with β-$Ni(OH)_2$ has a notable effect on the photocatalytic activity of CIS. Even a small amount of β-$Ni(OH)_2$ (5 wt. % Ni) induces a ~3 times improvement of the activity of CIS NCF, yielding a hydrogen evolution rate of 350 μmol h^{-1}. Further, the hydrogen generation activity exhibits a linear response to the Ni content, reaching a maximum of ~400 μmol h^{-1} (or ca. 20 mmol h^{-1} g_{cat}^{-1} mass activity) at 10 wt. % Ni (10-Ni/CIS NCF). An additional increase in the Ni content (up to 15 wt. % Ni) results in a notable reduction of the hydrogen evolution rate (~320 μmol h^{-1}). This decline is attributed to the relatively increased electron-hole pair recombination at the β-$Ni(OH)_2$/CIS interface in the highly Ni-loaded sample. The impact of β-$Ni(OH)_2$ modification on charge transfer and photoactivity enhancement will be discussed in more detail thought spectroscopic and electrochemical investigations (see below, **chapter 3.4.3**).

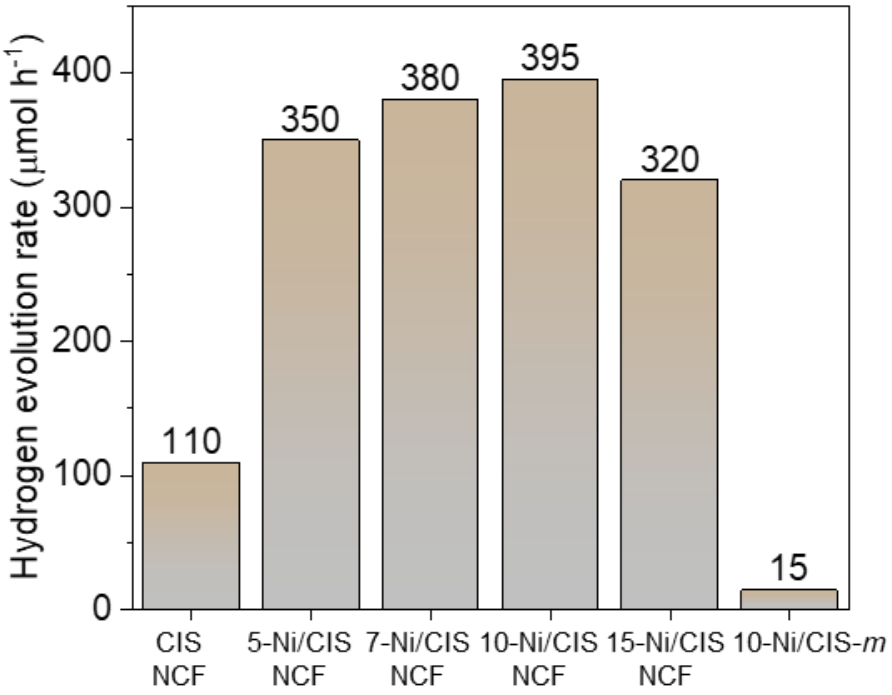

Figure 3-104. H_2 evolution rates of the mesoporous CIS and Ni-modified CIS NCFs. The H_2-evolution rate of the bulk 10 wt. % Ni-loaded CIS (10-Ni/CIS-*m*) catalyst is also given. The rate of H_2 evolution for each catalyst was determined by the average H_2 production over a 3-hour irradiation period.

In addition to the compositional effect, the open-pore architecture also significantly contributes to enhancing the photocatalytic activity. To validate this, we prepared a 10 wt. % Ni-modified CIS bulk reference sample (denoted as 10-Ni/CIS-*m*) through Ni photo-deposition on the surface of CIS microparticles and measured its hydrogen evolution performance under the same conditions. The XRD pattern of 10-Ni/CIS-*m* confirmed the cubic thiospinel structure of CIS, while the EDS results evidenced a 10.2 wt. % Ni loading (**Figure 3-105a-b**, **Table 3-17**). Moreover, N_2-physisorption measurement on this material indicated a BET surface area of 68 m^2 g^{-1} (**Figure 3-105c**, **Table 3-18**). As can be observed in **Figure 3-104**, 10-Ni/CIS-*m* displays a significantly lower H_2-evolution activity (~15 μmol h^{-1}) compared to the mesoporous counterpart (10-Ni/CIS NCF), highlighting that the nano-grain composition and large internal surface area are favorable for enhancing the photocatalytic performance.

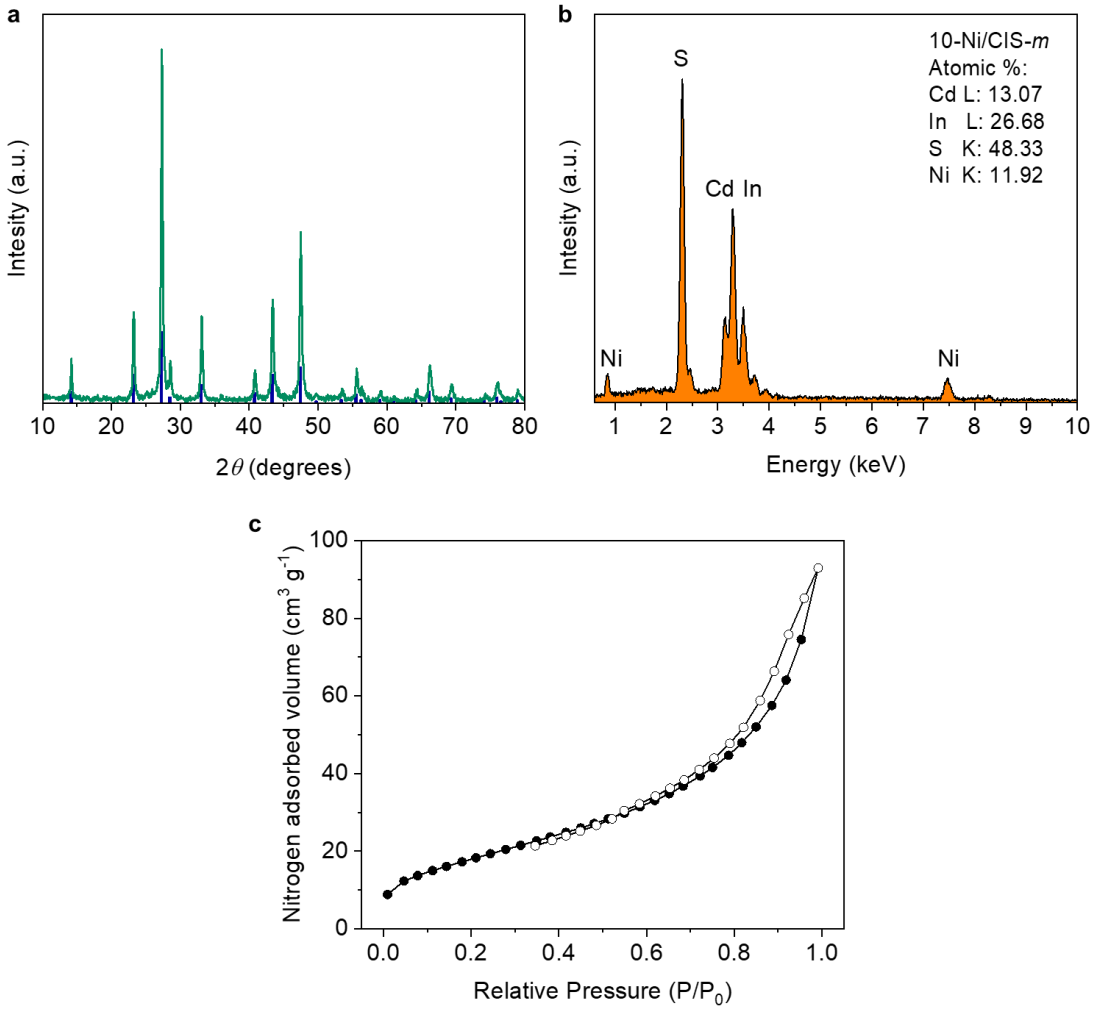

Figure 3-105. (a) Typical XRD pattern and (b) EDS spectrum of bulk 10-Ni/CIS-*m*. The blue lines in panel (a) correspond to the standard diffraction of cubic $CdIn_2S_4$ (space group: Fd3m), according to JCPDS card no. 27-0060. (c) Nitrogen adsorption (filled cycles) and desorption (open cycles) isotherms at –196 ºC for the bulk 10-Ni/CIS-*m* reference material.

The effect of different hole scavengers and catalyst concentrations in this photocatalytic system was also investigated by comprehensive control experiments. By keeping the catalyst concentration constant (1 mg mL^{-1}), we examined various hole scavengers, such as methanol (MeOH, 10% v/v), ethanol (EtOH, 10% v/v), 5 M NaOH/EtOH mixture (10% v/v), triethylamine (TEA, 10% v/v) and triethanolamine (TEOA, 10% v/v). The notable variations in the obtained hydrogen evolution reaction rates point to the oxidation process as the rate-limiting step (**Figure 3-106**). Among the examined compounds, TEOA was found to be the most effective electron donor for this photocatalytic system. Subsequently, assessment of the photocatalytic activity using different mass loadings of the 10-Ni/CIS NCF catalyst demonstrated a notable increase in the rate of H_2 evolution, reaching a maximum activity at 1 mg mL^{-1} (**Figure 3-107**). Further increasing the catalyst concentration (> 1.5 mg mL^{-1}) led to an abrupt reduction of the photocatalytic efficiency by a factor of ~2.3–2.5x. The reduction in the photocatalytic activity is attributed to increased light scattering caused by the excessive catalyst particles. Consequently, under optimized condition, an apparent quantum yield (AQY) of ~52% is obtained at 420 ± 10 nm, considering 100% absorption of the incident photons. To best of our knowledge, this activity is among the best reported for $CdIn_2S_4$-based and thiospinel-based photocatalysts (**Table I, Annex I**).

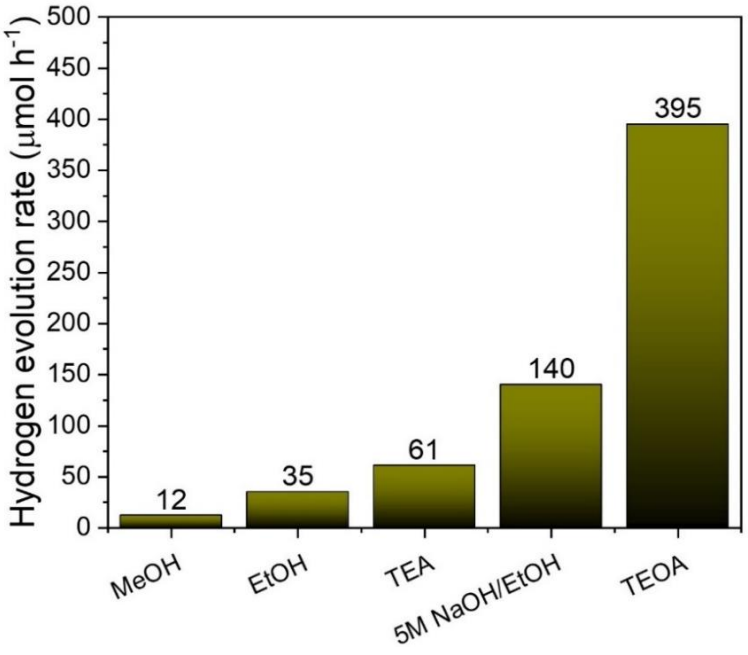

Figure 3-106. H_2 evolution activity of 10-Ni/CIS NCF photocatalyst, using different sacrificial reagents: methanol (MeOH, 10% v/v), ethanol (EtOH, 10% v/v), triethylamine (TEA, 10% v/v), 5M NaOH/Ethanol (EtOH, 10% v/v) and triethanolamine (TEOA, 10% v/v). Reaction conditions: 20 mg of photocatalyst in 20 mL aqueous solution containing the respective hole scavenger, 300-W Xe-lamp equipped with a UV-cut off filter ($\lambda \geq 420$ nm).

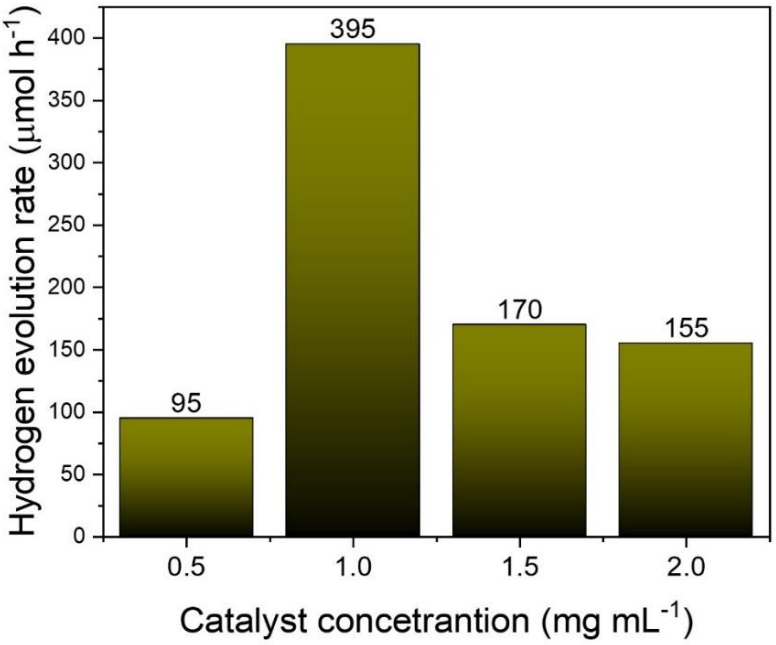

Figure 3-107. H_2 evolution activity of 10-Ni/CIS NCF photocatalyst, using different catalyst loading. Reaction conditions: 10–40 mg of photocatalyst in 20 mL aqueous solution of TEOA (10% v/v), 300-W Xe-lamp equipped with a UV-cut off filter ($\lambda \geq 420$ nm).

Apart from water reduction, the oxidation of TEOA may also contribute to the overall production of hydrogen [182]. It is well known that TEOA oxidation can yield acetaldehyde (CH_3CHO) and diethanolamine ($HN(CH_2CH_2OH)_2$), where sequential oxidation of these compounds may contribute to the generation of hydrogen [169,170]. To elucidate this, we performed a control experiment on 10-Ni/CIS NCF using TEOA (10% v/v) and $NaIO_3$ (0.1 M) as the hole and electron scavenger, respectively. Since the reduction of IO_3^- (E_o= 1.2 V vs RHE) is thermodynamical more favorable than water reduction (E_o = 0 V vs RHE), this experiment can provide a means for exploring potential hydrogen generation via the photo-oxidation of the sacrificial reagent (TEOA). In this process, the photogenerated electrons can induce the reduction of IO_3^-, while the photogenerated hole drives the oxidation of TEOA. Interestingly, throughout this experiment, no hydrogen was detected (by gas chromatography) even after a 3-hour illumination period, thus confirming that the water is the only hydrogen source.

Moreover, the 10-Ni/CIS NCF photocatalyst exhibited excellent stability as evidenced by the consistent hydrogen evolution rate obtained throughout the stability experiments. After each catalytic run, the photocatalyst was isolated from the reaction solution by centrifugation, washed with ethanol and water, and then redispersed in a fresh solution. As depicted in **Figure**

3-108, 10-Ni/CIS NCF exhibit excellent photochemical stability even after four 5-hour catalytic cycles, where no obvious activity decay can be detected. The total amount of hydrogen generated over 20 hours of visible-light irradiation is 7.91 mmol (~190 mL at 20 °C), which is equivalent to an average H_2-evolution rate of 0.40 mmol h^{-1}.

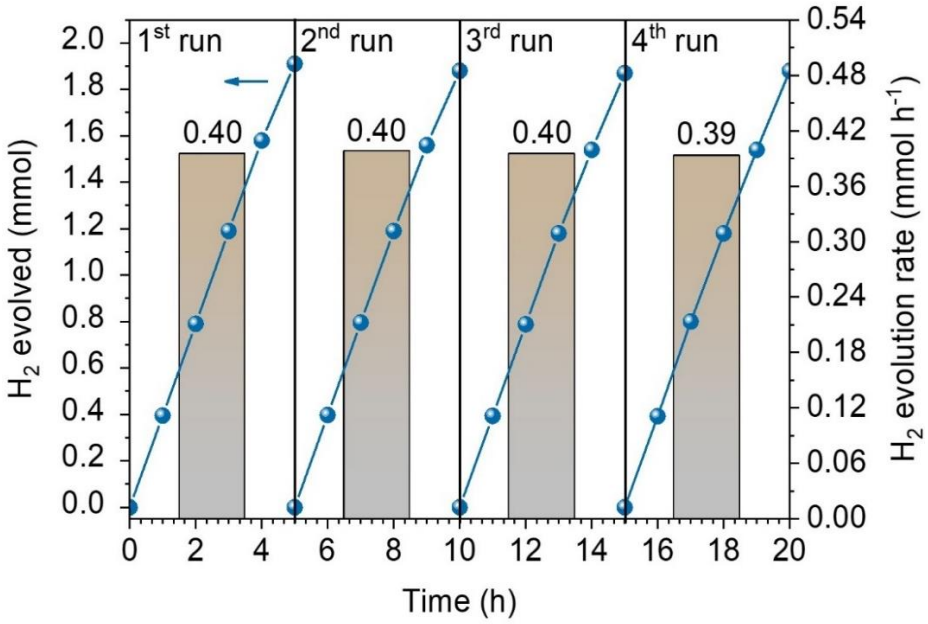

Figure 3-108. Photocatalytic stability test of 10-Ni/CIS NCF. The columns depict the corresponding H_2 evolution rate of each catalytic run. Reaction conditions: 20 mg of photocatalyst in 20 mL aqueous solution of TEOA (10% v/v), 300-W Xe-lamp equipped with a UV-cut off filter ($\lambda \geq 420$ nm).

Moreover, post-catalytic XPS measurement of the catalyst showed no chemical degradation under the examined conditions (**Figure 3-109**). The Cd 3d XPS spectrum of the recycled catalyst (10-Ni/CIS NCF) showed a doublet peak at 405.1 and 411.9 ± 0.1 eV, corresponding to the respective Cd $3d_{5/2}$ and Cd $3d_{3/2}$ of Cd^{2+} ions. Similarly, the In 3d XPS spectrum displayed a doublet peak attributed to the In $3d_{5/2}$ (445.0 ± 0.1 eV) and In $3d_{3/2}$ (452.5 ± 0.1 eV) core-levels of the In^{3+} ions in $CdIn_2S_4$ thiospinel. The S 2p XPS signal at 161.9 ± 0.2 eV is attributed to the S^{2-} valence state, while the broad peak at 168.8 ± 0.2 eV is due to the formation of SO_x species, originating from the surface oxidation of the sample and/or photo-corrosion. In the Ni 2p XPS core-level region, the two prominent peaks of Ni $2p_{3/2}$ and Ni $2p_{1/2}$ at 856.1 and 873.9 ± 0.2 eV, respectively, correspond to the Ni(II) of $Ni(OH)_2$, while the strong satellite peaks at 861.9 and 879.7 ± 0.2 eV further confirms the existence of paramagnetic Ni^{2+}. Also, post-reaction EDS characterization further affirmed that 10-Ni/CIS NCF retained its

chemical integrity even after 20 hours of light irradiation (**Figure 3-110a**). Nevertheless, N_2 physisorption measurement (**Figure 3-110b**) revealed a slight deterioration in the mesoporous structure of the recycled catalyst, possibly due to minor photo-corrosion and/or some nanoparticle rearrangement in the porous structure.

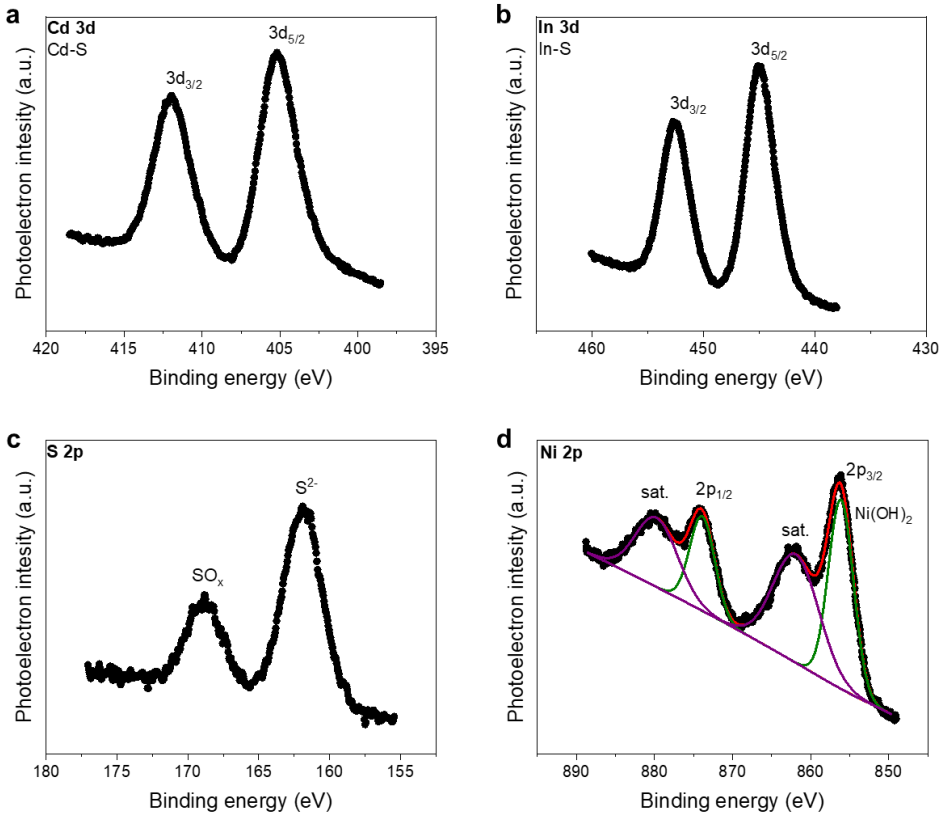

Figure 3-109. Typical XPS spectra of (a) Cd 3d, (b) In 3d, (c) S 2p and (d) Ni 2p of the 10-Ni/CIS NCF photocatalyst after four-five hours catalytic experiments.

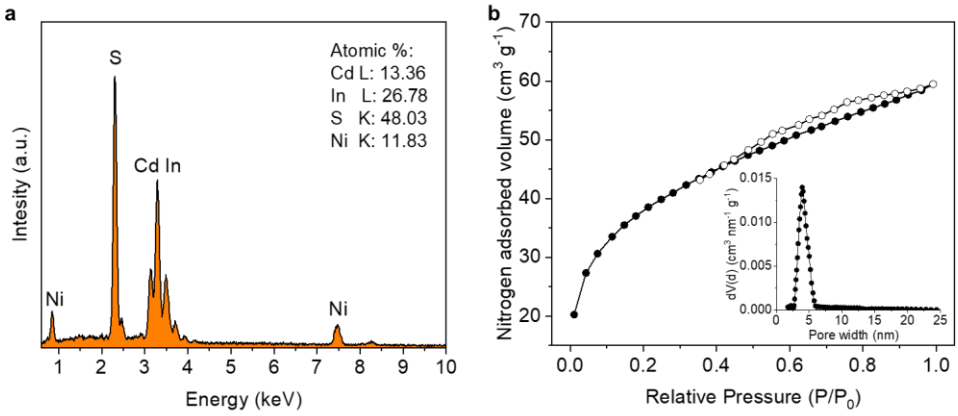

Figure 3-110. (a) Typical EDS spectrum, showing a 9.95 wt. % Ni content, and (b) N_2 adsorption-desorption isotherms at –196 ºC of the of the reused 10-Ni/CIS NCF catalyst. Analysis of the adsorption data gives a surface area of 133 $m^2\ g^{-1}$, a total pore volume of 0.1 $cm^3\ g^{-1}$ and an average pore width of 4.0 nm.

3.4.3 Energy band structure and charge transfer kinetics

The impact of β-$Ni(OH)_2$ modification on the charge transfer and separation dynamics was investigated by electrochemical spectroscopy. As can be seen in **Figure 3-111**, Mott-Schottky plots of the inverse square space-charge capacitance ($1/C_{SC}^2$) as a function of applied voltage (E) were measured for the mesoporous CIS and Ni-modified CIS NCFs catalysts. All samples were drop-casted on fluorine-doped tin oxide (FTO, 1 Ω sq^{-1}) substrate, and the reported electrochemical potential values were converted to the reversible hydrogen electrode (RHE) scale at pH 7. Apparently, the positive slope of the Mott-Schottky plots of mesoporous CIS suggests n-type conductivity. On the other hand, a bell-shaped $1/C_{SC}^2$–E curve can be observed for the Ni-modified materials, indicating the existence of p-n junction. As a proof of concept, we have acquired the Mott-Schottky plot of β-$Ni(OH)_2$ microparticles under identical experimental conditions. In **Figure 3-112**, β-$Ni(OH)_2$ microparticles clearly show a steep negative gradient of the $1/C_{SC}^2$–E curve, providing direct evidence of the p-type conductivity. As such, the formation of p-n junctions among the p-type β-$Ni(OH)_2$ and n-type CIS NCFs undoubtedly dictates the band edge alignment and, thus, the charge transfer and separation dynamics at the interface. The flat band potential (E_{FB}) of the samples was determined by the intersection point of the Mott-Schottky plots ($1/C_{SC}^2$ =0). Taking into consideration, the calculated E_{FB} potentials and the optical bandgap (E_g) (as determined form UV-vis/NIR absorption spectra, **Figure 3-102** and **3-103**), the respective conduction (E_C) and valence (E_V) band edge levels for each catalyst can be obtained. In this analysis, we assume the E_{FB} potential as a good approximation of the conduction or valence band edge position for heavily n-type and p-type semiconductors, respectively. Typically, for many heavily doped semiconductors, such as CIS and β-$Ni(OH)_2$, the Fermi level is located within ~0.1–0.4 eV from the band edge [46]. The calculated band-edge potentials are summarized in **Table 3-19**, and the corresponding band diagrams of each catalyst are depicted in **Figure 3-113**. From this analysis, the E_{FB} level of CIS NCF is determined to be –0.97 V, while upon deposition of β-$Ni(OH)_2$, the E_{FB} of the Ni/CIS heterostructures undergoes a significantly change. Specifically, the Ni/CIS NCFs materials present a systematic downwards shift of the E_{FB} from –0.72 V to –0.54 V. The anodic shift of the E_{FB} level stems from the formation of p-n junctions between β-$Ni(OH)_2$ and CIS components. Since the Fermi level of β-$Ni(OH)_2$ (ca. 5.2–5.4 eV vs vacuum) [183] is much lower than that of CIS (ca. 4.0 eV vs vacuum), an electron flow from CIS to β-$Ni(OH)_2$ nanoparticles will take place upon contact, until their Fermi levels align. The net effect of this process will decrease the donor concertation (N_D) in CIS. Supporting this conclusion,

the N_D of CIS NCF was determined to be ~1.1 × 10^{18} cm^{-3}, much higher than those of the Ni-modified samples (~0.55–5.0 × 10^{17} cm^{-3}), see **Table 3-19**. The gradual reduction of N_D concertation confirms an electron migration from the mesoporous CIS to β-$Ni(OH)_2$ nanoparticles, in good agreement with the observed potential drop of CIS's E_{FB} level. Notably, compared to the mesoporous 10-Ni/CIS NCF, the bulk 10-Ni/CIS-*m* reference sample exhibits a less anodic shift of E_{FB} (–0.57 V) and lower N_D concertation loss (~3.7 × 10^{17} cm^{-3}) compared to the CIS microparticles (E_{FB} ~ –0.77 V, N_D ~ 6.6 × 10^{17} cm^{-3}, see **Figure 3-62**), suggesting weak electronic interactions between β-$Ni(OH)_2$ and CIS microparticles.

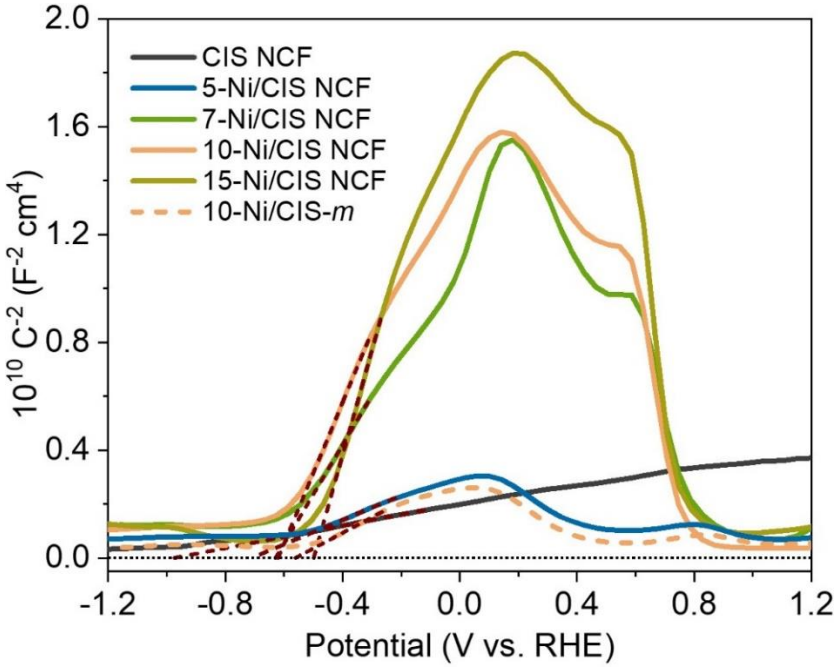

Figure 3-111. Mott-Schottky plots measured in 0.5 M Na_2SO_4 electrolyte (pH= 6.87) using a standard three-electrode cell.

Table 3-19. Electrochemical properties of the different CIS and Ni/CIS catalysts.

Catalyst	E_{FB} (V vs RHE, pH 7)	E_V† (V vs RHE, pH 7)	Donor concentration (N_D, cm^{-3})	R_{ct} (Ω)
CIS NCF	–0.97	1.60	1.06 × 10^{18}	565
5-Ni/CIS NCF	–0.70	1.89	5.04 × 10^{17}	346
7-Ni/CIS NCF	–0.63	1.89	1.17 × 10^{17}	265
10-Ni/CIS NCF	–0.62	1.86	8.15 × 10^{16}	238
15-Ni/CIS NCF	–0.50	1.95	5.52 × 10^{16}	373
10-Ni/CIS-*m*	–0.56	1.77	3.70 × 10^{17}	1104

†The valence band energy (E_V) of the catalysts was estimated from $E_V = E_{FB} + E_g$.

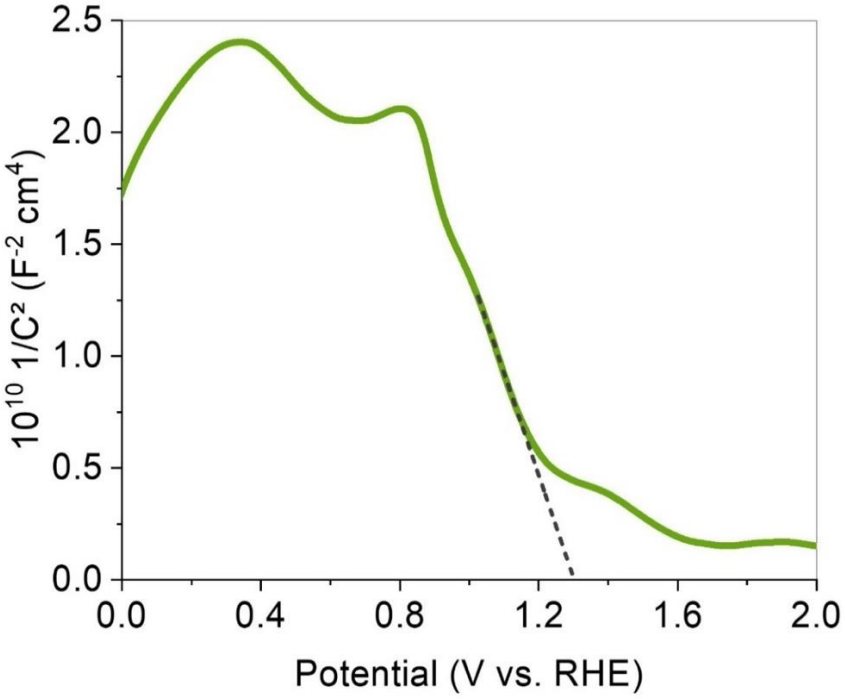

Figure 3-112. Mott-Schottky plots of as prepared β-$Ni(OH)_2$ microparticles measured in 0.5 M Na_2SO_4 electrolyte (pH=6.87) using a standard three-electrode cell. The linear fit of the data (dashed line) yields a E_{FB} of ~1.30 V vs RHE, while the positive slope indicates p-type conductivity.

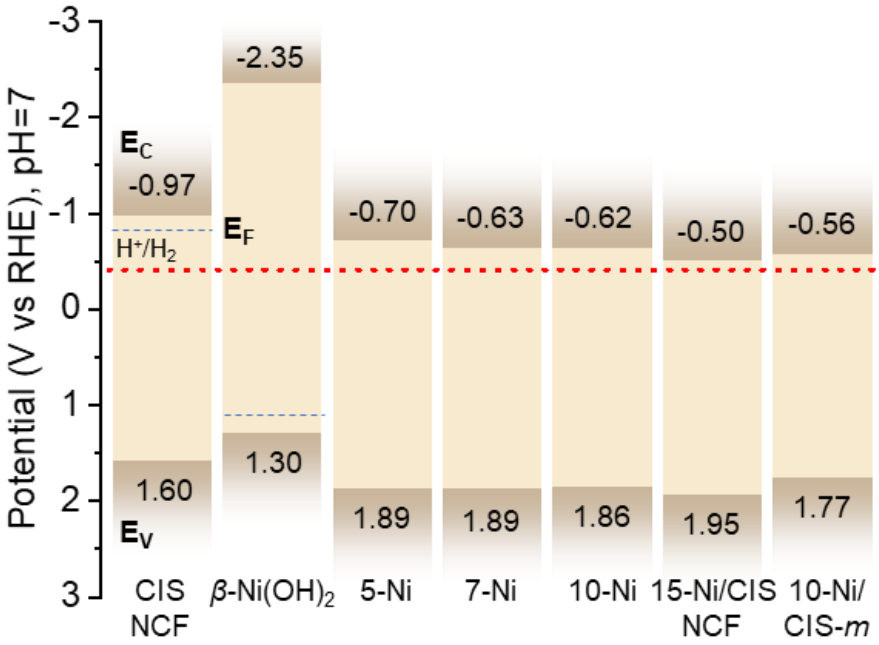

Figure 3-113. Energy band diagrams (E_V: valence band, E_C: conduction band, E_F: Fermi level, red dashed line: H^+/H_2 redox potential) for the mesoporous CIS and Ni/CIS NCFs and bulk 10-Ni/CIS-*m*.

The position of the Fermi level, defined by the carrier concentration, also serves as valuable descriptor for further investigating the electronic interaction between β-$Ni(OH)_2$ and CIS semiconductors. From valence band XPS (VB-XPS) experiments, the energy difference of the Fermi level and the E_V of mesoporous CIS and 10-Ni/CIS NCFs is determined to be 1.93 and 1.78 eV, respectively (**Figure 3-114**). This downshift of the Fermi level upon β-$Ni(OH)_2$ deposition clearly affirms an electron injection from CIS to β-$Ni(OH)_2$, as inferred from the above electrochemical analysis. Thus, we can conclude that the changes of the CIS band-edge positions induced by β-$Ni(OH)_2$ hybridization play a critical role to enhance photo-carrier dissociation and transfer efficiency.

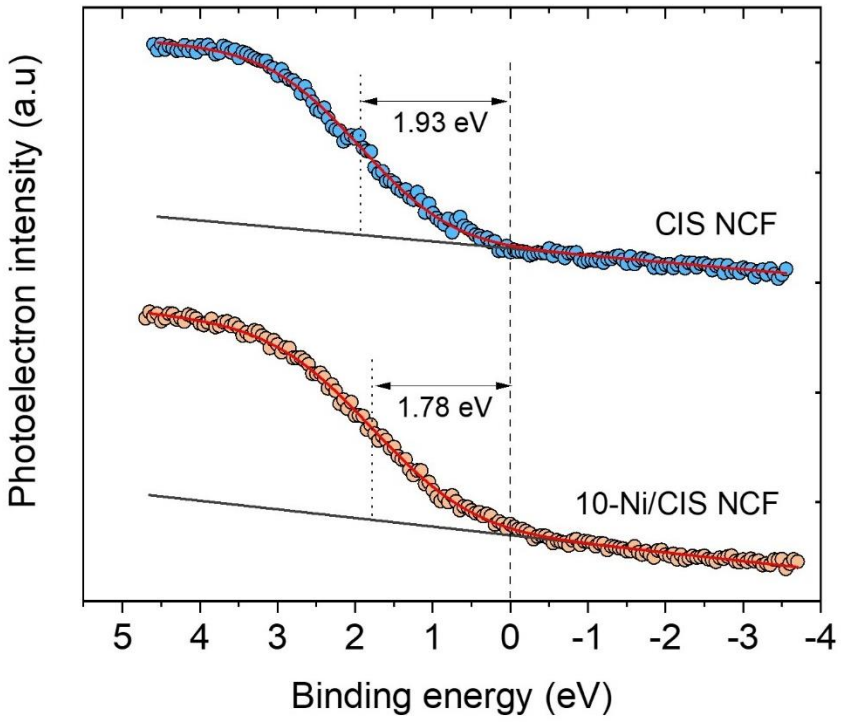

Figure 3-114. Valence band XPS (VB-XPS) spectra of the mesoporous CIS and 10-Ni/CIS NCF catalysts.

In order to further investigate the effect of β-$Ni(OH)_2$ deposition on the charge-transfer properties in Ni/CIS mesostructures, the electrochemical impedance spectroscopy (EIS) and time-resolved PL (TRPL) spectroscopy experiments were conducted as well. The EIS Nyquist spectra of the pristine CIS and different Ni-modified samples drop-casted on FTO electrodes are displayed in **Figure 3-115**. A simple equivalent circuit model (inset of **Figure 3-115**) was employed to fit the EIS plots and extract the charge-transfer resistance (R_{ct}) of the catalysts (**Table 3-20**). The R_{ct} values of the Ni-modified catalysts (238–373 Ω) imply a much smaller

impedance compared to the pristine CIS NCF (565 Ω) and the isolated β-Ni(OH)$_2$ microparticles (3437 Ω) (**Figure 3-116**), suggesting an enhanced charge transfer efficiency at the β-Ni(OH)$_2$/CIS contact, see **Table 3-19**. Notably, the decreasing trend of R_{ct} observed after β-Ni(OH)$_2$ deposition correlates well with the results from the hydrogen production experiments (**Figure 3-104**). It turns out that the catalyst containing 10 wt. % Ni (10-Ni/CIS NCF) exhibits the lowest charge transfer resistance (R_{ct} ~ 238 Ω), which is consistent with its superior photocatalytic activity. Interestingly, the bulk 10-Ni/CIS-*m* reference sample shows a much lower charge transfer efficiency (R_{ct} ~ 1104 Ω) across the catalyst/electrolyte interface, which a direct result of the poor electronic contact between β-Ni(OH)$_2$ and CIS microparticles, in agreement with our previous EIS results for 10-Ni/CIS-*m*.

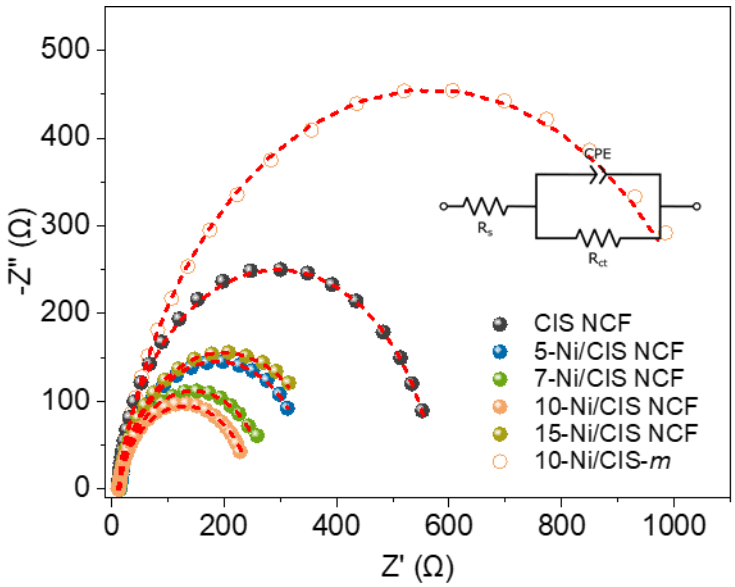

Figure 3-115. Nyquist plots for the mesoporous CIS and Ni/CIS NCFs and bulk 10-Ni/CIS-*m*. Inset: equivalent circuit model to fit the EIS data.

Table 3-20. Nyquist equivalent circuit fitted parameters of the prepared materials.

Sample	**R_s (Ω)**	**C_{dl} (F)**	**R_{ct} (Ω)**	**x^2**
CIS NCF	12.46	46×10^{-6}	565	3.60×10^{-3}
5-Ni/CIS NCF	14.72	185×10^{-6}	346	1.95×10^{-4}
7-Ni/CIS NCF	13.51	195×10^{-6}	265	3.06×10^{-3}
10-Ni/CIS NCF	12.19	144×10^{-6}	238	4.16×10^{-3}
15-Ni/CIS NCF	12.70	221×10^{-6}	373	2.16×10^{-3}
10-Ni/CIS-*m*	13.79	58×10^{-6}	1104	3.53×10^{-3}
β-Ni(OH)$_2$	13.36	39×10^{-6}	3437	3.13×10^{-3}

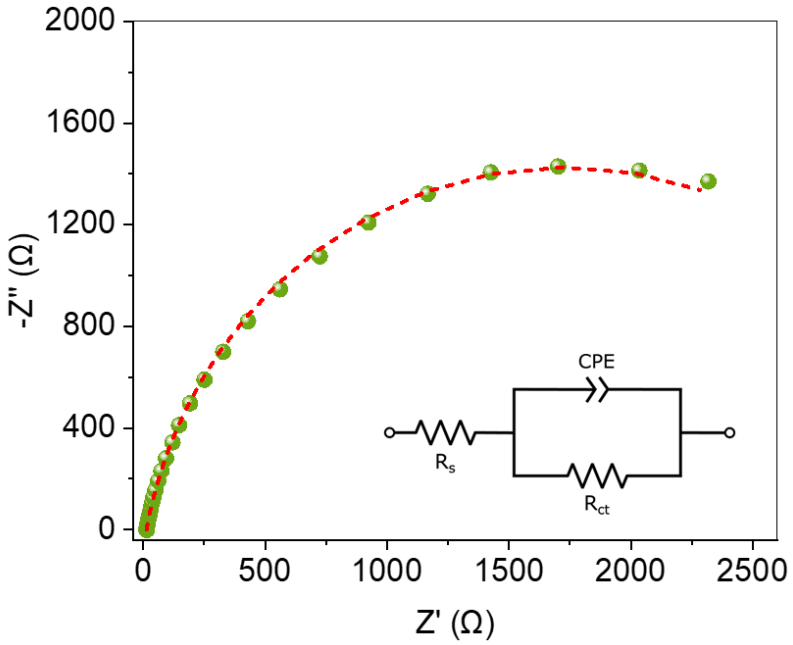

Figure 3-116. Nyquist plot of the β-Ni(OH)$_2$ microparticles. Inset: equivalent circuit model to fit the EIS data.

Figure 3-117 depicts the PL decay curves of different catalysts measured under 375 nm pump laser excitation. To investigate the kinetic characteristics of the photoexcited charge carriers the TRPL spectra were fitted by a biexponential function: $I(t) = y_0 + \Sigma_i \alpha_i \cdot e^{-t/\tau i}$ (i = 1, 2), where α_i are the amplitude fractions ($\Sigma_i \alpha_i = 1$) and τ_i are the lifetimes for the surface-mediated (τ_1, fast) and intrinsic band-to-band (τ_2, slow) recombination of excitons. All the TRPL fitting parameters are listed in **Figure 3-117**. The fitting results indicated that the 10-Ni/CIS NCF catalyst exhibits an average electron-hole pair lifetime ~1.3–1.4 times larger (4.68 ns) than that of the CIS NCF (3.41 ns) and bulk 10-Ni/CIS-*m* analogue (3.66 ns), suggesting a more efficient migration of the photogenerated carriers for 10-Ni/CIS NCF catalyst. Furthermore, a more detailed look of the τ-component fractions indicateed a predominant recombination of excitons on the surface for CIS NCF and 10-Ni/CIS-*m*; both sample exhibit a ~69–70% contribution of the fast τ_1-component. On the contrary, a significantly lower contribution (~30 %) of defect trapping was observed for 10-Ni/CIS NCF, indicating a lower carrier-recombination loss at the nanostructure interface. Transient photocurrent (TPC) experiments confirmed also the same conclusions. **Figure 3-118** shows that the mesoporous 10-Ni/CIS NCF generates a much higher photocurrent density than CIS NCF and 10-Ni/CIS-*m*, suggesting that a more efficient dissociation and migration pathway of the photogenerated carriers exists over the nano-heterostructure photocatalyst. Obviously, the formation of p-n β-

$Ni(OH)_2/CdIn_2S_4$ nano-heterojunction instigates an improved interfacial charge transfer and separation effect, resulting to a more effective utilization of the photogenerated carriers for redox reactions at the catalyst surface.

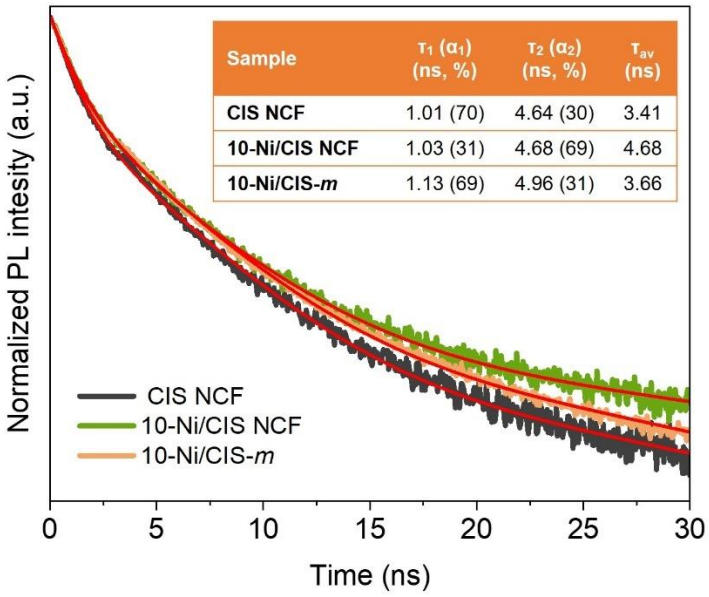

Figure 3-117. Time-resolved photoluminescence (TRPL) spectra of mesoporous CIS and 10-Ni/CIS NCF and bulk 10-Ni/CIS-*m*. Inset: the PL decay parameters of samples. The average lifetime (τ_{av}) was calculated as $\tau_{av}=(\sum_i \alpha_i \tau_i^2)/(\sum_i \alpha_i \tau_i)$ (i = 1, 2). The red lines are fit to the experimental data.

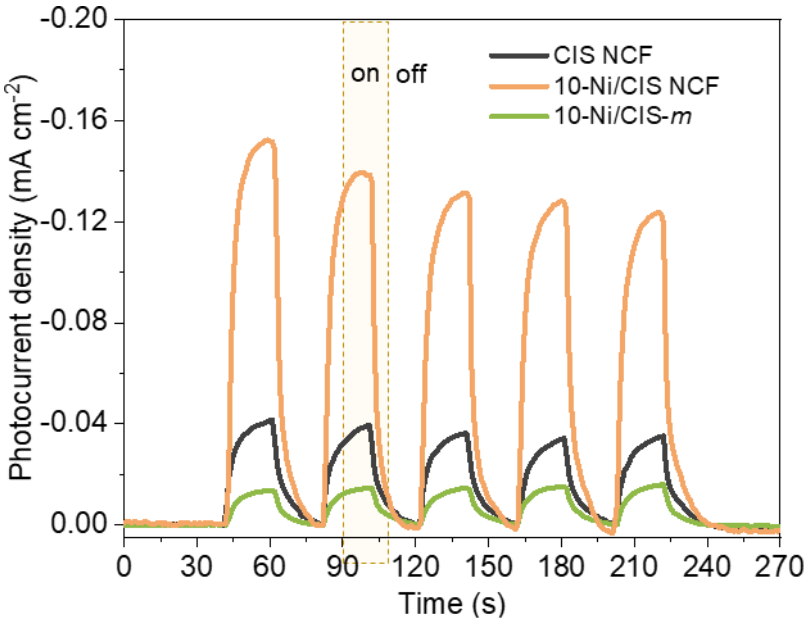

Figure 3-118. Transient photocurrent (TPC) response of mesoporous CIS and 10-Ni/CIS NCF and bulk 10-Ni/CIS-*m*.

In light of all the above results, a band alignment model and charge transfer mechanism for the photocatalytic hydrogen evolution reaction over β-$Ni(OH)_2$/CIS nano-heterojunctions is proposed in **Figure 3-119**. Specifically, β-$Ni(OH)_2$ is a p-type semiconductor with a Fermi level well below that of CIS (~5.2–5.4 eV vs ~4.0 eV) and the close contact between these two semiconductors can result to an electron flow from CIS to β-$Ni(OH)_2$ until their Fermi levels react equilibrium. The outcome of this process will generate a depletion region, that is, a positively charged area in the CIS side, leading to an upward shift of both E_C and E_V edge positions near the heterojunction interface. Simultaneously, an accumulation region, that is, a negatively charged area will develop in the β-$Ni(OH)_2$ side, shifting its band-edges to lower energies. Thus, a build-in potential, defined by the electrochemical potential of CIS NCF (ca. 4.0 eV) and β-$Ni(OH)_2$ (ca. 5.2–5.4 eV), of about 1.2–1.4 V will be established within the interface, generating a strong internal electric field directed from CIS to β-$Ni(OH)_2$. The redistribution of the charge carriers at the p-n β-$Ni(OH)_2$/$CdIn_2S_4$ heterojunction is in line with the observations from the EIS and VB-XPS analysis. Indeed, all these effects undoubtedly will contribute positively to the photocatalytic activity of the Ni/CIS NCFs catalysts. Under visible light irradiation, only CIS gets excited and generates electron-hole pairs, as β-$Ni(OH)_2$ does not absorb light within this wavelength range ($\lambda \geq 420$ nm) due to its substantial energy gap (~3.64 eV). Due to the favorable type-II band scheme (CIS has a more positive E_V and E_C edges than β-$Ni(OH)_2$) and the generation of strong internal electric field at the p-n junction, the photogenerated holes in the VB of CIS are thermodynamically transferred to β-$Ni(OH)_2$, where they are effectively consumed by the sacrificial agent (TEOA). This β-$Ni(OH)_2$-mediated hole-transport pathway has the ability to spatially separate the photogenerated charge carriers, thus promoting the accumulation of electrons on the CIS surface (mainly on the adjacent Cd and In atoms) [141], where they can reduce protons to hydrogen. This mechanistic model is in good agreement with the experimental results from EIS, TRPL and TPC studies. Moreover, the highly porous architecture of the Ni/CIS heterojunctions provides an increased active-site exposure and enhanced mass transfer kinetics, both of which are crucial for improving the efficiency of photocatalytic hydrogen evolution. Supporting evidence for the improved electrolyte permeability of 10-Ni/CIS NCF was obtained through contact angle measurements. The contact angle analysis in **Figure 3-120** indicates a higher diffusion rate and better penetration of water into the mesoporous architecture of 10-Ni/CIS NCF compared to both CIS NCF and bulk 10-Ni/CIS-*m*. In particular, the water contact angle measures ~14º for 10-Ni/CIS NCF, ~20º for CIS NCF and ~30º for 10-Ni/CIS-*m* after diffusion for 400 ms. This affirms that both Ni modification and open-pore structure are crucial features of the Ni/CIS NCFs,

enhancing the wettability of the photocatalyst and thereby increasing the water-catalyst interface area.

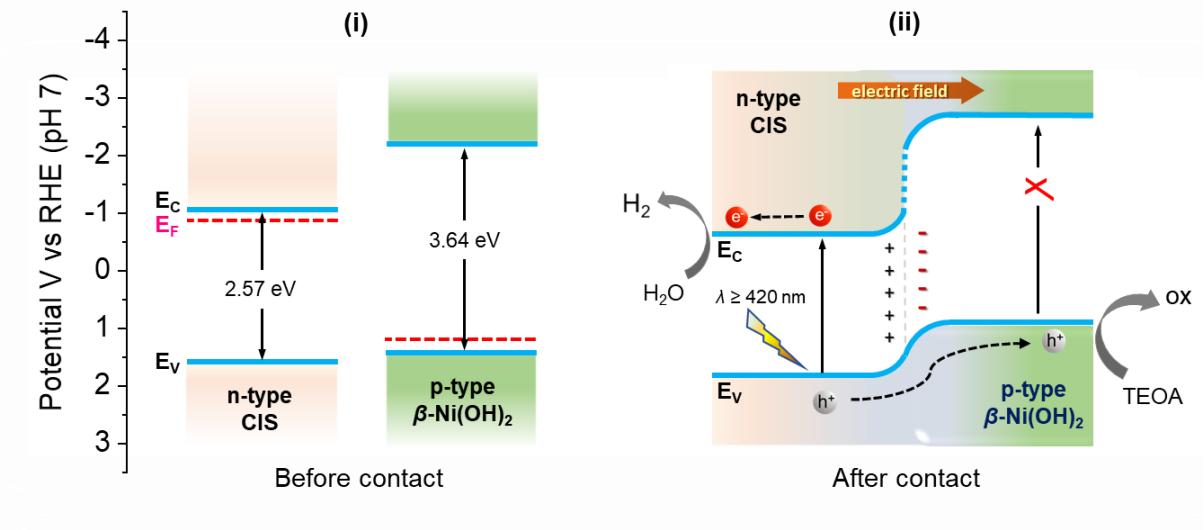

Figure 3-119. Energy bad diagrams of the n-type CIS and p-type β-$Ni(OH)_2$ semiconductors before (i) and after (ii) contact (E_V: valence band energy, E_C: conduction band energy, E_F: Fermi level). The band alignment model of the p-n junction upon contact of CIS and β-$Ni(OH)_2$ nanoparticles depicts the charge-transfer mechanism of the photocatalytic H_2 production by the mesoporous Ni/CIS NCFs.

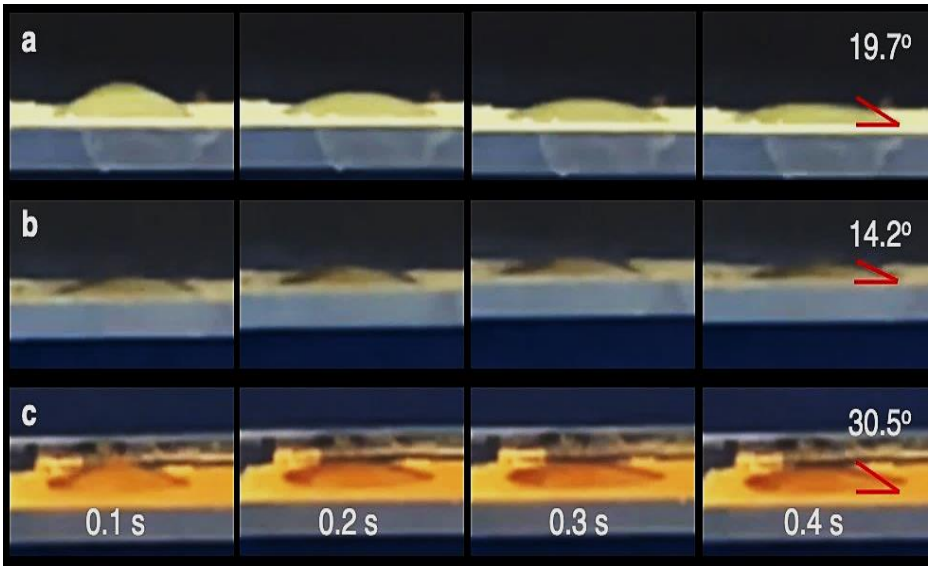

Figure 3-120. Contact angle measurements of the mesoporous (a) CIS and (b) 10-Ni/CIS NCF, and (c) bulk 10-Ni/CIS-*m*. The diameter of the water droplet was approximately 2 nm.

3.4.4 Conclusions

In this project, mesoporous networks of interconnected β-$Ni(OH)_2$-modified $CdIn_2S_4$ nanocrystals were successfully prepared by a polymer-templated chemical method, followed by a photochemical deposition process. Characterization by UV-vis/NIR, electrochemical impedance and photoluminescence spectroscopy unveiled that Ni deposition effectively tune the kinetics of charge transfer and separation, resulting to a significantly improved photocatalytic activity for hydrogen production. The p-type β-$Ni(OH)_2$ nanoparticles serve as efficient hole-transfer mediator, facilitating the transport of photoexcited holes from the n-type $CdIn_2S_4$ photocatalyst to the sacrificial agent. Furthermore, the mesoporous structure of the prepared materials provides a superior exposure of active sites for redox reactions and facilitates the rapid electrolyte transport between the nanoparticles. Consequently, the catalyst with 10 wt. % Ni loading displays a remarkable photocatalytic activity and stability for the water reduction reaction, yielding a hydrogen evolution rate of 0.4 mmol h^{-1} (or 20 mmol g_{cat}^{-1} h^{-1} mass activity) under $\lambda \geq 420$ nm light irradiation with an apparent quantum yield of ~52% at 420 nm.

Chapter 4: Concluding Remarks

A new cost-effective synthetic protocol for obtaining mesoporous architectures of thiospinel nanocrystals has been successfully developed and reported. In contrast to conventional solvothermal and high-temperature solid-state methods, this chemical process enables the synthesis of ultrasmall thiospinel nanoparticles with tunable size and composition. Such colloidal nanoparticles can constitute functional structural units to assemble 3D mesostructured networks through a polymer-templating chemical method. Consequently, the controlled synthesis of $ZnIn_2S_4$ nanoparticles with sizes ranging from 4 to 11 nm, and their subsequent integration into mesoporous architectures with large internal surface areas and well-defined pores, has been achieved. Benefiting from the open pore architecture and small grain size, the synthesized mesoporous structures exhibit exceptional photocatalytic activity for hydrogen evolution, yielding a hydrogen evolution rate of 234 μmol h^{-1} and an apparent quantum yield (AQY) of 25% at 375 nm and 17.2% at 420 nm.

We further demonstrated the versatility of our synthetic protocol by successfully preparing mesoporous architectures consisting of $CdIn_2S_4$ nanoparticles of various sizes (from 6 to 11 nm). Interestingly, $CdIn_2S_4$ nanocrystals exhibited a unique hexagonal crystal structure, which has not been previously reported. Moreover, by employing Ni_2P nanosheets as co-catalyst within the porous structure of $CdIn_2S_4$, we successfully engineering $Ni_2P/CdIn_2S_4$ heterostructures with enhanced electronic properties and distinct structural characteristics. These beneficial aspects led to a remarkable photocatalytic performance, achieving a hydrogen evolution rate of 581 μmol h^{-1} and an apparent quantum yield of 61.7% at 420 nm. This activity represents a record for $CdIn_2S_4$-based photocatalysts and ranks among the highest reported for thiospinel-based systems.

Mesoporous networks comprising closely integrated Co_2P nanoparticles and $CdIn_2S_4$ nanocrystals with a high internal surface area were also constructed and investigated as photocatalysts for the hydrogen evolution reaction. The results demonstrate that $Co_2P/CdIn_2S_4$ Mott-Schottky heterojunctions establish sustainable pathways for the photoexcited electrons to transfer to the catalyst surface, thereby significantly enhanced photoactivity. Specifically, the $Co_2P/CdIn_2S_4$ photocatalyst containing 10 wt. % Co_2P achieves a hydrogen evolution rate of 417 μmol h^{-1} and an apparent quantum yield of 56.1% at 420 nm.

The photochemical deposition of Ni-species on the porous surface of $CdIn_2S_4$ mesoporous frameworks led to the formation of high surface area β-$Ni(OH)_2$-modified $CdIn_2S_4$

photocatalysts, which exhibited high photoreduction activity towards hydrogen production. The p-type β-$Ni(OH)_2$ nanoparticles act as efficient hole-transfer mediators, facilitating the transportation of photoexcited holes from the n-type $CdIn_2S_4$ photocatalyst to the electrolyte, thus enhancing the efficiency of electron-hole pair separation. Consequently, the catalyst containing 10 wt. % Ni exhibits a hydrogen evolution rate of 395 μmol h^{-1} and an apparent quantum yield of 52% at 420 nm, while demonstrating remarkable photo-corrosion resistance during long-term operation.

The impact of each co-catalyst on the electrochemical properties of thiospinel materials and the mechanism underlying hydrogen evolution were elucidated using a combination of various physicochemical and spectroscopic techniques, including electron microscopy (TEM/FESEM), X-ray diffuse scattering, in-situ irradiated X-ray photoelectron spectroscopy (XPS), (photo)electrochemical spectroscopy, and time-resolved photoluminescence (PL). Thorough these investigations, a comprehensive understanding of the intricate charge transfer dynamics in these photocatalytic systems has been achieved. This knowledge is essential for the rationally design of next-generation photocatalysts for clean energy production.

Annex I: Photocatalytic comparison with other reported materials

Table I. Comparison of the photocatalytic H_2-production activities and quantum yields of different thiospinel-based catalysts.

Photocatalyst	Reaction Conditions	Light Source	H_2 evolution rate		Quantum efficiency (QE)	Ref.
			($\mu mol\ h^{-1}$)	($\mu mol\ g^{-1}\ h^{-1}$)		
3 wt. % Pt/ 5 wt. % Co_9S_8/ $CdIn_2S_4$	50 mg catalyst, 20% v/v TEOA	300 W Xe lamp ($\lambda \geq 420$ nm)	54	1083.6	5.5% at 420 nm	[160]
$CdIn_2S_4$@CoAl-LDH	2 mg catalyst, 10% v/v TEOA	300 W Xe lamp ($\lambda \geq 420$ nm)	1.6	793.4	0.2% at 450 nm	[184]
$CdIn_2S_4/In(OH)_3/Zn_2GeO_4$	50 mg catalyst, 0.35 M Na_2S, 0.25 M Na_2SO_3	300 W Xe lamp ($\lambda \geq 420$ nm)	71	1426.90	9.1% at 420 nm	[185]
1 wt.% MoS_2/ $CdIn_2S4$	50 mg catalyst, 0.35 M Na_2S, 0.25 M Na_2SO_3	300 W Xe lamp ($\lambda \geq 420$ nm)	47.3	2365	5.2% at 400 nm	[186]
$CdIn_2S_4/In(OH)_3$/NiCr-LDH	50 mg catalyst, 0.35 M Na_2S, 0.25 M Na_2SO_3	300 W Xe lamp ($\lambda \geq 420$ nm)	54.65	1093	1.7% at 420 nm	[187]
$CdIn_2S_4$/rGO/ZnS QDs	50 mg catalyst, 6% v/v TEOA	300 W Xe lamp ($\lambda \geq 420$ nm)	341	6820	19.3% at 430 nm	[188]
$CdIn_2S_4/CNFs/Co_4S_3$	50 mg catalyst, 20% v/v lactic acid	300 W Xe lamp ($\lambda \geq 420$ nm)	1293.5	25870	16.3% at 420 nm	[60]
$CdIn_2S_4$/ZnS	20 mg catalyst, 0.35 M Na_2S, 0.25 M Na_2SO_3	300 W Xe lamp	74.8	3743	2.2% at 365 nm	[189]
$CdIn_2S_4/ZnIn_2S_4$	4 mg catalyst, 0.35 M Na_2S, 0.25 M Na_2SO_3	300 W Xe lamp ($\lambda \geq 420$ nm)	50.7	12670	18.7% at 420 nm	[84]
Co-Pi/$CdIn_2S_4$	10 mg catalyst, 20% v/v MeOH	500 W Xe lamp ($\lambda \geq 420$ nm)	72.8	7280	14.1% at 405 nm	[190]
g-$C_3N_4/ZnIn_2S_4$	50 mg catalyst, 20% v/v TEOA	300 W Xe lamp ($\lambda \geq 420$ nm)	139	2780	7.1% at 420 nm	[191]
$Mo_2C/ZnIn_2S_4$	20 mg catalyst, 20% v/v TEOA	300 W Xe lamp ($\lambda > 400$ nm)	442.2	22110	71.6% at 420 nm	[192]
$MoS_2/ZnIn_2S_4$/RGO	50 mg catalyst, 10% v/v lactic acid	300 W Xe lamp	289.5	5791	54.2% at 420 nm	[193]
$Cu_2MoS_4/ZnIn_2S_4$	20 mg catalyst, 20% v/v TEOA	300 W Xe lamp ($\lambda \geq 400$ nm)	162	8103	7.4% at 420 nm	[194]
MoS_2 QDs/Vs-$ZnIn_2S_4$	50 mg catalyst, 10% v/v lactic acid	300 W Xe lamp ($\lambda > 300$ nm)	344	6884	63.9% at 420 nm	[195]
$Sb_2S_3/ZnIn_2S_4$	50 mg catalyst, 20% v/v TEOA	300 W Xe lamp	84	1685	3.8% at 420 nm	[196]
$MoSe_2/ZnIn_2S_4$	60 mg catalyst, 0.35 M Na_2S, 0.25 M Na_2SO_3	300 W Xe lamp ($\lambda \geq 420$ nm)	133.7	2228	21.4% at 420 nm	[197]
PtS QDs/$ZnIn_2S_4$	10 mg catalyst, 0.1 M ascorbic acid	300 W Xe lamp ($\lambda \geq 420$ nm)	207.7	20777	13.3% at 430 nm	[198]

$ZnIn_2S_4$@$NiCo_2S_4$	20 mg catalyst, 10% v/v TEOA	300 W Xe lamp (λ≥420 nm)	32	1950	9.3% at 420 nm	[199]
$NiSe_2$/$ZnIn_2S_4$	20 mg catalyst, 10% v/v TEOA	300 W Xe lamp (λ≥420 nm)	29.7	1487	6.1% at 420 nm	[200]
$Ni_{12}P_5$/$CdIn_2S_4$	30 mg catalyst, 10% v/v TEOA	300 W Xe lamp (λ≥420 nm)	150.3	5010	23.5% at 400 nm	[201]
Ni_2P/$ZnIn_2S_4$	50 mg catalyst, 10% v/v lactic acid	300 W Xe lamp (λ>400 nm)	103.3	2066	7.7% at 420 nm	[202]
CoP/$ZnIn_2S_4$	20 mg catalyst, 0.35 M Na_2S, 0.25 M Na_2SO_3	300 W Xe lamp (λ≥420 nm)	175.5	8775	24.1% at 420 nm	[203]
Pt/Cu_3P/$ZnIn_2S_4$	50 mg catalyst, 0.35 M Na_2S, 0.25 M Na_2SO_3	300 W Xe lamp (λ≥420 nm)	128	2561	22.3% at 420 nm	[204]
$Ni_{12}P_5$/$ZnIn_2S_4$	50 mg catalyst, 0.35 M Na_2S, 0.25 M Na_2SO_3	300 W Xe lamp (λ≥420 nm)	113	2263	20.5% at 420 nm	[205]
CoP@$ZnIn_2S_4$	10 mg catalyst, 10% v/v TEOA	300 W Xe lamp (λ≥420 nm)	103	10300	16.2% at 420 nm	[206]
6-ZIS NCF ($ZnIn_2S_4$)	**30 mg catalyst, 10% v/v TEA**	**300 W Xe lamp**	**234**	**7800**	**25.0% at 375 nm, 17.2% at 420 nm**	**This work**
15-Ni_2P/CIS NCF (Ni_2P/$CdIn_2S_4$)	**20 mg catalyst, 10% v/v TEOA**	**300 W Xe lamp (λ≥420 nm)**	**586**	**29300**	**61.7% at 420 nm**	**This work**
10-CP/CIS NCF (Co_2P/$CdIn_2S_4$)	**20 mg catalyst, 10% v/v TEOA**	**300 W Xe lamp (λ≥420 nm)**	**417**	**20850**	**56.1% at 420 nm**	**This work**
10-Ni/CIS NCF (β-$Ni(OH)_2$/$CdIn_2S_4$)	**20 mg catalyst, 10% v/v TEOA**	**300 W Xe lamp (λ≥420 nm)**	**395**	**19750**	**52.0% at 420 nm**	**This work**

References

1. Abe, J.O.; Popoola, A.P.I.; Ajenifuja, E.; Popoola, O.M. Hydrogen Energy, Economy and Storage: Review and Recommendation. *Int. J. Hydrog. Energy* **2019**, *44*, 15072–15086.
2. Luo, X.; Wang, J.; Dooner, M.; Clarke, J. Overview of Current Development in Electrical Energy Storage Technologies and the Application Potential in Power System Operation. *Appl. Energy* 2015, *137*, 511–536.
3. Ren, J.; Musyoka, N.M.; Langmi, H.W.; Mathe, M.; Liao, S. Current Research Trends and Perspectives on Materials-Based Hydrogen Storage Solutions: A Critical Review. *Int. J. Hydrog. Energy* **2017**, *42*, 289–311.
4. Rand, D.A.J. A Journey on the Electrochemical Road to Sustainability. *J. Solid State Electr.* **2011**, *15*, 1579–1622.
5. Abas, N.; Kalair, A.; Khan, N. Review of Fossil Fuels and Future Energy Technologies. *Futures* **2015**, *69*, 31–49.
6. Stern, P.C.; Janda, K.B.; Brown, M.A.; Steg, L.; Vine, E.L.; Lutzenhiser, L. Opportunities and Insights for Reducing Fossil Fuel Consumption by Households and Organizations. *Nat. Energy* **2016**, *1*, 1–6.
7. Midilli, A.; Ay, M.; Dincer, I.; Rosen, M.A. On Hydrogen and Hydrogen Energy Strategies: I: Current Status and Needs. *Renew. Sustain. Energy Rev.* **2005**, *9*, 255–271.
8. Höök, M.; Tang, X. Depletion of Fossil Fuels and Anthropogenic Climate Change—A Review. *Energy Policy* **2013**, *52*, 797–809.
9. Al-Ghussain, L. Global Warming: Review on Driving Forces and Mitigation. *Environ. Prog. Sustain. Energy* **2019**, *38*, 13–21.
10. Abbasi, T.; Abbasi, S.A. Decarbonization of Fossil Fuels as a Strategy to Control Global Warming. *Renew. Sustain. Energy Rev.* **2011**, *15*, 1828–1834.
11. Mazloomi, K.; Gomes, C. Hydrogen as an Energy Carrier: Prospects and Challenges. *Renew. Sustain. Energy Rev.* **2012**, *16*, 3024–3033.
12. Rosen, M.A.; Koohi-Fayegh, S. The Prospects for Hydrogen as an Energy Carrier: An Overview of Hydrogen Energy and Hydrogen Energy Systems. *Energy Ecol. Environ.* **2016**, *1*, 10–29.
13. Hwang, H.T.; Varma, A. Hydrogen Storage for Fuel Cell Vehicles. *Curr. Opin. Chem. Eng.* **2014**, *5*, 42–48.
14. Abdalla, A.M.; Hossain, S.; Nisfindy, O.B.; Azad, A.T.; Dawood, M.; Azad, A.K. Hydrogen Production, Storage, Transportation and Key Challenges with Applications: A Review. *Energy Convers. Manag.* **2018**, *165*, 602–627.
15. Megia, P.J.; Vizcaino, A.J.; Calles, J.A.; Carrero, A. Hydrogen Production Technologies: From Fossil Fuels toward Renewable Sources. A Mini Review. *Energy and Fuels* **2021**, *35*, 16403–16415.
16. Hisatomi, T.; Domen, K. Reaction Systems for Solar Hydrogen Production via Water Splitting with Particulate Semiconductor Photocatalysts. *Nat. Catal. 2019 2:5* **2019**, *2*, 387–399.

17. Nishioka, S.; Osterloh, F.E.; Wang, X.; Mallouk, T.E.; Maeda, K. Photocatalytic Water Splitting. *Nature Reviews Methods Primers 2023 3:1* **2023**, *3*, 1–15.

18. Acar, C.; Dincer, I.; Naterer, G.F. Review of Photocatalytic Water-Splitting Methods for Sustainable Hydrogen Production. *Int. J. Energy Res.* **2016**, *40*, 1449–1473.

19. Wang, Q.; Domen, K. Particulate Photocatalysts for Light-Driven Water Splitting: Mechanisms, Challenges, and Design Strategies. *Chem. Rev.* **2020**, *120*, 919–985.

20. Chen, S.; Takata, T.; Domen, K. Particulate Photocatalysts for Overall Water Splitting. *Nat. Rev. Mater.* **2017**, *2*, 1–17.

21. Hisatomi, T.; Kubota, J.; Domen, K. Recent Advances in Semiconductors for Photocatalytic and Photoelectrochemical Water Splitting. *Chem. Soc. Rev.* **2014**, *43*, 7520–7535.

22. Navarro Yerga, R.M.; Consuelo Álvarez Galván, M.; del Valle, F.; Villoria de la Mano, J.A.; Fierro, J.L.G. Water Splitting on Semiconductor Catalysts under Visible-Light Irradiation. *ChemSusChem* **2009**, *2*, 471–485.

23. Fujishima, A.; Honda, K. Electrochemical Photolysis of Water at a Semiconductor Electrode. *Nature 1972 238:5358* **1972**, *238*, 37–38.

24. Chen, X.; Shen, S.; Guo, L.; Mao, S.S. Semiconductor-Based Photocatalytic Hydrogen Generation. *Chem. Rev.* **2010**, *110*, 6503–6570.

25. Li, X.; Yu, J.; Low, J.; Fang, Y.; Xiao, J.; Chen, X. Engineering Heterogeneous Semiconductors for Solar Water Splitting. *J. Mater. Chem. A* **2015**, *3*, 2485–2534.

26. Li, J.; Wu, N. Semiconductor-Based Photocatalysts and Photoelectrochemical Cells for Solar Fuel Generation: A Review. *Catal. Sci. Technol.* **2015**, *5*, 1360–1384.

27. Osterloh, F.E. Inorganic Nanostructures for Photoelectrochemical and Photocatalytic Water Splitting. *Chem. Soc. Rev.* **2013**, *42*, 2294–2320.

28. Prabakar, K.; Minkyu, S.; Inyoung, S.; Heeje, K. CdSe Quantum Dots Co-Sensitized TiO_2 Photoelectrodes: Particle Size Dependent Properties. *J. Phys. D App.l Phys.* **2009**, *43*, 012002.

29. Kongkanand, A.; Tvrdy, K.; Takechi, K.; Kuno, M.; Kamat, P. V. Quantum Dot Solar Cells. Tuning Photoresponse through Size and Shape Control of CdSe-TiO_2 Architecture. *J. Am. Chem. Soc.* **2008**, *130*, 4007–4015.

30. Sumanth Kumar, D.; Jai Kumar, B.; Mahesh, H.M. Quantum Nanostructures (QDs): An Overview. *Synthesis of Inorganic Nanomaterials: Advances and Key Technologies* **2018**, 59–88.

31. Grela, M.A.; Colussi, A.J. Kinetics of Stochastic Charge Transfer and Recombination Events in Semiconductor Colloids. Relevance to Photocatalysis Efficiency. *Journal of Physical Chemistry* **1996**, *100*, 18214–18221.

32. Lo, A.Y.; Taghipour, F. Ordered Mesoporous Photocatalysts for CO_2 Photoreduction. *J. Mater. Chem. A* **2021**, *9*, 26430–26453.

33. Papadas, I.T.; Vamvasakis, I.; Tamiolakis, I.; Armatas, G.S. Templated Self-Assembly of Colloidal Nanocrystals into Three-Dimensional Mesoscopic Structures: A Perspective on Synthesis and Catalytic Prospects. *Chemistry of Materials* **2016**, *28*, 2886–2896.

34. Ha, T.D.C.; Lee, H.; Vamvasakis, I.; Armatas, G.S.; Oh, Y.; Kim, M.G. Recent Developments in Porous Metal Chalcogenides for Environmental Remediation and Sustainable Energy. *EcoMat* **2023**, *5*, e12419.

35. Vamvasakis, I.; Subrahmanyam, K.S.; Kanatzidis, M.G.; Armatas, G.S. Template-Directed Assembly of Metal-Chalcogenide Nanocrystals into Ordered Mesoporous Networks. *ACS Nano* **2015**, *9*, 4419–4426.

36. Wan, Y.; Yang, H.; Zhao, D. "Host-Guest" Chemistry in the Synthesis of Ordered Nonsiliceous Mesoporous Materials. *Acc. Chem. Res.* **2006**, *39*, 423–432.

37. Kim, K.W.; Park, B.; Kim, J.; Jo, C.; Kim, J.K. Recent Progress in Block Copolymer Soft-Template-Assisted Synthesis of Versatile Mesoporous Materials for Energy Storage Systems. *J. Mater. Chem. A* **2023**, *11*, 7358–7386.

38. Huo, Q.; Margolese, D.I.; Ciesla, U.; Demuth, D.G.; Feng, P.; Gier, T.E.; Sieger, P.; Firouzi, A.; Chmelka, B.F.; Schüth, F.; et al. Organization of Organic Molecules with Inorganic Molecular Species into Nanocomposite Biphase Arrays. *Chemistry of Materials* **1994**, *6*, 1176–1191.

39. Monnier, A.; Schüth, F.; Huo, Q.; Kumar, D.; Margolese, D.; Maxwell, R.S.; Stucky, G.D.; Krishnamurty, M.; Petroff, P.; Firouzi, A.; et al. Cooperative Formation of Inorganic-Organic Interfaces in the Synthesis of Silicate Mesostructures. *Science (1979)* **1993**, *261*, 1299–1303.

40. Attard, G.S.; Glyde, J.C.; Göltner, C.G. Liquid-Crystalline Phases as Templates for the Synthesis of Mesoporous Silica. *Nature* **1995**, *378*, 366–368.

41. Grosso, D.; Cagnol, F.; Soler-Illia, G.J.D.A.A.; Crepaldi, E.L.; Amenitsch, H.; Brunet-Bruneau, A.; Bourgeois, A.; Sanchez, C. Fundamentals of Mesostructuring Through Evaporation-Induced Self-Assembly. *Adv. Funct. Mater.* **2004**, *14*, 309–322.

42. Soler-Illia, G.J.A.A.; Azzaroni, O. Multifunctional Hybrids by Combining Ordered Mesoporous Materials and Macromolecular Building Blocks. *Chem. Soc. Rev.* **2011**, *40*, 1107–1150.

43. Teng, F.; Hu, K.; Ouyang, W.; Fang, X. Photoelectric Detectors Based on Inorganic p-Type Semiconductor Materials. *Adv. Mater.* **2018**, *30*, 1706262.

44. Khan, M.R.; Chuan, T.W.; Yousuf, A.; Chowdhury, M.N.K.; Cheng, C.K. Schottky Barrier and Surface Plasmonic Resonance Phenomena towards the Photocatalytic Reaction: Study of Their Mechanisms to Enhance Photocatalytic Activity. *Catal. Sci. Technol.* **2015**, *5*, 2522–2531.

45. Chiarello, G.L.; Aguirre, M.H.; Selli, E. Hydrogen Production by Photocatalytic Steam Reforming of Methanol on Noble Metal-Modified TiO_2. *J. Catal.* **2010**, *273*, 182–190.

46. Zhang, Z.; Yates, J.T. Band Bending in Semiconductors: Chemical and Physical Consequences at Surfaces and Interfaces. *Chem. Rev.* **2012**, *112*, 5520–5551.

47. Kumari, P.; Bahadur, N.; Kong, L.; O'Dell, L.A.; Merenda, A.; Dumée, L.F. Engineering Schottky-like and Heterojunction Materials for Enhanced Photocatalysis Performance – a Review. *Mater. Adv.* **2022**, *3*, 2309–2323.

48. Xu, D.; Zhang, S.N.; Chen, J.S.; Li, X.H. Design of the Synergistic Rectifying Interfaces in Mott-Schottky Catalysts. *Chem. Rev.* **2023**, *123*, 1–30.

49. Zhang, L.; Jaroniec, M. Toward Designing Semiconductor-Semiconductor Heterojunctions for Photocatalytic Applications. *Appl. Surf. Sci.* **2018**, *430*, 2–17.

50. Xu, M.; Ye, T.; Dai, F.; Yang, J.; Shen, J.; He, Q.; Chen, W.; Liang, N.; Zai, J.; Qian, X. Rationally Designed n–n Heterojunction with Highly Efficient Solar Hydrogen Evolution. *ChemSusChem* **2015**, *8*, 1218–1225.

51. Wang, X.; Liu, G.; Chen, Z.G.; Li, F.; Wang, L.; Lu, G.Q.; Cheng, H.M. Enhanced Photocatalytic Hydrogen Evolution by Prolonging the Lifetime of Carriers in ZnO/CdS Heterostructures. *ChemComm* **2009**, 3452–3454.

52. Low, J.; Jiang, C.; Cheng, B.; Wageh, S.; Al-Ghamdi, A.A.; Yu, J. A Review of Direct Z-Scheme Photocatalysts. *Small Methods* **2017**, *1*, 1700080.

53. Xu, Q.; Zhang, L.; Yu, J.; Wageh, S.; Al-Ghamdi, A.A.; Jaroniec, M. Direct Z-Scheme Photocatalysts: Principles, Synthesis, and Applications. *Materials Today* **2018**, *21*, 1042–1063.

54. Di, T.; Xu, Q.; Ho, W.K.; Tang, H.; Xiang, Q.; Yu, J. Review on Metal Sulphide-Based Z-Scheme Photocatalysts. *ChemCatChem* **2019**, *11*, 1394–1411.

55. Reza Gholipour, M.; Dinh, C.T.; Béland, F.; Do, T.O. Nanocomposite Heterojunctions as Sunlight-Driven Photocatalysts for Hydrogen Production from Water Splitting. *Nanoscale* **2015**, *7*, 8187–8208.

56. Mamiyev, Z.; Balayeva, N.O. Metal Sulfide Photocatalysts for Hydrogen Generation: A Review of Recent Advances. *Catalysts* **2022**, *12*, 1316.

57. Khan, M.M.; Rahman, A. Chalcogenides and Chalcogenide-Based Heterostructures as Photocatalysts for Water Splitting. *Catalysts* **2022**, *12*, 1338.

58. Ozel, F.; Kılıc, H.S.; Coskun, H.; Deveci, I.; Sarılmaz, A.; Balıkcıoglu, A.; Gundogdu, Y.; Aljabour, A.; Ozen, A.; Gezgin, S.Y.; et al. A General Review on the Thiospinels and Their Energy Applications. *Mater. Today Energy* **2021**, *21*, 100822.

59. Sun, T.; Gao, P.; He, Y.; Wu, Z.; Liu, J.; Rong, X. Dual Z-Scheme TCN/ZnS/ $ZnIn_2S_4$ with Efficient Separation for Photocatalytic Nitrogen Fixation. *J. Colloid Interface Sci.* **2024**, *654*, 602–611.

60. Guo, S.; Li, Y.; Xue, C.; Sun, Y.; Wu, C.; Shao, G.; Zhang, P. Controllable Construction of Hierarchically $CdIn_2S_4$/CNFs/Co_4S_3 Nanofiber Networks towards Photocatalytic Hydrogen Evolution. *J. Chem. Eng.* **2021**, *419*, 129213.

61. Ling, C.; Ye, X.; Zhang, J.; Zhang, J.; Zhang, S.; Meng, S.; Fu, X.; Chen, S. Solvothermal Synthesis of $CdIn_2S_4$ Photocatalyst for Selective Photosynthesis of Organic Aromatic Compounds under Visible Light. *Scientific Reports* **2017**, *7*, 1–16.

62. Wang, L.; Cheng, B.; Zhang, L.; Yu, J. In Situ Irradiated XPS Investigation on S-Scheme TiO_2@$ZnIn_2S_4$ Photocatalyst for Efficient Photocatalytic CO_2 Reduction. *Small* **2021**, *17*, 2103447.

63. Bra, S.; Vamvasakis, I.; Andreou, E.K.; Vailakis, G.; Kopidakis, G.; Armatas, G.S. Modulating Interfacial Charge Redistribution of $Ni_2P/CuCo_2S_4$ p-n Nano-Heterojunctions for Efficient Electrocatalytic Overall Water Splitting. *Int. J. Hydrog. Energy* **2023**, *48*, 25300–25314.

64. Yadav, G.; Ahmaruzzaman, M. $CdIn_2S_4$-Based Advanced Composite Materials: Structure, Properties, and Applications in Environment and Energy – A Concise Review. *Inorganic and Nano-Metal Chemistry* **2023**.

65. Yang, R.; Mei, L.; Fan, Y.; Zhang, Q.; Zhu, R.; Amal, R.; Yin, Z.; Zeng, Z. $ZnIn_2S_4$-Based Photocatalysts for Energy and Environmental Applications. *Small Methods* **2021**, *5*, 2100887.

66. Song, Y.; Zhang, J.; Dong, X.; Li, H. A Review and Recent Developments in Full-Spectrum Photocatalysis Using $ZnIn_2S_4$-Based Photocatalysts. *Energy Technology* **2021**, *9*, 2100033.

67. Chen, Y.; Hu, S.; Liu, W.; Chen, X.; Wu, L.; Wang, X.; Liu, P.; Li, Z. Controlled Syntheses of Cubic and Hexagonal $ZnIn_2S_4$ Nanostructures with Different Visible-Light Photocatalytic Performance. *Dalton Trans.***2011**, *40*, 2607–2613.

68. Shen, S.; Guo, P.; Zhao, L.; Du, Y.; Guo, L. Insights into Photoluminescence Property and Photocatalytic Activity of Cubic and Rhombohedral $ZnIn_2S_4$. *J Solid State Chem* **2011**, *184*, 2250–2256.

69. Zhang, Z.; Huang, L.; Zhang, J.; Wang, F.; Xie, Y.; Shang, X.; Gu, Y.; Zhao, H.; Wang, X. In Situ Constructing Interfacial Contact $MoS_2/ZnIn_2S_4$ Heterostructure for Enhancing Solar Photocatalytic Hydrogen Evolution. *Appl. Catal. B* **2018**, *233*, 112–119.

70. Shi, X.; Mao, L.; Yang, P.; Zheng, H.; Fujitsuka, M.; Zhang, J.; Majima, T. Ultrathin $ZnIn_2S_4$ Nanosheets with Active (110) Facet Exposure and Efficient Charge Separation for Cocatalyst Free Photocatalytic Hydrogen Evolution. *Appl. Catal. B* **2020**, *265*, 118616.

71. Shen, S.; Zhao, L.; Guo, L. Morphology, Structure and Photocatalytic Performance of $ZnIn_2S_4$ Synthesized via a Solvothermal/Hydrothermal Route in Different Solvents. *Journal of Physics and Chemistry of Solids* **2008**, *69*, 2426–2432.

72. Khan, A.A.; Chowdhury, A.; Kumari, S.; Hussain, S. The Facile Soft-Template-Morphology-Controlled (STMC) Synthesis of $ZnIn_2S_4$ Nanostructures and Their Excellent Morphology-Dependent Adsorption Properties. *J. Mater. Chem. A***2020**, *8*, 1986–2000.

73. Li, H.; Chen, Z.H.; Zhao, L.; Yang, G.D. Synthesis of $TiO_2@ZnIn_2S_4$ Hollow Nanospheres with Enhanced Photocatalytic Hydrogen Evolution. *Rare Metals* **2019**, *38*, 420–427.

74. Li, M.; Su, J.; Guo, L. Preparation and Characterization of $ZnIn_2S_4$ Thin Films Deposited by Spray Pyrolysis for Hydrogen Production. *Int. J. Hydrog. Energy* **2008**, *33*, 2891–2896.

75. Shang, L.; Zhou, C.; Bian, T.; Yu, H.; Wu, L.Z.; Tung, C.H.; Zhang, T. Facile Synthesis of Hierarchical $ZnIn_2S_4$ Submicrospheres Composed of Ultrathin Mesoporous Nanosheets as a Highly Efficient Visible-Light-Driven Photocatalyst for H_2 Production. *J. Mater. Chem. A* **2013**, *1*, 4552–4558.

76. Yang, W.; Liu, B.; Fang, T.; Jennifer, W.A.; Christophe, L.; Li, Z.; Zhang, X.; Jiang, X. Layered Crystalline $ZnIn_2S_4$ Nanosheets: CVD Synthesis and Photo-Electrochemical Properties. *Nanoscale* **2016**, *8*, 18197–18203.

77. Shi, X.; Dai, C.; Wang, X.; Hu, J.; Zhang, J.; Zheng, L.; Mao, L.; Zheng, H.; Zhu, M. Protruding Pt Single-Sites on Hexagonal $ZnIn_2S_4$ to Accelerate Photocatalytic Hydrogen Evolution. *Nat. Commun. 2022 13:1* **2022**, *13*, 1–10.

78. Xing, F.; Liu, Q.; Huang, C. Mo-Doped $ZnIn_2S_4$ Flower-Like Hollow Microspheres for Improved Visible Light-Driven Hydrogen Evolution. *Solar RRL* **2020**, *4*, 1900483.

79. Du, C.; Zhang, Q.; Lin, Z.; Yan, B.; Xia, C.; Yang, G. Half-Unit-Cell $ZnIn_2S_4$ Monolayer with Sulfur Vacancies for Photocatalytic Hydrogen Evolution. *Appl. Catal. B* **2019**, *248*, 193–201.

80. Jiao, X.; Chen, Z.; Li, X.; Sun, Y.; Gao, S.; Yan, W.; Wang, C.; Zhang, Q.; Lin, Y.; Luo, Y.; et al. Defect-Mediated Electron-Hole Separation in One-Unit-Cell $ZnIn_2S_4$ Layers for Boosted Solar-Driven CO_2 Reduction. *J. Am. Chem. Soc.* **2017**, *139*, 7586–7594.

81. Liu, C.; Zhang, Q.; Zou, Z. Recent Advances in Designing $ZnIn_2S_4$-Based Heterostructured Photocatalysts for Hydrogen Evolution. *J. Mater. Sci. Technol.* **2023**, *139*, 167–188.

82. Wang, S.; Guan, B.Y.; Lu, Y.; Lou, X.W. Formation of Hierarchical In_2S_3-$CdIn_2S_4$ Heterostructured Nanotubes for Efficient and Stable Visible Light CO_2 Reduction. *J. Am. Chem. Soc.* **2017**, *139*, 17305–17308.

83. Wang, T.; Chai, Y.; Ma, D.; Chen, W.; Zheng, W.; Huang, S. Multidimensional CdS Nanowire/$CdIn_2S_4$ Nanosheet Heterostructure for Photocatalytic and Photoelectrochemical Applications. *Nano Res.* **2017**, *10*, 2699–2711.

84. Dang, X.; Xie, M.; Dai, F.; Guo, J.; Liu, J.; Lu, X. The in Situ Construction of $ZnIn_2S_4$/$CdIn_2S_4$ 2D/3D Nano Hetero-Structure for an Enhanced Visible-Light-Driven Hydrogen Production. *J. Mater. Chem. A* **2021**, *9*, 14888–14896.

85. Rao, Y.; Sun, M.; Zhou, B.; Wang, L.; Wang, Z.; Yan, T.; Shao, Y. Facile Deposition of $CoMoS_4$ on Flower-like $CdIn_2S_4$ Microspheres: Enhanced Charge Separation and Efficient Photocatalytic Hydrogen Evolution. *Int. J. Hydrog. Energy* **2024**, *51*, 133–144.

86. Yu, Y.; Chen, G.; Wang, G.; Lv, Z. Visible-Light-Driven $ZnIn_2S_4$/$CdIn_2S_4$ Composite Photocatalyst with Enhanced Performance for Photocatalytic H_2 Evolution. *Int. J. Hydrog. Energy* **2013**, *38*, 1278–1285.

87. Yu, M.; Hu, Q.; Gong, X.; Yu, H.; Wang, S.; Li, Z.; Chen, Y.; Li, S. The Construction of Three-Dimensional $CdIn_2S_4$/MoS_2 Composite Materials for Efficient Hydrogen Production. *J. Alloys Compd.* **2022**, *892*, 162168.

88. Zhang, Z.; Cao, Y.; Zhang, F.; Li, W.; Li, Y.; Yu, H.; Wang, M.; Yu, H. Tungsten Oxide Quantum Dots Deposited onto Ultrathin $CdIn_2S_4$ Nanosheets for Efficient S-Scheme Photocatalytic CO_2 Reduction via Cascade Charge Transfer. *J. Chem. Eng.* **2022**, *428*, 131218.

89. Wu Ren, T.; Liu, Y.; Yu, S. Synthesis of Core–Shell SnS_2/$CdIn_2S_4$ Heterojunction Photocatalyst for Visible Light Driven Hydrogen Evolution. *Mater. Lett.* **2021**, *304*, 130611.

90. Huang, L.; Li, B.; Su, B.; Xiong, Z.; Zhang, C.; Hou, Y.; Ding, Z.; Wang, S. Fabrication of Hierarchical Co_3O_4@$CdIn_2S_4$ p–n Heterojunction Photocatalysts for Improved CO_2 Reduction with Visible Light. *J. Mater. Chem. A* **2020**, *8*, 7177–7183.

91. Zhu, J.; Cheng, Y.; Zhang, W.; Zhao, J.; Sun, Q.; Hu, X.; Miao, H. Interfacial Charge and Surface Defect Regulation for High-Efficiency $CdIn_2S_4$-Based Photoanodes. *Appl. Surf. Sci.* **2022**, *601*, 154188.

92. Peng, Z.Y.; Jiang, Y.; Xiao, Y.; Xu, H.; Zhang, W.; Ni, L. $CdIn_2S_4$ Surface-Decorated Ta_3N_5 Core-Shell Heterostructure for Improved Spatial Charge Transfer: In-Situ Growth, Synergistic Effect and Efficient Dual-Functional Photocatalytic Performance. *Appl. Surf. Sci.* **2019**, *487*, 1084–1095.

93. Lai, T.; Peng, S.; Shu, H.; -, al; Bai, X.; Wu, W.; Lv, H. Effects of Cu^{2+} Doping on Structure, Morphology and Photocatalytic Hydrogen Production Performance of Porous $CdIn_2S_4$ Microsphere. *IOP Conf. Ser. Mater. Sci. Eng.* **2020**, *735*, 012041.

94. Bai, X.; Li, J. Photocatalytic Hydrogen Evolution over Cr^{3+}Doped Porous $CdIn_2S_4$ Photocatalysts under Visible Light Irradiation. *Adv. Mat. Res.* **2012**, *486*, 181–186.

95. Shi, Y.; Li, M.; Yu, Y.; Zhang, B. Recent Advances in Nanostructured Transition Metal Phosphides: Synthesis and Energy-Related Applications. *Energy Environ. Sci.* **2020**, *13*, 4564–4582.

96. Shi, Y.; Zhang, B. Recent Advances in Transition Metal Phosphide Nanomaterials: Synthesis and Applications in Hydrogen Evolution Reaction. *Chem. Soc. Rev.* **2016**, *45*, 1529–1541.

97. Blanchard, P.E.R.; Grosvenor, A.P.; Cavell, R.G.; Mar, A. X-Ray Photoelectron and Absorption Spectroscopy of Metal-Rich Phosphides M_2P and M_3P (M = Cr-Ni). *Chemistry of Materials* **2008**, *20*, 7081–7088.

98. Yang, Z.; Liu, L.; Wang, X.; Yang, S.; Su, X. Stability and Electronic Structure of the Co–P Compounds from First-Principle Calculations. *J. Alloys Compd.* **2011**, *509*, 165–171.

99. Callejas, J.F.; Read, C.G.; Roske, C.W.; Lewis, N.S.; Schaak, R.E. Synthesis, Characterization, and Properties of Metal Phosphide Catalysts for the Hydrogen-Evolution Reaction. *Chemistry of Materials* **2016**, *28*, 6017–6044.

100. Blaugher, R.D.; Hulm, J.K.; Yocom, P.N. Superconducting Phosphides of the Transition Metals. *Journal of Physics and Chemistry of Solids* **1965**, *26*, 2037–2039.

101. Chen, J.H.; Whitmire, K.H. A Structural Survey of the Binary Transition Metal Phosphides and Arsenides of the D-Block Elements. *Coord. Chem. Rev.* **2018**, *355*, 271–327.

102. Xiao, P.; Sk, M.A.; Thia, L.; Ge, X.; Lim, R.J.; Wang, J.Y.; Lim, K.H.; Wang, X. Molybdenum Phosphide as an Efficient Electrocatalyst for the Hydrogen Evolution Reaction. *Energy Environ. Sci.* **2014**, *7*, 2624–2629.

103. Pu, Z.; Liu, T.; Amiinu, I.S.; Cheng, R.; Wang, P.; Zhang, C.; Ji, P.; Hu, W.; Liu, J.; Mu, S. Transition-Metal Phosphides: Activity Origin, Energy-Related Electrocatalysis Applications, and Synthetic Strategies. *Adv. Funct. Mater.* **2020**, *30*, 2004009.

104. Morales-Guio, C.G.; Stern, L.A.; Hu, X. Nanostructured Hydrotreating Catalysts for Electrochemical Hydrogen Evolution. *Chem. Soc. Rev.* **2014**, *43*, 6555–6569.

105. Kibsgaard, J.; Tsai, C.; Chan, K.; Benck, J.D.; Nørskov, J.K.; Abild-Pedersen, F.; Jaramillo, T.F. Designing an Improved Transition Metal Phosphide Catalyst for Hydrogen Evolution Using Experimental and Theoretical Trends. *Energy Environ. Sci.* **2015**, *8*, 3022–3029.

106. Ray, A.; Sultana, S.; Paramanik, L.; Parida, K.M. Recent Advances in Phase, Size, and Morphology-Oriented Nanostructured Nickel Phosphide for Overall Water Splitting. *J. Mater. Chem. A* **2020**, *8*, 19196–19245.

107. Wan, H.; Li, L.; Chen, Y.; Gong, J.; Duan, M.; Liu, C.; Zhang, J.; Wang, H. One Pot Synthesis of $Ni_{12}P_5$ Hollow Nanocapsules as Efficient Electrode Materials for Oxygen Evolution Reactions and Supercapacitor Applications. *Electrochim. Acta* **2017**, *229*, 380–386.

108. Laursen, A.B.; Patraju, K.R.; Whitaker, M.J.; Retuerto, M.; Sarkar, T.; Yao, N.; Ramanujachary, K. V.; Greenblatt, M.; Dismukes, G.C. Nanocrystalline Ni_5P_4: A Hydrogen Evolution Electrocatalyst of Exceptional Efficiency in Both Alkaline and Acidic Media. *Energy Environ. Sci.* **2015**, *8*, 1027–1034.

109. Laursen, A.B.; Wexler, R.B.; Whitaker, M.J.; Izett, E.J.; Calvinho, K.U.D.; Hwang, S.; Rucker, R.; Wang, H.; Li, J.; Garfunkel, E.; et al. Climbing the Volcano of Electrocatalytic Activity While Avoiding Catalyst Corrosion: Ni_3P, a Hydrogen Evolution Electrocatalyst Stable in Both Acid and Alkali. *ACS Catal.* **2018**, *8*, 4408–4419.

110. Liu, P.; Rodriguez, J.A. Catalysts for Hydrogen Evolution from the [NiFe] Hydrogenase to the $Ni_2P(001)$ Surface: The Importance of Ensemble Effect. *J. Am. Chem. Soc.* **2005**, *127*, 14871–14878.

111. Sun, Z.; Zheng, H.; Li, J.; Du, P. Extraordinarily Efficient Photocatalytic Hydrogen Evolution in Water Using Semiconductor Nanorods Integrated with Crystalline Ni_2P Cocatalysts. *Energy Environ. Sci.* **2015**, *8*, 2668–2676.

112. Chen, Y.; She, H.; Luo, X.; Yue, G.H.; Peng, D.L. Solution-Phase Synthesis of Nickel Phosphide Single-Crystalline Nanowires. *J. Cryst. Growth* **2009**, *311*, 1229–1233.

113. Muthuswamy, E.; Savithra, G.H.L.; Brock, S.L. Synthetic Levers Enabling Independent Control of Phase, Size, and Morphology in Nickel Phosphide Nanoparticles. *ACS Nano* **2011**, *5*, 2402–2411.

114. Ni, Y.; Jin, L.; Hong, J. Phase-Controllable Synthesis of Nanosized Nickel Phosphides and Comparison of Photocatalytic Degradation Ability. *Nanoscale* **2011**, *3*, 196–200.

115. Liu, Z.; Huang, X.; Zhu, Z.; Dai, J. A Simple Mild Hydrothermal Route for the Synthesis of Nickel Phosphide Powders. *Ceram. Int.* **2010**, *36*, 1155–1158.

116. Guan, Q.; Li, W.; Zhang, M.; Tao, K. Alternative Synthesis of Bulk and Supported Nickel Phosphide from the Thermal Decomposition of Hypophosphites. *J. Catal.* **2009**, *263*, 1–3.

117. Wang, X.; Kolen'ko, Y. V.; Bao, X.-Q.; Kovnir, K.; Liu, L. One-Step Synthesis of Self-Supported Nickel Phosphide Nanosheet Array Cathodes for Efficient Electrocatalytic Hydrogen Generation. *Angewandte Chemie* **2015**, *127*, 8306–8310.

118. Yu, T.; Si, Y.; Lv, Z.; Wang, K.; Zhang, Q.; Liu, X.; Wang, G.; Xie, G.; Jiang, L. $Cd_{0.5}Zn_{0.5}S/Ni_2P$ Noble-Metal-Free Photocatalyst for High-Efficient Photocatalytic Hydrogen Production: Ni_2P Boosting Separation of Photocarriers. *Int. J. Hydrog. Energy* **2019**, *44*, 31832–31840.

119. Gao, W.Z.; Xu, Y.; Chen, Y.; Fu, W.F. Highly Efficient and Selective Photocatalytic Reduction of Nitroarenes Using the Ni_2P/CdS Catalyst under Visible-Light Irradiation. *ChemComm* **2015**, *51*, 13217–13220.

120. Yang, Y.; Zhou, C.; Wang, W.; Xiong, W.; Zeng, G.; Huang, D.; Zhang, C.; Song, B.; Xue, W.; Li, X.; et al. Recent Advances in Application of Transition Metal Phosphides for Photocatalytic Hydrogen Production. *J. Chem. Eng.***2021**, *405*, 126547.

121. Deng, R.; Guo, M.; Wang, C.; Zhang, Q. Recent Advances in Cobalt Phosphide-Based Materials for Electrocatalytic Water Splitting: From Catalytic Mechanism and Synthesis Method to Optimization Design. *Nano Materials Science* **2022**.

122. Wang, J.; Liu, Z.; Zheng, Y.; Cui, L.; Yang, W.; Liu, J. Recent Advances in Cobalt Phosphide Based Materials for Energy-Related Applications. *J. Mater. Chem. A* **2017**, *5*, 22913–22932.

123. Liu, X.; Zhuang, H. Recent Progresses in Photocatalytic Hydrogen Production: Design and Construction of Ni-Based Cocatalysts. *Int. J. Energy Res.* **2021**, *45*, 1480–1495.

124. Xu, Y.; Xu, R. Nickel-Based Cocatalysts for Photocatalytic Hydrogen Production. *Appl. Surf. Sci.* **2015**, *351*, 779–793.

125. Chen, Y.; Rui, K.; Zhu, J.; Dou, S.X.; Sun, W. Recent Progress on Nickel-Based Oxide/(Oxy)Hydroxide Electrocatalysts for the Oxygen Evolution Reaction. *Chemistry – A European Journal* **2019**, *25*, 703–713.

126. Xie, L.; Hao, J.G.; Chen, H.Q.; Li, Z.X.; Ge, S.Y.; Mi, Y.; Yang, K.; Lu, K.Q. Recent Advances of Nickel Hydroxide-Based Cocatalysts in Heterogeneous Photocatalysis. *Catal. Commun.* **2022**, *162*, 106371.

127. Lawson, K.; Wallbridge, S.P.; Catling, A.E.; Kirk, C.A.; Dann, S.E. Determination of Layered Nickel Hydroxide Phases in Materials Disordered by Stacking Faults and Interstratification. *J. Mater. Chem. A* **2023**, *11*, 789–799.

128. Oliva, P.; Leonardi, J.; Laurent, J.F.; Delmas, C.; Braconnier, J.J.; Figlarz, M.; Fievet, F.; Guibert, A. de Review of the Structure and the Electrochemistry of Nickel Hydroxides and Oxy-Hydroxides. *J. Power Sources* **1982**, *8*, 229–255.

129. Hall, D.S.; Lockwood, D.J.; Bock, C.; MacDougall, B.R. Nickel Hydroxides and Related Materials: A Review of Their Structures, Synthesis and Properties. *Proceedings of the Royal Society A: Mathematical, Physical and Engineering Sciences* **2015**, *471*.

130. Vamvasakis, I.; Papadas, I.T.; Tzanoudakis, T.; Drivas, C.; Choulis, S.A.; Kennou, S.; Armatas, G.S. Visible-Light Photocatalytic H_2 Production Activity of β-$Ni(OH)_2$-Modified CdS Mesoporous Nanoheterojunction Networks. *ACS Catal.***2018**, *8*, 8726–8738.

131. Huang, L.; Gao, R.; Xiong, L.; Devaraji, P.; Chen, W.; Li, X.; Mao, L. Two Dimensional Ni_2P/CdS Photocatalyst for Boosting Hydrogen Production under Visible Light Irradiation. *RSC Adv.* **2021**, *11*, 12153–12161.

132. Huang, H.B.; Luo, S.H.; Liu, C.L.; Yi, T.F.; Zhai, Y.C. High-Surface-Area and Porous Co_2P Nanosheets as Cost-Effective Cathode Catalysts for Li-O2 Batteries. *ACS Appl. Mater Interfaces* **2018**, *10*, 21281–21290.

133. Li, S.; Wang, L.; Liu, S.; Xu, B.; Xiao, N.; Gao, Y.; Song, W.; Ge, L.; Liu, J. In Situ Synthesis of Strongly Coupled Co_2P-CdS Nanohybrids: An Effective Strategy to Regulate Photocatalytic Hydrogen Evolution Activity. *ACS Sustain. Chem. Eng.* **2018**, *6*, 9940–9950.

134. Brunauer, S.; Deming, L.S.; Deming, W.E.; Teller, E. On a Theory of the van Der Waals Adsorption of Gases. *J. Am. Chem. Soc.* **1940**, *62*, 1723–1732.

135. Ravikovitch, P.I.; Wei, D.; Chueh, W.T.; Haller, G.L.; Neimark, A. V. Evaluation of Pore Structure Parameters of MCM-41 Catalyst Supports and Catalysts by Means of Nitrogen and Argon Adsorption. *Journal of Physical Chemistry B* **1997**, *101*, 3671–3679.

136. Juhás, P.; Davis, T.; Farrow, C.L.; Billinge, S.J.L. PDFgetX3: A Rapid and Highly Automatable Program for Processing Powder Diffraction Data into Total Scattering Pair Distribution Functions. *J Appl Crystallogr* **2013**, *46*, 560–566.

137. Farrow, C.L.; Juhas, P.; Liu, J.W.; Bryndin, D.; Boin, E.S.; Bloch, J.; Proffen, T.; Billinge, S.J.L. PDFfit2 and PDFgui: Computer Programs for Studying Nanostructure in Crystals. *Journal of Physics: Condensed Matter* **2007**, *19*, 335219.

138. Sawant, R.R.; Rajpure, K.Y.; Bhosale, C.H. Determination of $CdIn_2S_4$ Semiconductor Parameters by (Photo)Electrochemical Technique. *Physica B Condens Matter* **2007**, *393*, 249–254.

139. Ting, L.R.L.; Deng, Y.; Ma, L.; Zhang, Y.J.; Peterson, A.A.; Yeo, B.S. Catalytic Activities of Sulfur Atoms in Amorphous Molybdenum Sulfide for the Electrochemical Hydrogen Evolution Reaction. *ACS Catal.* **2016**, *6*, 861–867.

140. Frame, F.A.; Osterloh, F.E. CdSe-MoS_2: A Quantum Size-Confined Photocatalyst for Hydrogen Evolution from Water under Visible Light. *J. Phys. Chem. C* **2010**, *114*, 10628–10633.

141. Wang, H.; Xia, Y.; Li, H.; Wang, X.; Yu, Y.; Jiao, X.; Chen, D. Highly Active Deficient Ternary Sulfide Photoanode for Photoelectrochemical Water Splitting. *Nat. Commun.* **2020**, *11*, 1–11.

142. Jiang, C.; Wang, H.; Wang, Y.; Ji, H. All Solid-State Z-scheme CeO_2/$ZnIn_2S_4$ Hybrid for the Photocatalytic Selective Oxidation of Aromatic Alcohols Coupled with Hydrogen Evolution. *Appl. Catal. B* **2020**, *277*, 119235.

143. Liu, B.; Liu, X.; Liu, J.; Feng, C.; Li, Z.; Li, C.; Gong, Y.; Pan, L.; Xu, S.; Sun, C.Q. Efficient Charge Separation between UiO-66 and $ZnIn_2S_4$ Flowerlike 3D Microspheres for Photoelectronchemical Properties. *Appl. Catal. B* **2018**, *226*, 234–241..

144. Billinge, S.J.L.; Kanatzidis, M.G. Beyond Crystallography: The Study of Disorder, Nanocrystallinity and Crystallographically Challenged Materials with Pair Distribution Functions. *ChemComm* **2004**, *4*, 749–760.

145. Rouquerol, J.; Rouquerol, F.; Llewellyn, P.; Maurin, G.; Sing, K.S.W. Adsorption by Powders and Porous Solids: Principles, Methodology and Applications: Second Edition. *Adsorption by Powders and Porous Solids: Principles, Methodology and Applications: Second Edition* **2013**, 1–626.

146. Armatas, G.S.; Kanatzidis, M.G. Size Dependence in Hexagonal Mesoporous Germanium: Pore Wall Thickness versus Energy Gap and Photoluminescence. *Nano Lett.* **2010**, *10*, 3330–3336.

147. Zuo, G.; Wang, Y.; Teo, W.L.; Xian, Q.; Zhao, Y. Direct Z-Scheme TiO_2–$ZnIn_2S_4$ Nanoflowers for Cocatalyst-Free Photocatalytic Water Splitting. *Appl. Catal. B* **2021**, *291*, 120126.

148. Ouyang, C.; Huang, W.; Tang, H.; Liu, W.; Gu, X.; Hong, Z.; Zhi, M. Hierarchical MoO_2/$ZnIn_2S_4$ Schottky Heterojunction Stimulated Photocatalytic H_2 Evolution under Visible Light. *ACS Appl. Energy Mater.* **2022**, *5*, 12739–12751.

149. Kambhampati, P. Nanoparticles, Nanocrystals, and Quantum Dots: What Are the Implications of Size in Colloidal Nanoscale Materials? *Journal of Physical Chemistry Letters* **2021**, *12*, 4769–4779.

150. Smith, A.M.; Nie, S. Semiconductor Nanocrystals: Structure, Properties, and Band Gap Engineering. *Acc. Chem. Res.* **2010**, *43*, 190–200.

151. Wood, D.M. Classical Size Dependence of the Work Function of Small Metallic Spheres. *Phys. Rev. Lett.* **1981**, *46*, 749.

152. Pala, I.R.; Arachchige, I.U.; Georgiev, D.G.; Brock, S.L. Reversible Gelation of II–VI Nanocrystals: The Nature of Interparticle Bonding and the Origin of Nanocrystal Photochemical Instability. *Angewandte Chemie* **2010**, *49*, 3661–3665.

153. Donika, F.G.; Radautsan, S.I.; Kiosse, G.A.; Mustya, I.B. Crystallographic Structure of a Two-Packet Polytype $ZnIn_2S_4$ (II), *Kristallografiya*, **1972**, *13*, 663-667.

154. Lopez-Rivera, S.A.; Martinez, L.; Fontal, B.; Giriat, W.; Medina, F. Raman Study of a $ZnIn_2S_4$ Layered Compound. *Semicond. Sci. Technol.* **1995**, *10*, 645.

155. Jia, T.; Liu, M.; Zheng, C.; Long, F.; Min, Z.; Fu, F.; Yu, D.; Li, J.; Lee, J.H.; Kim, N.H. One-Pot Hydrothermal Synthesis of La-Doped $ZnIn_2S_4$ Microspheres with Improved Visible-Light Photocatalytic Performance. *Nanomaterials* **2020**, *10*, 2026.

156. Syrbu, N.N.; Bogdanash, M.; Moldovyan, N.A. Vibrational Modes in $ZnAl_2S_4$ and $CdIn_2S_4$ Crystals. *Infrared Phys. Technol.* **1996**, *37*, 763–768.

157. Zhang, Y.J.; Tang, H.M.; Gao, S.P. Density Functional Theory Study of $ZnIn_2S_4$ and $CdIn_2S_4$ Polymorphs Using Full-Potential Linearized Augmented Plane Wave Method and Modified Becke–Johnson Potential. *physica status solidi (b)* **2020**, *257*, 1900485.

158. Shi, Y.F.; Wang, Y.; Wu, L.M. Hexagonal MIn_2S_4 (M = Mn, Fe, Co): Formation and Phase Transition. *J. Phys. Chem. C* **2013**, *117*, 20054–20059.

159. Wang, Z.; Qi, Z.; Fan, X.; Leung, D.Y.C.; Long, J.; Zhang, Z.; Miao, T.; Meng, S.; Chen, S.; Fu, X. Intimately Contacted Ni_2P on CdS Nanorods for Highly Efficient Photocatalytic H_2 Evolution: New Phosphidation Route and the Interfacial Separation Mechanism of Charge Carriers. *Appl. Catal. B* **2021**, *281*, 119443.

160. Li, C.; Zhao, Y.; Liu, X.; Huo, P.; Yan, Y.; Wang, L.; Liao, G.; Liu, C. Interface Engineering of $Co_9S_8/CdIn_2S_4$ Ohmic Junction for Efficient Photocatalytic H_2 Evolution under Visible Light. *J. Colloid Interface Sci.* **2021**, *600*, 794–803.

161. Chen, W.; Huang, T.; Hua, Y.X.; Liu, T.Y.; Liu, X.H.; Chen, S.M. Hierarchical $CdIn_2S_4$ Microspheres Wrapped by Mesoporous g-C_3N_4 Ultrathin Nanosheets with Enhanced Visible Light Driven Photocatalytic Reduction Activity. *J. Hazard. Mater.* **2016**, *320*, 529–538.

162. Zhen, W.; Ning, X.; Yang, B.; Wu, Y.; Li, Z.; Lu, G. The Enhancement of CdS Photocatalytic Activity for Water Splitting via Anti-Photocorrosion by Coating Ni_2P Shell and Removing Nascent Formed Oxygen with Artificial Gill. *Appl. Catal. B* **2018**, *221*, 243–257.

163. Wang, W.; An, T.; Li, G.; Xia, D.; Zhao, H.; Yu, J.C.; Wong, P.K. Earth-Abundant Ni_2P/g-C_3N_4 Lamellar Nanohydrids for Enhanced Photocatalytic Hydrogen Evolution and Bacterial Inactivation under Visible Light Irradiation. *Appl. Catal. B* **2017**, *217*, 570–580.

164. Finlayson, M.F.; Wheeler, B.L.; Kakuta, N.; Park, K.H.; Bard, A.J.; Campion, A.; Fox, M.A.; Webber, S.E.; White, J.M. Determination of Flat-Band Position of CdS Crystals, Films, and Powders by Photocurrent and Impedance Techniques. Photoredox Reaction Mediated by Intragap States. *Journal of Physical Chemistry* **1985**, *89*, 5676–5681.

165. Wang, P.; Luo, Y.; Zhang, G.; Wu, M.; Chen, Z.; Sun, S.; Shi, Z. MnO_x-Decorated Nickel-Iron Phosphides Nanosheets: Interface Modifications for Robust Overall Water Splitting at Ultra-High Current Densities. *Small* **2022**, *18*, 2105803.

166. Ma, X.; Li, W.; Li, H.; Dong, M.; Geng, L.; Wang, T.; Zhou, H.; Li, Y.; Li, M. Novel Noble-Metal-Free $Co_2P/CdIn_2S_4$ Heterojunction Photocatalysts for Elevated Photocatalytic H_2 Production: Light Absorption, Charge Separation and Active Site. *J. Colloid Interface Sci.* **2023**, *639*, 87–95.

167. Liu, G.; Wang, M.; Xu, Y.; Wang, X.; Li, X.; Liu, J.; Cui, X.; Jiang, L. Porous CoP/Co_2P Heterostructure for Efficient Hydrogen Evolution and Application in Magnesium/Seawater Battery. *J. Power Sources* **2021**, *486*, 229351.

168. Cotton, F.A.; Goodgame, D.M.L.; Goodgame, M. The Electronic Structures of Tetrahedral Cobalt(II) Complexes. *J. Am. Chem. Soc.* **1961**, *83*, 4690–4699.

169. Kamat, P. V.; Jin, S. Semiconductor Photocatalysis: "tell Us the Complete Story! ". *ACS Energy Lett.* **2018**, *3*, 622–623.

170. Schneider, J.; Bahnemann, D.W. Undesired Role of Sacrificial Reagents in Photocatalysis. *Journal of Physical Chemistry Letters* **2013**, *4*, 3479–3483.

171. Luyen Doan, T.L.; Nguyen, D.C.; Kang, K.; Ponnusamy, A.; Eya, H.I.; Dzade, N.Y.; Kim, C.S.; Park, C.H. Advanced Mott-Schottky Heterojunction of Semi-Conductive MoS_2 Nanoparticles/Metallic CoS_2 Nanotubes as an Efficient Multifunctional Catalyst for Urea-Water Electrolysis. *Appl. Catal. B* **2024**, *342*, 123295.

172. Zhang, B.; Shan, J.; Wang, W.; Tsiakaras, P.; Li, Y. Oxygen Vacancy and Core–Shell Heterojunction Engineering of Anemone-Like CoP@CoOOH Bifunctional Electrocatalyst for Efficient Overall Water Splitting. *Small* **2022**, *18*, 2106012.

173. Péan, E. V.; Barreau, N.; Vidal, J.; Latouche, C.; Jobic, S. Theoretical Investigation of $CdIn_2S_4$: A Possible Substitute for CdS in $CuIn_{1-x}Ga_xSe_2$ -Based Photovoltaic Devices. *Phys. Rev. Mater.* **2017**, *1*, 064605.

174. Bi, W.; Zhang, L.; Sun, Z.; Li, X.; Jin, T.; Wu, X.; Zhang, Q.; Luo, Y.; Wu, C.; Xie, Y. Insight into Electrocatalysts as Co-Catalysts in Efficient Photocatalytic Hydrogen Evolution. *ACS Catal.* **2016**, *6*, 4253–4257.

175. Xia, C.; Li, P.; Gandi, A.N.; Schwingenschlögl, U.; Alshareef, H.N. Is $NiCo_2S_4$ Really a Semiconductor? *Chemistry of Materials* **2015**, *27*, 6482–6485.

176. Robel, I.; Kuno, M.; Kamat, P. V. Size-Dependent Electron Injection from Excited CdSe Quantum Dots into TiO_2 Nanoparticles. *J. Am. Chem. Soc.* **2007**, *129*, 4136–4137.

177. Lin, Y.F.; Hsu, Y.J. Interfacial Charge Carrier Dynamics of Type-II Semiconductor Nanoheterostructures. *Appl. Catal. B* **2013**, *130–131*, 93–98.

178. Liang, Z.; Zhong, X.; Li, T.; Chen, M.; Feng, G. DFT Study on the Hydrogen Evolution Reaction for Different Facets of Co_2P. *ChemElectroChem* **2019**, *6*, 260–267.

179. Zhang, W.; Yang, H.; Fu, W.; Li, M.; Li, Y.; Yu, W. Directly Hydrothermal Growth of $CdIn_2S_4$ Nanosheet Films on FTO Substrates for Photoelectric Application. *J. Alloys Compd.* **2013**, *561*.

180. Sun, M.; Zhao, X.; Zeng, Q.; Yan, T.; Ji, P.; Wu, T.; Wei, D.; Du, B. Facile Synthesis of Hierarchical $ZnIn_2S_4/CdIn_2S_4$ Microspheres with Enhanced Visible Light Driven Photocatalytic Activity. *Appl. Surf. Sci.* **2017**, *407*, 328–336.

181. Ikeda, K.; Vedanand, S. OPTICAL SPECTRUM OF SYNTHETIC THEOPHRASTITE, $NI(OH)_2$. *Neues Jahrbuch Fur Mineralogie-monatshefte* **1999**.

182. Costantino, F.; Kamat, P. V. Do Sacrificial Donors Donate H_2 in Photocatalysis? *ACS Energy Lett.* **2022**, *7*, 242–246.

183. Digdaya, I.A.; Adhyaksa, G.W.P.; Trześniewski, B.J.; Garnett, E.C.; Smith, W.A. Interfacial Engineering of Metal-Insulator-Semiconductor Junctions for Efficient and Stable Photoelectrochemical Water Oxidation. *Nat. Commun.2017 8:1* **2017**, *8*, 1–8.

184. Peng, L.; Yu, C.; Ma, Y.; Xie, G.; Xie, X.; Wu, Z.; Zhang, N. Self-Assembled Transition Metal Chalcogenides@CoAl-LDH 2D/2D Heterostructures with Enhanced Photoactivity for Hydrogen Evolution. *Inorg. Chem. Front.* **2022**, *9*, 994–1005.

185. Li, X.; Yan, X.; Zhao, N.; Zhao, J.; Lu, B.; Zhang, X.; Zhang, X.; Yu, H. Facile Synthesis of Ternary $CdIn_2S_4/In(OH)_3/Zn_2GeO_4$ Nanocomposite with Enhanced Visible-Light Photocatalytic H_2 Evolution. *J. Photochem. Photobiol. A Chem.* **2018**, *360*, 298–305.

186. Prabhu, Y.T.; Kumari, R.; Gautam, A.; Sreedhar, B.; Pal, U. Highly Oriented MoS_2@$CdIn_2S_4$ Nanostructures for Efficient Solar Fuel Generation. *Nano-Structures & Nano-Objects* **2021**, *26*, 100682.

187. Fu, R.; Gong, Y.; Li, C.; Niu, L.; Liu, X. $CdIn_2S_4/In(OH)_3$/Nicr-Ldh Multi-Interface Heterostructure Photocatalyst for Enhanced Photocatalytic H_2 Evolution and Cr(VI) Reduction. *Nanomaterials* **2021**, *11*, 3122.

188. Xue, C.; An, H.; Yan, X.; Li, J.; Yang, B.; Wei, J.; Yang, G. Spatial Charge Separation and Transfer in Ultrathin $CdIn_2S_4$/RGO Nanosheet Arrays Decorated by ZnS Quantum Dots for Efficient Visible-Light-Driven Hydrogen Evolution. *Nano Energy* **2017**, *39*, 513–523.

189. Xie, L.; Liu, G.; Suo, R.; Xie, Z.; Liu, H.; Chen, J.; Chen, J.; Lu, C.Z. Construction of a Z-Scheme $CdIn_2S_4$/ZnS Heterojunction for the Enhanced Photocatalytic Hydrogen Evolution. *J. Alloys Compd.* **2023**, *948*, 169692.

190. Xu, J.; Li, Q.; Sui, D.; Jiang, W.; Liu, F.; Gu, X.; Zhao, Y.; Ying, P.; Mao, L.; Cai, X.; et al. In Situ Photodeposition of Cobalt Phosphate (CoH_xPO_y) on $CdIn_2S_4$ Photocatalyst for Accelerated Hole Extraction and Improved Hydrogen Evolution. *Nanomaterials* **2023**, *13*, 420.

191. Lin, B.; Li, H.; An, H.; Hao, W.; Wei, J.J.; Dai, Y.; Ma, C.; Yang, G. Preparation of 2D/2D g-C_3N_4 Nanosheet@$ZnIn_2S_4$ Nanoleaf Heterojunctions with Well-Designed High-Speed Charge Transfer Nanochannels towards High-Efficiency Photocatalytic Hydrogen Evolution. *Appl. Catal. B* **2018**, *220*, 542–552.

192. Du, C.; Yan, B.; Yang, G. Self-Integrated Effects of 2D $ZnIn_2S_4$ and Amorphous Mo_2C Nanoparticles Composite for Promoting Solar Hydrogen Generation. *Nano Energy* **2020**, *76*, 105031.

193. Zhang, S.; Wang, L.; Liu, C.; Luo, J.; Crittenden, J.; Liu, X.; Cai, T.; Yuan, J.; Pei, Y.; Liu, Y. Photocatalytic Wastewater Purification with Simultaneous Hydrogen Production Using MoS_2 QD-Decorated Hierarchical Assembly of $ZnIn_2S_4$ on Reduced Graphene Oxide Photocatalyst. *Water Res.* **2017**, *121*, 11–19.

194. Li, F.; Jiang, J.; Li, N.; Gao, Y.; Ge, L. Design and Fabrication of Hollow Structured $Cu_2MoS_4/ZnIn_2S_4$ Nanocubes with Significant Enhanced Photocatalytic Hydrogen Evolution Performance. *Int. J. Hydrog. Energy* **2021**, *46*, 37847–37859.

195. Zhang, S.; Liu, X.; Liu, C.; Luo, S.; Wang, L.; Cai, T.; Zeng, Y.; Yuan, J.; Dong, W.; Pei, Y.; et al. MoS_2 Quantum Dot Growth Induced by S Vacancies in a $ZnIn_2S_4$

Monolayer: Atomic-Level Heterostructure for Photocatalytic Hydrogen Production. *ACS Nano* **2018**, *12*, 751–758.

196. Xiao, Y.; Wang, H.; Jiang, Y.; Zhang, W.; Zhang, J.; Wu, X.; Liu, Z.; Deng, W. Hierarchical $Sb_2S_3/ZnIn_2S_4$ Core–Shell Heterostructure for Highly Efficient Photocatalytic Hydrogen Production and Pollutant Degradation. *J. Colloid Interface Sci.* **2022**, *623*, 109–123.

197. Zeng, D.; Xiao, L.; Ong, W.J.; Wu, P.; Zheng, H.; Chen, Y.; Peng, D.L. Hierarchical $ZnIn_2S_4/MoSe_2$ Nanoarchitectures for Efficient Noble-Metal-Free Photocatalytic Hydrogen Evolution under Visible Light. *ChemSusChem* **2017**, *10*, 4624–4631.

198. Liu, F.; Gao, Y.; Chi, X.; Zhu, Z.; Wang, X.; Guan, R. A PtS QDs/$ZnIn_2S_4$ Heterojunction Catalyst for Efficient Photocatalytic Hydrogen Production and Reduction of p-Nitrophenol. *J. Environ. Chem. Eng.* **2022**, *10*, 108840.

199. Li, W.; Ma, H.; Liu, Z.; Li, J.; Fang, P.; Xiong, R.; Pan, C.; Wei, J. In Situ Electronic Redistribution Tuning of $ZnIn_2S_4$ Nanosheets on $NiCo_2S_4$ Hollow Tube for Boosted Photocatalytic Hydrogen Evolution. *Appl. Surf. Sci.* **2022**, *598*, 153801.

200. Lai, L.; Xing, F.; Cheng, C.; Huang, C. Hierarchical 0D $NiSe_2$/2D $ZnIn_2S_4$ Nanosheet-Assembled Microflowers for Enhanced Photocatalytic Hydrogen Evolution. *Adv. Mater. Interfaces* **2021**, *8*, 2100052.

201. Yang, W.; Xu, S.S.; Niu, Y.; Zhang, Y.; Xu, J. Ni12P5-Supported Marigold-Shaped $CdIn_2S_4$: A 2D/3D Non-Noble-Metal Catalyst for Visible-Light-Driven Hydrogen Production. *J. Phys. Chem. C* **2023**, *127*, 4853–4861.

202. Li, X. li; Wang, X. jing; Zhu, J. yu; Li, Y. pei; Zhao, J.; Li, F. tang Fabrication of Two-Dimensional $Ni_2P/ZnIn_2S_4$ Heterostructures for Enhanced Photocatalytic Hydrogen Evolution. *J. Chem. Eng.* **2018**, *353*, 15–24.

203. Xiang, Z.; Guan, H.; Zhang, B.; Zhao, Y. Electrostatic Self-Assembly of 2D-2D CoP/$ZnIn_2S_4$ Nanosheets for Efficient Photocatalytic Hydrogen Evolution. *Journal of the American Ceramic Society* **2021**, *104*, 504–513.

204. Yang, Z.; Shao, L.; Wang, L.; Xia, X.; Liu, Y.; Cheng, S.; Yang, C.; Li, S. Boosted Photogenerated Carriers Separation in Z-Scheme $Cu_3P/ZnIn_2S_4$ Heterojunction Photocatalyst for Highly Efficient H_2 Evolution under Visible Light. *Int. J. Hydrog. Energy* **2020**, *45*, 14334–14346.

205. Zeng, D.; Lu, Z.; Gao, X.; Wu, B.; Ong, W.J. Hierarchical Flower-like $ZnIn_2S_4$ Anchored with Well-Dispersed $Ni_{12}P_5$ Nanoparticles for High-Quantum-Yield Photocatalytic H_2 Evolution under Visible Light. *Catal. Sci. Technol.* **2019**, *9*, 4010–4016.

206. Wu, B.; Liu, N.; Lu, L.; Zhang, R.; Zhang, R.; Shi, W.; Cheng, P. A MOF-Derived Hierarchical CoP@$ZnIn_2S_4$ Photocatalyst for Visible Light-Driven Hydrogen Evolution. *ChemComm* **2022**, *58*, 6622–6625.